ABSTRACT

Title of Dissertation: Individual Blade Control for Vibration Reduction of a Helicopter with Dissimilar Blades

Beatrice Roget, Doctor of Philosophy, 2004

Dissertation directed by: Professor Inderjit Chopra
Department of Aerospace Engineering

A control method is proposed to reduce vibrations in helicopters using active trailing-edge flaps on the rotor blades. The novelty of the method is that each blade is controlled independently, taking into account possible blade dissimilarities. This is different from previous control approaches that assumed blades were identical and generated a single control input which is applied with adequate phase shift to each blade.

The controller is developed in discrete time, with the control inputs updated every rotor revolution. The method consists of performing simultaneous system identification (using Kalman filtering technique) and closed loop control (using a deterministic control law) at each time step. For the system identification, different inputs are applied to each blade, and the relationship between the individual blade inputs and the resulting loads in the fixed frame is estimated on-line, assuming a linear-time-periodic model of the helicopter.

A comprehensive rotor analysis, including all blade degrees of freedom and a free wake model for computing the inflow across the rotor disk, was used to investigate the controller performance in detail. The rotor model is based on a modern bearingless rotor that includes detailed modeling of trailing edge flap effects. The controller performance was tested at advance ratios from $\mu = 0.10$ to $\mu = 0.40$, both for a baseline rotor with identical blades and a damaged rotor with dissimilar blades. In the case of the dissimilar rotor, comprehensive analysis predicts that allowing independent control inputs for each blade dramatically improves the vibration reduction compared to restricting the control inputs to be specific phase shifted versions of each other. For example, at $\mu = 0.30$, the vibration index is reduced by over 90% using individual inputs, compared to only 45% using phase-shifted inputs, for both structural and aerodynamic blade dissimilarities. Required flap deflections are similar for both methods, around $\pm 2.5^{\circ}$.

In order to test the controller experimentally, a Mach-scale rotor model was fabricated. The rotor model consists of 4 blades with piezo-ceramic actuated trailing edge flaps. A new type of hinge using flexures was designed to improve the flap articulation and incorporated in each blade.

The smart rotor model is then fitted on a bearingless model-scale hub and tested both on a hover stand and in the Glenn L. Martin wind tunnel. Both rotating-frame as well as fixed-frame vibratory loads were targeted in the closed-loop control tests. These tests demonstrate the controller's ability to account for blade dissimilarities and generate different optimal inputs for each blade. For example, in hover, at 500 RPM, the 1/rev bending moment at the root of three of the blades was simultaneously reduced by 77% using three active blades.

In forward flight, the controller could simultaneously reduce the baseline 4/rev fixed frame vibration as well other harmonics of vibration such as 1/rev and 3/rev arising from blade dissimilarities. It was also possible to minimize vibration in the fixed frame for several loads simultaneously. However, for most control tests, increases in other loads (not included in the control objective) were observed. During most closed loop tests, the maximum allowable input to the actuators was reached. It was found that the method used to account for actuator saturation and maintain actuator input within acceptable limits had an important effect on controller performance. The best controller performance was obtained when control inputs are computed by solving the constrained minimization problem. However, this procedure is very time consuming and could not be implemented in real-time with the available computer.

It can be concluded that accounting for blade dissimilarities using individual inputs for each blade results in improved vibration reduction. However, to maximize the benefits of this control scheme, an efficient, practical method to limit control inputs needs to be devised.

Individual Blade Control for Vibration Reduction of a Helicopter with Dissimilar Blades

by

Beatrice Roget

Dissertation submitted to the Faculty of the Graduate School of the
University of Maryland, College Park in partial fulfillment
of the requirements for the degree of
Doctor of Philosophy
2004

Advisory Committee:

Professor Inderjit Chopra, Chairman/Advisor
Professor Robert Sanner
Professor Roberto Celi
Professor Norman Wereley
Professor Dianne O'Leary

DEDICATION

To my parents

ACKNOWLEDGEMENTS

I would like to thank my advisor Professor Chopra for his guidance, encouragement and patience during my graduate studies.

I would also like to thank the members of my committee, Dr. Roberto Celi, Dr Robert Sanner, Dr. Norman Wereley and Dr. Dianne O'Leary for their time and effort, and for providing helpful suggestions for my research.

I am very grateful to my colleagues in the Rotorcraft center for their help and friendship. I would like to thank Anubhav and Jinwei for their help with the comprehensive analysis part. Many students in the laboratory helped me with the experimental interface, in particular Jayant, Jinsong and Anne. I would also like to thank everyone who helped during the wind tunnel testing, especially Dr V.T. Nagaraj, Jayant, Jinsong, Anubhav, Anne, Jaina, and many others. I would like to give special thanks to Jaina for taking time to help me not only with the wind tunnel testing, hover tests and vacuum chamber tests, but also in improving the control algorithm for the experiments.

Finally, I thank my parents and my sisters and brothers, Nathalie, Celine, Diane, Gabriel, Flavie, and Timothee, for their love and support.

TABLE OF CONTENTS

LIST OF TABLES

LIST OF FIGURES

LIST OF SYMBOLS

EI_a	Actuator stiffness
EI_f	Flexure stiffness
F	Fixed frame hub vibration vector
F_{flap}	Force exerted by flap at actuator tip
h	Distance from actuator tip to flexure root
H	Measurement matrix
I	Identity matrix
J	Scalar non dimensional vibration objective function
K	Kalman gain vector
L	Actuator length
l	Flexure length
M_Λ	Actuator induced bending moment
M_y	Flap bending moment at blade root
N_b	Number of blades
N_h	Number of harmonics
P	Covariance of estimation error
Q	Covariance of process noise

r	Covariance of measurement noise
rev	Rotor revolution
R	Rotor radius (dimensional)
T	Transfer matrix relating flap inputs to hub vibration
W_z	Weighting matrix for fixed frame hub loads
W_γ	Weighting matrix for control inputs
$W_{\Delta\gamma}$	Weighting matrix for control input rates
x	State vector
z	Measurement vector
δ	Trailing edge flap deflection
γ	Command input for trailing edge flap
γ_{max}	Upper limit for command input
$\Delta\gamma$	Flap actuation increment in 1 rev
μ	Advance ratio
Ω	Rotor speed (dimensional)

Subscripts

k	Blade number
n	Iteration number
$(\,)_0$	Uncontrolled

Chapter 1

Introduction

1.1 Background

Helicopters are unique in their capability to hover, take off and land vertically, and perform low speed maneuvers, in addition to conventional cruise in forward flight. Because of their mission flexibility, they provide unparalleled capability for search and rescue missions, peace-keeping and combat operations, as well as the promise for a convenient mode of runway independent transportation. The source of this unique capability is the main rotor system, which generates lift and thrust, as well as provides most vehicle control forces simultaneously. However, the unsteady aeromechanical environment of the main rotor is a source of enormous fuselage vibration. For example, 90% of fuselage vibrations for the UH-60 helicopter originates from the main rotor. This vibration level is over 100% higher than the target value [1]. Reducing vibration levels of the helicopter would have many benefits such as reducing maintenance cost by increasing the fatigue life of critical structural components, reducing crew fatigue, improving crew awareness and reliability, and improving community acceptance by increasing passenger comfort.

1.2 Helicopter Vibrations

Most of the vibration and noise in the helicopter originates from the main rotor. In forward flight, the rotor blades encounter a highly complex flow field in the advancing and retreating sides of the rotor disk. This is due to time varying pitch angles, the unsteady vortex wake in the flow field, and their mutual effects and interactions with blade passage. Rotor blades encounter strong transonic effects at high speed, Blade Vortex Interaction (BVI) at low speed, dynamic stall at high disk loading, especially during high acceleration pull-ups and diving turns. The unsteady wake effects are due to the presence of the tip vortices in the flow field. This complex and unsteady aerodynamic environment combined with the structural dynamic response of the long, flexible rotor blades undergoing large deformations in flap, lag, and torsion, results in large oscillatory blade loads. These loads are then transmitted to the fuselage via the rotor hub shaft and pylon assembly.

1.2.1 Vibrations caused by Blade Dissimilarities

When the blades are identical (tracked rotor), the rotor hub acts as a filter and only kN_b/rev harmonic loads occurring at the hub are transmitted to the fuselage (where N_b is number of blades and k is an integer). On the other hand, if the blades are dissimilar or damaged, significant non-kN_b/rev loads are also transmitted to the helicopter fuselage (illustrated in Fig. 1.1). Even without apparent damage, minute dissimilarities under normal operating conditions can increase the fuselage vibration level. For example, in one typical recorded flight, 2/rev and 6/rev vertical vibration account for 19% and 5% of total pilot seat vibrations of the UH60A at a high speed flight [1].

Imbalance of the rotor blades originates from two primary sources: (1) inertial imbalance, and (2) aerodynamic imbalance. Inertial imbalance is caused by

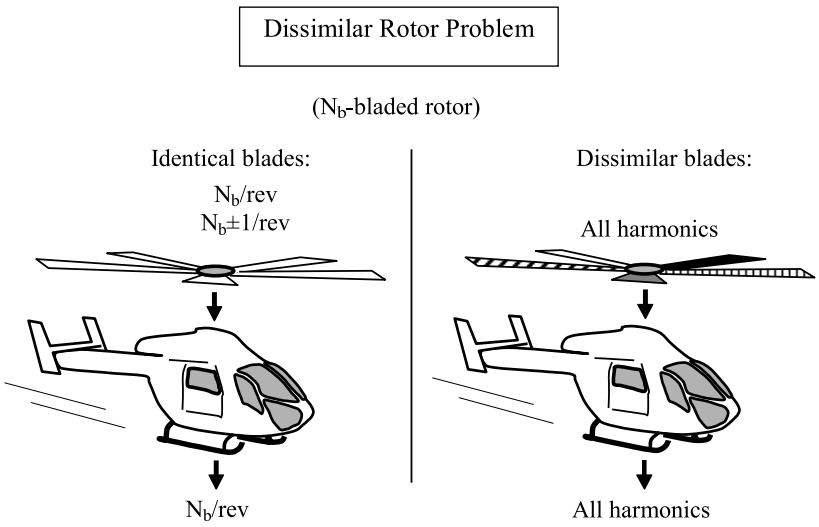

Figure 1.1: Fixed frame loads for a dissimilar rotor

differences in mass and/or mass distribution between the rotor blades, and occurs when the center of inertia does not coincide with the rotational axis of the rotor. This results in a 1/rev radial force at the hub. The aerodynamic imbalance occurs when the aerodynamic forces and moments acting on the rotor differ from one blade to another blade. This can be due to differences in blade twist, airfoil shape, or blade drag characteristics. Aerodynamic imbalance causes the dynamic structural blade response to differ, and as a consequence, different blade tips do not follow the same path. In this case, the rotor is said to be "out of track".

1.3 Vibration Reduction Mechanisms

High vibration translates directly into high maintenance and operating cost and degrades crew and systems effectiveness. Therefore, there is a need of passive and active control devices to reduce vibrations.

1.3.1 Passive vibration control methods

Traditionally, vibration reduction is achieved by passive means such as pendulum absorbers [2–4] or modal placement methods [5, 6]. The main disadvantage of passive methods is that they have limited effectiveness over a narrow range of operating conditions. Vibration suppressors can be easily installed at critical points inside the fuselage, and do not require detailed knowledge of vibration sources. However, they are associated with large weight penalties and degrade rapidly away from the tuned flight condition. Vibration absorbers can also be installed directly on the rotor hub, and can be self-tuning with the rotor speed. However, in addition to a large weight penalty, they create an increase in parasite drag. Other passive methods such as aeroelastic optimization [7] and composite couplings [8] do not have any weight penalty but the vibration reduction achieved is at most 10 to 40% at a particular flight condition. The target reduction level for the next generation rotorcraft is one order of magnitude lower than current levels and this could be achieved by an active control mechanism. Several approaches of active control have been investigated by researchers, which can be efficient over a wide range of operating conditions and result in limited weight penalty. In the following sections, three control techniques are discussed: Active control of structural response (ACSR), Higher Harmonic Control (HHC), and Individual Blade Control (IBC).

1.3.2 Active control of structural response

Active control of structural response (ACSR) is a method to reduce vibrations in the helicopter cabin using high authority actuators at critical locations in the fuselage. A practical drawback of this method is that it requires a detailed model of the coupled rotor-fuselage dynamics in order to determine the optimal placement of actuators for maximum vibration reduction. Two helicopter

manufacturers have implemented the ACSR method: for example, Westland helicopters on the production EH-101 [9, 10] and Sikorsky on the S-76 [11] and S-92 [12] helicopters.

ACSR implements control in the fixed frame of the helicopter. Active control methods in the rotating frame have greater flexibility because they eliminate vibration directly at its source, and do not need to be redesigned with changes in airframe or crew station layout. In addition, they offer significant benefits, such as performance enhancement and stall alleviation. They are implemented by actuating the rotor blades at higher harmonics of the blade frequency of rotation to generate unsteady forces, which when properly phased counteract existing vibratory air loads. Several implementation techniques have been considered, described in the following sections.

1.3.3 Higher Harmonic Control

Higher Harmonic Control (HHC) uses actuation of the non-rotating swashplate to change the pitch angles of rotor blades to reduce vibration. The swashplate is actuated at a frequency of N_b/rev in both collective and cyclic (longitudinal and lateral) modes. A N_b/rev collective input results in N_b/rev variation in blade pitch angle, while a N_b/rev cyclic input results in $(N_b - 1)$/rev and $(N_b + 1)$/rev variation in blade pitch angle. Blade pitch variations in turn result in mostly $(N_b - 1)$/rev, N_b/rev and $(N_b + 1)$/rev harmonics in the rotating frame loads, which are the dominating harmonics contributing to the fixed frame vibration (for a rotor with identical blades). Therefore, only N_b/rev input is desired for N_b/rev vibration reduction.

HHC has been demonstrated to reduce vibrations through numerical simulations [13–17], model and full scale wind tunnel tests [18–21], as well as full-scale flight tests [22–24]. Typical pitch input requirements are smaller than 3 degrees.

Although substantial vibration reduction was achieved using HHC at several flight conditions, two major disadvantages of this method are: (1) the high actuation power required to force the rotor blades at N_b/rev and (2) the large weight penalty associated with the increased authority hydraulic actuators. Moreover, an additional drawback comes from the fact that only N_b/rev excitation of the swashplate is practical for reduction of the N_b/rev vibration in the fixed frame. However, other control objectives such as stall alleviation or blade loads reduction may require excitation of the blades at other harmonics [25]. This is not possible using HHC, since non-N_b/rev swashplate excitation would result in the pitch variation with azimuth to be different from blade to blade. This in turn would create a large 1/rev in the fixed frame. An extension of the HHC technique was therefore developed to improve on these limitations, termed as IBC (Individual Blade Control).

1.3.4 Individual Blade Control

The term IBC was first introduced to refer to a control technique that uses blade root actuators in the rotating frame to individually control each blade pitch [26]. More generally, the term IBC can be used for any control method that uses a system in the rotating frame to modify blade loads and achieve the control objective. The main advantage of the IBC technique is that it makes it possible to control each blade independently at any frequency (within the actuator bandwidth), not just integer multiples of the rotor frequency (1/rev). Thus, time domain control can be implemented, for example with a feedback loop for each blade in the rotating frame. In addition to vibration reduction, the IBC concept can be extended to other important applications, such as noise reduction, lag damping augmentation, and stall, flutter suppression.

1.3.5 IBC using blade pitch actuation

The first implementations of IBC were developed with other objectives than vibration reduction. An early study by Kretz [27] used a rotor with two blades, each controlled independently by actuators located in the fixed frame, to alleviate instabilities at high advance ratios. Another study by Guinn [26, 28] described a helicopter main rotor control design with blade actuators in the rotating frame, which would provide the 1/rev blade pitch input required for trim and control, independent of a swashplate.

Significant work on IBC was conducted by Ham [29–31]. The IBC system used hydraulic actuators mounted on the pitch links to independently control each blade. A control system was also designed, based on modal decomposition of blade dynamics, that used feedback of on-blade measurements to control the response of the blade first elastic flatwise mode.

Considerable effort has been devoted towards the practical implementation of IBC systems in the helicopter industry. Three of the key efforts are:

(1) A hydraulic actuator IBC system was developed and extensively tested both in wind tunnel and in flight on a B0105 helicopter [32–37]. Single frequency, open loop tests were conducted on this 4-bladed hingeless rotor. Significant reduction of vibration and noise levels was observed using a 2/rev blade pitch angle.

(2) A cooperative research program by ZF Luftfahrttechnik (ZFL) in Germany, NASA Ames Research Center, and Sikorsky led to the development of a similar blade root actuation system to provide independent blade control. This system was installed on the Sikorsky UH-60 and is currently under experimental investigation [38, 39].

(3) Recently, an experimental IBC system was developed, extensively tested,

and certified in Germany (ZFL) for the CH-53G [40, 41]. For this 6-bladed articulated rotor, promising results have been obtained in open loop control. For example, more than 60% vibration reduction was achieved locally without any increase in other locations, using a 5/rev IBC input. Noise reduction and reduction of required rotor power were also demonstrated using 2/rev IBC inputs. Closed loop control tests are currently underway to reduce several parameters simultaneously.

Thus, the IBC technique shows considerable potential to achieve diverse objectives, not only vibration reduction but also noise reduction and rotor performance enhancement. However, IBC using blade pitch actuation does present important drawbacks: it requires a heavy and complex hydraulic slip ring, as well as large actuation power to pitch the entire blade.

This naturally led to the idea of using on-blade actuation in order to palliate these drawbacks while retaining the advantages.

1.3.6 IBC using on-blade actuation

Both the HHC and the IBC methods described in the previous section modify blade airloads by varying the pitch angle of the entire blade. This is not an efficient way of producing the desired changes in airloads, because the inboard sections of the blade lie anyway in a region of relatively low dynamic pressure, and do not contribute significantly to the airloads.

On-blade actuation methods alter the high dynamic pressure airloads at the outboard stations. They include active flaps, active twist and active blade tip.

Active Flap

On-blade flaps are generally classified as plain flaps and servo-flaps. Deflecting a flap produces a local change in lift and pitching moment. A plain (or

trailing-edge) flap produces mainly a change in local lift, while a servo-flap (or moment flap) produces mainly a change in pitching moment which indirectly results in a change in elastic blade twist.

On-blade flaps have been used in the past for primary flight control. For example, Kaman helicopters [42, 43] use on-blade servo-flaps to control blade pitch. Kaman also investigated the use of servo-flaps for vibration reduction [44, 45]. In this study, steady and 1/rev deflections were controlled by the swashplate, while 4/rev control was introduced by electrohydraulic actuators in the rotating system. Flap deflections of up to ± 6 degrees were achieved at 4/rev, resulting in significant vibration reduction.

Recently, the potential of active plain flaps for vibration reduction was investigated on model-scale, four-bladed rotors at McDonnell Douglas [46–48], where the flaps were driven by a cam and cable linkage, and at Sikorsky [49], using rotating frame hydraulic actuators.

In addition to experimental studies, extensive analytical studies [50–54] have been performed. Using a model of the active flap, these studies predicted a level of vibration reduction comparable to conventional IBC while using moderate input angles.

However, the weight and complexity of the actuation system remains a major barrier to the practical implementation of this technique in real helicopters.

Successful development of smart material actuators in recent years has renewed interest for on-blade actuation IBC technique [55–57]. The smart material actuators are light weight, compact, and have low power requirement. Thus, they present a considerable potential for improved vibration control, noise control and performance enhancement.

Smart materials used for actuators respond to an external field (electric, magnetic, or thermal) and generate an induced strain in the host structure. Among smart materials, piezoelectric materials are particularly attractive because they

are compact, light weight and have a high bandwidth. When a piezoelectric material, such as a piezoceramic, is exposed to an electric field, it undergoes mechanical deformation, which can then be transmitted to the structure. Piezoceramics are generally produced in the form of thin sheets or fibers that can be embedded in a structure. A review of the state of the art of smart structures and integrated systems can be found in Reference [58]. Considerable research has been devoted to the development of a smart actuation system for helicopter rotors.

Piezoelectric materials can also be used to actuate flaps. Extensive research has been conducted at the University of Maryland on model scaled rotors using piezo-bender elements [59–61]. Piezoelectric benders consist of two or more piezoelectric sheets stacked together such that actuating layers on opposite sides of the neutral axis results in opposite strains: the opposite strains then cause the entire bender to flex. After improvements on the original design, up to $\pm 4^\circ$ flap deflections were obtained at rotor speed of 1800 rpm [62]. Closed loop Mach-scaled control tests in wind tunnel demonstrated dramatic vibration reduction in the 4/rev fixed frame loads. Researchers at MIT and NASA have investigated the use of piezo-bender actuated flaps on a model scale rotor, resulting in improved actuator designs [63, 64]. The smart rotor was tested both in hover and forward flight at reduced tip speeds. Deflection of $\pm 5^\circ$ were obtained at 760 rpm, which could alter significantly the blade torsion and flap bending loads. Modifications of the conventional straight piezo bender have also been proposed, such as the C-Block actuator [65, 66].

Another type of actuators uses piezoelectric stacks, constructed by laminating multiple piezoelectric layers. Piezo-stacks offer greater actuation force at the cost of lower displacements. Several designs for stroke amplification have been proposed, resulting in actuators such as such as the X-frame actuator [67–69]. This actuator was integrated in a Mach-scale blade with trailing edge flap and

tested in hover.

Active Twist

Piezoelectric materials can be embedded in rotor blades and actuated to produce a controllable blade twist. This technique was implemented by Chen and Chopra [70–72], by embedding piezoelectric monolithic elements at $+45°$ under the upper skin and $-45°$ under the lower skin of the rotor blade. Blade tip twist amplitudes of $\pm 0.25°$ were achieved, and significant changes in the hub loads were measured. Another way to induce blade twist is to integrate active piezoceramic fibers in a resin matrix to create a composite material (Active Fiber Composite, ACF) [73–76]. When this composite ply is cured in a $+45°/-45°$ orientation on the blade, actuation results in a linear twist along the blade. Several research teams have tested the active blade twist concept using ACF on model scale rotors [77–79], achieving tip blade twists of up to $\pm 1°$.

Active Blade tip

Bernhard and Chopra [80–82] proposed an actuation mechanism using a bending-torsion coupled composite beam with piezoceramic sheets bonded on its surface. Actuating the beam in bending results in a tip twist, which was used to rotate a moving blade tip (10% of blade span). A Mach-scaled model was built, and up to $\pm 2.8°$ deflections were obtained at 2000 rpm in hover. This resulted in over 50% variation in the steady rotor thrust level at $8°$ collective.

Full-scale implementation

While most experimental investigations have been based on model scale rotors, some effort has been made toward full scale implementation of smart structure actuators for on-blade control of helicopters. Eurocopter is developing two

types of smart actuators: piezo-ceramic actuators combined with a 15% chord flap integrated in modified BK117 blades [83, 84], and electromagnetic actuators combined with a 25% chord flap integrated in a modified Dauphin blade segment [85, 86]. Fink [87] used an electromagnetic actuator to drive a 46% chord flap on a OH-58 Kiowa Warrior rotor blade. At McDonnell-Douglas/Boeing [88–90], a detailed feasibility study was conducted for a full scale active flap. The flap is to be integrated in a MD900 Explorer rotor blade and is actuated by a scaled up version of the X-frame actuator described above. This rotor was successfully tested in hover and is currently being prepared for forward flight testing. Lee and Chopra [91] developed a bi-directional flap actuator driven by piezostacks, based on lever arm amplification. The actuator was designed to deflect a trailing edge flap on a blade section of a full-scale MD900 helicopter. This section model was successfully tested in the wind tunnel (non-rotating) and in the vacuum chamber (rotating).

1.3.7 Reducing vibration caused by rotor imbalance

The vibration reduction approaches described in previous sections assume identical rotor blades, and do not consider the additional vibration which arises when blades are dissimilar. The IBC approach, either through complete blade feathering or using some on-blade actuation system, allows each blade to be controlled independently, and therefore can be used to reduce vibration arising from blade dissimilarities (at non-kN_b/rev frequencies). However, existing control methodologies do not make use of this capability. They use the same phase-shifted control inputs to all blades, assuming a tracked rotor (identical blades). Instead, separate methods have been developed to minimize vibration caused by rotor imbalance. These methods can be divided into two groups, manual adjustments methods, and active in-flight methods.

Manual adjustments methods

The magnitude of rotor imbalance can be minimized during manufacture and assembly by imposing tight tolerances. However, such a procedure leads to high manufacturing cost. Also, even with blades properly matched, subsequent warping and play in the pitch and sweep angle adjustment linkages may result in substantial imbalance.

Inertial imbalance is usually corrected by adding mass to one or more of the blades. Aerodynamic imbalance is often corrected by adjusting a pitch link that is attached to the blade and rotor hub. The pitch link is a manually adjustable variable-length link. Varying the length of the pitch link results in changes in pitch angle at the blade root, causing that particular blade to follow a different path. Another method uses plastically deformable tabs provided on the trailing edge of each rotor blade. The tabs extend the trailing edge about one inch for a section of the blade span. Bending the tabs changes the effective camber of the rotor blade and thus changes the aerodynamic forces it generates. Trim tabs and/or pitch link lengths are set when the rotor is stationary. The rotor is then subjected to a series of whirl tests during which the track of each blade is determined either manually, using a marking device at the blade tips, or using sensors to detect vibrations transmitted to the helicopter fuselage. The rotor is then stopped and tabs or pitch link lengths are adjusted iteratively until acceptable tracking is obtained.

A major problem with this approach is that it requires highly skilled trained personnel. Also, because tab position and pitch link length can vary over time, this procedure must be performed periodically, which results in a significant increase in helicopter down-time and operating costs. Also, the method is approximate and is based on the assumption that unwanted vibrations originating from imbalance will be minimized when all blade tips follow the same path.

Moreover, a tracking adjustment that is optimum in hover may not be optimal for other flight conditions.

Active in-flight methods

Considering the various drawbacks of manually adjusting track, efforts have been devoted towards developing systems capable of making in-flight tracking corrections. For instance, the Kaman SH-2G Super Seasprite and K-MAX helicopters [42, 43], as well as the Bell 214ST have the ability to perform track adjustments during flight. The Seasprite and K-MAX use an electro-mechanically actuated servo-flap, while the Bell helicopter uses an electro-mechanical actuator between the pitch horn and the pitch link to adjust the pitch of the blade. The tracking device in both rotorcrafts is embedded in the primary flight control linkage, and therefore needs to be robust and heavy. As a result, a large weight penalty is a common drawback of these approaches.

As in the case of active vibration reduction research, the recent development of smart materials has allowed actuator systems to be proposed for in-flight rotor tracking adjustment. The advantage of using smart material actuators is that the control system is light weight and can be decoupled from the primary flight control system. For example, McKillip [92] proposed using a remotely controllable trim tab system actuated by shape memory alloy material (SMA). A SMA material can be plastically deformed at room temperature and, when heated to a higher temperature, the material returns to its original undeformed shape. Other researchers also proposed and tested systems for in-flight tracking of helicopters that used SMA actuators for flap deflection [93–96]. Another system proposed by Hall et al. [97], employs a trailing-edge flap, and a piezoelectric actuator for deflecting the flap. Recently, a novel approach for providing 1/rev vibration reduction was developed, which used SMA-actuated two-position

tracking tabs [98]. This system was installed and successfully tested on a Bensen autogiro.

1.4 Control Strategies for vibration reduction

For reduction of the baseline kN_b/rev vibration, all blades are actuated in the same manner when they pass through a particular azimuth. In other words, there is a precise $\frac{2\pi}{N_b}$ phase shift between actuation signals from blade to blade. This mode of control is illustrated in Figure 1.2. It can be readily seen that using such phase shifted inputs to reduce vibration caused by blade dissimilarity is inefficient. Indeed, because of the filtering role of the rotor, the vibratory loads generated in the fixed frame by blade actuations will be dominantly N_b/rev. The generated non-N_b/rev vibratory loads will be small, because it originates from the small rotor imbalance (Figure 1.3). Therefore, a very large command input would be necessary to see some effect on the vibration caused by rotor imbalance, and it would most likely lead to actuator saturation. On the other hand, if the blades are actuated independently, the differences in airloads produced on each blade would lead to significant non-N_b/rev vibratory loads being generated at the hub,and it may be possible to target both N_b/rev and non-N_b/rev vibratory loads using a small actuator command input, as illustrated in Fig 1.4.

1.4.1 Review of Previous Control Algorithm

The first effort that used active control for vibration in helicopter rotors was by Kretz et al. [99]. McCloud and Kretz [100] in a follow up work tested the HHC method of active control on a full-scale jet-flap rotor in the 40×80 ft wind tunnel. This work examined the response of the blade loads and vibrations in the rotating frame to HHC. The concept of a linear, quasi-static representation of the

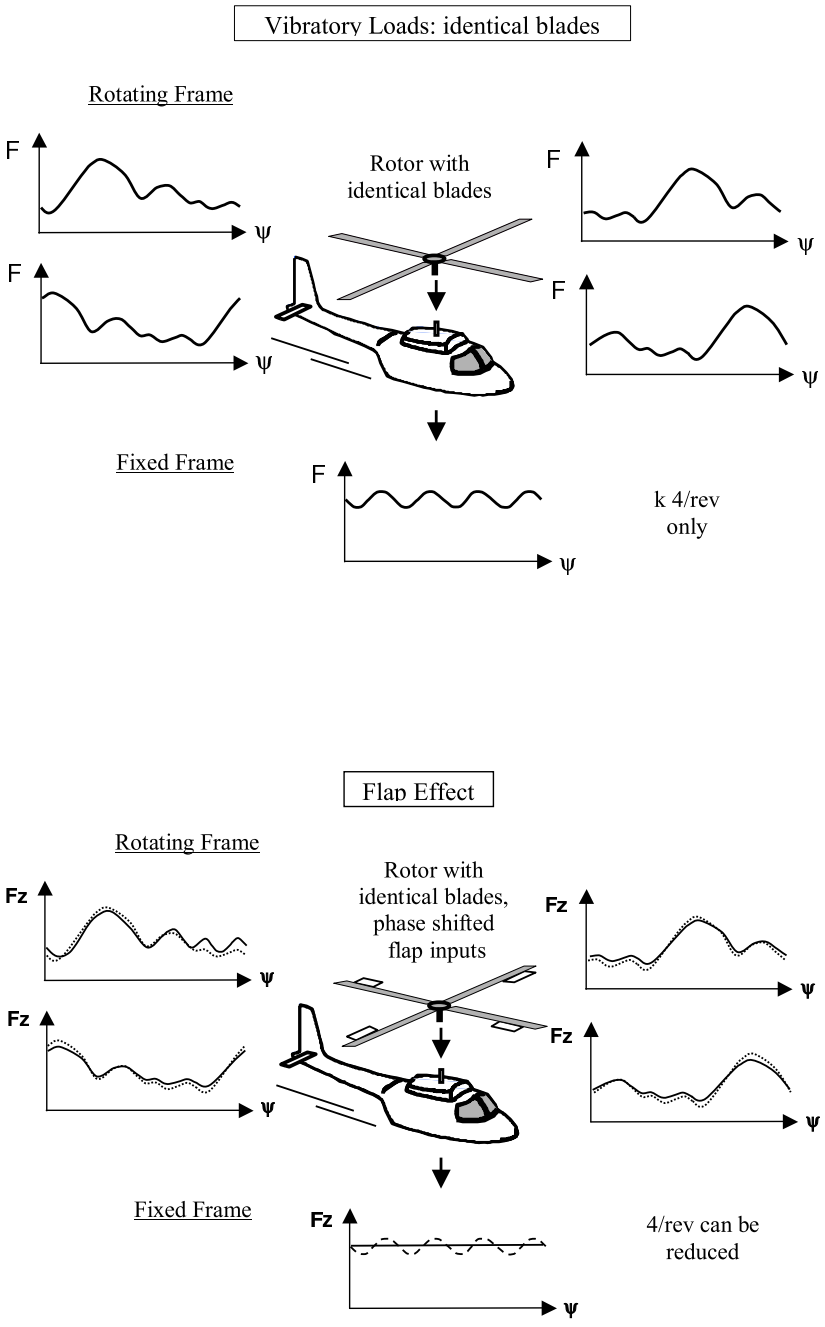

Figure 1.2: Phase shifted control scheme for an identical bladed rotor

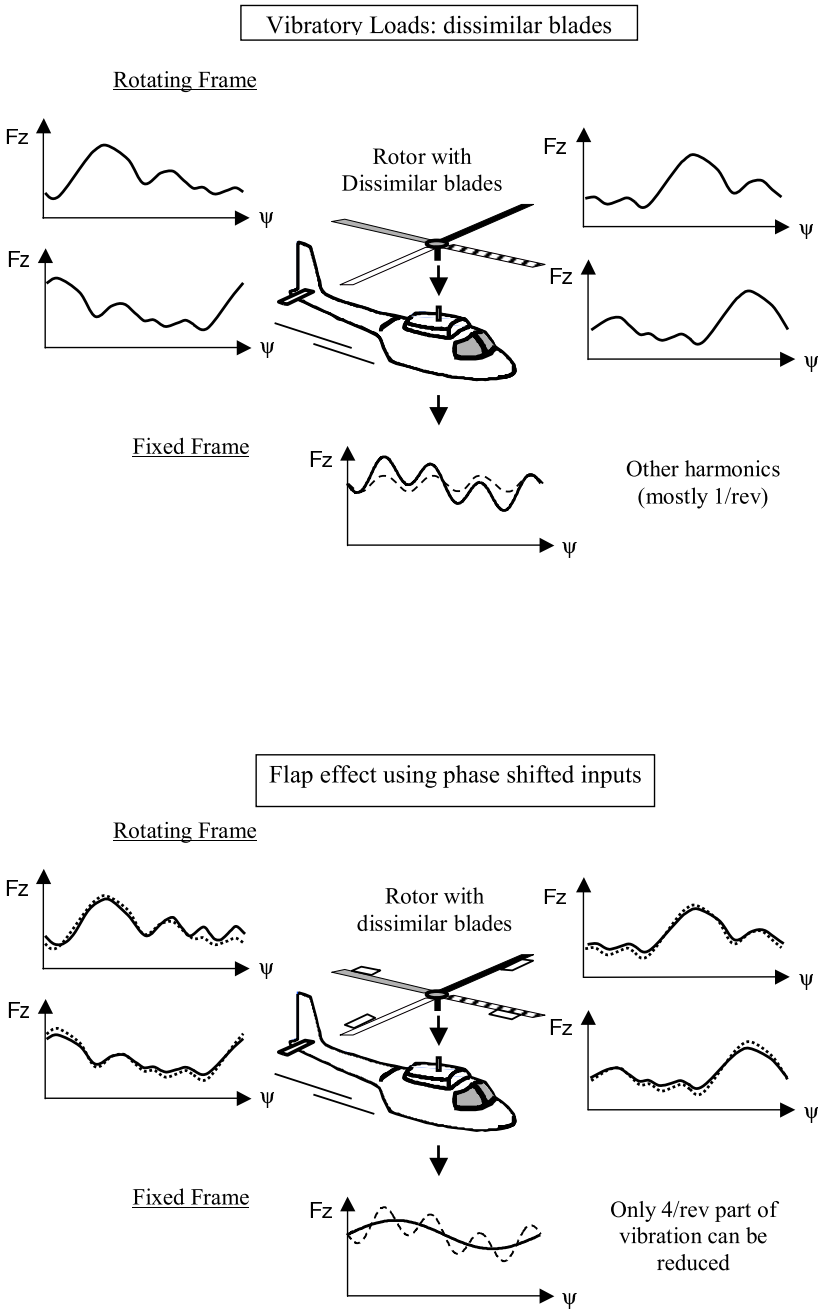

Figure 1.3: Phase shifted control scheme for a dissimilar bladed rotor

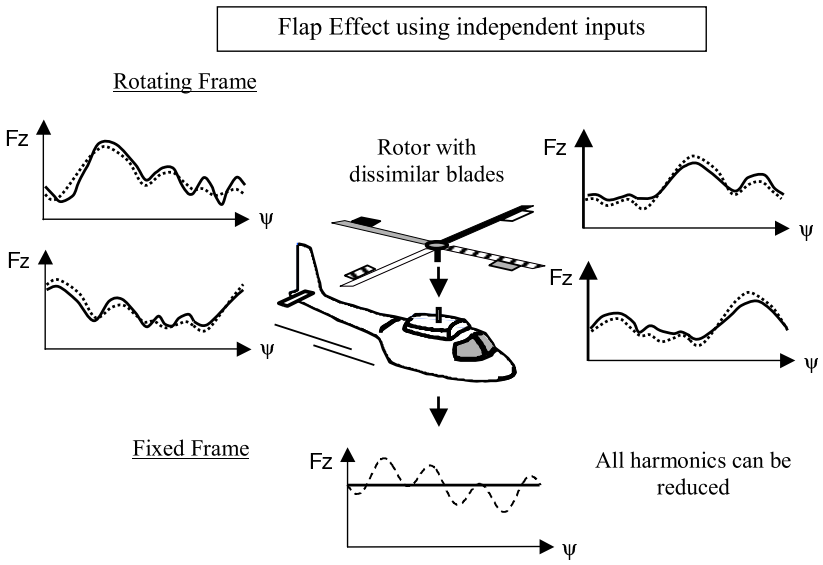

Figure 1.4: Independent control inputs for a dissimilar bladed rotor

responses (including the notation T for the transfer matrix) was introduced. The transfer matrix was evaluated from the wind tunnel data by the least-squares method. The open-loop control required to minimize a quadratic performance function was then calculated. It was shown that substantial fuselage vibration reduction can be obtained using HHC. The concept of using periodic inputs to a rotor blade control device to counteract the periodic vibratory loads in general referred to as multicyclic control.

McCloud [101] further advanced the idea of using transfer matrices for multicyclic control, for a four bladed, articulated, controllable-twist rotor. The transfer matrix concept was used to determine the HHC input magnitudes and phases required to minimize the sum of the squares of the vibratory loads. The algorithm was subsequently tested on a full-scale rotor in two wind tunnel tests. It was shown that the HHC could substantially reduce not only the rotor blade bending loads, but also the N_b/rev vibration at the fuselage stations instrumented with accelerometers. This work clearly established the validity of using the linear transfer matrix representation. However, this work also showed the

the transfer matrix was not invariant with airspeed, but rather was strongly dependent on the flight conditions. Shaw and Albion [19] in a later study confirmed these findings from the observations gathered from testing a model-scale four bladed hingeless rotor.

Shaw and Albion [19] also demonstrated the feasibility of designing a closed-loop, HHC vibration control system which obtains a deterministic control law based on the linear transfer matrix concept. However, to be effective at several flight speeds, a method had to be devised to adapt or re-identify the transfer matrix elements with each flight condition. A Kalman filter was adopted for this purpose and was found to be quite successful in low-speed flight. However, in a later work, which tested a three bladed scaled CH-47D rotor, Shaw [102] showed that the same level of vibration reduction (up to 90% reduction) can be achieved even when using transfer matrices identified offline. These findings favored the off-line identification method compared to the Kalman filter approach. Indeed, several other researchers also have reported problems when using the classic Kalman filter approach for system identification.

Johnson [103] reviewed the state of the art of the class of self-tuning multicyclic algorithms. The basic single input/ single output algorithms were derived and demonstrated. Most controllers proposed by previous researchers were described ranging from the simplest open-loop time invariant controller to an adaptive closed loop controller with online identification. One of the primary conclusions of this work was that even a fixed gain closed loop controller with the feed back of the measured vibration would provide good performance under suitable conditions.

Chopra and McCloud [104] numerically examined the controllers discussed by Johnson [103] using a multiple input/multiple output simulation. The open loop time invariant system was reported to be effective only for a limited range of operating conditions. Also controller parameters estimated for one flight condition

was found to give poor performance when applied to another flight condition. The closed loop fixed gain controller was found to be effective under low noise conditions. Algorithms that involved real-time estimation of the uncontrolled vibration levels and system parameters were also evaluated in this work.

DuVal et al. [105, 106] proposed a new vibration controller to implement Higher Harmonic Control, which used the state feedback approach. This approach has considerable theoretical differences compared to the multicyclic control approach pioneered by Shaw [19, 102]. In this approach, the states in which vibration is to be suppressed are passed through undamped oscillators that are tuned to resonate at the target N_b/rev frequency. This is equivalent to placing an infinite weight on the N_b/rev part of vibration. A dynamic model of the rotorcraft was used and was combined with the standard linear-quadratic-gaussian (LQG) technique to obtain a set of feedback gains that insured stable control action. The potential advantages of state feedback over adaptive multicyclic approach are :

1. Elimination of the on-line identification process.
2. Elimination of the harmonic analysis of blade loads and responses.
3. Ability to accurately predict stability of the controller from linear system theory
4. Chances of better control authority in maneuvering flight conditions

However, this approach has a drawback of requiring a dynamic model of the rotorcraft, which in most cases is quite approximate. Also the dynamic model would be aircraft specific compromising the generality of this method. Also, the success of this method is yet to be demonstrated for a range of flight regimes. The study performed by Du Val et al. [105] considered only the hovering flight condition.

Hall and Wereley [107, 108] compared the performance of the conventional discrete-time multicylic controller with a continuous-time state feedback controller. They derived the continuous-time equivalent of the HHC algorithm based on the T-matrix formulation and showed that it is essentially similar to the algorithm based on frequency shaped cost function introduced by DuVal et al [105]. They also concluded that implementation of HHC in continuous time rather than discrete time may significantly improve stability, while there would be only marginal improvement in performance.

Kottapalli [109] developed a neural network based controller to reduce vibratory hub loads. The hub loads were characterized in this case using a metric that consisted of five vibratory hub load components obtained from a wind tunnel test of a four bladed rotor with individual blade control. The single input single output neural network controller devised was constrained to converge in six iterations and not use any gradient based optimization technique. The algorithm was reported to be successfully converging to the global minimum within six iterations without using gradient based optimization techniques. This work also compared this control algorithm with a classical one-step deterministic controller and concluded that the two methods were roughly comparable, with the neural net control being slightly more robust.

Recently, Spencer [110] developed a real-time neural network based feedback control system that adaptively activates rotors with smart materiel actuators for vibration reduction. The controller was designed to be capable of broadband activation which necessitated a time domain solution rather than a frequency domain solution as in the case of multicyclic control. The controller developed was tested in a simulated study of four bladed Sikorsky S-76 and five bladed Boeing MD-900 rotors with on-board trailing edge flaps. The proposed algorithm was reported to be insensitive to actuator dynamics and has shown better performance in vibration suppression compared to frequency limited higher harmonic

approaches. Wind tunnel tests were conducted for two Mach scale smart rotor systems that used two different actuation devices, a trailing edge flap [62] and an active tip twist [111]. The controller was reported to be robust and possessing the capability to adaptively learn to control the rotor vibrations with no a-priori information.

Recently, closed-loop wind tunnel tests on a 4-bladed Mach scale rotor using piezo-bimorphs actuated trailing edge flaps were conducted in the Glenn L. Martin wind tunnel [62]. This actuation system successfully minimized 4/rev hub loads by over 90% for steady and transient flight conditions. A neural network based adaptive controller was used where the controller assumed identical blades [112–114]. As a result, large 1/rev loads arising out of rotor dissimilarities could not be controlled. Any attempt to target these non-kN_b/rev loads led to excessive flap requirements. This resulted in saturation of actuators and enormously degraded control performance. In the present study, a new control methodology is used which takes into account blade dissimilarities and reduces both kN_b and non-kN_b/rev loads [115].

1.5 Motivation and Objectives

Despite considerable amount of progress in control algorithms and implementation of the control systems on the actual aircraft, the dream of completely reducing the vibrations to obtain a jet smooth aircraft is still far fetched. One of the primary reasons is the inability to reduce all harmonics of rotor vibration simultaneously. Most of the vibration control approaches assumed identical blades and hence were able to affect only the N_b/rev harmonic of the vibration. Therefore, the primary goal of this dissertation is to devise a control scheme which can affect all the harmonics of rotor vibration. To this end, three major objectives are:

1. Develop a control scheme which considers blade dissimilarities to find optimal actuation for each blade individually. Because this scheme allows each blade to have an independent actuation, it has the ability to affect non-N_b/rev harmonic as well as N_b/rev harmonics of the hub loads.

2. Investigate the performance of the controller analytically using a comprehensive rotor craft analysis (UMARC [116]) as the helicopter model. Analysis would include mathematical modeling of blade dissimilarities and modeling of control scheme that uses active trailing edge flaps. The controller would be tested for different flight regimes and variation in blade dissimilarities.

3. Investigate the performance of the controller experimentally using a smart model scale rotor. The model rotor blades would be built and would incorporate an active trailing edge flap that is actuated by a piezo electric bimorph. The design of the flap system will be optimized to maximize control authority.

1.6 Organization of the Dissertation

This dissertation is organized in three parts. In the first part, the control algorithm is described (Chapter 2) and its performance investigated using a comprehensive rotor analysis (Chapters 3 to 5). In the second part, the fabrication process of a set of Mach scaled blades equipped with piezoelectric bender actuated trailing edge flaps is described (Chapter 6). In the third part, results of tests conducted in vacuum chamber, on hover stand, and in wind tunnel are presented (Chapters 7 and 8).

Chapter 2

Control Algorithm

2.1 Introduction

A control algorithm is developed to achieve vibration reduction in the special case when the rotor blades have dissimilarities, resulting in non-kN_b/rev harmonics in the fixed frame hub vibratory loads.

In theory, reduction of fixed system vibratory loads can be achieved by using the same control inputs to all blades with the appropriate phase. However, when the rotor is dissimilar, the required trailing-edge flap deflection angles for minimization may become too large [62]. Because some degree of rotor dissimilarity is always present, it is necessary to control each trailing-edge flap individually. In order to control the blades independently, it may be necessary to obtain individual information from each blade. In view of the complexities associated with acquiring rotating frame data, the present control scheme is designed to use exclusively fixed frame measurements to extract individual blade information. To this effect, different control inputs are applied to each blade, as illustrated in Figure 2.1. Different control inputs respectively generated for each blade can attempt to minimize both the baseline kN_b/rev vibration and the dissimilarity-induced non-kN_b/rev loads. It is then possible to extract individual

blade information from the knowledge of the fixed frame load measurements and the individual flap control inputs, as explained in the following.

2.2 Algorithm for individual blade control

The linear quasi-static model relating the response vector F to the multicyclic pitch vector δ through a transfer function is described as :

$$F = F_0 + T\,\delta \tag{2.1}$$

F is a vector representing the fixed system hub loads sampled over one rotor revolution at N_s azimuthal points; F_0 represents the uncontrolled fixed system hub forces and moments; δ is a vector containing the N_b individual flap inputs, and T is a $(6N_s) \times (N_bN_s)$ transfer matrix. Note that this model assumes that the fixed system hub loads are periodic. For a 4-bladed rotor, Eq. (2.1) can be written as:

$$\begin{Bmatrix} F_x \\ F_y \\ F_z \\ M_x \\ M_y \\ M_z \end{Bmatrix} = \begin{Bmatrix} F_{x0} \\ F_{y0} \\ F_{z0} \\ M_{x0} \\ M_{y0} \\ M_{z0} \end{Bmatrix} + \begin{bmatrix} T_{11} & T_{12} & T_{13} & T_{14} \\ T_{21} & T_{22} & T_{23} & T_{24} \\ T_{31} & T_{32} & T_{33} & T_{34} \\ T_{41} & T_{42} & T_{43} & T_{44} \\ T_{51} & T_{52} & T_{53} & T_{54} \\ T_{61} & T_{62} & T_{63} & T_{64} \end{bmatrix} \begin{Bmatrix} \delta_1 \\ \delta_2 \\ \delta_3 \\ \delta_4 \end{Bmatrix} \tag{2.2}$$

The fixed system hub loads are numbered from 1 to 6 in the order shown in Eq. (2.2). Each transfer matrix T_{lk} is a $(N_s) \times (N_s)$ matrix relating the l^{th} hub load F_l to the flap input δ_k to blade k. In the case of perfectly identical blades, for any load F_l, there exists a relationship between the transfer matrices T_{lk} and T_{lk+1}:

$$T_{lk+1} = S\,T_{lk} \tag{2.3}$$

where S is a matrix operator that permutes the transfer matrix rows:

$$S = \begin{bmatrix} 0 & I_p \\ I_q & 0 \end{bmatrix} \tag{2.4}$$

with $p = (N_b - 1)\,\frac{N_s}{N_b}$ and $q = \frac{N_s}{N_b}$.

Using this global model, the identification problem involves determination of the transfer matrix, given the control inputs and measured vibration outputs. The transfer matrix varies with helicopter operating conditions (e.g., thrust, airspeed). Therefore, the identification method should be made on-line to track the transfer matrix in real-time. In the present study, the Kalman filter method is used. It is a computationally efficient algorithm designed to update parameter estimates recursively on the basis of a single measurement. Although the uncontrolled vibration vector F_0 can be obtained from measurements with no flap control inputs, it should be estimated along with the transfer matrix T because it will vary with flight conditions and helicopter characteristics. Eq. (2.1) can then be rewritten as:

$$F = [T F_0] \left\{ \begin{array}{c} \delta \\ 1 \end{array} \right\} \tag{2.5}$$

At any iteration n, the typical form for the j^{th} measurement is (measurement model):

$$\begin{aligned} (F_j)_n &= [\delta_n\ 1] \left\{ \begin{array}{c} (T_j)_n^T \\ (F_{0j})_n \end{array} \right\} \\ &= H_n\, x_n + v_n \\ &= z_n \end{aligned} \tag{2.6}$$

where (T_j) is the j^{th} row of T. Following the notations used in Ref. [124], z_n is the measurement vector, x_n is the state vector to be estimated, and H_n represents the measurement matrix. The measurement noise v_n is also included

in the measurement model, and is assumed to be a zero-mean, white sequence of constant covariance r. For simplicity, the subscript j is omitted in these notations. Because the loads are periodic and sampled over one rotor revolution, the state vector dynamics (system model) is assumed quasi-static and is written as:

$$x_n = x_{n-1} + w_{n-1} \tag{2.7}$$

where w_{n-1} is the process noise, assumed to be a zero-mean, white sequence of constant covariance Q. Based on the measurement and system models, the Kalman filter discrete equations for updating state estimates are written as:

$$\textit{Kalman gain matrix}:$$

$$K_n = P_{n-1}{H_n}^T \left[H_n P_{n-1} {H_n}^T + r\right]^{-1} \tag{2.8}$$

$$\textit{Error covariance update}:$$

$$P_n = \left[I - K_n H_n\right]\left[P_{n-1} + Q\right] \tag{2.9}$$

$$\textit{State estimate update}:$$

$$x_n = x_{n-1} + K_n\left(z_n - H_n x_{n-1}\right) \tag{2.10}$$

Note that the Kalman gain vector K_n is same for all j measurements, so that the unknown parameters $[TF_0]$ can be identified in a single step:

$$[TF_0]_n = [TF_0]_{n-1} + \left(F_n - [TF_0]_{n-1}\left\{\begin{array}{c}\delta_n\\ \\ 1\end{array}\right\}\right){K_n}^T \tag{2.11}$$

This represents an important reduction in computation time since P_n and K_n are calculated only once for each time-cycle, and the computation of K_n only requires inversion of a scalar. Once the state estimates are obtained, the optimal control inputs can be determined.

In the present investigation, a deterministic controller is used. For this controller, all the model properties are known from the identification algorithm. The

individual multicyclic controls are based on the minimization of the performance function J, expressed as:

$$\begin{aligned} J &= J_F + J_\delta \\ J_F &= Y^T W_F Y \\ J_\delta &= \delta^T W_\delta \delta + \Delta\delta^T W_{\Delta\delta} \Delta\delta \\ where\ Y &= F - (F_0)_{mean} \end{aligned} \tag{2.12}$$

For simplicity, the subscript n indicating the iteration number is omitted. The weighting matrices W_F, W_δ, and $W_{\Delta\delta}$ are applied to the output response, the individual flap input controls, and the individual flap control rates, respectively. Typically, these are diagonal matrices. Some diagonal elements of W_F can be set to zero to keep the corresponding vibration component uncontrolled. W_δ limits the flap control amplitude, and $W_{\Delta\delta}$ limits the control rate. The objective is to minimize the weighted norm of vector Y, which represents the vibratory part of the hub forces and moments: F is the vector of the fixed system hub loads and $(F_0)_{mean}$ is the vector of steady components for all hub loads. Therefore, when Y is minimized, the vibratory part of each hub loads is minimized while the trim conditions are still satisfied.

The optimal control input for each blade is obtained from the minimization of the performance function J, which means $\partial J/\partial\delta = 0$. This results in the optimal control solution in the form (for $W_{\Delta\delta} = 0$):

$$\begin{aligned} \left(\delta^{opt}\right)_n &= -DT^T W_F Y_n \\ where\ D &= [T^T W_F T + W_\delta]^{-1} \end{aligned} \tag{2.13}$$

Note that the control vector δ contains the individual inputs for each trailing edge flap. This means that if the blades are dissimilar, the control inputs to each blade will differ, even in the case where only one blade is damaged. For

example, for $N_b = 4$:

$$\delta^{opt} = \left\{ \delta_1^{opt} \; \delta_2^{opt} \; \delta_3^{opt} \; \delta_4^{opt} \right\}^T \tag{2.14}$$

2.2.1 Controller using restricted inputs

A more intuitive control strategy [115] could be used whereby only the control input corresponding to the damaged blade is different: For example, the following constraints could be imposed to guide the choice of the optimal control inputs:

1) All blades should contribute to the same level in the reduction of the kN_b/rev fixed frame load ($k > 1$).

2) The more a blade is different from the average blade, the more it should contribute to the reduction of the other harmonics of the fixed frame load.

3) If two blades are identical they should receive identical control inputs.

Using these constraints, an objective function to be minimized for each blade could then be defined. In Ref. [115], a controller imposing the previous constraints was tested. The controller performance achieved for the reduction of the vertical hub load alone was very good (99% reduction in 150 revolutions without noise). However, the constraints were found to be too limiting in the case of multiple loads control, leading to less vibration reduction.

2.3 Modifications for real-time application

2.3.1 Use of harmonics

The controller detailed in previous sections is based on description of vibration and control inputs as vectors of samples over one rotor revolution. This

approach requires manipulation of large size matrices (for example, if $N_s = 60$ points per rotor revolution, with 6 hub loads and 4 blades, the T matrix' size is 360 by 240). It was used only for testing the controller analytically using a comprehensive helicopter simulation code. When the controller is tested in real time, harmonics are used instead of time samples to reduce the size of the matrices in the identification problem. In that case, the linear quasi-static model relating the response vector F to the input vector γ through a transfer function is described as:

$$F_h = (F_0)_h + T_h\,\gamma \tag{2.15}$$

F_h is a vector representing the fixed system hub loads harmonics. $(F_0)_h$ represents the uncontrolled fixed system hub forces and moments; γ is a vector containing the N_b individual flap inputs harmonics, and T_h is a $(12N_h) \times (2N_bN_h)$ transfer matrix. The controller is then developed in the same way as before.

2.3.2 Computation of optimal inputs

Optimal inputs are computed based on the minimization of the performance function J, which results in:

$$\begin{aligned} \left(\gamma^{opt}\right)_n &= -DT_h^T W_F Y_n \\ where\ D &= [T_h^T W_F T_h + W_\gamma]^{-1} \end{aligned} \tag{2.16}$$

Because the matrix D is symmetric positive definite, the conjugate gradient method can be used to efficiently compute optimal weights, in order to decrease computation time.

2.4 Imposing limits on the control command

The weight matrix associated with the flap actuation, W_γ, is a diagonal matrix. The choice of W_γ is important because it determines the amplitude of the control command. It is desired that the control command reaches the maximum allowed value, γ_{max}.

There are several ways to impose this constraint on the flap actuation:

1. adjust (increase) the weights associated to the control inputs until their amplitude becomes lower than the maximum bound.

2. Apply a scaling factor to the command inputs which exceed γ_{max}.

3. Truncate the command input whenever it exceeds the maximum.

However, none of these approaches solve the real problem, which can be formulated as:

$$\gamma_{optimal} = \begin{array}{c} min \\ max_t(\gamma_k) < \gamma_{max}, \\ k = 1\,to\,4 \end{array} \left\{ \| F_0 + T \times \{\gamma_1\ \gamma_2\ \gamma_3\ \gamma_4\}^T - F_{obj} \| \right\} \quad (2.17)$$

where $max_t(\gamma_k)$ signifies the maximum value of the control input for flap k expressed in the time domain over one revolution. This constrained minimization problem can be solved using Matlab function $FMINCON$, which uses a sequential quadratic programming (SQP) method. In this method, the function solves a quadratic programming (QP) subproblem at each iteration. An estimate of the Hessian of the Lagrangian is updated at each iteration using the BFGS formula [131, 132]. This method yields the best results (minimum objective function), however, it is too costly in computer time to use in a real-time application.

In Chapter 4, a simplified analysis is used to investigate controller performance. A value is chosen for W_δ and no explicit limit is imposed on the magnitude of the flap deflection.

In Chapter 5, a comprehensive analysis is used. Limits of ± 4 degrees are chosen for the flap deflection, and imposed by increasing W_δ for the flaps which exceed the maximum value.

In Chapters 7 and 8, a model scale rotor with active trailing edge flaps is used to investigate experimentally controller performance.

Chapter 7 presents results when the control objective is a rotating frame load. In this case flap effects on the target loads are decoupled and it is possible to adjust W_γ for each blade in order to maintain flap actuations below the maximum value.

Chapter 8 presents results when the control objective is a combination of fixed frame loads. In this case, flap effects are coupled and adjusting the weights becomes too expensive in terms of computation time. Therefore, the scaling and truncating methods are used. Identified transfer matrices and uncontrolled vibration are used to create a model of the rotor in the experiment. Based on this model, optimal control inputs are generated by solving the constrained optimization problem defined in Equation 2.17, and compared to the control inputs obtained by the other methods of applying limits.

2.5 Closed-loop identification problem

Closed-loop and open-loop system identification performance may differ significantly. During open-loop identification, random excitation of the system ensures that the system will always generate diverse enough outputs for correct identification. In closed-loop identification, however, the control commands are chosen to minimize helicopter vibration. As the controller approaches a steady-

state optimal control solution, the control commands from one step to the next will not be very different since they are nearly optimal. In this situation, the identified parameters can prematurely converge to values different from the real solution. Another problem can arise when the measurements are contaminated with noise. As the controller reduces the vibration, the stage may be reached where the noise begins to dominate the residual measured vibration signals. The system identification algorithm may therefore erroneously attempt to identify a matrix relating the small changes in control to the random changes in the measurement signal. It should be noted that in some cases, vibration could be well controlled even with a poorly identified transfer matrix. However, in other cases, poorer identification resulted in seriously degraded controller performance, hence it was necessary to improve the closed loop identification.

In order to improve the closed-loop control performance, random input angles of small amplitude are added to the computed optimal control inputs when the identified parameters approach their converged value. An index is defined to quantify the parameter identification convergence, for each blade k, at iteration n:

$$(J_k^{conv})_n = \frac{1}{N_s^2} \sum_{i=1}^{N_s} \sum_{j=1}^{N_s} |T(i,j)|_n - |T(i,j)|_{n-1} \tag{2.18}$$

When the convergence index for each blade becomes small enough, the computed optimal inputs for each flap are applied without additional input.

Using this method, the results are presented in Figure 2.2, for open-loop identification, original closed-loop identification, and modified closed-loop identification. These results are obtained for a dissimilar rotor. The mass of blade 4 is increased uniformly by 1%, while the mass of other blades is kept at the baseline value. The figures on the left show a representation of the identified transfer matrix for blade 1 (T_1), after convergence. The matrix columns are plotted versus the line number, the matrix size is $N_s = 60$. The figures on the

right show the time history of the norm of the identified transfer matrices for each blade. This norm is defined as:

$$|T_k| = \frac{1}{N_s} \sum_{i=1}^{N_s} \sum_{j=1}^{N_s} |T_k(i,j)| \tag{2.19}$$

During open-loop identification (figure 2.2(a)), the inputs are random, ensuring that the transfer matrices converge to the correct values. It is verified that the norm of the transfer matrix corresponding to the identical blades 1, 2, and 3 is equal, while it is different for blade 4. The relationship between T1, T2 and T3 (equation 2.4) is also verified. Figure 2.2(a) also shows that the system is not time invariant. For a time invariant system, each column of T_k is a permutation of the first column, so that the columns have the same amplitude. Figure 2.2(b) shows the closed-loop identification. The identified transfer matrix after convergence is very different than the open loop identified matrix. This is because convergence is reached too early, at iteration 110, when the control inputs converge. In this case, the final transfer matrix norms are different for all four blades. Finally, Figure 2.2(c) shows the closed-loop identification, with the modified scheme. It is seen that adding small random angles to control inputs before convergence improves the transfer matrix identification, which becomes similar to the open-loop case. The benefit of this system-probing method on the identification performance is quite apparent in Figure 2.2. However, in this case, the controller performance was not improved significantly: even with the poorly identified transfer matrix from Figure 2.2(b), vibration was completely cancelled after convergence of the control algorithm.

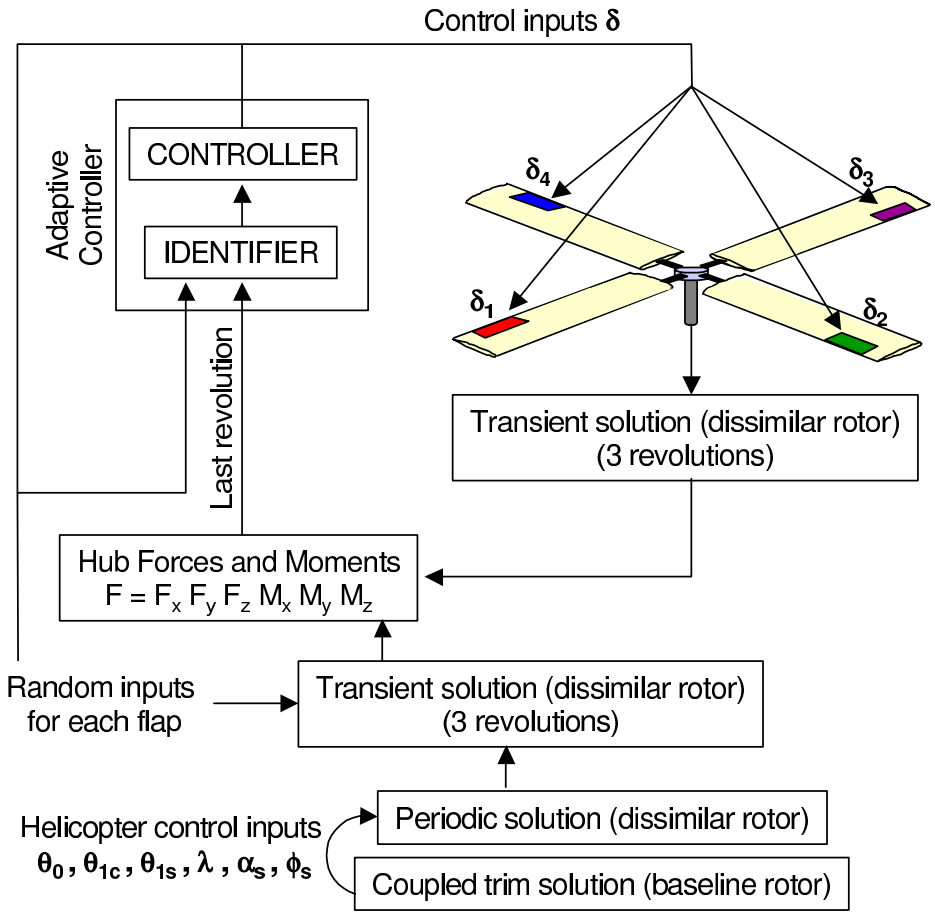

Figure 2.1: Individual flap control scheme block diagram

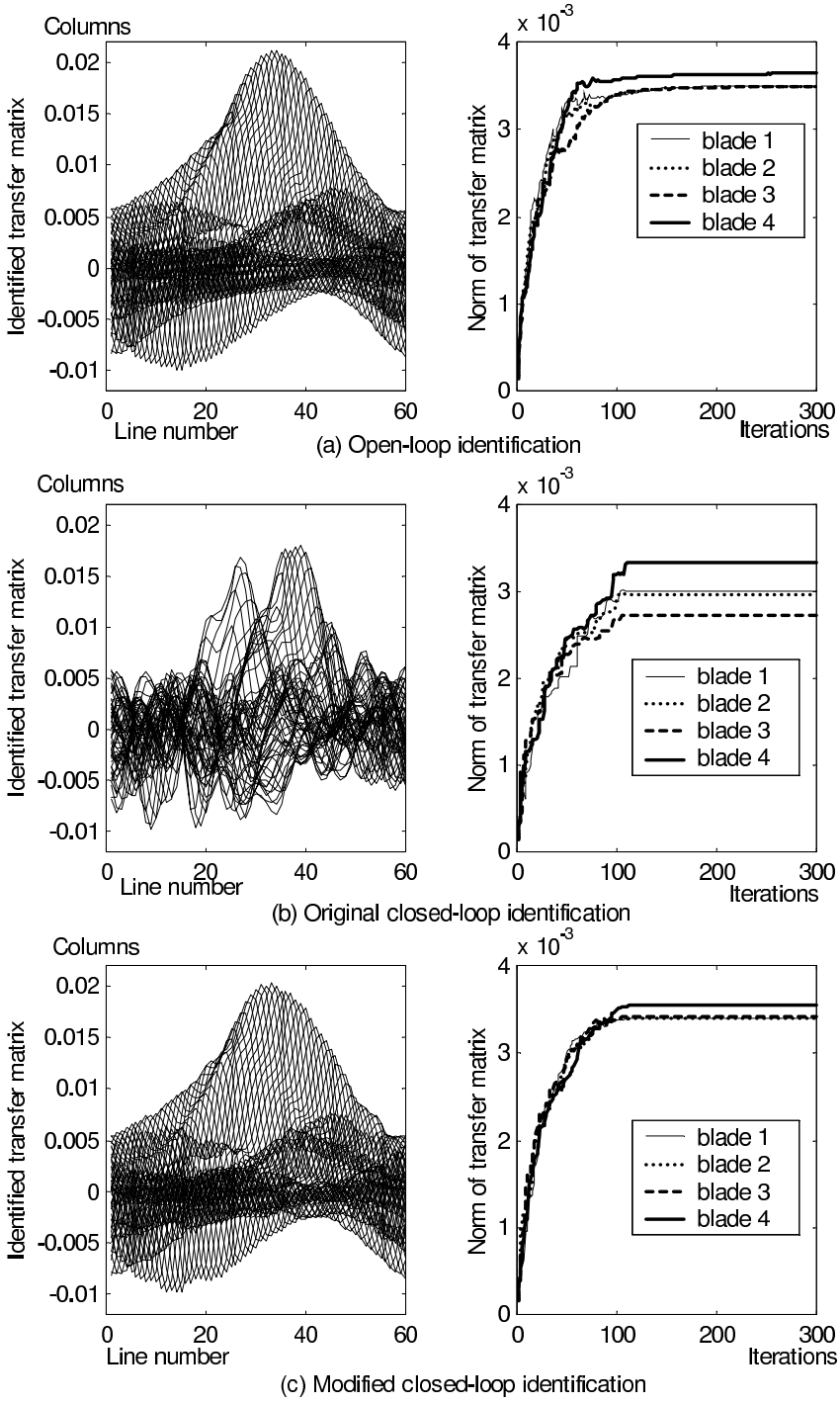

Figure 2.2: Open-loop and closed-loop identification

Chapter 3

Comprehensive rotor analysis model

The comprehensive rotor analysis model used is the University of Maryland Advanced Rotorcraft Code (UMARC) [116]. The sections that follow briefly describe the mathematical modeling of the rotor blade dynamics, aerodynamics, vehicle trim and the calculation of hub loads in UMARC.

3.1 Structural modeling

The blade is modeled as a slender elastic beam undergoing flap bending, lag bending, elastic twist and axial deflections. Coupled nonlinear differential equations that are formulated for moderately large deflections are used (Hodges and Dowell [117]). The geometric terms in the flap, lag, axial and torsion equations are preserved up to the second order.

The blade is discretized into a number of beam elements, each consisting of fifteen degrees of freedom. Continuity of slope and displacement is preserved for flap and lag bending deflections between structural finite elements, while continuity of displacement is maintained for axial and torsional deflections. This element insures consistent linear variation of bending moments and torsional moments and quadratic variation of axial force within each element. The degrees

of freedom used are symbolically represented as u,v,v',w,w' and $\hat{\phi}$, which correspond to the axial displacement, lag displacement, slope of lag displacement, flap displacement, slope of flap displacement and the elastic torsional displacement respectively. A Hermite interpolating polynomial (which preserves continuity of slope and displacement) is used for the flap and lag deflections while a Lagrange polynomial (which preserves continuity of displacement only) is used for axial and torsional deflections. Using the interpolating polynomials, the distribution of deflections over a beam element is expressed in terms of elemental nodal displacements q_i. For the i_{th} beam element, the blade deflections are expressed as follows:

$$u_i(s) = \begin{Bmatrix} u(s) \\ v(s) \\ w(s) \\ \hat{\phi}(s) \end{Bmatrix} = \begin{bmatrix} H_u & 0 & 0 & 0 \\ 0 & H & 0 & 0 \\ 0 & 0 & H & 0 \\ 0 & 0 & 0 & H_{\hat{\phi}} \end{bmatrix} q_i \tag{3.1}$$

where s is the coordinate along the element and the elemental nodal displacement vector q_i is defined as:

$$q_i = [u_1, u_2, u_3, u_4, v_1, v_1', v_2, v_2', w_1, w_1', w_2, w_2', \hat{\phi}_1, \hat{\phi}_2, \hat{\phi}_3]^T \tag{3.2}$$

The interpolating polynomials for the shape functions are given by

$$H_u^T = \begin{Bmatrix} -4.5s^3 + 9s^2 - 5.5s + 1 \\ 13.5s^3 - 22.5s^2 + 9s \\ -13.5s^3 + 18s^2 - 4.5s \\ 4.5s^3 - 4.5s^2 + s \end{Bmatrix} \tag{3.3}$$

$$H^T = \begin{Bmatrix} 2s^3 - 3s^2 + 1 \\ l_i(s^3 - 2s^2 + s) \\ -2s^3 + 3s^2 \\ l_i(s^3 - s^2) \end{Bmatrix} \tag{3.4}$$

$$H_{\hat{\phi}}^{T} = \left\{ \begin{array}{c} 2s^3 - 3s + 1 \\ -4s^2 + 4s \\ 2s^2 - s \end{array} \right\} \tag{3.5}$$

where $s = x_i/l_i$ and l_i is the length of i^{th} beam element.

Hamilton's variational principle is used to derive the system equations of motion. For a conservative system, Hamilton's principle states that the true motion of a system between prescribed initial and final conditions is that particular motion for which the time integral of the difference between the potential and kinetic energies is minimum. The generalized Hamilton's principle for a non-conservative system is given by:

$$\delta\Pi = \int_{t_1}^{t_2} (\delta U - \delta T - \delta W) dt = 0 \tag{3.6}$$

where δU is the virtual variation of strain energy and δT is the virtual variation of kinetic energy. The δW is the work done by external forces. In the case of a rotor blade the total energy is the sum of energy contributions for each of the finite element used in the discretization. For instance, the elemental variation of energy for the i^{th} element (Δ_i=δU-δT-δW) can be reduced to a matrix form represented by

$$\Delta_i = \delta q_i^T (M_{bi}\ddot{q}_i + C_{bi}\dot{q}_i + K_{bi}q_i - F_{bi}) \tag{3.7}$$

where $(M_b)_i$, $(C_b)_i$, $(K_b)_i$ and $(F_b)_i$ are elemental mass, damping, stiffness and load matrices, respectively. The elemental mass, stiffness and damping matrices include contributions from axial deflections, flap bending, lag bending and elastic torsion. For instance, the mass and stiffness matrix contributions resulting from the flap degree of freedom (w, w') can be written as:

$$[m_{ij}] = \int_0^1 m H_i H_j ds \tag{3.8}$$

$$[k_{ij}] = \int_0^1 (F_A H_i' H_j' + (EI_z sin^2(\theta_0) + [EI_y cos^2(\theta_0)) H_i \, '' H_j'')) ds \tag{3.9}$$

where EI_y and EI_z are flexural rigidities in the longitudinal and transverse directions, $F_A = \int_x^1 mxdx$ and θ_0 represents the pitch angle at the blade section corresponding to this finite element. The shape functions H_i correspond to the Hermite polynomials presented in Eq. 3.4. All the variables are non-dimensionalized, hence w actually implies the displacement non-dimensionalized with blade radius. All the integrations in the above equations are conducted using a six point Gauss quadrature formula.

The equation of virtual energy for the whole blade can be obtained by assembling the elemental mass, stiffness and damping matrices to form global mass, stiffness and damping matrices (M_b, K_b and C_b). The equation of virtual energy for the blade can then be written as:

$$\delta\Pi = \int_{\psi_i}^{\psi_F} (M_b \ddot{q} + C_b \dot{q} + K_b q - F_b) \delta q d\psi = 0 \tag{3.10}$$

As the virtual displacements δq in Eq. 3.10 are arbitrary, the integrand must vanish. The motion of the blades is then modeled by the following second order system:

$$M_b \ddot{q} + C_b \dot{q} + K_b q = F_b \tag{3.11}$$

An eigenanalysis is conducted on these matrices to determine the generalized eigenvalues and eigenvectors. The eigenvalues are the square of the natural frequencies of this system, while the eigenvectors represent the natural vibration mode shapes.

3.2 Aerodynamic Modeling

The blade response is dependent on the aerodynamic forces experienced by the individual blades. The aerodynamic forces at any instant of time depend on the acceleration, velocity and position in space of the rotor blade. Therefore, mathematically they generate contributions to all the terms of Eq. 3.11. This section describes the mathematical formulation for obtaining the contributions from aerodynamic forces in mass, stiffness, damping matrices and the load vector. Quasi-steady aerodynamic modeling is used here for explaining the methodology. This can be replaced by more sophisticated models which include inflow distributions from a free wake approach [118], look up tables for aerodynamic coefficients, indicial models for unsteady aerodynamic forcing [119], and dynamic stall model [120]. Using the quasi-steady aerodynamic modeling, one could represent aerodynamic forces in the deformed frame of reference of a blade section. In the quasi-steady approach, the normal (U_P), tangential (U_T) and radial (U_R) components of the free stream velocity are calculated at each section of the rotor blade. Blade motion and deformation are accounted for appropriately in the calculation of these components. The final non-dimensionalized form of the aerodynamic forces in the deformed frame of reference is given by :

$$(L_w)_c = \frac{\gamma}{6a}(c_0 U_T^2 - (c_1 + d_0) U_T U_P + d_1 |U_P| U_P) \tag{3.12}$$

$$(L_v)_c = \frac{\gamma}{6a}(-d_0 U_T^2 - (c_0 U_P - d_1 |U_P|) U_T + (c_1 - d_2) U_P^2) \tag{3.13}$$

$$(L_u)_c = \frac{\gamma}{6a}(-d_0 U_R U_T) \tag{3.14}$$

Here, c_0, c_1 represent linear variation of C_l with angle of attack, d_0, d_1, d_2 represent quadratic variation of C_d with angle of attack and f_0, f_1 represent linear variation of pitching moment with angle of attack. The quantity γ is the Lock number (ratio of aerodynamic forces to inertial forces) and a is the lift-curve-slope.

The aerodynamic forces in the undeformed frame are obtained by using the orthogonal co-ordinate transformation:

$$\left\{ \begin{array}{c} (L_u^A)_C \\ (L_v^A)_C \\ (L_w^A)_C \end{array} \right\} = (T_{DU})^T \left\{ \begin{array}{c} (L_u)_C \\ (L_v)_C \\ (L_w)_C \end{array} \right\} \tag{3.15}$$

Considering only the flap degree of freedom for simplicity, one could expand aerodynamic contribution in the flap direction $(L_w^A)_C$ as follows:

$$(L_w^A)_C = (L^A)_0 + (L^A)_L + (L^A)_{NL} \tag{3.16}$$

where L_0^A is the deformation independent aerodynamic forcing, L_L^A depends linearly on the blade motions and L_{NL}^A is the non-linear contribution to aerodynamic forcing by the blade elastic deformation. One could linearize Eq. 3.16 with respect to the degrees of freedom (w and w') to give :

$$(L_w^A)_C = (L^A)_0 + (L^A)_{NL}|_0 + (A_w + A_{wNL})w \tag{3.17}$$

$$+ (A_{w'} + A_{w'NL})w' + (A_{\dot{w}} + A_{\dot{w}NL})\dot{w} + A_{\ddot{w}}\ddot{w} \tag{3.18}$$

Equation 3.18 is the forcing function (right hand side) for the global mass, damping and stiffness matrices obtained from the finite element modeling of the rotor blade. For the numerical stability of the aeroelastic analysis the motion dependent terms of the linearized expression (e.g., A_w, $A_{\dot{w}}$, etc.), are taken to the left hand side. These represent the additional entries in the mass, stiffness and damping matrices caused by aerodynamic forcing. Again, these contributions can be partitioned into contributions from flap, lag, axial and torsion deflections. Using only the flap degree of freedom for simplifying the expressions, the

aerodynamic mass, damping and stiffness matrices are given by:

$$(M_b^A)^i = -\frac{\gamma}{6} l_i \int_0^1 H_s^T A_{\ddot{w}} H_s ds \tag{3.19}$$

$$(K_b^A)^i = -\frac{\gamma}{6} l_i \int_0^1 (H_s^T((A_w + A_{wNL})H_s + (A_{w'} + A_{w'NL})H_s'))ds \tag{3.20}$$

$$(C_b^A)^i = -\frac{\gamma}{6} l_i \int_0^1 H_s^T (A_{\dot{w}} + A_{\dot{w}NL}) H_s d\ s \tag{3.21}$$

Also, the forcing vector is given by

$$(Q_b^A) = \frac{\gamma}{6} l_i \int_0^1 H_s^T \left((L^A)_0 + (L^A)_{NL}\ |_0 \right) ds \tag{3.22}$$

where l_i is the length of the element under consideration and H_s are the shape functions described in the previous section. The element matrices are assembled to determine the global aerodynamic mass, stiffness and damping matrices and the load vector which forms the right hand side. The full blade equations of motion are obtained by accumulating the structural and aerodynamic contributions in mass, damping, and stiffness matrices.

3.3 Temporal finite element method

The finite element equation for the rotor blade after the spatial finite element discretization is of the form:

$$M(\psi)\ddot{q} + C(\psi)\dot{q} + K(\psi)q = F(q, \psi) \tag{3.23}$$

This equation essentially represents an ODE system with time varying coefficients that involves many degrees of freedom. To reduce the computational

time, the equations could be transformed into the normal mode space. This significantly reduces the degrees of freedom while preserving the underlying physics. The blade natural vibration modes determined from the eigenanalysis are used for this modal transformation. The blade displacement is assumed to be decoupled in space and time and is hence expressed as:

$$q = \phi(x)p_b(t) \tag{3.24}$$

where ϕ is a matrix whose columns consist of the natural vibration mode shapes and p_b is the vector of normal mode coordinates. The ODE representing the motion of the blade can be now transformed to the normal mode coordinates as

$$\bar{M}\ddot{p_b} + \bar{C}\dot{p_b} + \bar{K}p_b = \bar{F} \tag{3.25}$$

where

$$\bar{M} = \phi^T M \phi \tag{3.26}$$

$$\bar{C} = \phi^T C \phi \tag{3.27}$$

$$\bar{K} = \phi^T K \phi \tag{3.28}$$

$$\bar{F} = \phi^T F \phi \tag{3.29}$$

are the modal mass, damping and stiffness matrices and the load vector, respectively. Again using the Hamilton principle and following the same approach as that used to construct the spatial finite element method, the blade equation can be rewritten as:

$$\int_0^{2\pi} \delta p_b(\bar{M}\ddot{p_b} + \bar{C}\dot{p_b} + \bar{K}p_b - \bar{F})d\psi = 0 \tag{3.30}$$

Integrating by parts and applying periodic boundary conditions ($\bar{M}(\psi) = \bar{M}(\psi + 2\pi)$) one gets:

$$\int_0^{2\pi} (-\delta\dot{p_b}^T \bar{M}\delta\dot{p_b} + \delta\dot{p_b}^T \bar{C}\delta p_b + \delta p_b^T \bar{K}\delta p_b - \delta p_b^T \bar{F}) = 0 \tag{3.31}$$

The time from 0 to 2π is discretized into Lagrangian time elements each having 6 degrees of freedom. The temporal node coordinates are denoted by ξ and the normal mode coordinate in any element is assumed to vary as p_b=$H_t\xi$ where H_t are Lagrange polynomial based shape functions which satisfy the boundary conditions. Continuity of the generalized displacements is assumed between the time elements. The equations can be now rewritten of the form:

$$K_t^G \Delta\xi^G = Q^G \tag{3.32}$$

where

$$K_t^G = \sum_{i=1}^{N_t} \int_{\psi_i}^{\psi_{i+1}} (-\dot{H_t}^T \bar{M} \dot{H_t} + H_t^T \bar{C} \dot{H_t} + H_t^T \bar{K} H_t) \tag{3.33}$$

and

$$Q^G = \sum_{i=1}^{N_t} H_t^T \bar{F} \tag{3.34}$$

These form a system of non-linear algebraic equations, which are solved using Newton's method to calculate the blade response.

3.4 Vehicle trim procedure

There are many forms of trim solutions. Broadly they can be classified into two categories: free flight and wind tunnel trim.

For free flight or propulsive trim, it is assumed that the engine can supply the necessary power required to maintain the flight condition. For a steady flight, the comprehensive propulsive trim solution can be obtained by satisfying the three force (vertical, longitudinal and lateral) and three moment (pitch, roll and yaw) vehicle equilibrium equations. For example, for a specified gross weight and level flight speed, the trim solution gives the rotor pitch controls (collective θ_0, cyclic θ_{1c} and θ_{1s}), vehicle orientation (longitudinal shaft tilt α_s and lateral shaft tilt ϕ_s) and tail rotor pitch (collective θ_{tr}).

For wind tunnel trim, the cyclic and collective controls are iteratively adjusted to obtain zero first harmonic flapping and a target thrust condition. This is essentially a way to simulate test conditions in a wind tunnel. Therefore it is justified to neglect the fuselage loads and tail rotor loads. Also, the longitudinal, lateral and vertical force equilibrium equations need not be satisfied.

In general, the expressions for the vehicle equilibrium can be expressed as:

$$F = 0 \tag{3.35}$$

where exact form $F^T = [F_1, ..F_n]$ depends on the trim condition considered.

The following equations are derived from the force equilibrium of a helicopter in steady flight:

$$F_1 = D_F \cos\theta_{FP} + H\cos\alpha_s - T\sin\alpha_s \tag{3.36}$$

$$F_2 = Y_F + Y\cos\phi_s + T\sin\phi_s + T_{tr} \tag{3.37}$$

$$\begin{aligned} F_3 &= T\cos\alpha_s\cos\phi_s - D_F\sin\theta_{FP} + \\ &\quad H\sin\alpha_s - Y\sin\phi_s - W - L_{ht} \end{aligned} \tag{3.38}$$

$$\begin{aligned} F_4 &= M_{xR} + M_{xF} + Y_F(\bar{h}\cos\phi_s + y_{cg}\sin\phi_s) \\ &\quad + W(\bar{h}\sin\phi_s - y_{cg}\cos\phi_s) + T_{tr}(\bar{h} - z_{tr}) \end{aligned} \tag{3.39}$$

$$\begin{aligned} F_5 &= M_{y_R} + M_{y_F} + W(\bar{h}\sin\alpha_s - x_{cg}\cos\alpha_s) \\ &\quad - D_F(\bar{h}cos(\alpha_s + \theta_{FP}) + x_{cg}sin(\alpha_s + \theta_{FP})) \\ &\quad + L_{ht}(x_{ht} - x_{cg}) \end{aligned} \tag{3.40}$$

$$\begin{aligned} F_6 &= M_{zR} + M_{zF} + T_{tr}(x_{tr} - x_{cg}) - D_F y_{cg}\cos\alpha_s \\ &\quad - Y x_{cg}\cos\phi_s \end{aligned} \tag{3.41}$$

where F_1, F_2 and F_3 are, respectively, the vehicle force equilibrium residuals in X, Y and Z directions in the fuselage axes, and F_4, F_5 and F_6 are the vehicle

rolling, pitching and yawing moment equilibrium residuals about the vehicle center of gravity, respectively.

The terms H, Y and T are respectively rotor drag, side force and thrust. The terms D_F, Y_F and W are respectively fuselage drag, side force and gross weight. The terms T_{tr}, x_{tr} and z_{tr}, denote the tail rotor thrust, the distance of the tail rotor hub behind the vehicle center of gravity and the distance of tail rotor hub above the vehicle center of gravity. The horizontal tail is located at a distance x_{ht} behind the vehicle center of gravity. The terms in the three moment equations, e.g. M_{xR} and M_{xF}, denote the rotor and fuselage moments, respectively. The forces act on the rotor hub and the moments act about the rotor hub. In addition, x_{cg} and y_{cg} and $\bar{h}$ are, respectively, the relative location of the rotor hub center with respect to the vehicle center of gravity in the X_F, Y_F and Z_F directions; α_s (positive for forward flight) and ϕ_s (positive advancing side down) are the longitudinal and lateral shaft tilts, respectively, and θ_{FP} is the flight path angle relative to an axis perpendicular to the gravity vector.

3.5 Coupled trim procedure

The convergence of the steady response for a fixed control setting is called uncoupled trim. In a coupled trim procedure, this method is coupled with the solution of the vehicle trim equations to solve to the final converged trim-response solution. As the trim analysis is non-linear in nature, an accurate initial guess is necessary. A trim analysis of a rigid rotor blade is conducted to find the initial control estimate. The vehicle force and moment equations and the blade flapping equations are solved using a non-linear equation solver.

The response of the rotor to the initial control estimate is found by solving the rotor equations using the temporal finite element method. A force summation is conducted on the basis of the blade response obtained to yield the aerodynamic

forces and moments produced by the deformed blade. The time averaged values (over one rotor revolution) of rotor forces and moments are substituted in the corresponding vehicle trim equations to obtain the residuals of these equations. The final objective of the coupled trim procedure is to find the control estimate which drives these residuals towards zero. Newton's method, based on the evaluation of a trim Jacobian matrix, is used to find the final control estimate.

A finite difference approximation is used to calculate the control Jacobian. The initial controls are perturbed one at a time and the variation of the residuals are used to calculate individual terms of the control Jacobian. The control settings are updated using the control Jacobian and the value of the residual vector. The whole process is conducted in a loop process until the residues to the vehicle trim equations are below a specified error bound.

3.6 Calculation of blade loads and hub loads

The loads at the hub are calculated by accumulating the contributions of the loads transfered by each rotor blade at the hub center. The loads transfered by any individual rotor blade can be calculated by spanwise integration of the sectional blade loads from hub center to the blade tip. The blade section loads consist of contributions from both aerodynamic and inertial components and can be expressed as:

$$L_u = L_u^A + L_u^I \tag{3.42}$$

$$L_v = L_v^A + L_v^I \tag{3.43}$$

$$L_w = L_w^A + L_w^I \tag{3.44}$$

$$M_u = M_\phi^A + M_u^I \tag{3.45}$$

$$M_v = v' M_\phi^A + M_v^I \tag{3.46}$$

$$M_w = w' M_\phi^A + M_w^I \tag{3.47}$$

Integrating these sectional loads components in the spanwise direction yields expressions for the blade loads at the hub in the rotating frame given by:

$$\left\{ \begin{array}{c} F_x \\ F_y \\ F_z \end{array} \right\} = \int_0^R \left\{ \begin{array}{c} L_u \\ L_v \\ L_w \end{array} \right\} dx \tag{3.48}$$

$$\left\{ \begin{array}{c} M_x \\ M_y \\ M_z \end{array} \right\} = \int_0^R \left\{ \begin{array}{c} -L_v w + L_w v + M_u \\ L_u w - L_w (x+u) + M_v \\ -L_u v + L_v (x+u) + M_w \end{array} \right\} dx \tag{3.49}$$

These sectional loads are in the rotating frame and are directed along the undeformed blade axes.

The hub loads are needed to calculate the steady rotor forces T, H, Y, M_{xR}, M_{yR} and M_{zR} which are required for evaluating the vehicle trim. In addition, the hub loads form the feed-back input to the controller algorithm. The controller algorithm would perform system identification and generate control inputs to minimize the vibratory harmonics of the hub loads.

The rotor hub loads are obtained by summing the load contributions from

the individual blades. In the fixed frame, the hub loads are expressed as:

$$F_X^H(\psi) = \sum_{m=1}^{N_b} \left(F_x^m cos\psi_m - F_y^m sin\psi_m - F_z^m cos\psi_m \beta_p\right) \quad (3.50)$$

$$F_Y^H(\psi) = \sum_{m=1}^{N_b} (F_x^m sin\psi_m + F_x^m cos\psi_m - F_z^m sin\psi_m \beta_p) \quad (3.51)$$

$$F_Z^H(\psi) = \sum_{m=1}^{N_b} (F_z^m + F_x^m \beta_p) \quad (3.52)$$

$$M_X^H(\psi) = \sum_{m=1}^{N_b} \left(M_x^m cos\psi_m - M_y^m sin\psi_m - M_z^m cos\psi_m \beta_p\right) \quad (3.53)$$

$$M_Y^H(\psi) = \sum_{m=1}^{N_b} \left(M_x^m sin\psi_m + M_y^m cos\psi_m - M_z^m sin\psi_m \beta_p\right) \quad (3.54)$$

$$M_Z^H(\psi) = \sum_{m=1}^{N_b} (M_z^m + M_x^m \beta_p) \quad (3.55)$$

where F_x^m, F_y^m and F_z^m are the shear loads and M_x^m, M_y^m, M_z^m are the moments due to the m^{th} blade. If the N_b blades are identical, only the loads at integer multiple of N_b/rev appear in the fixed frame. If the blades are dissimilar, all harmonics appear in the fixed frame. The UMARC modeling allows for all the blades to be dissimilar in both aerodynamic and structural dynamic properties.

3.7 Modeling of the active trailing edge flap

The control mechanism is physically devised using an active trailing edge flap embedded in each rotor blade.

3.7.1 Inertial Modeling

Each spatial element has a trailing edge flap of specified flap-chord ratio. This parameter is set to zero to represent a blade element with no trailing edge flap. In the present analysis, one flap is modeled on each blade. The flap properties

are assumed uniform along the length of the spatial element. These properties are the flap sectional mass m_f and mass moments S_f and I_f, the hinge location, e, and the empirical flap aerodynamic effectiveness ϵ_H, ϵ_N, and ϵ_M. It is assumed that the trailing edge flap properties are included in the blade properties itself. This means the inplane stiffness is reduced over the flap region, where the trailing edge is interrupted. The motion of the trailing edge flap is prescribed, therefore there are no explicit trailing edge flap degrees of freedom, and the effects of the flaps are represented in the blade equations of motion as contributions to the nonlinear load vector. Trailing edge flap inertial contributions to the equations of motion and the hub loads are calculated as follows: first, the acceleration vector, a, of a trailing edge mass particle with respect to an inertial frame is expressed. The inertial contribution to the blade sectional loads and moments associated with a trailing edge flap mass element dm are then written in the undeformed frame of reference as:

$$\{L_u\ L_v\ L_w\} = -\int\int a\ dm \tag{3.56}$$

$$\{M_x\ M_y\ M_z\} = -\int\int \rho_D \times a\ dm \tag{3.57}$$

where ρ_D is the position vector of the mass element relative to a point on the blade deformed elastic axis. The rotating system hub loads are then calculated via force summation. The inertial contribution to the trailing edge flap hinge moment is calculated as:

$$M_H = -\int\int (\rho_H \times a) \cdot \hat{i}_H\ dm \tag{3.58}$$

where ρ_H is the position vector of the mass element relative to a point on the flap hinge axis, and $\hat{i}_H$ is a unit vector along the flap hinge axis.

3.7.2 Aerodynamic Modeling

The trailing edge flap contributes to both steady and unsteady components of sectional aerodynamic forces. The steady effects can be modeled using a lookup table or even with quasi-static approach which linearizes the effect of the flap using a constant coefficient. The unsteady aerodynamic formulation for flap/airfoil combination was first developed in a classic study by Theodorsen [121]. The airfoil sectional loads and flap hinge moment that results from sinusoidal flap motions are expressed as the sum of two components. The first component uses a frequency-domain transfer function $C(k)$ related to the shed vorticity. For the special case of harmonic airfoil motion, the function C(k) is provided in closed form as a complex valued function of the reduced frequency, $k = cw/2V$. The second component primarily contains terms relating to non-circulatory (apparent mass) effects. For example, the airfoil pitching moment resulting from trailing edge flap deflection and rate is presented in [121] as:

$$\begin{aligned} M_\alpha = & - \quad \rho b^2 \left[\left(T_4 + T_{10} \right) V^2 \delta + \left(T_1 - T_8 - \left(e - \alpha \right) T_4 + \frac{1}{2} T_{11} \right) v b \dot{\delta} \right] \cdots \\ & - \quad \underline{\rho b^2 \left[\left(T_7 + \left(e - a \right) T_1 \right) b^2 \ddot{\delta} \right]} \\ & + \quad \underline{\underline{2 \rho V b^2 \pi \left(a + \frac{1}{2} \right) C\left(k \right) \left\{ \frac{1}{\pi} T_{10} V \delta + b \frac{1}{2\pi} T_{11} \dot{\delta} \right\}}} \end{aligned} \tag{3.59}$$

where the parameters T_1, T_2, etc. are scalar functions of the flap hinge location e [121]. Reference [123] classifies the terms in this equation based on their origin: non-circulatory (double underline), unsteady circulatory (single underline), and quasi-steady circulatory (no underline). This allows the moment to be written in coefficient form as:

$$C_M = \underline{\underline{C_M^i}} + \underline{\pi \left(a + \frac{1}{2} \right) C(k) \delta_{qs}} + C_M^{qs} \tag{3.60}$$

where

$$C_M^{qs} = -\frac{1}{2}\left[\left(T_4 + T_{10}\right)\delta + \left\{T_1 - T_8 - \left(e - a\right)T_4 + \frac{1}{2}T_{11}\right\}\left(\frac{\dot{\delta}c}{2V}\right)\right] \quad (3.61)$$

$$C_M^{i} = -\frac{1}{2}\left[T_7 + \left(e - a\right)T_1\right]\left(\frac{\ddot{\delta}c^2}{4V^2}\right) \quad (3.62)$$

$$\delta_{qs} = \frac{1}{\pi}T_{10}\delta + \frac{1}{2\pi}T_{11}\left(\frac{\dot{\delta}c}{2V}\right) \quad (3.63)$$

Similar expressions are derived in Reference [123] for the flap lift and hinge moment coefficient.

For the present analysis arbitrary motions of airfoil/flap combination are considered. A formulation for arbitrary airfoil/flap motions can be developed with the indicial response of aerodynamic loads following step changes in flap and airfoil motion. This approach was first developed by Wagner [122] and subsequently investigated in detail by Hariharan and Leishman [123]. The trailing edge flap aerodynamic modeling in UMARC is based on the model proposed by Hariharan and Leishman [123] to calculate sectional aerodynamic loads and flap hinge moment using indicial concepts. Milgram [54] integrated this trailing edge flap model in to the mathematical modeling framework of UMARC.

The flap effectiveness in producing incremental lift and pitching moments can be reduced because of the finite thickness of the boundary layer over the flap portion of the profile. Aerodynamic hinge moments can be reduced as well. In Reference [123], these are accounted for with parameters ϵ_N, ϵ_M, and ϵ_H for the normal force, pitching moment, and hinge moment, respectively. In the present analysis these parameters are set to unity.

3.8 Dissimilar Blade Modeling

Most aeroelastic analyses of helicopter blades assume that the blades are identical. However, in reality, blade dissimilarities exist, which can have a strong influence on the blade response and loads. In UMARC, if blades are dissimilar, the blade response is calculated for each blade individually. The blade response for the *mth* blade can be obtained from th finite element in time equations given as (Eq 3.32):

$$K^G_{t\ m}\,\Delta\xi^G_m = Q^G_m \tag{3.64}$$

Once the blade response for each blade has been calculated, the blade loads for the *mth* blade at any blade section are calculating using a force summation method, then integrated over the span to obtain the contribution to the hub loads (in the rotating frame):

$$\left\{\begin{array}{c} F_x \\ F_y \\ F_z \end{array}\right\}_m = \int_0^R \left\{\begin{array}{c} L_u \\ L_v \\ L_w \end{array}\right\}_m dx \tag{3.65}$$

$$\left\{\begin{array}{c} M_x \\ M_y \\ M_z \end{array}\right\}_m = \int_0^R \left\{\begin{array}{c} -L_v w + L_w v + M_u \\ L_u w - L_w(x+u) + M_v \\ -L_u v + L_v(x+u) + M_w \end{array}\right\}_m dx \tag{3.66}$$

The hub loads are then obtained by summing load contributions from the individual blades (Equations 3.50 to 3.55). For a tracked rotor, only the N_b/rev forces and moments would appear in these forces and moments. For a dissimilar rotor, however, all harmonics would appear. In order to model blade dissimilarities, the comprehensive analysis is modified so that the following properties can be varied for each blade at any spanwise finite element along the blade:

1. Flap stiffness EI_y

2. Lag stiffness EI_z

3. Torsion stiffness GJ

4. Mass m

5. Aerodynamic coefficient c_0

6. Aerodynamic coefficient d_0

7. Pitching moment coefficient c_{mac}

where c_0, d_0, and c_{mac} are lift, drag and pitching moment parameters defined in:

$$C_l = c_0 + c_1\alpha \tag{3.67}$$

$$C_d = d_0 + d_1|\alpha| + d_2\alpha^2 \tag{3.68}$$

$$C_m = f_0 + f_1\alpha = c_{mac} + f_1\alpha \tag{3.69}$$

Chapter 4

Feasibility Study using Simplified Analysis

4.1 Introduction

This chapter describes the study conducted to examine the feasibility and performance of the control scheme described in the previous chapter. The purpose of this study is to investigate the ability of the control scheme to reduce all harmonics of vibration in the fixed frame.

The feasibility study is performed for a 4-bladed hingeless rotor model and uses a simplified analysis model with only the flap degree of freedom. Each rotor blade is modeled using ten spatial finite elements along the blade span. Five rotating natural flap modes for each blade are used for modal analysis. Eight time finite elements with fourth order shape functions are used along the azimuth to calculate the blade response. Using these values, a converged blade solution is obtained. The blade first flap frequency is 1.11/rev.

The trailing-edge flap chord is 20% of the blade chord and its length is 18% of the radius. It is located at 0.83R. This corresponds to $\frac{\partial \alpha}{\partial \delta} = 0.50$, where $\frac{\partial \alpha}{\partial \delta}$ is the rate of change of effective angle of attack due to flap input [130]. A maximum

flap input limit of ± 5 degrees is imposed. Level flight conditions corresponding to $\mu = 0.30$ and $C_T/\sigma = 0.07$ are considered. The controller parameters are: $W_F = 1$, $W_\delta = 2.5e-4$ and $W_{\Delta\delta} = 5e-6$. For measuring loads and to generate flap control inputs, 60 sample points per rotor revolution are used. To start the initial control iteration, small random flap angles are used as control inputs. As the controller adapts, the rate of change of the flap control inputs are restricted in order to avoid high transient loads at the hub.

The objective of the controller is to minimize oscillations in the vertical hub shear force, a key component that causes vibration at the pilot seat. All loads are non-dimensionalized with respect to a reference force defined as $m_0(\Omega R)^2$, where m_0 is the mass per unit length of an equivalent uniform blade with the same flap inertia, and ΩR is the blade tip speed. For each case, the helicopter rotor is first trimmed at the specified flight condition. The baseline vertical hub vibration is determined and the controller is activated.

4.2 Simulation of rotor imbalance

To simulate rotor dissimilarities among the four blades, one blade is assumed to contain a fault and the other blades are kept identical. The fault modeling approach is based on Ganguli et al [129]. Four types of rotor dissimilarities are simulated: (i) moisture absorption, (ii) loss of trim mass, (iii) damaged trailing edge flap, and (iv) bending stiffness damage. Moisture absorption in a blade can occur in a humid environment and results in changes in the blade mass properties. To simulate this damage, the mass of the damaged blade is increased uniformly along the elastic axis by 3%. The masses of the other blades are kept fixed at the baseline value. Loss of trim mass is modeled by removing 5% of baseline mass from particular section of a rotor blade. This section is chosen between 94% and 95% of the blade span. To simulate a damaged trailing edge flap, it is

assumed that the damaged flap has a steady 0.1-degree deflection angle in the uncontrolled state compared to zero deflection angles of the undamaged flaps. Therefore, the damaged blade has additional lift at the tip, causing out-of-track condition. The stiffness damage is modeled by reducing the bending stiffness of a particular section of the blade to 85% of the baseline value. This section extends from the root to 10% of the rotor radius. Finally, the controller behavior in the case of a real dissimilar rotor is studied. In this case, some inherent damages or imbalances are present. This is simulated by randomly introducing differences in each blade mass and stiffness properties within 5% of the baseline properties.

4.3 Comparison of control methods

Figure 4.1 shows the performance of different flap control methodologies for the reduction of the hub rolling moment, with moisture absorption damage in blade 4. The figures on the left represent the optimal flap inputs for all blades, while the figures on the right show the hub rolling moment, both before and after control. To obtain figures 4.1(a), the collective flap control method is used, where the same phase-shifted flap input is applied to all blades. Figures 4.1(b) correspond to the individual flap control with restricted inputs: different flap inputs are applied to different blades, however, identical flap inputs are applied to blades that are identical. Finally, figures 4.1(c) are obtained using the present flap control methodology, without any restriction for the flap inputs. The flap amplitude required in theory for the collective flap control is not practical ($-25°$ to $12°$). This can be explained by dividing the required flap input in two parts: one part is necesary for reducing the 4/rev vibration (kN_b/rev); another part is required to cancel the effect of the dissimilarities (non-kN_b/rev). With the first control method, the 4/rev component can be cancelled using a flap input of relatively small amplitude ($\pm$1.5deg). However, it is very difficult to cancel the

effect of the damage in blade 4 using the same input for all blades: the required flap input is extremely high (-25° to 12°). A similar observation was made from the recent rotor model test in the wind tunnel to minimize vibratory hub loads with bimorph-actuated flaps. With rotor dissimilarities, the flap requirements became excessive, resulting in saturation of actuators and enormously degraded performance [62]. With the second control method, individual flap control with restricted inputs, the required flap amplitude is reduced (-1.7° to 4.5°). However, only 80% vibration reduction is achieved. The vibration reduction achieved with the present control methodology is more than 99%. At the same time the required flap angles are only ± 1.3 deg in amplitude. Small flap angles get translated into a low actuation power for vibration minimization. Thus figure 4.1 clearly illustrates the advantage of the present control methodology.

4.4 Closed loop results

Figures 4.2 to 4.5 show the controller performance with a fault in blade 4 to minimize the vertical fixed frame vibratory hub shear. Figure 4.6 shows the controller performance with a fault in all blades. Figures 4.2(a) to 4.6(a) show the time history of the vertical hub shear. In all fault cases, this load is reduced completely (by more than 99%) in less than 120 rotor revolutions. In figures 4.2(b) to 4.6(b), the harmonic content of the vertical hub load is shown, for the baseline rotor with controller off, the damaged rotor with controller off and the damaged rotor with the controller on. For the baseline rotor with identical blades, only 4/rev fixed system loads are present. It is seen that most faults introduce a significant 1/rev component, and smaller 2/rev and 3/rev components. The bending stiffness damage effect is more significant on the 3/rev component (figure 4.5(b)). Apparently, damage does not introduce any hub load harmonic above 4/rev using this simple rotor model. As shown in figures 4.2(c) to 4.6(c),

the controller generates dissimilar flap angles for all blades, and the dominant harmonic component of these inputs is 3/rev (figures 4.2(d) to 4.6(d)). It is interesting to note that even though damage is incorporated in one blade (blade 4), the flap input to each blade is somewhat different. We should also note that even though there are no load harmonics above 4/rev, the controller seems to require small flap inputs at 6/rev and higher. Because these higher harmonic inputs may be difficult to implement, and may not be required for vibration reduction, it would be interesting to examine the effect of removing them on the controller performance. Figure 4.7 shows the controller performance when simultaneous reduction of several fixed frame loads is attempted. In this case, the vertical hub shear, the pitching moment and rolling moment vibrations are reduced simultaneously, with equal weights: $W_{F_z} = W_{M_y} = W_{M_x} = 1$. All three loads are reduced by 99% after 150 rotor revolutions. As expected, the amplitude of the required flap inputs is increased compared to the single load control. However the flap amplitude remains realistic (less than ± 3 deg).

Figure 4.8 shows the effect of a change in flight condition on the controller performance. This is shown for the moisture absorption damage in blade 4. The advance ratio is suddenly increased at iteration 150 from 0.3 to 0.35. Figure 4.8(a) shows that this sudden change results in increased vibration. However, the controller is able to identify the new transfer matrices and cancel vibration in about 50 revolutions. The identification of the new transfer matrices is apparent in figure 4.8(b). The control angles required for the new flight condition are larger in amplitude: about ± 2.5 deg. amplitude for $\mu = 0.35$, compared to less than ± 1.5 deg. for $\mu = 0.3$ (figure 4.8(c)). It should be mentioned that some vertical hub load time history show substantial transients during controller learning. This problem can be alleviated by applying tighter constraints on the flap inputs (increasing W_δ or fixing a limit to the maximum increase in flap deflection at each iteration), but this also increases the controller learning period.

All previous results have been obtained using computed hub loads. In order to make the simulations more realistic, noise is added to the numerical predictions. The results are presented in figure 4.9 in the case of moisture absorption damage in blade 4 (similar results are obtained for other damage cases). The vertical hub load variations are shown for different levels of white noise. The noise amplitude is indicated in percentage of the uncontrolled vibration amplitude, for the damaged rotor. Three cases are simulated: 1%, 5 % and 10 % noise. Although the performance of the controller deteriorates as the noise level is increased, in all simulated cases the controller is able to reduce the vibration amplitude to about the same level as the noise amplitude. The algorithm is robust to the presence of noise in the measurements.

4.5 Summary

The real time adaptive control algorithm described in Chapter 2 is tested using a simplified helicopter model. The control scheme uses on-blade trailing edge flaps which are actuated independently, accounting for individual blade dissimilarities. Fixed frame hub loads are used as the feedback to the controller.

Using numerical simulation, the controller is tested in the presence of rotor dissimilarities, modeled by changes in mass, stiffness, and aerodynamic properties of the damaged blade. The controller generates different control inputs for each blade according to their individual dissimilarities and successfully minimizes vibration. The vibration is reduced by 99 % within 150 revolutions in all test cases. The controller is shown to be robust to the presence of noise in the measurements and can adapt to changes in flight condition.

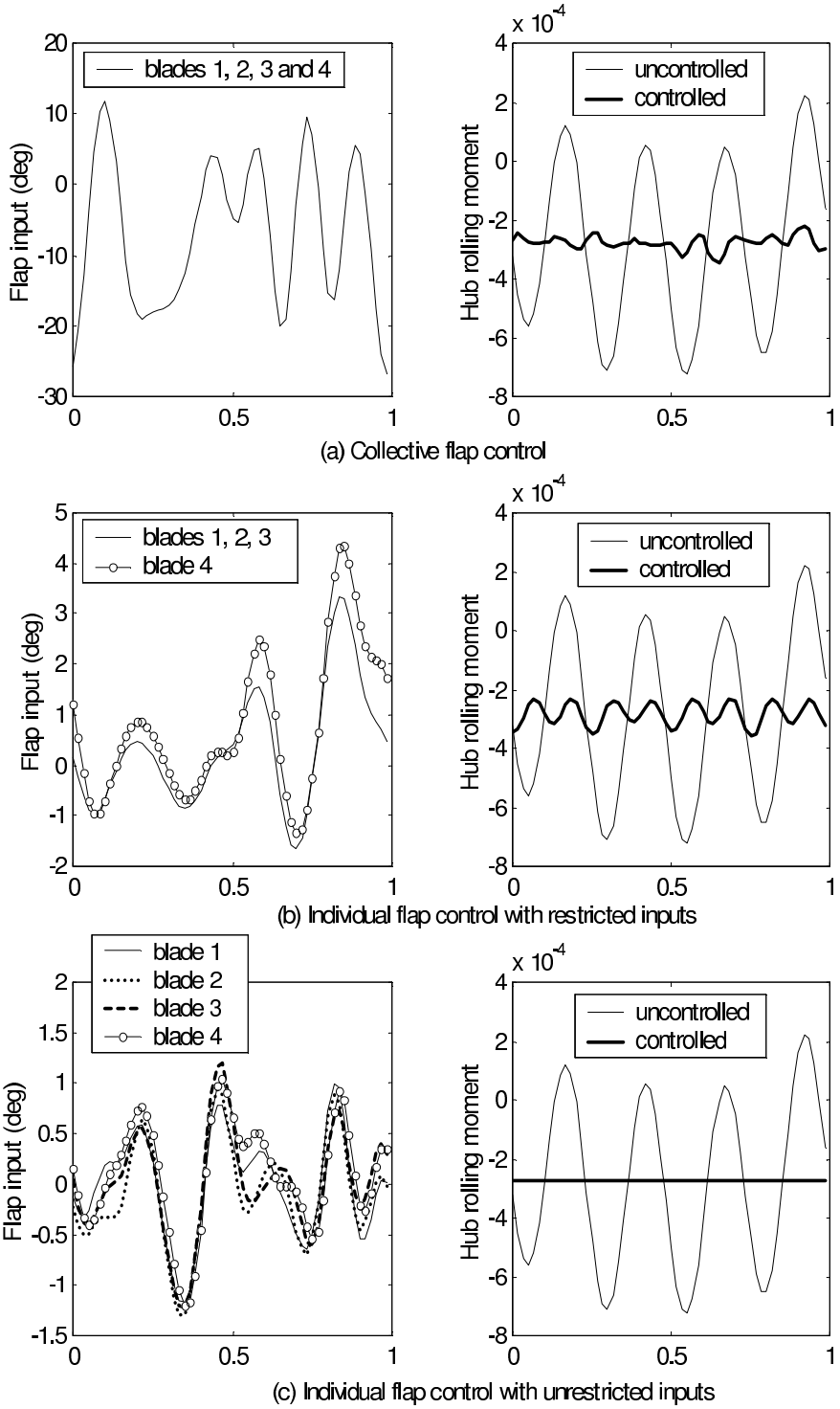

Figure 4.1: Performance of different flap control methodologies for hub rolling moment control

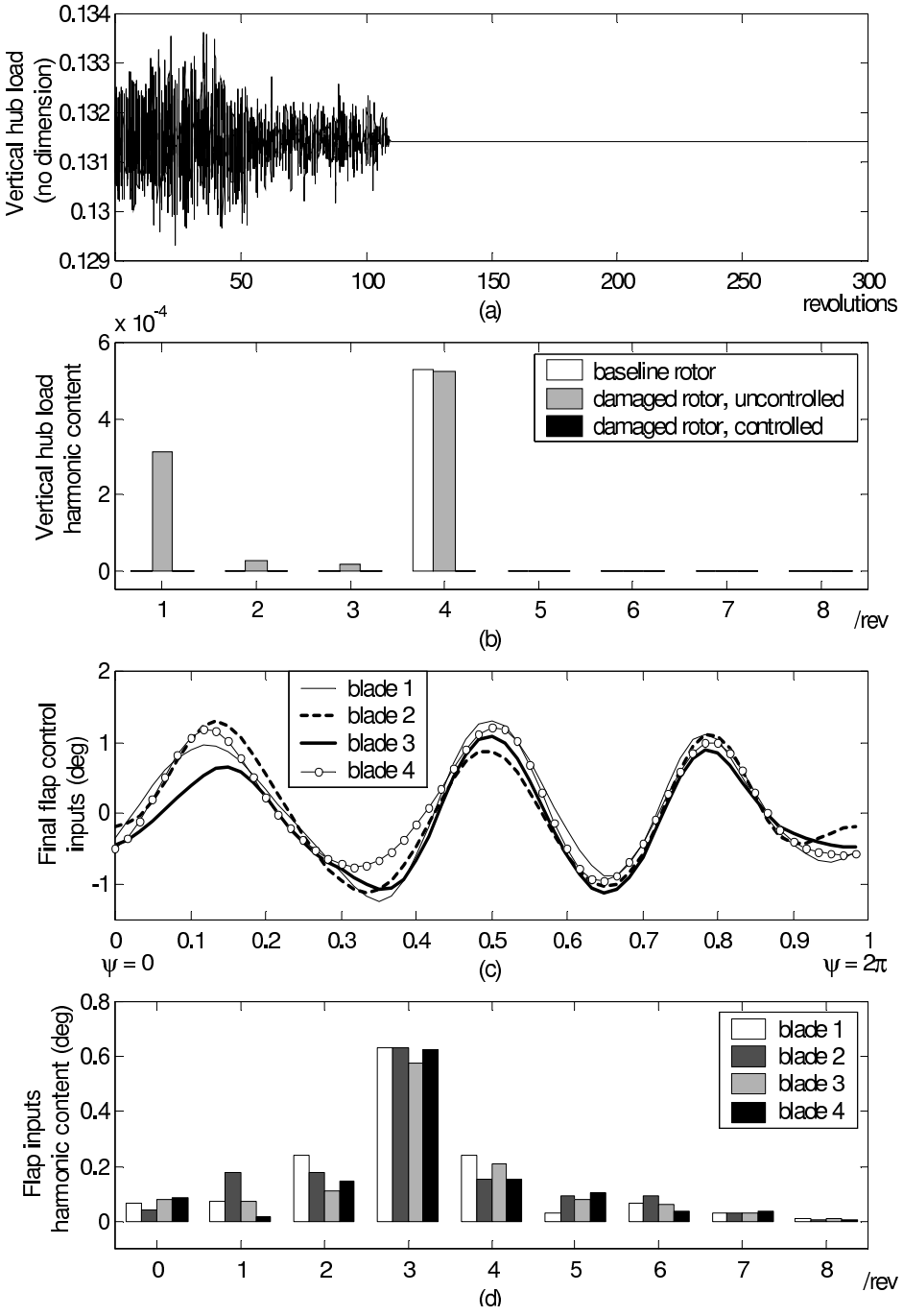

Figure 4.2: Moisture absorption damage; (a) vertical hub load time history; (b) harmonic content of vertical shear; (c) optimal flap angles; (d) harmonic content of flap angles.

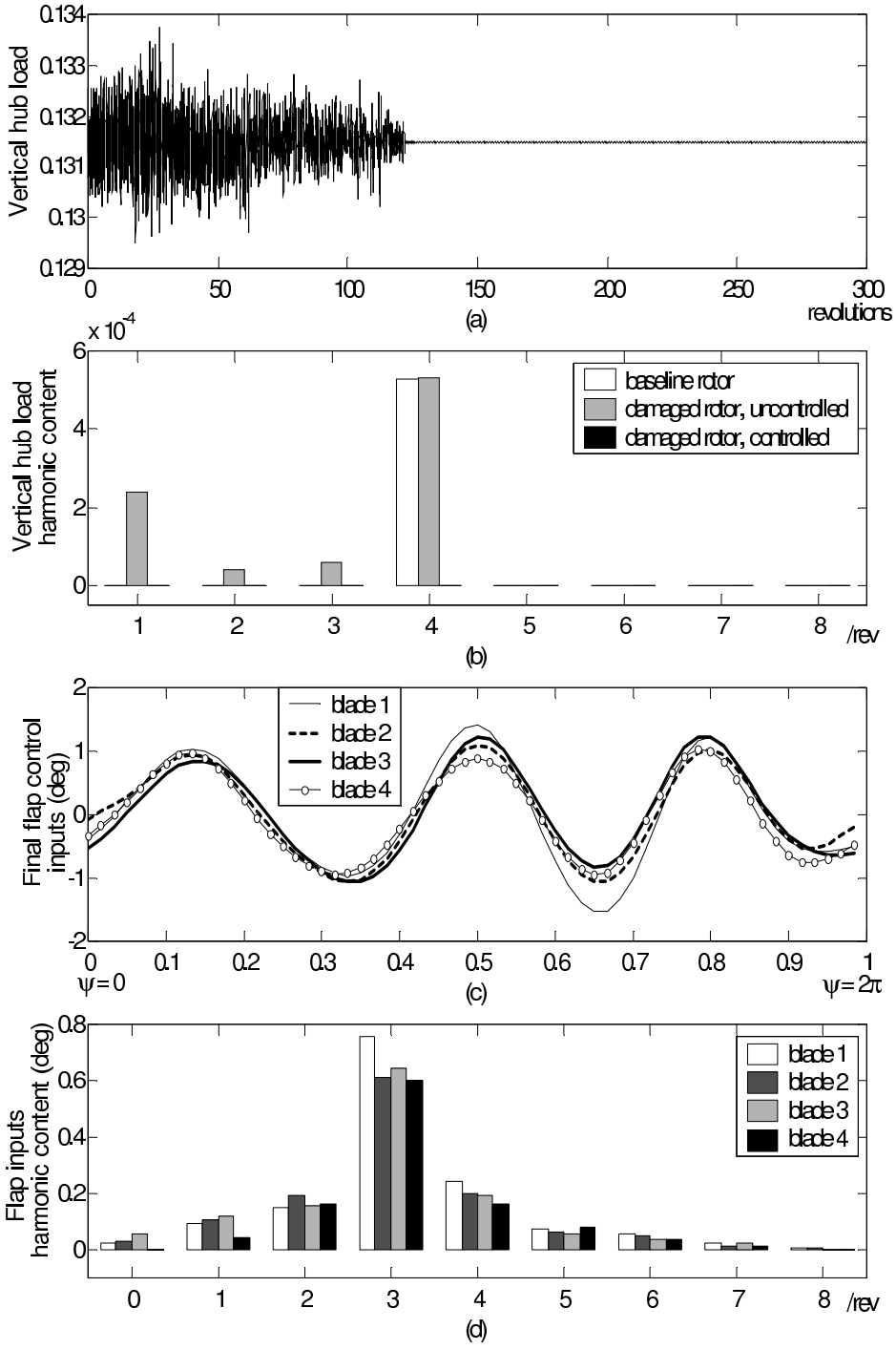

Figure 4.3: Loss of trim mass damage; (a) vertical hub load time history; (b) harmonic content of vertical shear; (c) optimal flap angles; (d) harmonic content of flap angles.

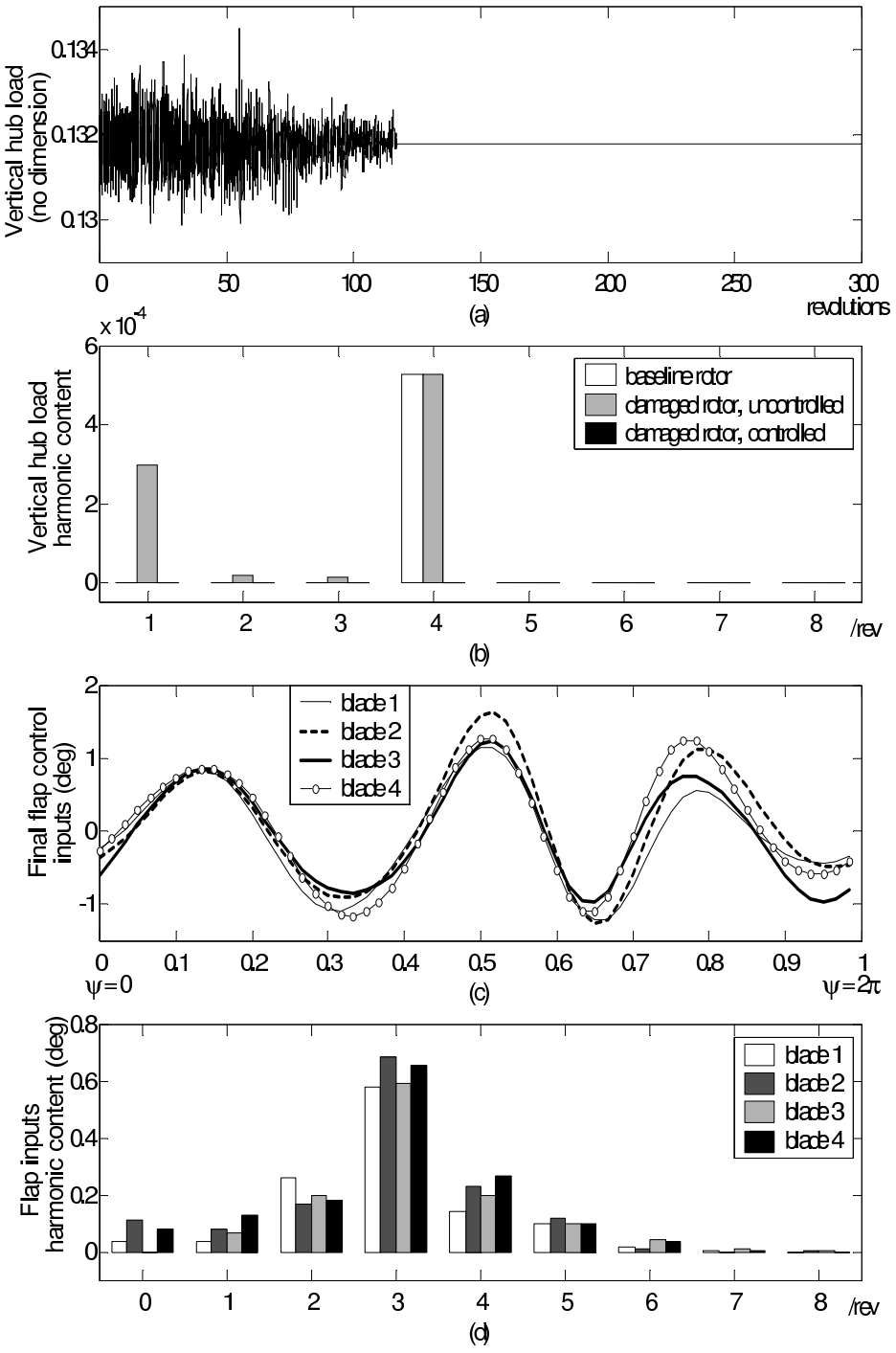

Figure 4.4: Damaged trailing-edge flap; (a) vertical hub load time history; (b) harmonic content of vertical shear; (c) optimal flap angles; (d) harmonic content of flap angles.

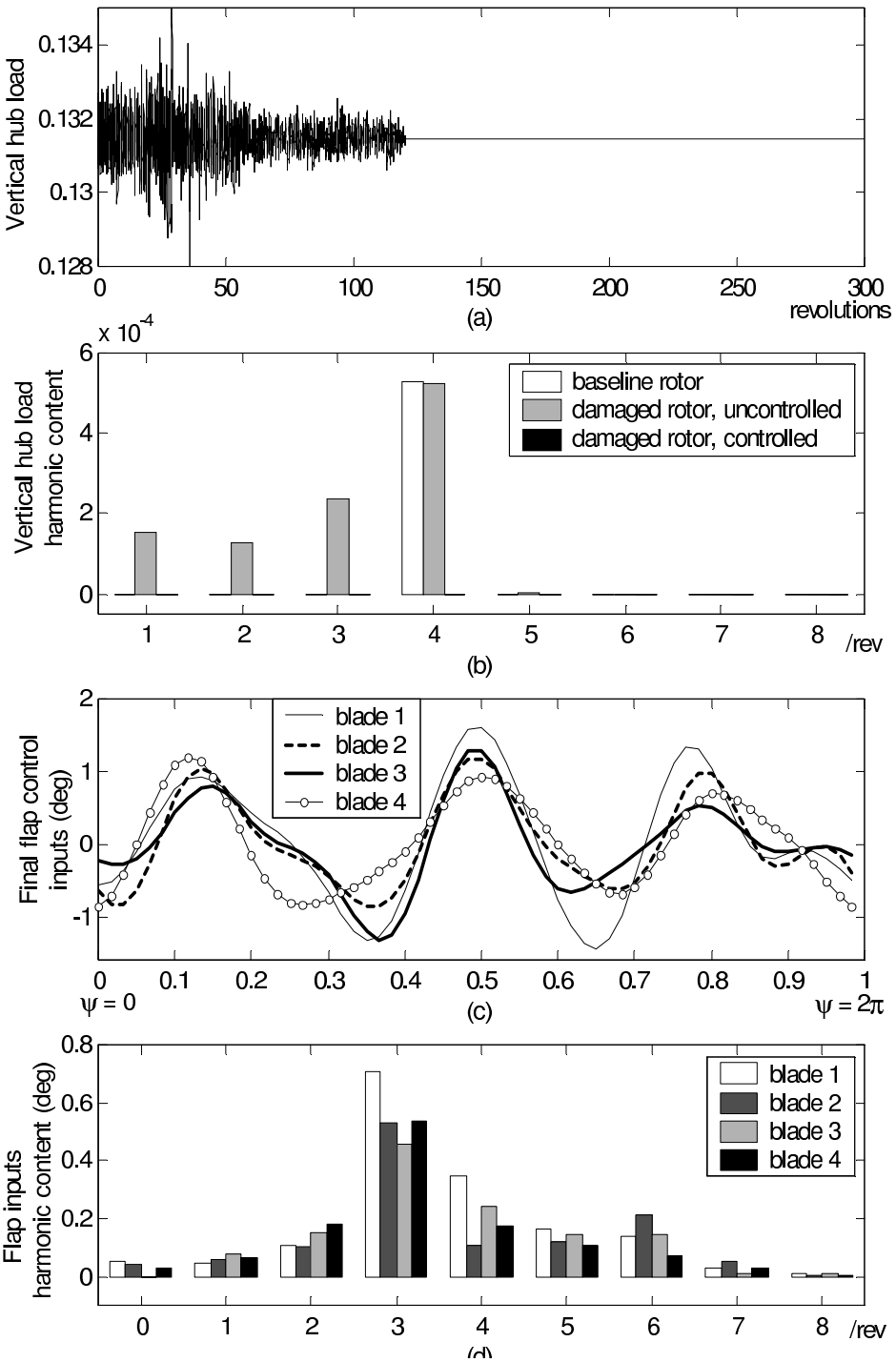

Figure 4.5: Bending stiffness damage; (a) vertical hub load time history; (b) harmonic content of vertical shear; (c) optimal flap angles; (d) harmonic content of flap angles.

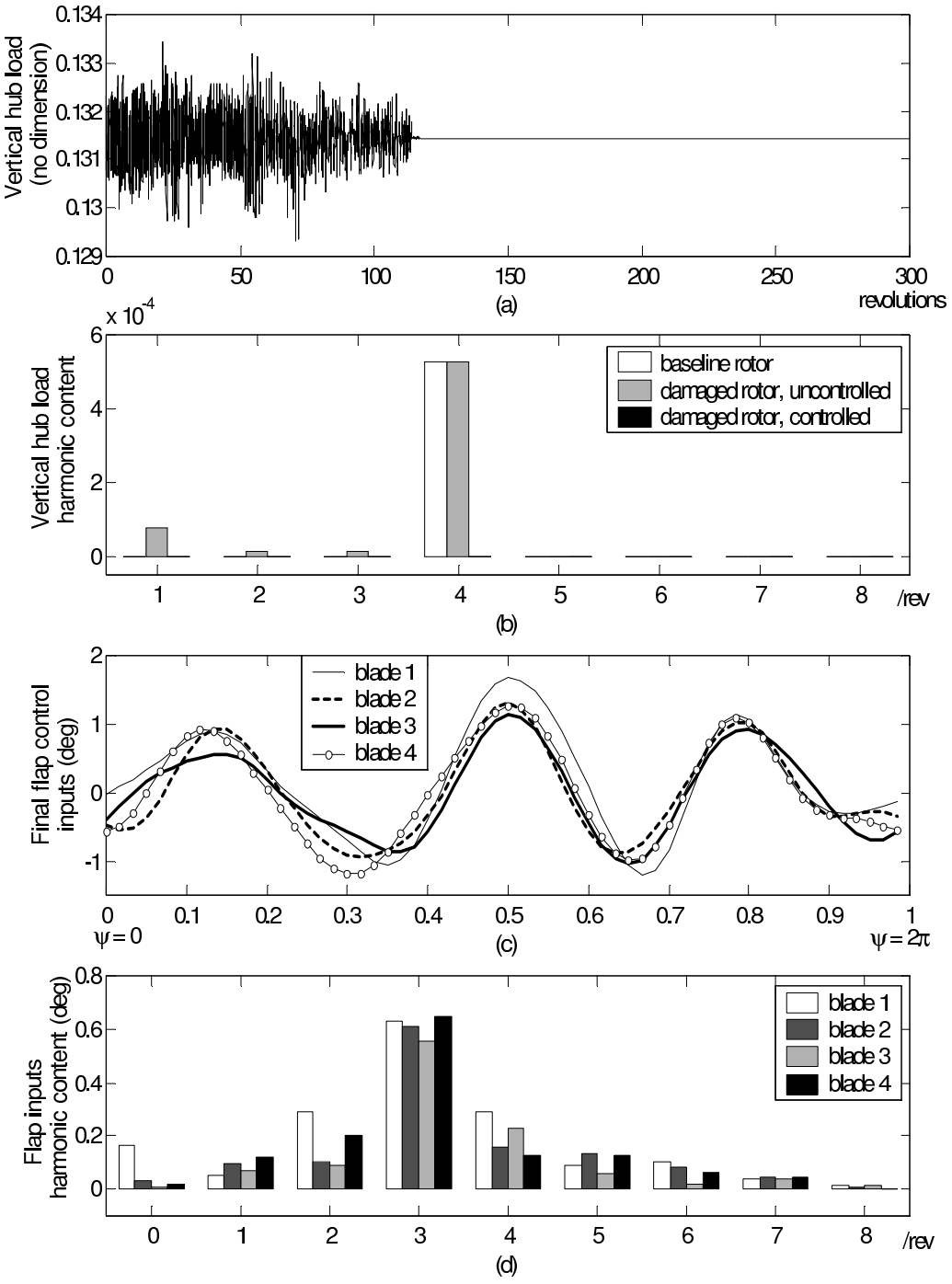

Figure 4.6: Various damages in blade mass and stiffness; (a) vertical hub load time history; (b) harmonic content of vertical shear; (c) optimal flap angles; (d) harmonic content of flap angles.

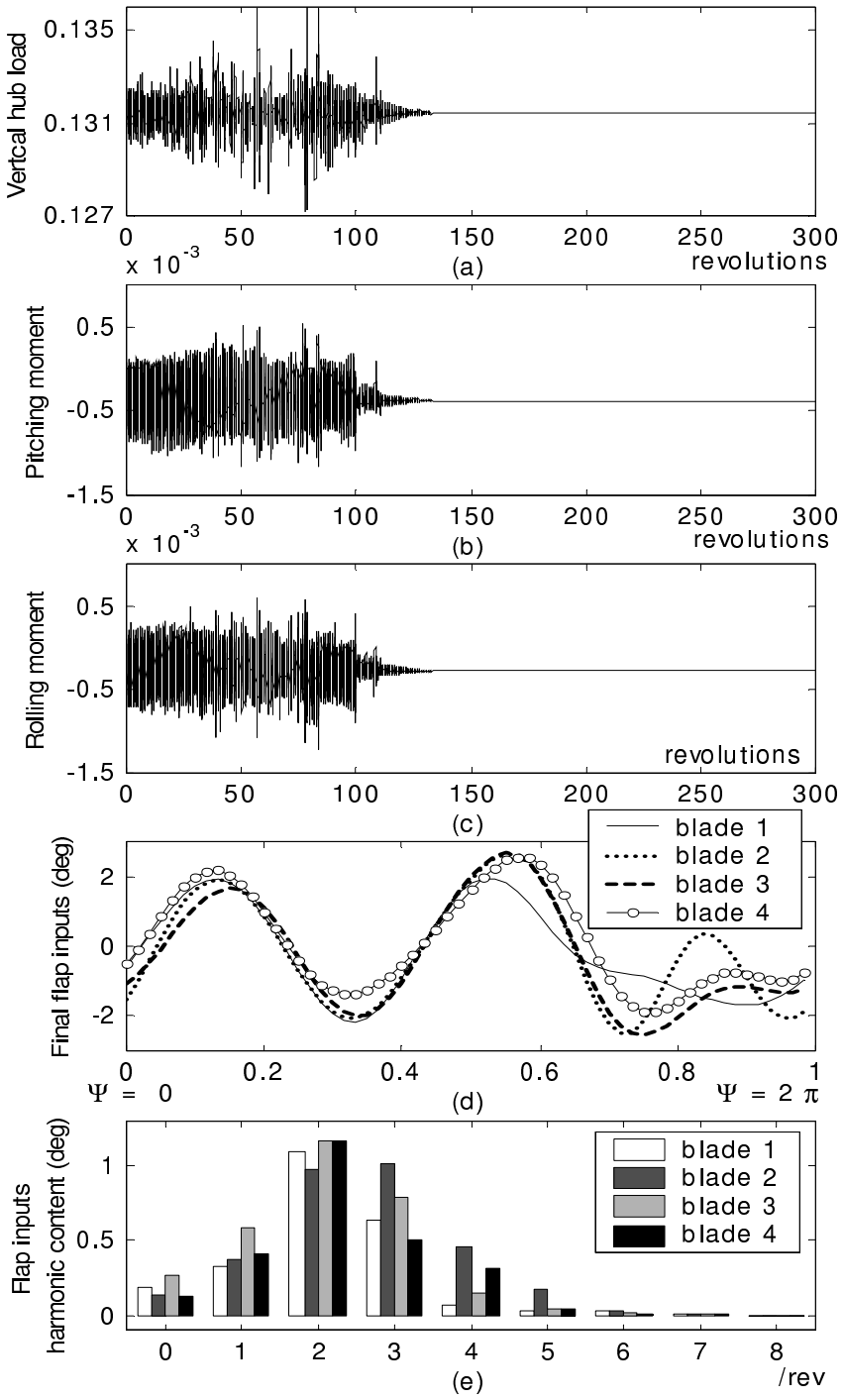

Figure 4.7: Multiple loads control with moisture absorption in blade 4; (a) vertical hub load; (b) hub pitching moment; (c) hub rolling moment; (d) optimal flap angles; (e) harmonic content of flap inputs.

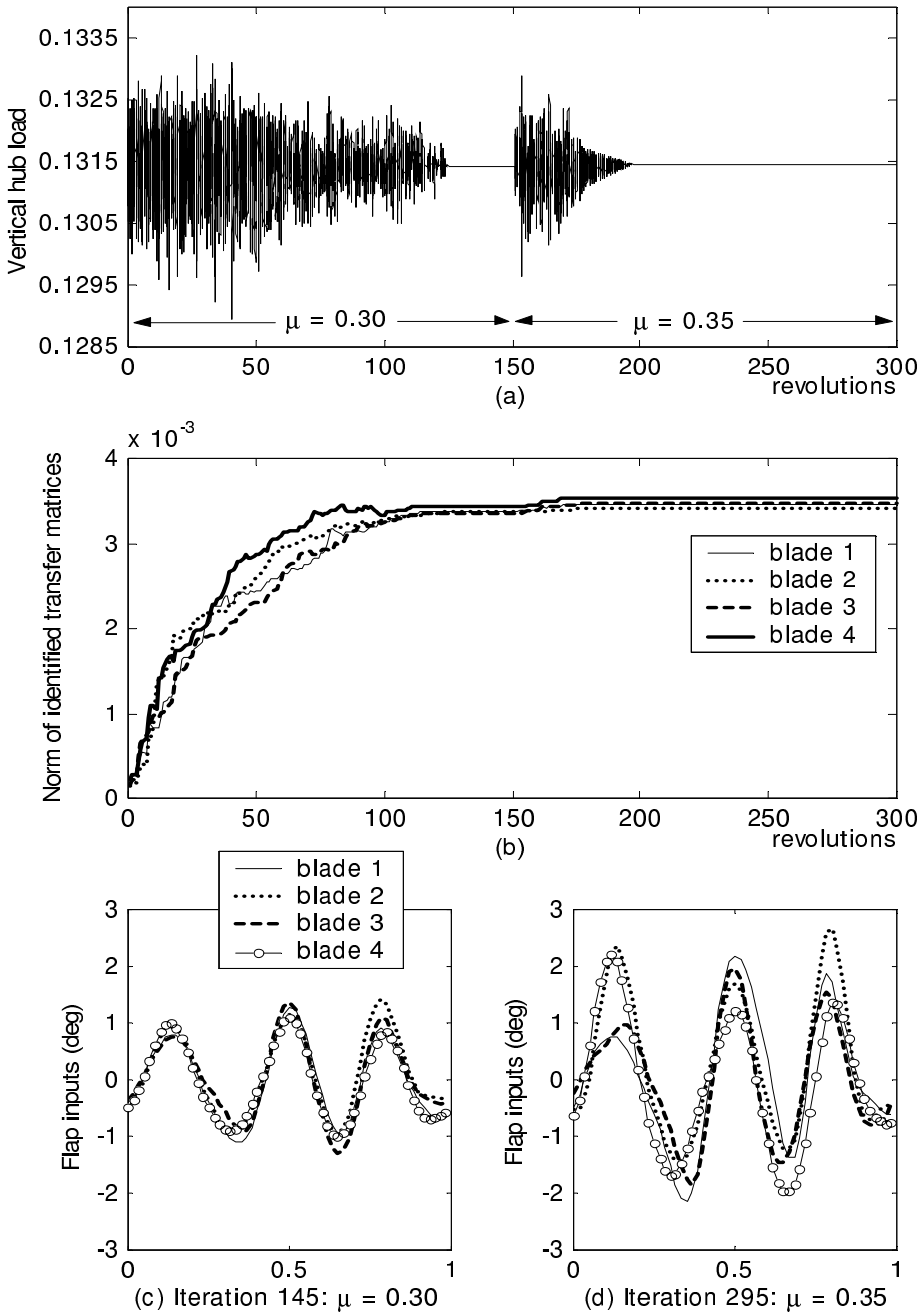

Figure 4.8: Effect of a change in advance ratio at iteration 150; (a) vertical hub shear time history; (b) time history of the identified transfer matrices norm; (c) optimal flap angles before advance ratio change; (d) optimal flap angles after advance ratio change.

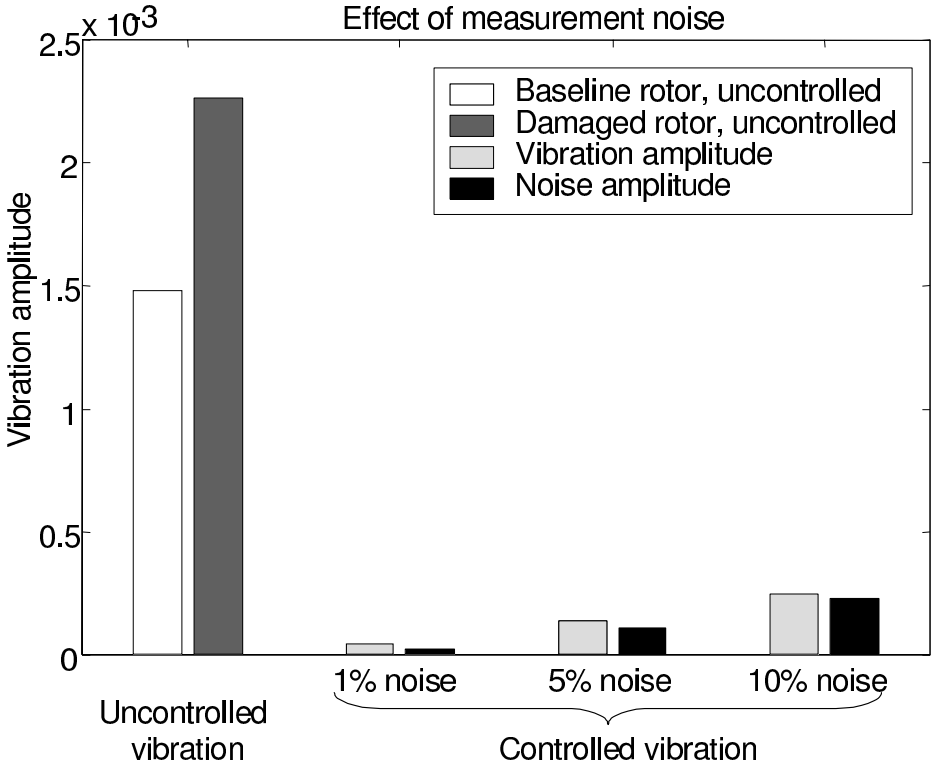

Figure 4.9: Effect of measurement noise on vibration reduction with moisture absorption damage in blade 4.

Chapter 5

Controller Simulation using Comprehensive Analysis

This chapter examines the performance of the individual blade control algorithm using a comprehensive analysis code (UMARC [116]) as the helicopter model. The code methodology is described in Chapter 2.

5.1 Helicopter model

A bearingless rotor model is used, based on the MD900 helicopter. The model features multiple load paths for the flexbeam/torque tube configuration, viscoelastic snubber, kinematics of control linkage, and non-linear bending-torsion coupling within the flexbeam [126]. Each rotor blade is divided into 20 finite elements undergoing flap, lag and torsion degrees of motion. In the present analysis, 4 flap modes, 3 lag modes, and 2 torsion modes are used. The characteristics of the model rotor are presented in Table 5.1. A refined pseudo-implicit free wake model developed by Bagai and Leishman [127] is incorporated in the analysis.

The rotor is first trimmed to zero first harmonic flapping and a target C_T/σ (wind tunnel trim). The shaft angle is specified to provide propulsive trim. After

Table 5.1: MD-900 rotor characteristics

Parameters	**Symbol**	**Value**
Number of blades	N_b	5
Rotor radius	R	16.925 ft
Rotor speed	Ω	392 RPM
Chord (nominal)	c/R	0.0492
Lock number (nominal)	γ	9.17
Solidity	$N_b c/\pi R$	0.0779
Lift curve slope	c_1	7.10
Lift coefficient at $\alpha = 0$	c_0	0.1123
Pitching moment coefficient	$c_{m_{ac}}$	-0.008
Flap spanwise location / R	r_{mid}	0.83
Flap chord / nominal chord	c_f	0.25
Flap length / R	l_f	0.18
Twist	θ_{tw}	10°
Reference mass/span	m_{ref}	0.0655 slug/ft
Reference shear	$m_{ref}\Omega^2 R^2$	31,600 lb
Reference moment	$m_{ref}\Omega^2 R^3$	535,000 ft-lb

cyclic inputs have converged to the trim solution, the controller is activated. The analysis calculates the steady state hub loads resulting from a given flap input. Based on computed hub loads, the flap inputs are updated every rotor revolution.

5.2 Computation specifics

Controller performance is investigated under wind tunnel trim conditions at $\mu = 0.2$, $C_T/\sigma = 0.075$ and a forward shaft tilt angle of 5°. To simulate measurements, $N_s = 60$ samples are used for each rotor revolution. To initialize the

system identification procedure, a value is chosen for the system noise covariance matrix Q, and the measurement noise covariance r (scalar). No measurement noise is added to the computed vibration. Initial guesses are made for the state vector x_0 and estimate error covariance matrix, P_0. $x_0 = 0$, $P_0 = I_{(N_b N_s+1)}$, $Q = 10^{-5}.I_{(N_b N_s+1)}$, and $r = 10^{-5}$ are chosen. For the controller, a maximum flap deflection of $\delta_{max} = \pm 4^\circ$ is imposed by increasing W_δ if the required flap deflection becomes too large. An upper limit on $\Delta\delta_{max}$ is used to avoid large transient hub loads.

First the transfer matrices relating the flap control inputs to hub loads are identified. Then the performance of the controller with identical rotor blades (baseline) is described. Next, the effect of rotor dissimilarities on the hub vibration is determined. Finally, the controller performance for reducing hub vibration with dissimilar rotor is investigated. Comparison is made with a controller that does not account for blade dissimilarities.

In a second stage, controller performance is investigated under wind tunnel trim conditions at advance ratios from $\mu = 0.10$ to $\mu = 0.40$, with $C_T/\sigma = 0.075$. The present individual control method is compared with a controller with identical motion for all flaps.

5.3 Transfer matrix identification

First, the transfer matrix relating the flap control inputs to the fixed system hub forces and moments is identified. Results are shown for the baseline rotor. A representation of the transfer matrices, T_{l1}, $(l = 1\,to\,6)$ for blade 1 is shown in Figure 5.1. Each of these transfer matrices relate the flap control input to blade 1, δ_1 (a 60×1 vector) to one of the six resulting fixed frame load, for example the vertical shear F_z (also a 60×1 vector). Therefore each matrix is of size 60×60.

In Figure 5.1, the columns are plotted versus azimuth for one rotor revolu-

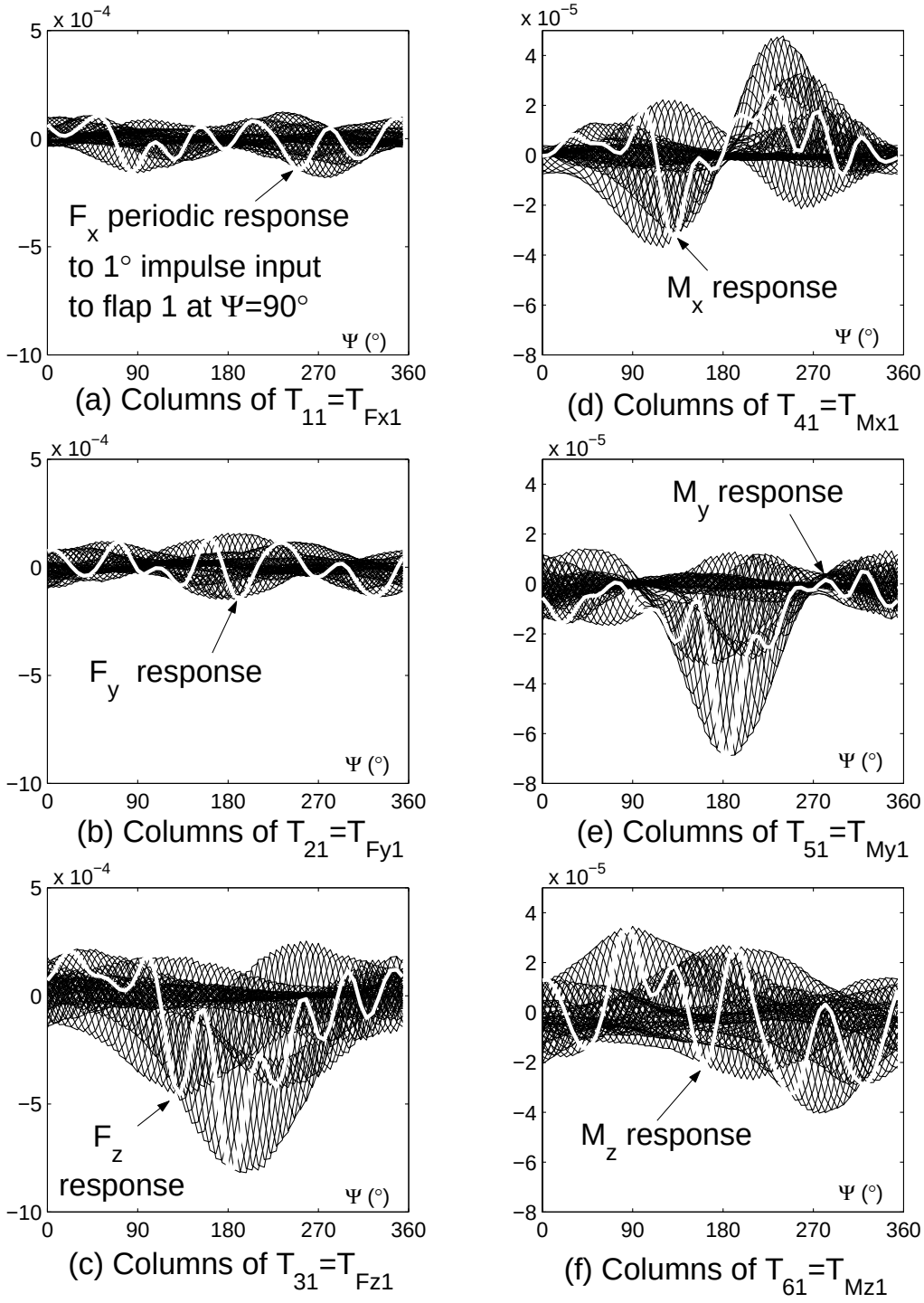

Figure 5.1: Representation of input/output transfer matrix for blade 1 (baseline rotor, $\mu = 0.2$)

tion. Each column vector represents the hub force or moment resulting from an impulsive unit flap input, at a particular azimuth, for a specific blade. For example, the curves highlighted in white in Figure 5.1 are the 16th columns of matrices T_{l1}, $l = 1, 6$. They correspond to the fixed frame hub forces and moments resulting from an impulsive input of amplitude 1° at $\Psi = 90^\circ$ to blade 1. This is easily seen if the vector δ_i corresponding to this impulsive input is expanded as:

$$\delta_i = \left\{ \begin{array}{c} \delta^1 \\ \vdots \\ \delta^{16} \\ \vdots \\ \delta^{60} \end{array} \right\} = \left\{ \begin{array}{c} 0 \\ \vdots \\ 1 \\ \vdots \\ 0 \end{array} \right\} \tag{5.1}$$

The resulting vertical shear in the fixed frame is then:

$$\begin{aligned} \Delta F_z &= T_{31} \times \{\delta_i\} \\ &= [T_{31}^1 \cdots T_{31}^{16} \cdots T_{31}^{60}] \times \{\delta_i\} \\ &= T_{31}^{16} \end{aligned} \tag{5.2}$$

which corresponds to the 16^{th} column of matrix $T_{31} = T_{F_z, blade\,1}$.

Note that from Figure 5.1, it is clear that the system is not time invariant: for a LTI system, the response does not depend on the time at which the input is applied, therefore each transfer matrix column would simply be a cyclically shifted version of the previous column. In other words, the transfer matrices would be circulant. The variations observed between columns in Figure 5.1 show that the transfer matrices were obtained with the helicopter in forward flight ($\mu = 0.2$), when the system is time periodic.

Figure 5.1 also shows that the longitudinal and lateral hub shears are much less sensitive to flap actuation than the vertical hub shear (about 3.5 times

Table 5.2: Predicted and measured non-dimensional 5/rev hub loads ($\mu = 0.2$)

Hub load	**Measured**	**Predicted**
Fx	0.0045	0.0030
Fy	0.0009	0.0030
Fz	0.0041	0.0022
Mx	$3.8\,10^{-4}$	$8.3\,10^{-5}$
My	$4.2\,10^{-4}$	$1.3\,10^{-4}$

less sensitive). On the other hand, the three hub moments have comparable sensitivities to the flap deflection. Sensitivity results obtained for the damaged rotor are very similar.

5.4 Control of baseline rotor

The computed uncontrolled vibratory loads (5/rev) are first compared with full-scale wind tunnel test data [128] in non-dimensional form in Table 5.2. UMARC shows acceptable correlation with full-scale wind tunnel test data. The predicted vibratory hub loads are of the same order of magnitude as test data.

The closed-loop control is then applied to the rotor model to reduce hub vibration through optimal flap inputs. In the first stage, the weighting matrix W_F is adjusted to control only one fixed system hub load at a time. The optimal control inputs reach convergence after about 150 rotor revolutions. Results are shown in Figures 5.2 and 5.4.

Figure 5.2 shows the effect of the optimal flap actuation on all fixed system

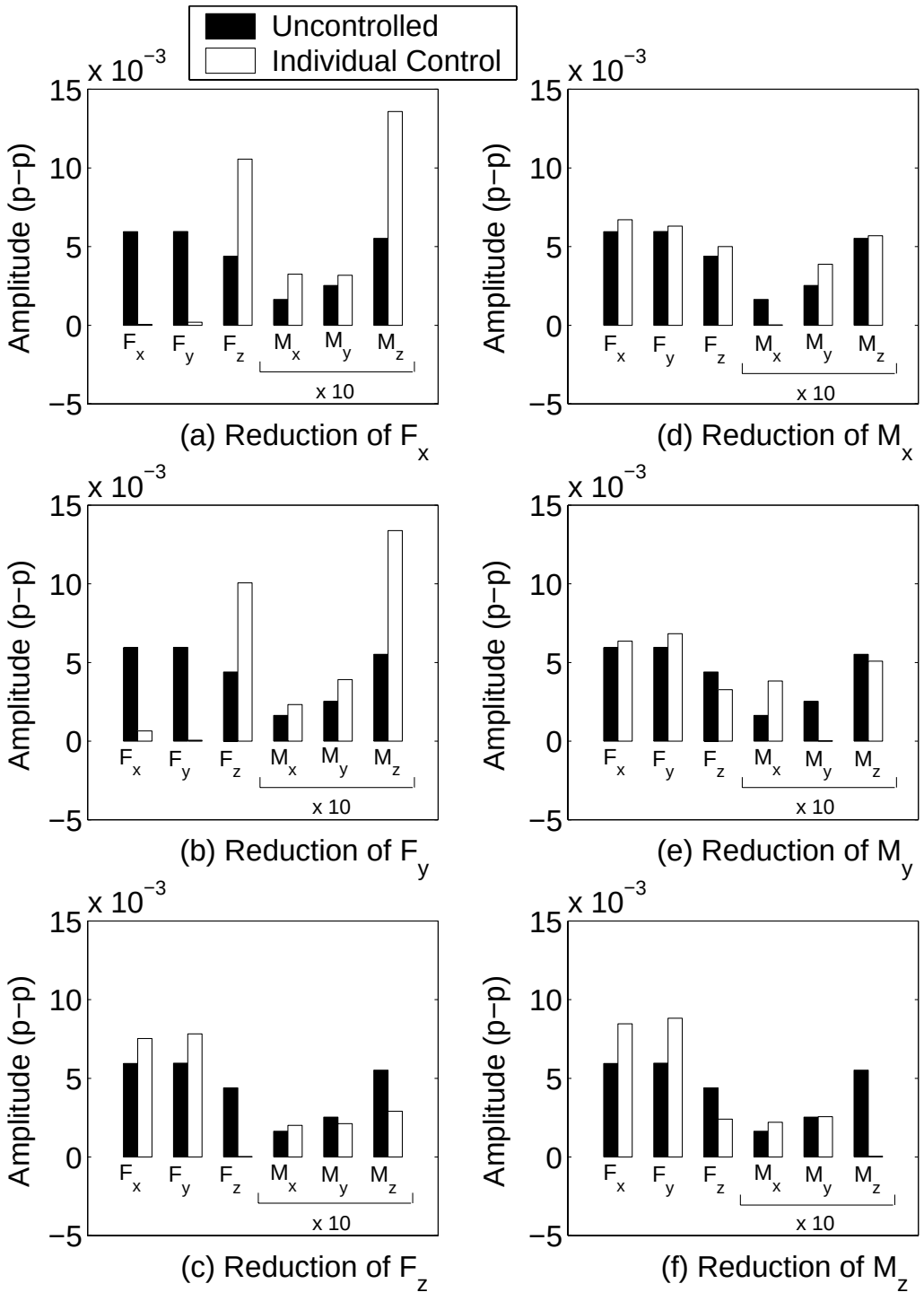

Figure 5.2: Controller performance to reduce each hub load separately (baseline rotor, $\mu = 0.2$)

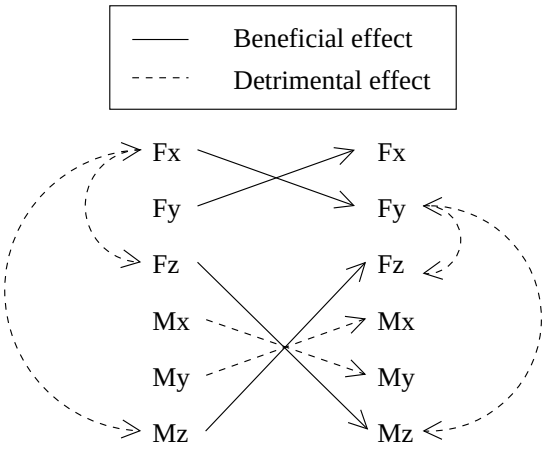

Figure 5.3: Multiple load vibration reduction: interaction between loads

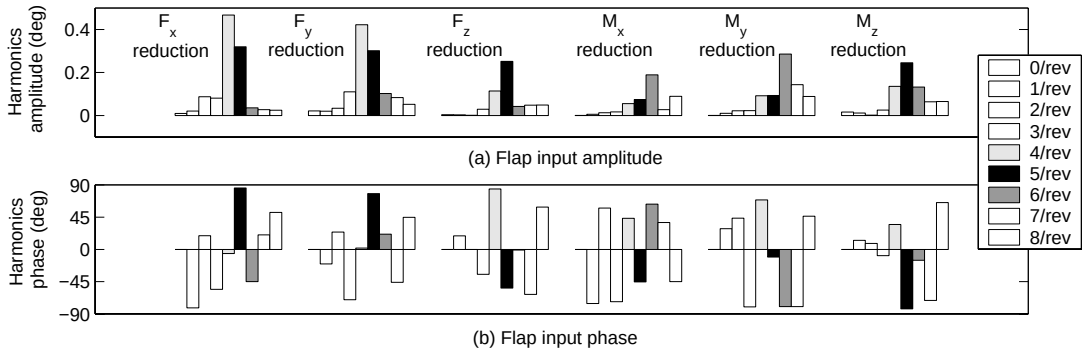

Figure 5.4: Optimal flap inputs required to reduce each hub load separately (baseline rotor, $\mu = 0.20$)

hub loads when the controller attempts to reduce one particular load. The uncontrolled and controlled peak-to-peak amplitude are represented for each hub load (non-dimensionalized as shown in Table 5.1).

For every one of six cases, the reduction of considered hub load is over 98%. However there are significant increases in other vibratory components. This is especially true when the objective to minimize F_x or F_y is implemented; the vibration amplitudes for the vertical hub shear and yawing moment are more than doubled. On the contrary, reducing of F_x also results in the reduction of oscillatory F_y, and vice versa. The reduction of F_z, M_x, or M_y has a relatively small detrimental effect on F_x and F_y vibration. The reduction of M_x leads to an increased M_y vibration, and vice versa. On the contrary, reducing the vertical shear F_z also results in a decreased vibratory hub yawing moment, and vice versa. These observations are summarized in Figure 5.3, where a dashed line signifies a detrimental effect and a continuous line indicates a beneficial effect between two loads. Note that the detrimental effects are equally present in the controller with identical flap motion for all blades and are not artifacts of the individual control algorithm.

Figure 5.4 shows both the amplitude and phase of the flap control inputs required to reduce each hub load. Note that this is still for the baseline rotor with identical blades, therefore the optimal input is identical for all blades. As shown by the transfer matrices in Figure 5.1, we observe that the largest flap deflection is needed for the reduction of the hub shears F_x and F_y (about 2° peak-to-peak). For all other loads, the deflection amplitude is comparably small, about 1° peak-to-peak. The most important flap harmonics, i.e. 4/rev, 5/rev and 6/rev for the 5-bladed rotor, are shown in shades of grey, whereas other harmonics are shown in white. Note that even though these three harmonics are dominant, actuating the flaps at other frequencies also contributes towards vibration reduction. In particular, the 7/rev and 8/rev flap components seem to

be important for the reduction of the hub vibratory moments M_x and M_y. The 2/rev and 3/rev components are also relatively important when the objective is to minimize the oscillatory in-plane shear F_x or F_y. The flap deflections required for minimizing F_x or F_y are very similar qualitatively, with large 4/rev and 5/rev components. Flap inputs corresponding to the reduction of F_z or M_z, have 5/rev as the dominant frequency. Flap inputs necessary to reduce M_x or M_y also appear qualitatively similar, with the 6/rev as dominant harmonic. However, Figure 5.4(b) shows that the phases of the 6/rev harmonic components are opposite to each other. These are in agreement with the relations shown in Figure 5.3.

In the second stage, simultaneous reduction of all loads is attempted. Weights are adjusted so that the norms of the weighted vibratory loads (non-dimensional) are equal in the objective function. Results are shown in Figure 5.5. It is not possible to reduce completely all six vibratory loads simultaneously. The vibration is reduced by more than 80% for three hub loads and more than 60% for the remaining hub loads. The flap deflection required is considerably increased while still remaining within limits of $\pm 4^\circ$. The 3/rev component is the dominant flap input. When a single load is targeted, the harmonic content of flap inputs is predominantly 4, 5 and 6/rev. However, for multiple loads, the 3/rev component can play a critical role depending on the target loads. This can happen when both (F_z, M_z), and (M_x, M_y) are included in the objective function. The hub moments M_x, M_y are generated by 4/rev and 6/rev components of rotating flapwise and torsion moments. If these components have comparable amplitudes, their phases can be manipulated such that the 5/rev components they generate in the fixed frame cancel each other. It is observed that the 4/rev rotating torsion moment is an order of magnitude smaller than the 4/rev rotating flapwise moment. It is also observed that, in order to cancel the 5/rev hub moments, the controller generates a large 4/rev rotating frame torsion moment. This can be achieved

by a large 3, 4 or 5/rev flap input. Only a large 3/rev flap input can reduce the hub moments without affecting F_z or M_z. A large 4 or 5/rev flap input will affect 5/rev F_z and M_z. This is why in this case we observe a dominant 3/rev flap input, with a smaller 5/rev component.

To verify this, the control input was restricted to 4, 5 and 6/rev. Results are shown in Figure 5.6. The performance deteriorated: F_z and M_z are reduced by only 50%, and M_y is reduced by less than 10%. The maximum flap deflection has significantly reduced (about 1.4° compared to 4°). If the maximum flap deflection is restricted to 1.4°, the controller would always reach this solution and 4, 5, 6/rev control inputs would dominate. However, increased flap deflections of ±4° are allowed. The controller can achieve greater vibration reduction using predominantly 3/rev flap inputs.

Next, the controller performance is assessed at a higher vibration level. Figure 5.7(a) shows predicted and full-scale wind tunnel test vibration levels at transition speed. UMARC overpredicts the 5/rev hub axial and side forces. The 5/rev normal force is underpredicted. The predicted 5/rev rolling and pitching moments are close to measurements. Figure 5.7(a) also shows the 5/rev hub loads after control. All loads show considerable reduction, with hub shears reduced by 90%. Figure 5.7(b) shows that the required control deflection is about 3.1° half peak-to-peak, and the harmonic content is dominantly 4/rev.

5.5 Effect of rotor dissimilarity

Rotor dissimilarities are introduced by modeling rotor faults. Two types of rotor faults are considered. The first fault is simulated by increasing the mass of the blade section corresponding to the trailing-edge flap in blade 1 by 1% (about 50 grams). The second fault is simulated by increasing the nose-down pitching moment coefficient for the same section from $c_m = -0.008$ to $c_m = -0.01$. The

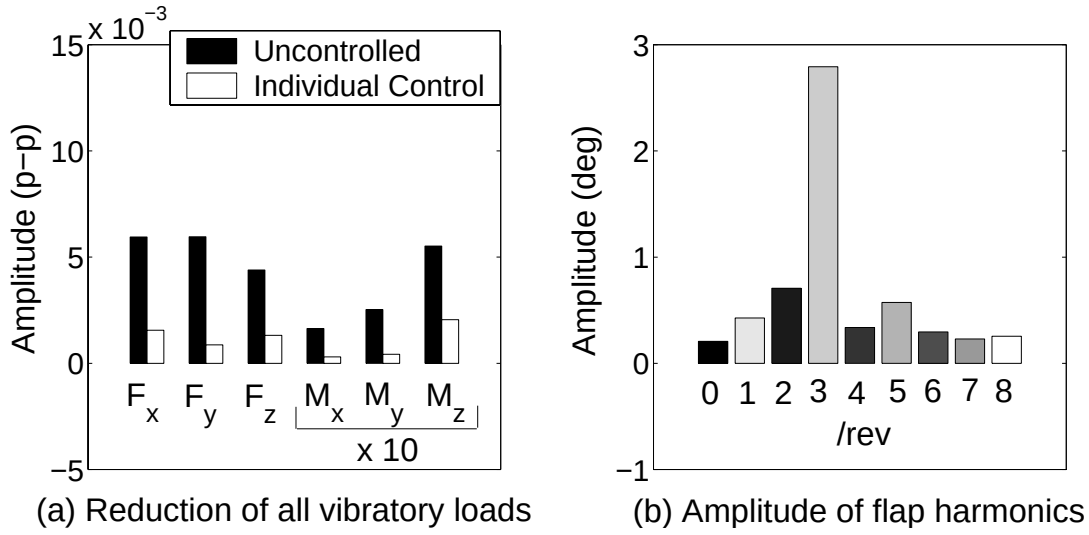

Figure 5.5: Simultaneous vibration reduction of all hub loads (baseline rotor, $\mu = 0.2$)

trailing edge flaps, of chord $c_f = 25\%$ of nominal blade chord, extend from $0.74R$ to $0.92R$ for each blade.

Figure 5.8 shows the magnitude of harmonics for the six fixed system hub loads, in the case of baseline and damaged rotor. Only the first five harmonics are shown, since the amplitudes of harmonics higher than 5/rev are negligible. For the baseline rotor, only 5/rev component is present for this 5-bladed rotor. Even though the extent of damage is very small, there is a significant effect on other vibratory harmonics. The mass damage introduces a large 1/rev component in the lateral and longitudinal hub shears. A moderate 1/rev vibration is also present in the rolling and pitching moments. The effect on the vertical hub shear and the yawing moment is small. By contrast, the effect of the aerodynamic damage is more significant on the rolling and pitching moments, especially as 1/rev and 2/rev components. It also introduces a 1/rev component in vertical shear. Unlike the mass damage, the increase in 1/rev lateral and longitudinal hub vibration due to moment fault is not significant.

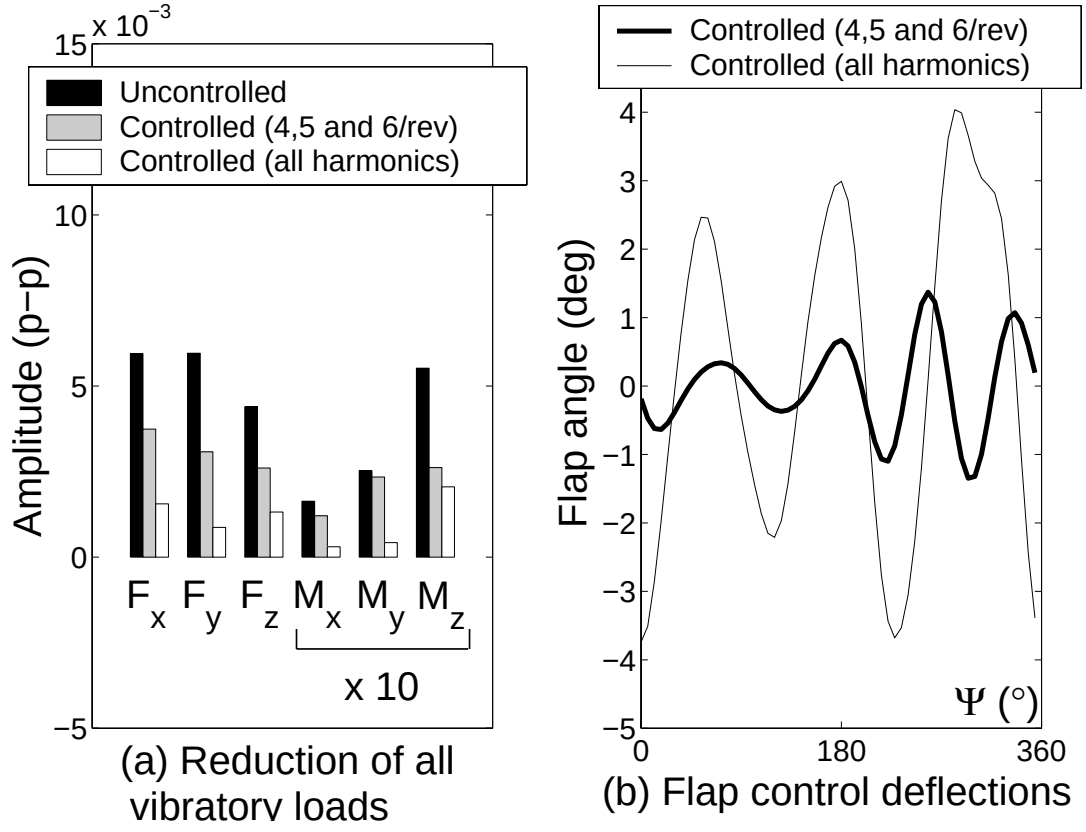

Figure 5.6: Effect of using limited input harmonics on simultaneous vibration reduction of all hub loads (baseline rotor, $\mu = 0.2$)

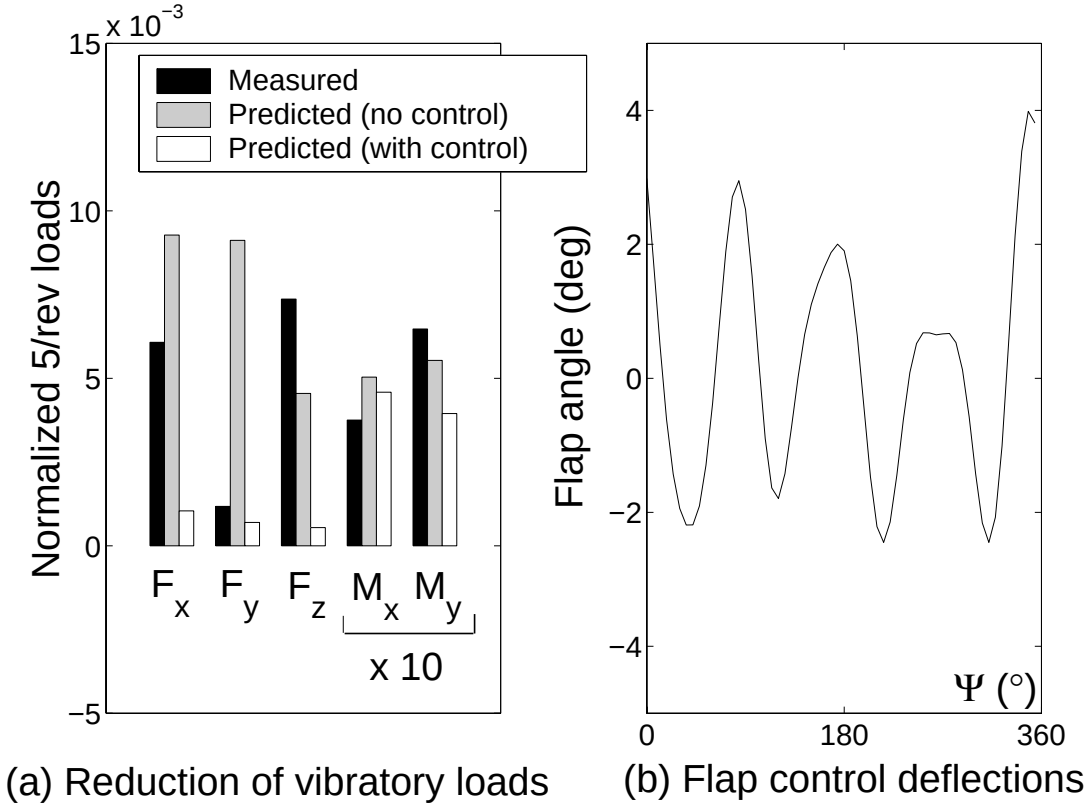

Figure 5.7: Vibration reduction at transition speed (baseline rotor, $\mu = 0.1$)

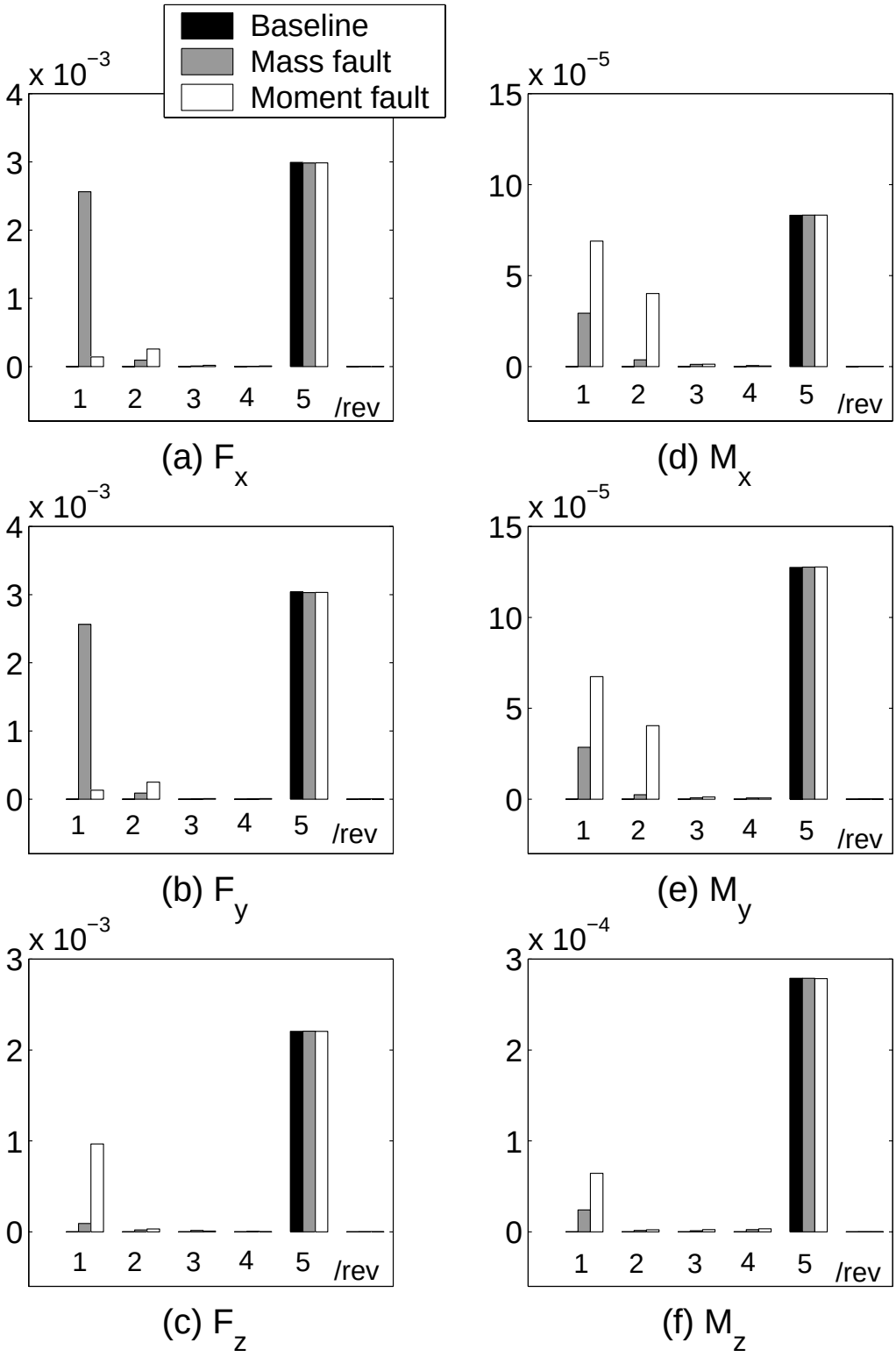

Figure 5.8: Effect of rotor faults on magnitude of hub loads harmonics ($\mu = 0.2$)

5.6 Control of dissimilar rotor

The performance of the present controller is now tested with dissimilar blades and compared to that of a controller using identical flap inputs. For purposes of discussion, the present controller will be referred to as "individual control". Controller using identical flap inputs for all blades will be referred to as "classical control". For classical control, the objective function only includes the kN_b/rev harmonics.

First, the mass fault is simulated in blade 1. Figure 5.9 presents the vibration reduction achieved when the objective function consists of only one hub load, using classical control and refined individual control. Using the present controller, the considered oscillatory load is reduced in all six cases by more than 98% in amplitude. However, the reduction of either F_x or F_y causes a dramatic increase in all other hub loads. The classical controller is unable to reduce either F_x or F_y vibration by more than 50%. This is because only the 5/rev harmonics is reduced: this controller has no effect on the 1/rev component, which is very large in F_x and F_y for the mass damage. Figure 5.10 shows the corresponding optimal control inputs. Because the blades are dissimilar, the controller now generates different flap inputs for each blade. Flap deflections required for minimizing either F_x or F_y show large variations from one blade to another. These variations translate into non-kN_b/rev loads in the fixed frame. These non-kN_b /rev counteract the large 1/rev components of F_x and F_y. On the contrary, the flap inputs generated for the reduction of other loads are similar for all blades. This is because the non-kN_b/rev harmonics are relatively small for these loads. In Figure 5.10, the optimal control input required for all blades using classical control is also shown. As expected, the inputs required using the classical method and the individual control method are different when the targeted hub load contains significant non-kN_b/rev harmonics.

The objective function is then modified to attempt reducing all fixed system hub loads simultaneously. Figure 5.11 shows the vibration reduction achieved and the flap control inputs required.

The maximum flap deflection of 4° is attained while only 40% reduction in vibratory amplitude for F_x is achieved. Note that the 3/rev harmonic is again dominant in the flap inputs for all blades. For this mass damage, the advantage of using individual flap inputs is less appealing. Vibrations can be reduced completely for each load separately but at the cost of increasing vibrations for other hub loads. For simultaneous control of all loads, individual control performance is only slightly improved compared to classical control. Inability of the individual controller to further reduce the hub vibrations stems from actuator saturation. Higher flap deflections will lead to better control. With flap deflection limited to ±6°, at least 60% vibration reduction is achieved for all loads (Figure 5.12). Performance of the classical controller, on the other hand, is inherently limited by its inability to reduce non-kN_b/rev vibrations. As a result, increasing the maximum flap deflection does not improve controller performance. Actuator saturation is caused by the following three reasons. The greatest effect of mass damage is felt in F_x and F_y vibrations. The sensitivity of F_x and F_y to flap deflections is small. The effect of reducing either F_x or F_y vibrations is detrimental for all other vibratory loads.

The pitching moment damage introduces significant 1 and 2/rev components in M_x and M_y. Also a large 1/rev component is induced in F_z. However the effect on F_x or F_y is small. Figure 5.13 shows the vibration reduction achieved when the objective function contains only one hub load. Figure 5.14 shows the corresponding flap deflections. Figure 5.13 shows that each load can be separately reduced by more than 98% using individual control. Using classical control, the pitching and rolling moment vibration is reduced by only 50% while the vertical vibration is reduced by 60%. The large non-kN_b/rev components

present in these vibratory loads can not be controlled using identical flap inputs. Note that the corresponding optimal flap inputs (Figure 5.14) are very similar for both methods. Hence vibration reduction can be improved without any increase in flap deflections, simply by using slightly different inputs for each flap. All loads are reduced separately with flap deflections less than 2° peak-to-peak.

Finally simultaneous reduction of all six hub loads in presence of pitching moment dissimilarity is described. The results are shown in Figure 5.15. Using individual control all loads are reduced by more than 70%. This is higher than the reduction achieved by classical control. The required flap deflections are similar for all blades, with a dominant 3/rev component and about 4° half peak-to-peak amplitude. Again, it is observed that small variations in deflection from flap to flap can result in greatly improved vibration reduction.

5.7 Effect of control input weight

Figure 5.16 shows the effect of varying the control input weight on the controller performance. The controller performance is measured by the vibration reduction (with vibration index defined as $\sqrt{J_F}$ in Eq. 2.13) as well as the maximum flap deflections. Three cases are considered: baseline rotor, rotor with mass fault in one blade, and rotor with aerodynamic fault in one blade. The control objective is to reduce all loads simultaneously.

Previous results (Figures 5.5, 5.13, and 5.16) are indicated by the dashed lines. For these results, the weighting matrices W_δ have been chosen such that the maximum flap deflection is 4°. For the baseline rotor as well as for damaged rotor, the maximum vibration reduction that can be achieved is about 88%. However, for the baseline rotor, flap deflections are identical for all blades, while for the damaged rotor, they are different. The maximum flap deflection required for baseline rotor is about 7.5°.

The flap deflections required for the rotor with a mass fault are much larger, up to 14°. However, when these deflections are limited to 4°, the vibration index is still reduced by about 65%. Note that a small increase in maximum flap deflection (e.g., from 4° to 6°) would result in greater vibration reduction (from 65% to 80%).

The flap deflections required for the rotor with a moment fault are very similar to the baseline rotor case (about 7.5°). This damage is simulated by a change in pitching moment for the blade section corresponding to the flap. Therefore, it would be possible to cancel the vibration caused by this fault (mostly at 1/rev and 2/rev) by imposing a steady deflection to the flap in the damaged blade. However, this steady input needs to be added to the input required for cancelling the baseline vibration (at 4/rev). Finally, the total flap deflection required reaches a maximum value that is larger than the maximum flap deflection generated by the controller.

5.8 Effect of advance ratio

The controller performance is now tested at different advance ratios for the baseline and the damaged rotor. The objective function includes only the fixed system hub shears F_x, F_y and F_z, with respective weights of 0.3, 0.3 and 1, chosen so that each load has comparable importance in the objective function at $\mu = 0.20$. Figure 5.17(a) shows the vibration index $\sqrt{J_F}$ for the baseline rotor and the rotor with a mass fault in blade 1, with and without control. The performance of a classical controller is also shown. Figure 5.17(b) represents the half peak-to-peak flap deflections. The vibration index is minimum at $\mu = 0.25$. It increases at low advance ratio ($\mu = 0.10$) and high advance ratio ($\mu = 0.40$). The mass fault introduces large 1/rev component in the F_x and F_y shears, while the effect on F_z is very small. For the baseline rotor, the vibration index $\sqrt{J_F}$

is reduced by more than 88% at all advance ratios, and up to 95% at $\mu = 0.20$. The flap deflection required is smaller than 4° half peak-to-peak, and about 1° half peak-to-peak at $\mu = 0.30$. For the damaged rotor with a mass fault in blade 1, the individual control method is compared with the classical controller. Using individual control, the vibration reduction achieved is very close to the baseline results for $\mu \geq 0.15$. However, the required flap deflections are larger (about 2.2° half peak-to-peak at $\mu = 0.30$). For $\mu \leq 0.15$, the 4° limit is reached, resulting in less vibration reduction. For example, at $\mu = 0.10$, the vibration index is reduced by 78% using this limited flap deflection. Using classical control, the flap deflection required is smaller. However, the vibration cannot be reduced by more than 75%, and vibration reduction is only 40% at $\mu = 0.25$. Using identical inputs for all blades, the non-kN_b/rev vibration originating from blade dissimilarities can not be reduced efficiently.

Figure 5.18(a) and 5.18(b) shows the vibration index $\sqrt{J_F}$ and flap deflections for the baseline rotor and the rotor with the aerodynamic moment fault in blade 1, with and without control. Contrary to the mass fault case, the vibration increase due to the moment fault becomes larger at higher advance ratios. Figure 5.18(a) shows that using individual control, it is possible to achieve the same level of vibration reduction as for the baseline rotor (the line "moment fault, individual control" is hidden by the "baseline, controlled" line). Moreover, Figure 5.18(b) shows that the required flap deflections are very close to the baseline rotor case; smaller than 4° half peak-to-peak at all advance ratios, and about 1° half peak-to-peak at $\mu = 0.30$. However, using classical control, it is not possible to control the non-kN_b/rev vibration caused by the moment damage (Figure 5.18(a)). Since this additional vibration increases with advance ratio, the performance of the classical control deteriorates at higher advance ratios. At $\mu = 0.10$, the vibration index can be reduced almost as well as for the baseline rotor (about 90% reduction). However, at $\mu = 0.30$, only 45% reduction can be

achieved. This clearly illustrates the advantage of using different inputs for each blade: at $\mu = 0.30$, the vibration reduction can be increased from 45% to 94%, with smaller flap deflections.

5.9 Summary and concluding remarks

The performance of the proposed control algorithm has been investigated. The control objective was reduction of helicopter hub vibrations using active trailing edge flaps. A comprehensive analytic model based on a modern bearingless rotor that includes modeling of trailing edge flap effects (UMARC [116]) is used for numerical simulation.

The controller performance was tested at advance ratios ranging from $\mu = 0.10$ to $\mu = 0.40$, both for the baseline rotor with identical blades and the damaged rotor with dissimilar blades. The proposed controller takes into account rotor dissimilarities and allows for different control inputs to be applied to each trailing edge flap. This new controller was compared to a classical controller which uses identical inputs for all trailing edge flaps. The rotor faults were modeled as changes in inertial and aerodynamic properties for the damaged blades. Observations from this study are as follows:

1. Longitudinal and lateral hub shears are about 3.5 times less sensitive to trailing edge flap deflections than other loads. For the baseline rotor, each hub vibratory load can be separately reduced by more than 98% using moderate flap inputs (1° half peak-to-peak at $\mu = 0.20$). For simultaneous control of all loads, reductions of more than 60% are achieved for all loads using flap inputs of amplitude 4° half peak-to-peak, with dominant 3/rev harmonic component.

2. A small mass fault adds a large 1/rev harmonic in the longitudinal and

lateral hub shears. When controlled simultaneously, all loads are reduced by at least 40%. This is only slightly better than the performance of a classical controller. This is because the limit of $\pm 4^\circ$ imposed on the flap deflection is reached.

3. The aerodynamic fault introduces significant 1/rev and 2/rev components in the hub rolling and pitching moments, as well as a large 1/rev harmonic in the vertical hub shear. When controlled simultaneously, all loads are reduced by more than 70%. This represents a significant improvement compared to the performance of the classical controller (50%).

4. Significant improvements in vibration reduction are predicted for all advance ratios from $0.10 \leq \mu \leq 0.40$ using the present individual control method as compared to a classical control method. At $\mu = 0.30$, the vibration index reduction is increased from less than 45% to more than 90% using less than 2.5° half peak-to-peak flap deflections for both the structural and aerodynamic faults.

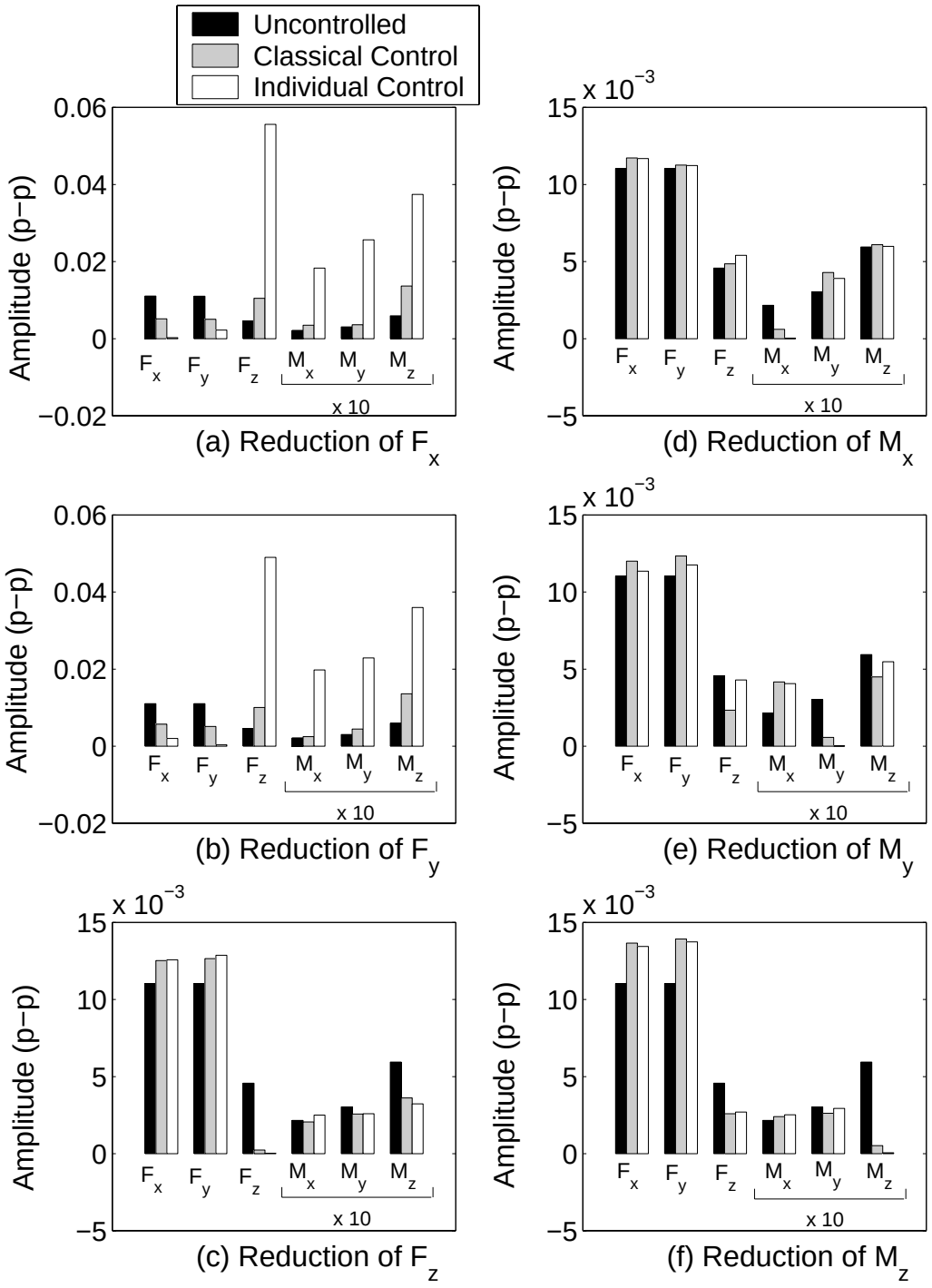

Figure 5.9: Controller performance to reduce each hub load separately (mass fault in blade 1, $\mu = 0.2$)

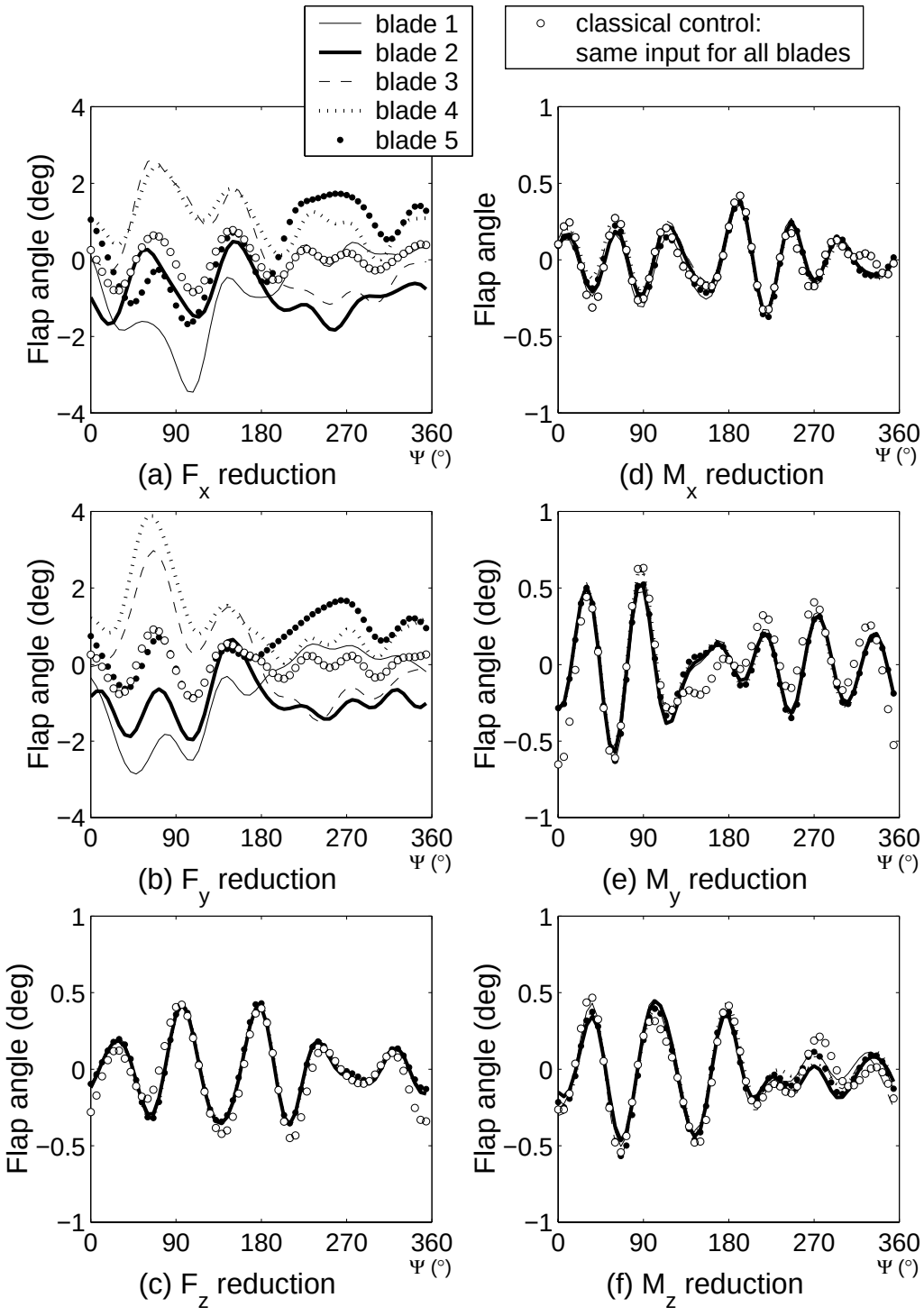

Figure 5.10: Optimal angles required to reduce each hub load separately (mass fault in blade 1, $\mu = 0.2$)

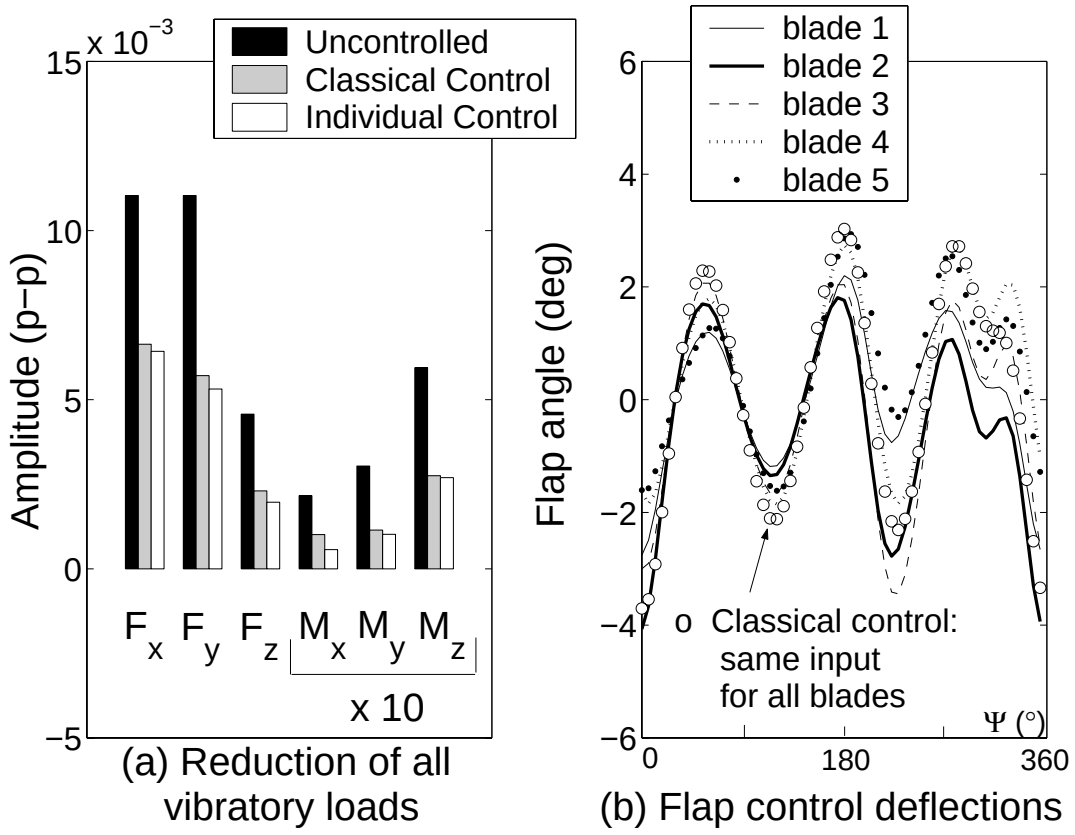

Figure 5.11: Simultaneous control of all hub loads with $\delta_{max} = 4°$ (mass fault in blade 1, $\mu = 0.2$)

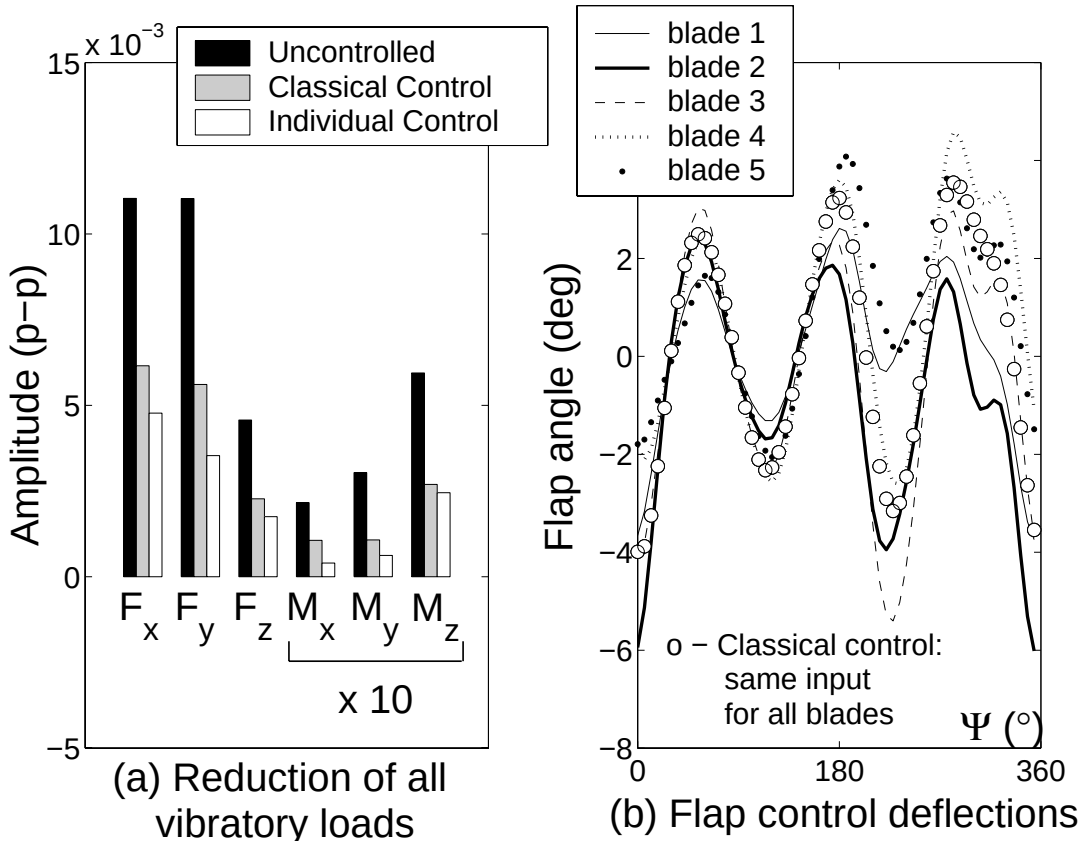

Figure 5.12: Simultaneous control of all hub loads with $\delta_{max} = 6°$ (mass fault in blade 1, $\mu = 0.2$)

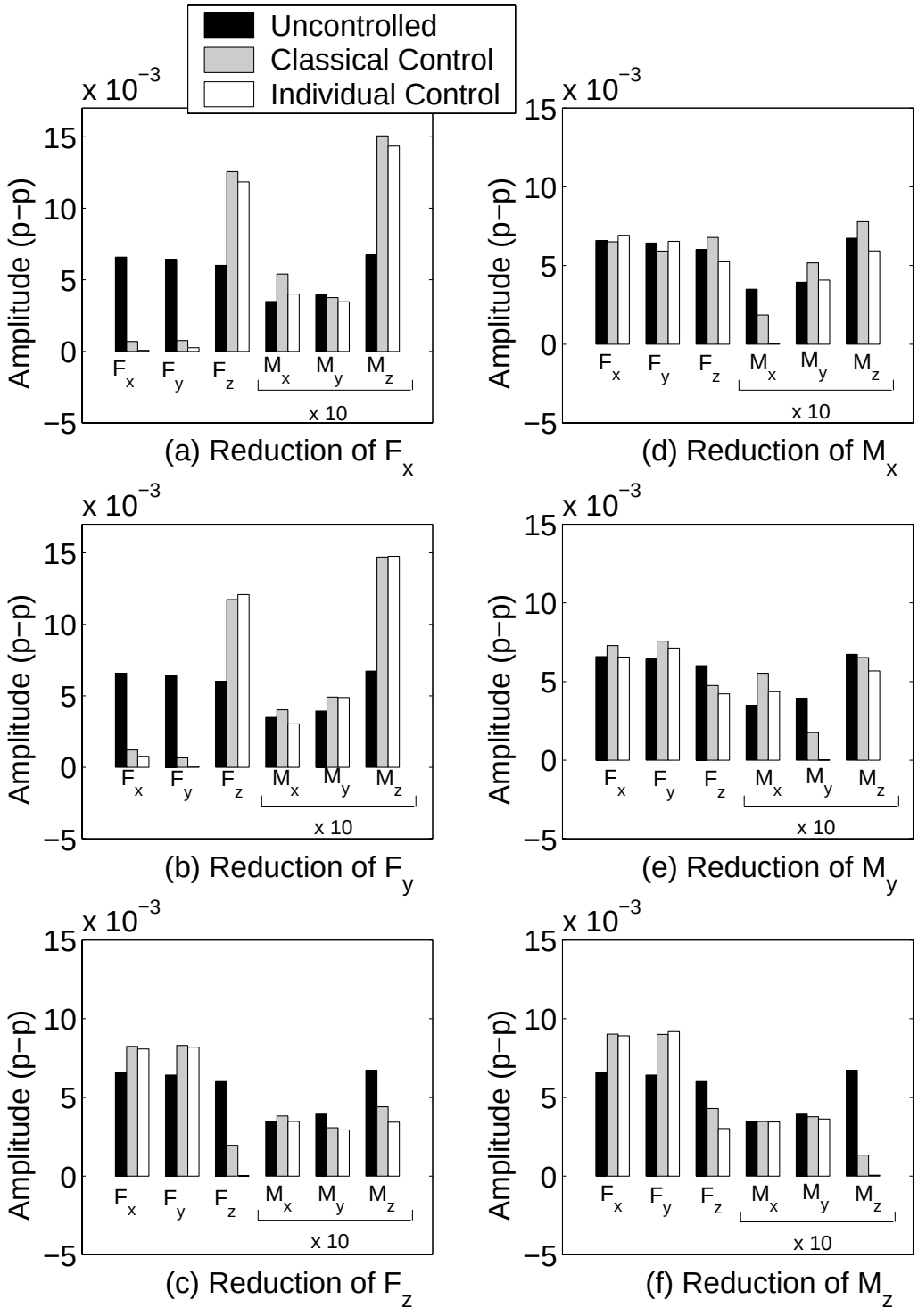

Figure 5.13: Controller performance to reduce each hub load separately (aerodynamic fault in blade 1, $\mu = 0.2$)

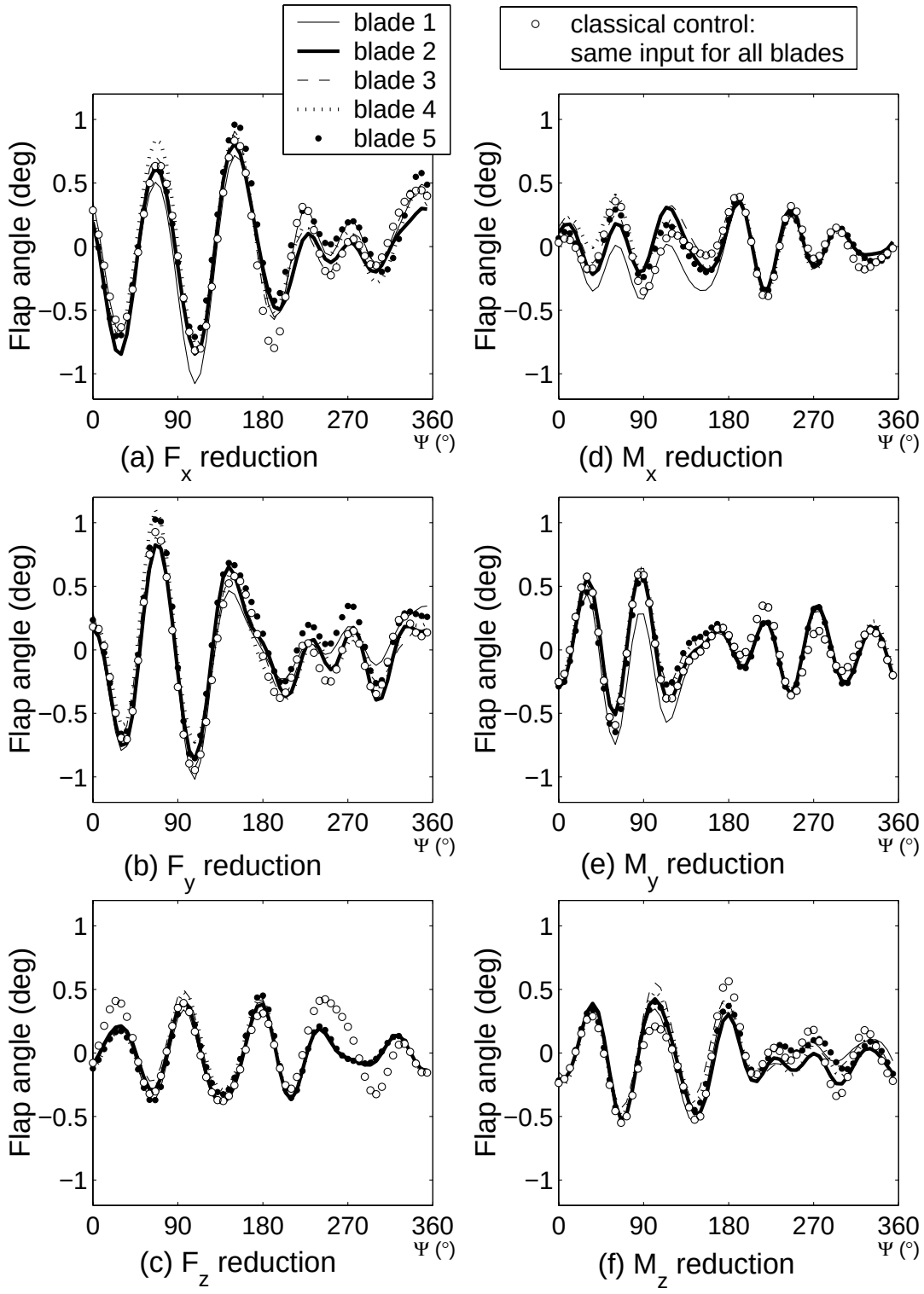

Figure 5.14: Optimal angles required to reduce each hub load separately (aerodynamic fault in blade 1, $\mu = 0.2$)

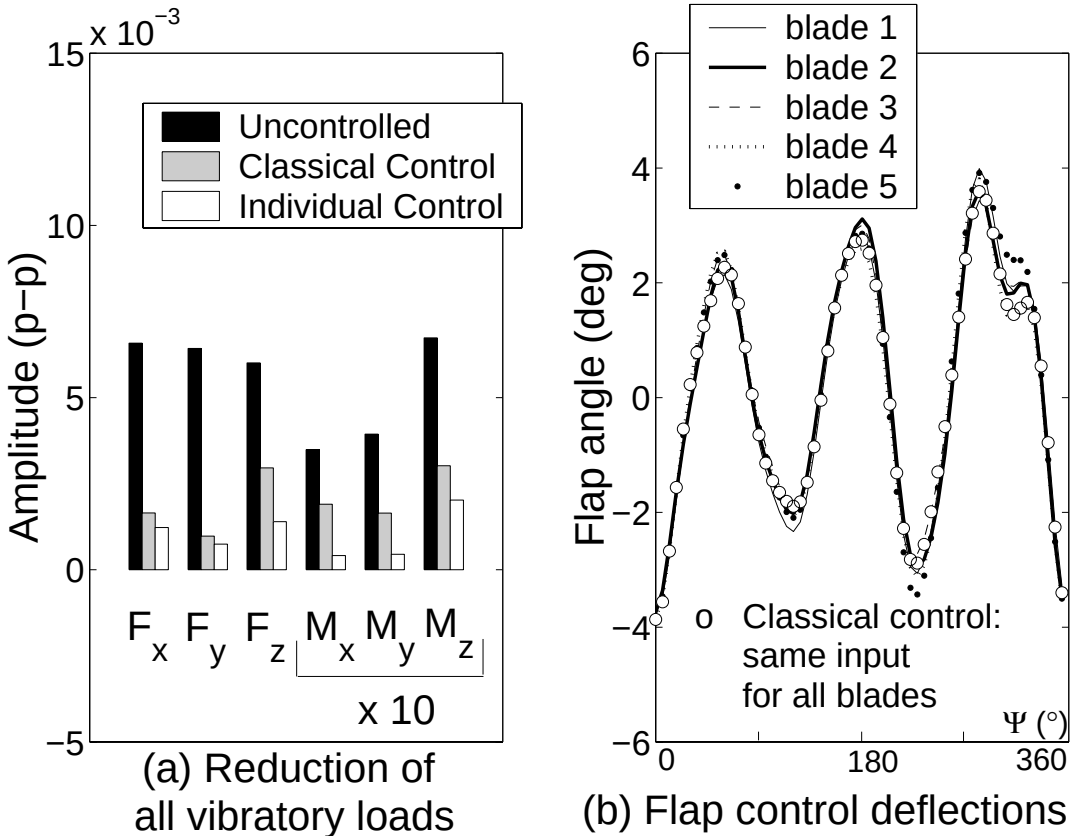

Figure 5.15: Simultaneous control of all hub loads (aerodynamic fault in blade 1, $\mu = 0.2$)

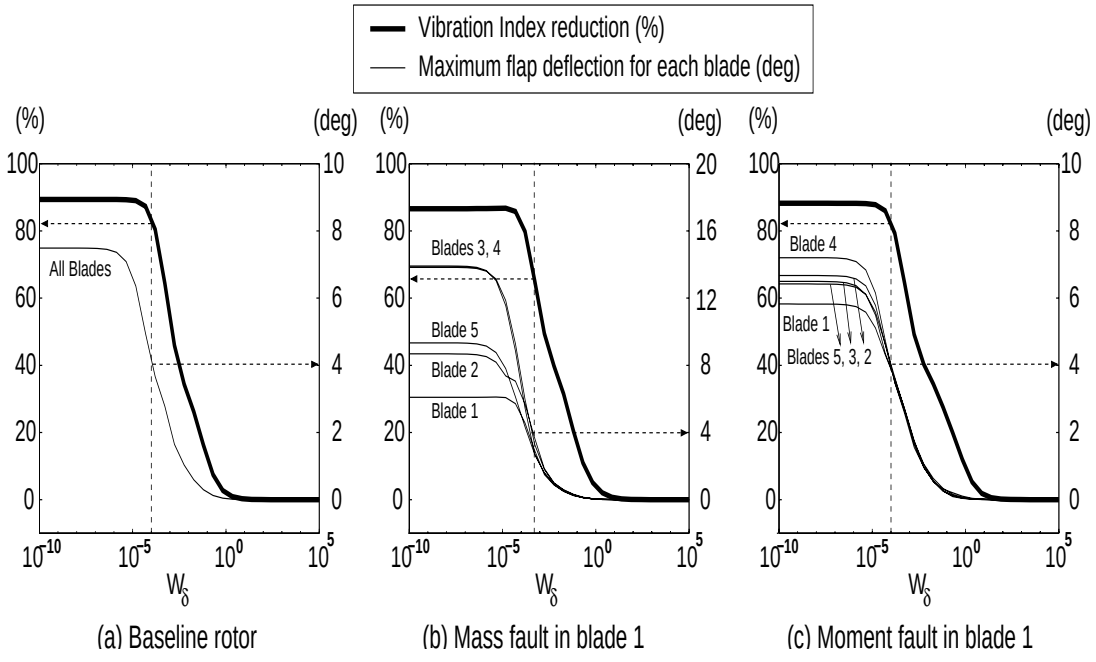

Figure 5.16: Effect of varying the weight applied to flap inputs

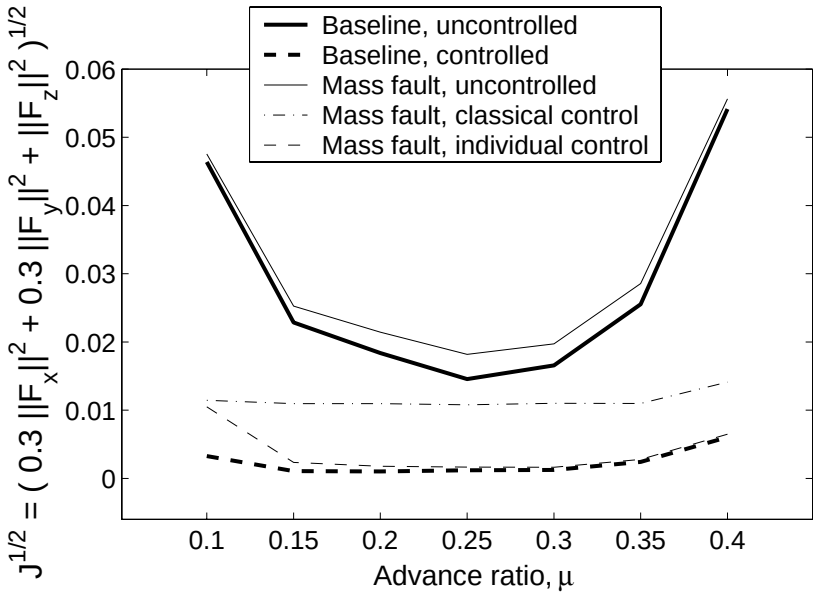

(a) Vibration Index with and without control

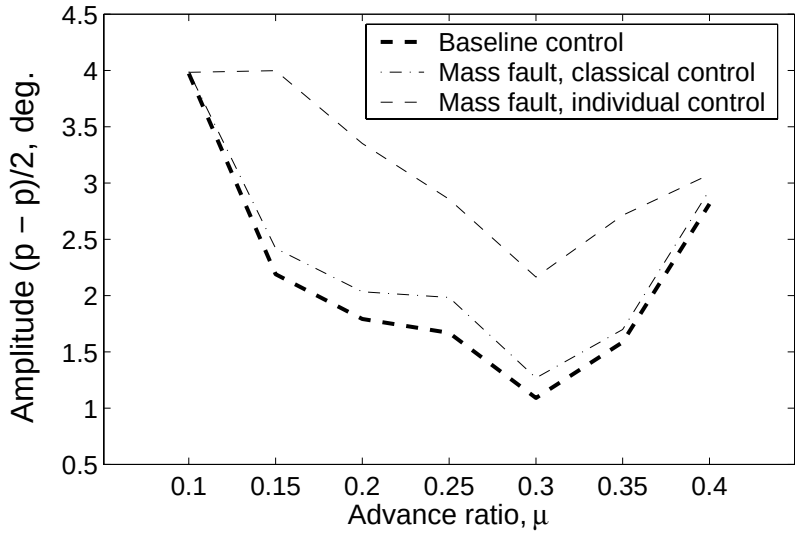

(b) Maximum half peak−to−peak flap deflection

Figure 5.17: Vibration index with and without control and required flap deflection for baseline rotor and rotor with mass fault in blade 1.

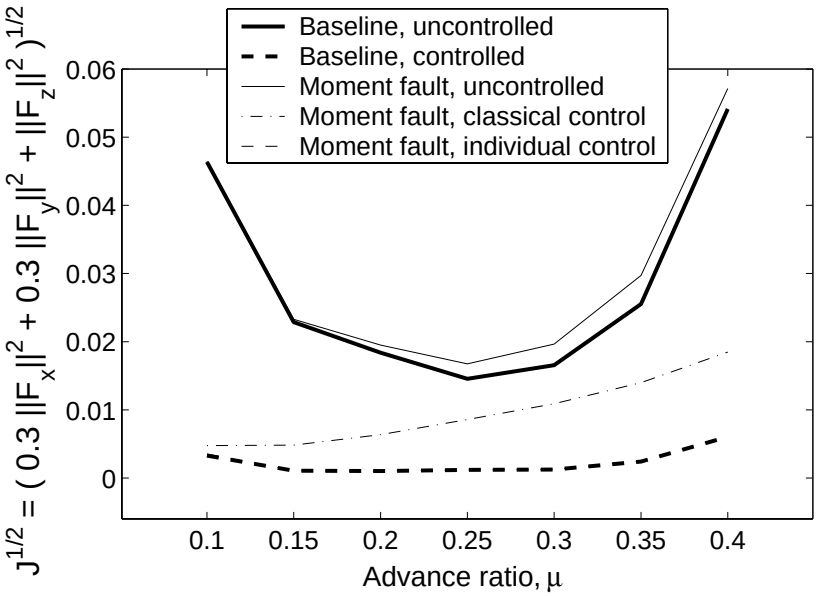

(a) Vibration Index with and without control

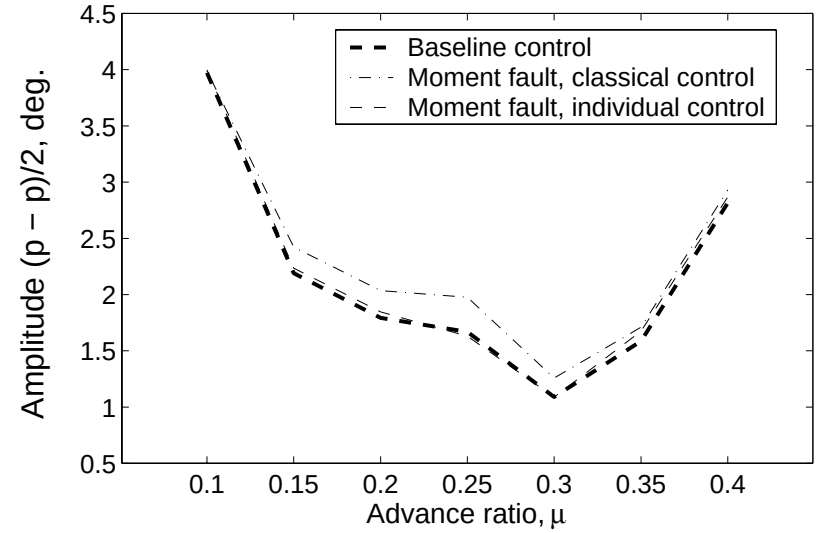

(b) Maximum half peak−to−peak flap deflection

Figure 5.18: Vibration index with and without control and required flap deflection for baseline rotor and rotor with moment fault in blade 1.

Chapter 6

Development of an Experimental Interface

The previous two chapters presented a detailed investigation of the predicted controller performance using mathematical models of the helicopter. The next step in the study is to validate experimentally the proposed controller using a Mach-scaled rotor with trailing edge flaps. This chapter describes the development of an experimental interface to test the controller. First, a flap and actuator system is designed and fabricated. This system is then integrated in model rotor blades. Finally, a controller interface is developed and tested.

6.1 Flap actuation system

The trailing edge flaps will be actuated using piezo-electric benders. The motion of the actuator is magnified and transmitted to the flaps using a leverage mechanism. Two types of leverage mechanism are designed: a hinge based mechanism, similar to Ref. [62], and a flexure based mechanism.

The hinge-based mechanism showed high sensitivity to free play at hinge and a drastic drop in peak-to-peak deflection in vacuum chamber rotating tests.

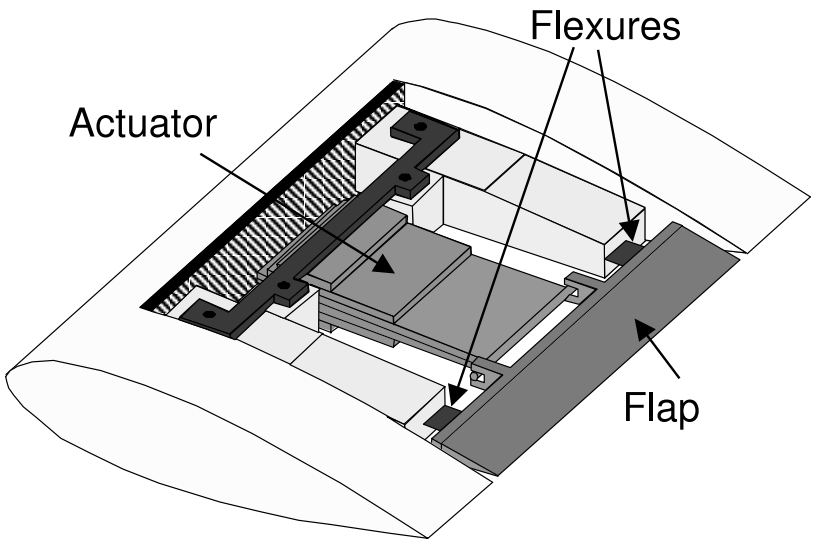

Figure 6.1: Flap leverage mechanism with flexure

To minimize the effect of friction generated by centrifugal force, a flexure-based mechanism is designed. In addition, the flexure hinge has advantages such as smoothness of movement, free of lubrication, and reduced free play [139, 140]. The amplification mechanism for both types of articulation is illustrated in Figure 6.2. In the flexure design, the flap articulation is realized by two tempered stainless steel shims, clamped on one side to the flap, and on the other side to the blade. The actuator motion is transmitted to the flap by means of a rod attached at the actuator tip which can glide inside a cusp attached to the flap (Figure 6.1).

Flexure parameters to be determined are its length, width, thickness, and position with respect to the actuator. These parameters were designed in order to maximize flap deflection in the vacuum chamber at the operating rotor speed of 1800 rpm. The maximum flap deflection is determined by the centrifugal loading at this rpm. The design process is as follows.

The effect of centrifugal load on flap deflection has two parts: (1) the effect on the actuator alone, and (2) the effect on the flexure-articulated flap.

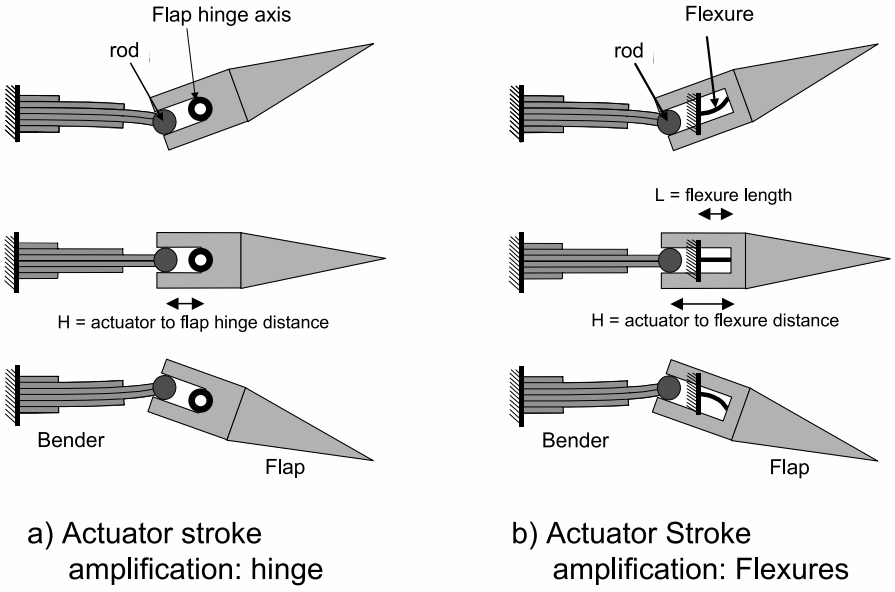

Figure 6.2: Stroke amplification using hinge and using flexures

The chordwise component of the centrifugal force creates a lengthwise varying axial load on the actuator, $T(x)$. Voltage applied to the piezoelectric actuator creates an induced bending moment M_Λ at the actuator tip, as shown in figure 6.3.

The governing differential equation for a cantilevered beam with an axial

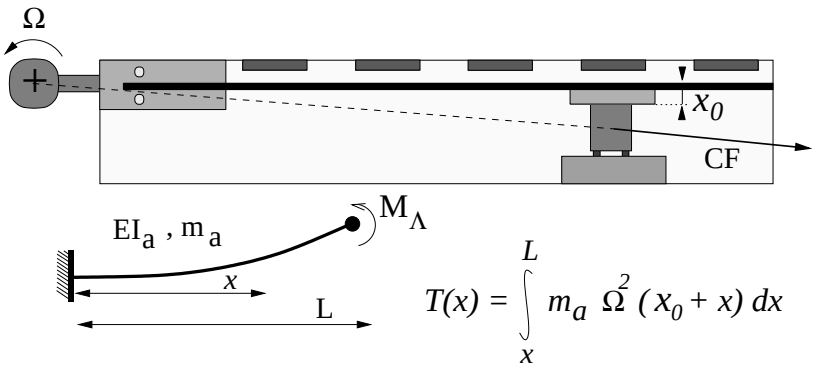

Figure 6.3: Effect of centrifugal loading on actuator

force is:

$$EI_f\, w^{(4)}(x) + (T(x)\, w(x))'' = 0 \tag{6.1}$$

and the following geometric and force boundary conditions must be applied:

$$\begin{aligned} w(0) &= 0 \\ w'(0) &= 0 \\ EI_f\, w''(L) &= M_\Lambda \\ EI_f\, w'''(L) &= 0 \end{aligned} \tag{6.2}$$

Assuming the actuator displacement is of the form:

$$w(x) = \frac{x^2}{L^2} q \tag{6.3}$$

the external work on the actuator can be expressed as:

$$\delta W_{ext} = M_\Lambda \delta w'(L) = 2\frac{M_\Lambda}{L}\delta q \tag{6.4}$$

Then, the actuator tip displacement can be found using Rayleigh-Ritz analysis:

$$w_{tip}(\Omega) = \frac{w_{tip}(0)}{1 + \frac{m\Omega^2}{4EI_a}(\frac{4}{15}L^4 + \frac{x_0}{6}L^3)} \tag{6.5}$$

$$w_{tip}(1800\, rpm) = 0.9986\, w_{tip}(0\, rpm)$$

The effect of centrifugal loadings on actuator deflection alone is thus negligible.

To predict the effect of centrifugal loading on the flexure-articulated flap, the static equilibrium of forces and moments on the flexure (as shown in figure 6.4) is considered and the location of the equivalent hinge axis for the flap is found to be:

$$\begin{aligned} x_e &= l - \frac{l}{2}\frac{a + 2bl/3}{a + bl/2} \\ where\ 2\,a &= -F_{flap}h - CF sin(\delta) x_{CG} \\ and\ 2\,b &= F_{flap} - CF sin(\delta) \end{aligned} \tag{6.6}$$

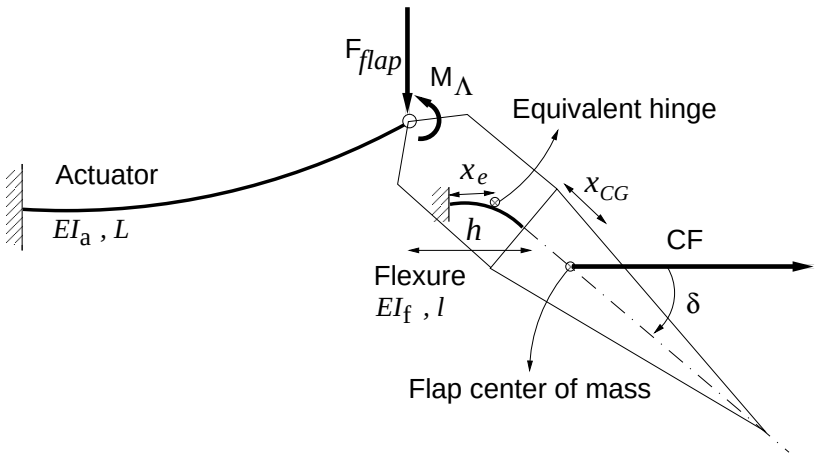

Figure 6.4: Forces and moments on the actuator-flap system

The flap deflection angle is equal to the bending slope at the tip of the flexure:

$$w'(l) = tan(\delta) = \frac{l}{EI_f}(a + \frac{bl}{2}) \tag{6.7}$$

The flap deflection angle can also be calculated as a function of the actuator tip deflection and the equivalent hinge axis location:

$$tan(\delta) = \frac{w(L)}{h - l + x_e} = \frac{\frac{L^2}{EI_a}(\frac{FL}{3} - \frac{M_\Lambda}{2})}{h - l + x_e} \tag{6.8}$$

In the above two equations, the unknowns are the flap deflection δ, and the force exerted by the flap at the actuator tip, F_{flap}. Because F_{flap} is a function of δ, these equations must be solved iteratively to obtain the predicted flap deflection under centrifugal loading.

Flexure design parameters (length l, thickness t, width w, and distance from actuator tip h) can then be optimized. The optimization objective is to maximize flap deflection at the nominal rotor speed (1800 rpm) while satisfying strength

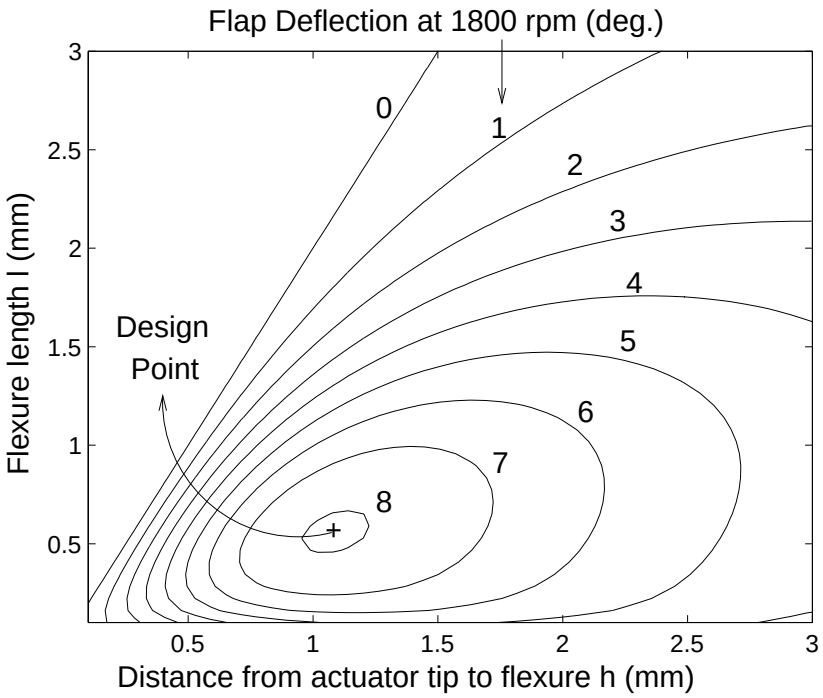

Figure 6.5: Numerical optimization of flexure parameters

constraints with a factor of safety of 1.5. The optimal design is found to be:

$$\begin{aligned} l_{opt} &= 0.6\,mm \\ t_{opt} &= 1\,mil \\ b_{opt} &= 10\,mm \\ h_{opt} &= 1.1\,mm \end{aligned}$$

Figure 6.5 shows contour lines of the predicted flap deflection at 1800 rpm with a flexure of optimal thickness and width, for varying l and h. The predicted maximum flap deflection is around 8.5 degrees half peak-to-peak. Figure 6.6 shows the complete blade, flap and actuator assembly, and figure 6.7 shows a close-up of the flexures.

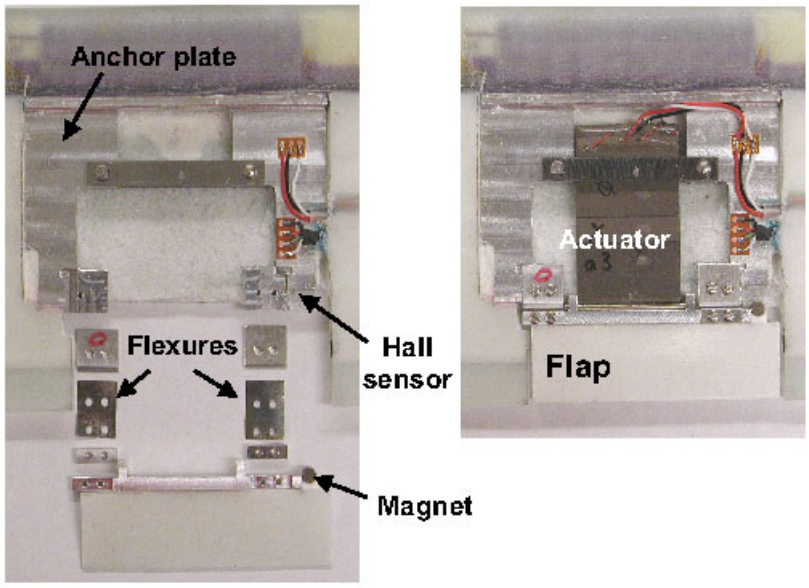

Figure 6.6: Flap and actuator assembly

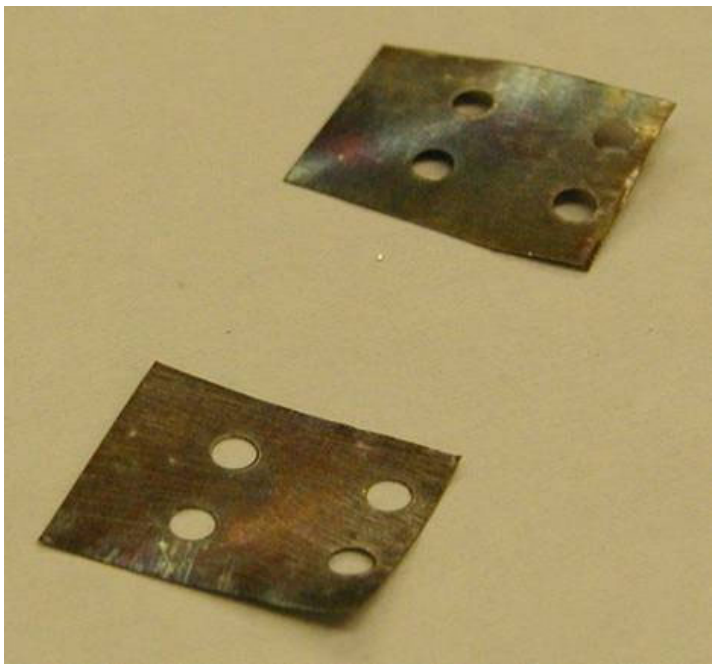

Figure 6.7: Flexures

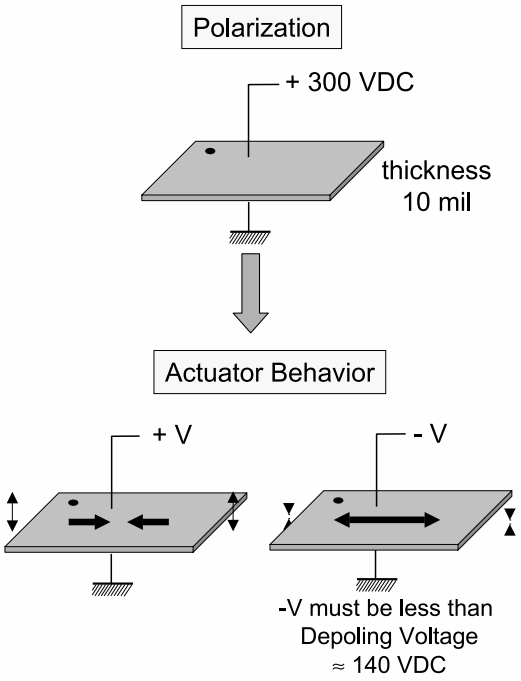

Figure 6.8: PZT sheet polarization and behavior

6.2 Actuator Fabrication

Actuators are manufactured using commercially available piezo-electric sheets. The thin sheets (dimension $2in \times 1in \times 10mils$) are made of a crystalline material (PZT-5H [134]) possessing piezo-electric properties: after polarization (application of a large DC electric field accross the thickness), when an electric field is applied to the material, the crystalline structure changes shape, producing dimensional changes in the material. This is illustrated in Figure 6.8. A voltage with the same polarity as the poling voltage causes expansion along the poling axis (i.e. along the thickness) and contraction perpendicular to the poling axis (i.e. in the plane of the sheet). A voltage with the opposite polarity has the opposite effect: contraction along the poling axis, and expansion perpendicular to the poling axis. When exposed to a high electric field opposite to the direction of polarization, the piezoceramic loses most of its piezoelectric capability.

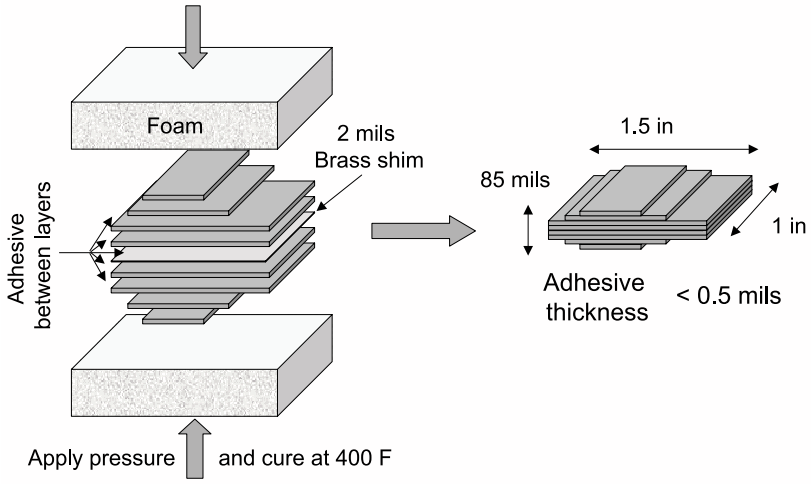

Figure 6.9: Actuator fabrication

This is called depoling of the piezoceramic. The DC depoling filed of PZT-5H is approximately $5.5kV/cm$ [58], or 140 Volts for the 10 mils thick sheets. Under dynamic excitation, the depoling field becomes lower than the DC value. An upper limit for actuation voltage opposite to the direction of polarization was therefore chosen as:

$$V_{max} = 120\, Volts \tag{6.9}$$

Bimorph is the registered trade name for a double plate ceramic element manufactured by Morgan Matroc. The two plates are bonded together, or to a center metal shim, so that they amplify their piezoelectric actions. Commercially available two-layer bimorphs offer sufficient free displacements but insufficient actuation force. To achieve both large stroke and large force output, four actuators were manufactured, following the design described in Ref. [133]. Actuators are fabricated by bonding together 8 piezoceramic sheets on to a middle brass shim using a high performace adhesive [138]. This is illustrated in Figure 6.9. The piezoelectric sheets are of different lengths, resulting in a tapered actuator. Tapering the bender thickness with varying individual sheet lengths can increase its efficiency [139]. The actuator is shown in figure 6.10. Electrical connections

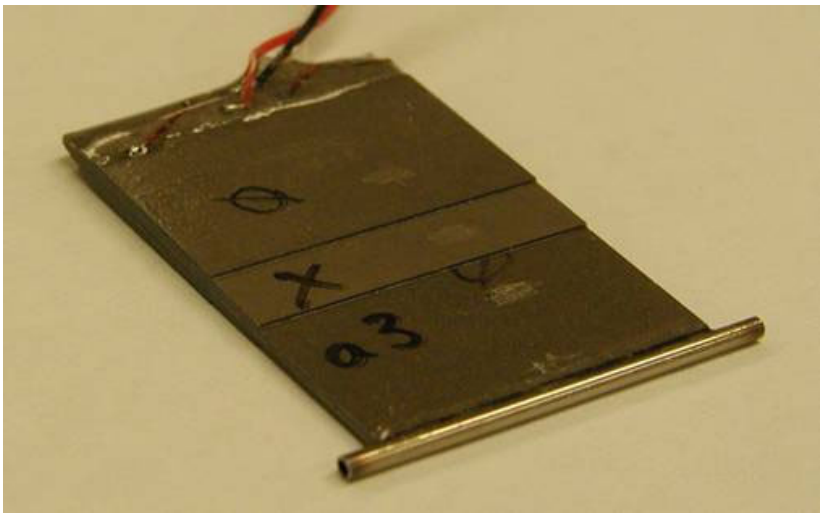

Figure 6.10: Actuator

to the actuator layers are such that when the top ceramic sheets expand, the bottom ceramic sheets contract (in the plane of the PZT sheets), resulting in a net bending of the actuator. Electrical connections are described in detail in [133].

The static force and stroke behavior for the four actuators built is shown in figure 6.11. In this test, the actuator is statically deformed by the application of a DC voltage, while a load is applied at the tip. The free length of the actuator is 1 in. Figure 6.11 shows that the maximum force (no stroke) is about 1800 grams and the free displacement (no force) is about 0.4 mm.

Because piezo sheets can be damaged by a high voltage applied opposite to the polarized direction, testing is performed using a modified sine wave, where voltages applied in the direction of polarization are three times larger than voltages applied opposite to the direction of polarization, as illustrated in Figure 6.12.

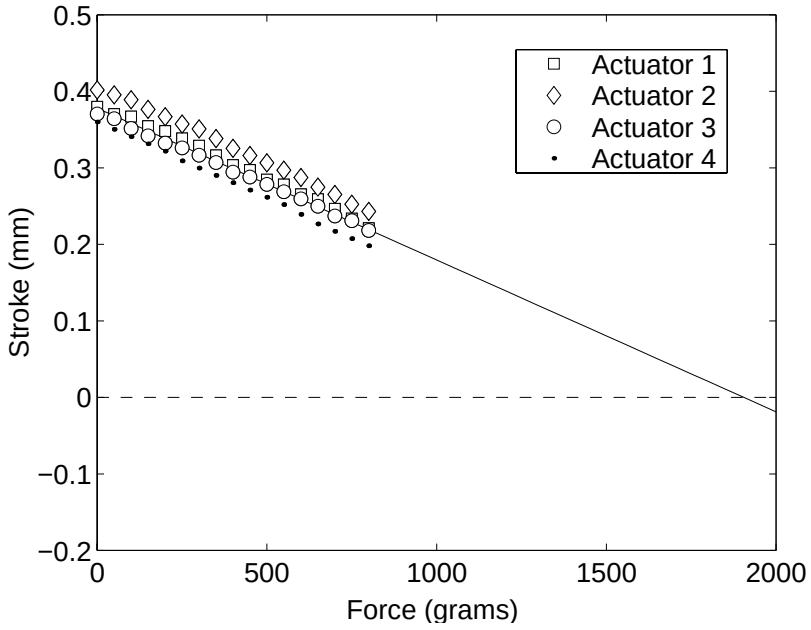

Figure 6.11: Actuator static force-stroke characteristics

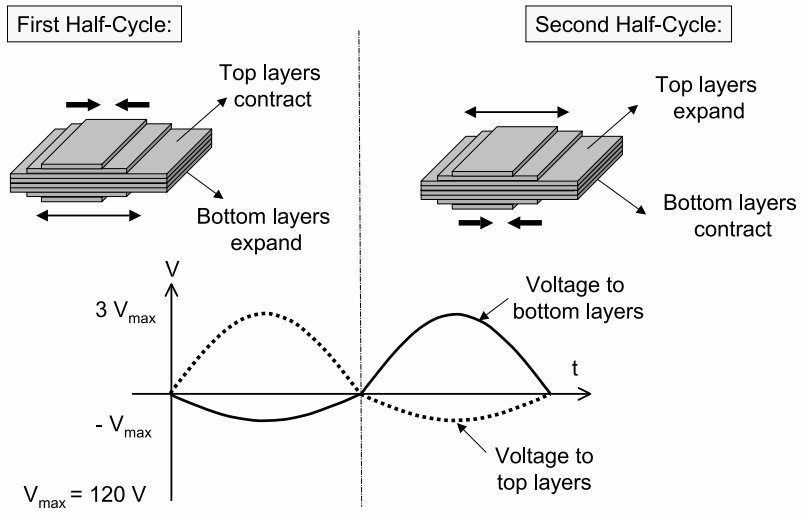

Figure 6.12: Excitation of actuator using 3:1 AC bias

Table 6.1: Mach scaled model parameters

Parameters	**Value**
Rotor diameter	5 ft
Airfoil section	NACA0012
Airfoil chord	3 in
Operating speed	1800 rpm
Tip speed	472 fts^{-1}
Flap span	2.4 in (8% span)
Flap chord	0.6 in (20% chord)
Radial location of flap	75% span

6.3 Blade Fabrication

In order to accommodate the new flexure design, Mach scaled rotor blades [133] are fitted with aluminum anchor plates as shown in figure 6.6. First, the foam core is manufactured by molding pieces of high density foam [135] to the NACA 0012 profile using the airfoil mold (Figure 6.3). The anchor plates are bonded to a graphite-epoxy composite spar using a high-strength film adhesive [136]. This assembly is then embedded in the foam core, wrapped in prepreg E-glass cloth [137], and cured in the NACA 0012 mold (Figure 6.14). Leading edge weights are used to ensure each blade section center of gravity is at the quarter-chord. The blade characteristics are summarized in Table 6.1.

A set of four blades was manufactured. A blade with flexure-articulated flap is shown in figure 6.15.

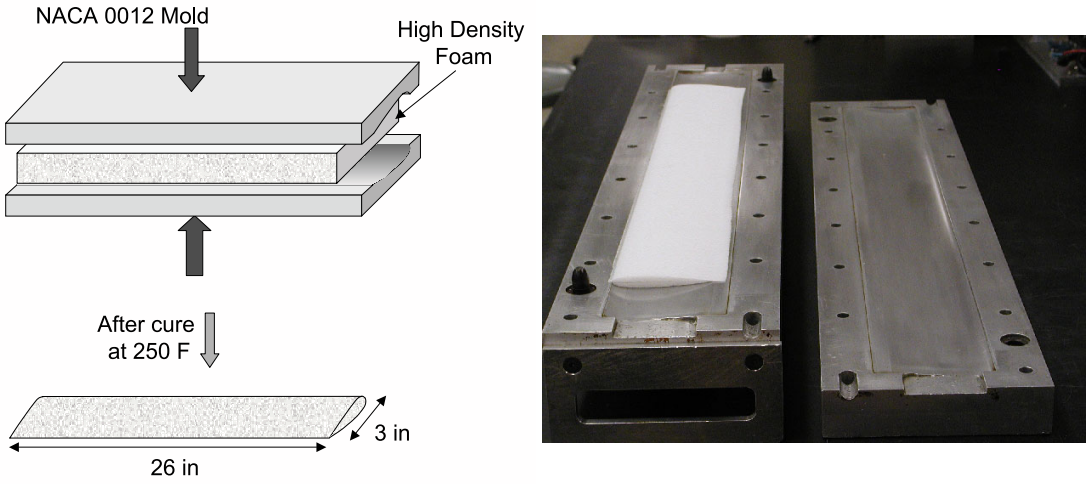

Figure 6.13: Blade foam core inside mold

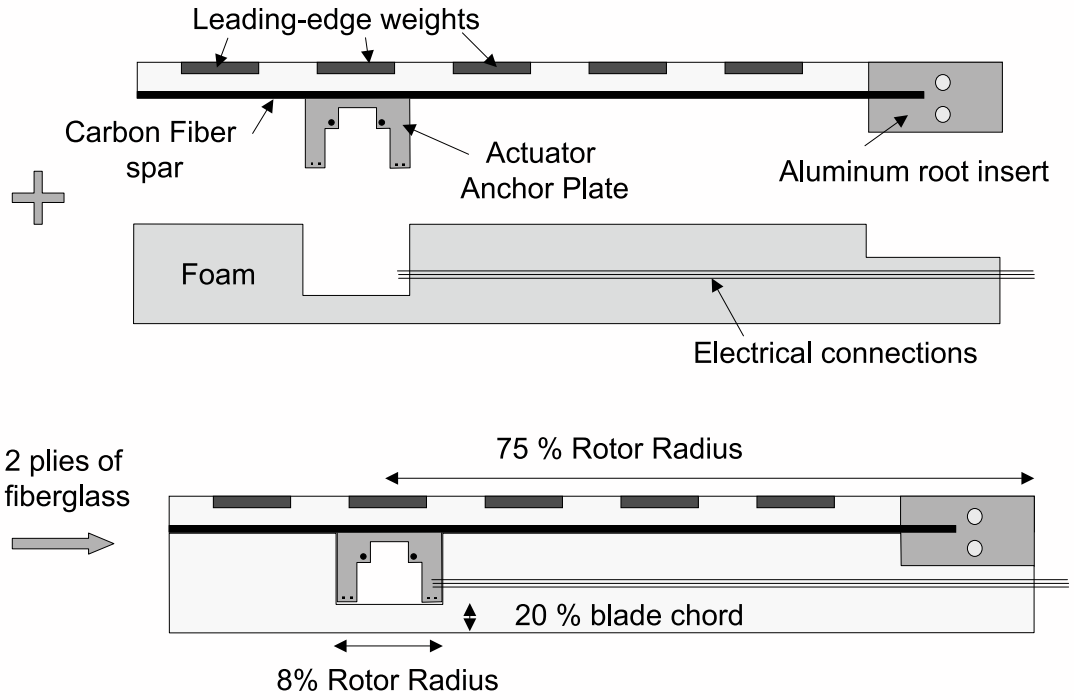

Figure 6.14: Blade manufacturing

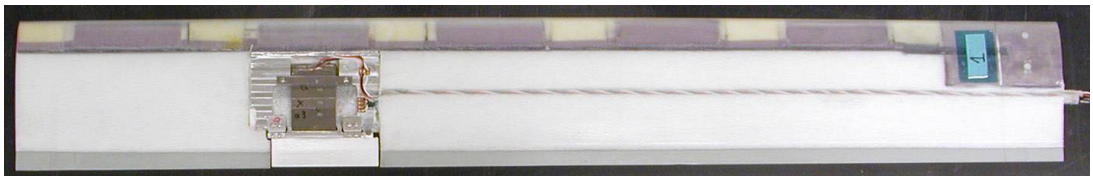

Figure 6.15: Blade

6.4 Vacuum Chamber Testing

Rotating test in vacuum chamber was conducted to characterize flap deflections under centrifugal loading (in the absence of aerodynamic forces). The vacuum chamber has a test section of 10 ft diameter and 4 ft height with a rigid non-articulated hub that accepts signals from a 100-channel slip-ring. Tests were conducted at pressures between 1 and 5 millibars. Flap deflections were determined using a Hall-effect transducer. The magnet for the Hall sensor was located on the flap, along the virtual flap hinge. The output signal from the Hall sensor was calibrated to read the flap deflection in degrees using a laser sensor system. Figure 6.16 shows flap deflection results in vacuum with an excitation of $190V_{RMS}$, at low frequency (5 Hz). These tests show improved flap deflections using the flexure design compared to the hinge design. Up to 6.5 degrees half peak-to-peak flap deflection is achieved at the nominal rotor speed of 1800 rpm.

6.5 Controller Interface

To implement the control algorithm, a dedicated computer (Pentium III, 550 MHz PC) was set up with data acquisition board (National Instruments PCI-MIO-16E-1, 12 bit DAQ board) to host the controller and perform data acquisition and waveform generation. This provides an efficient system to implement the control algorithm in real time directly in Visual C++. Double buffering is used on the data acquisition board for simultaneously down-loading the mea-

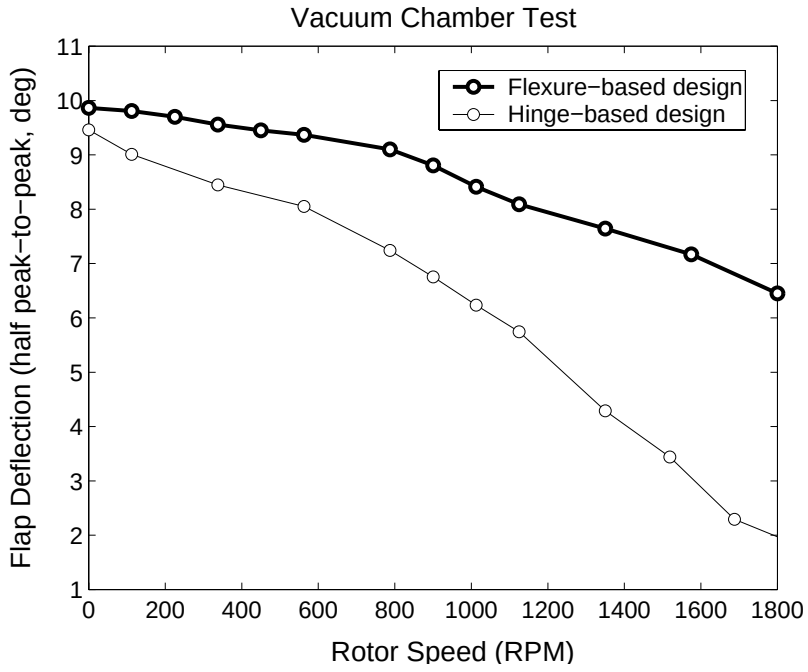

Figure 6.16: Vacuum chamber test

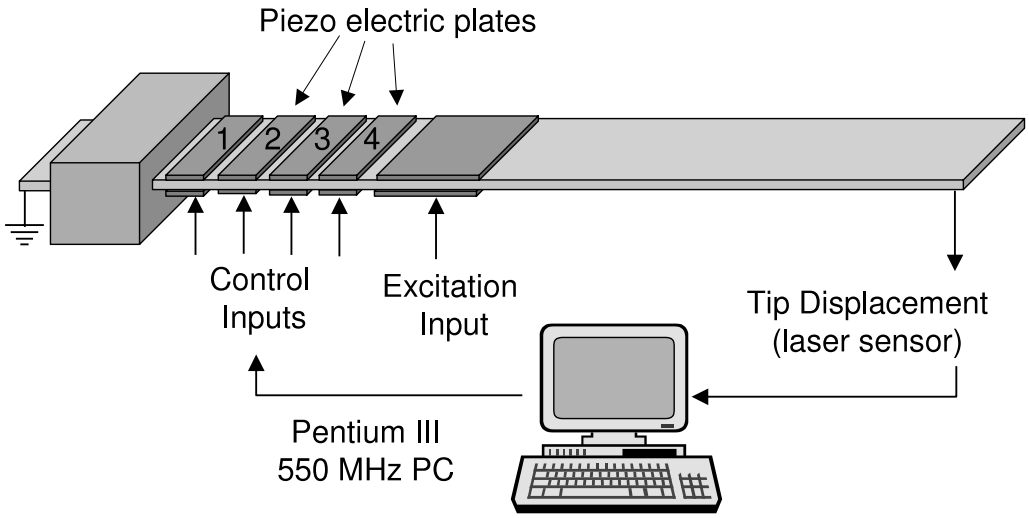

Figure 6.17: Controller test set-up

surements from the previous iteration and up-loading the command waveform for the next iteration to the data acquisition board. In order to test the experi-

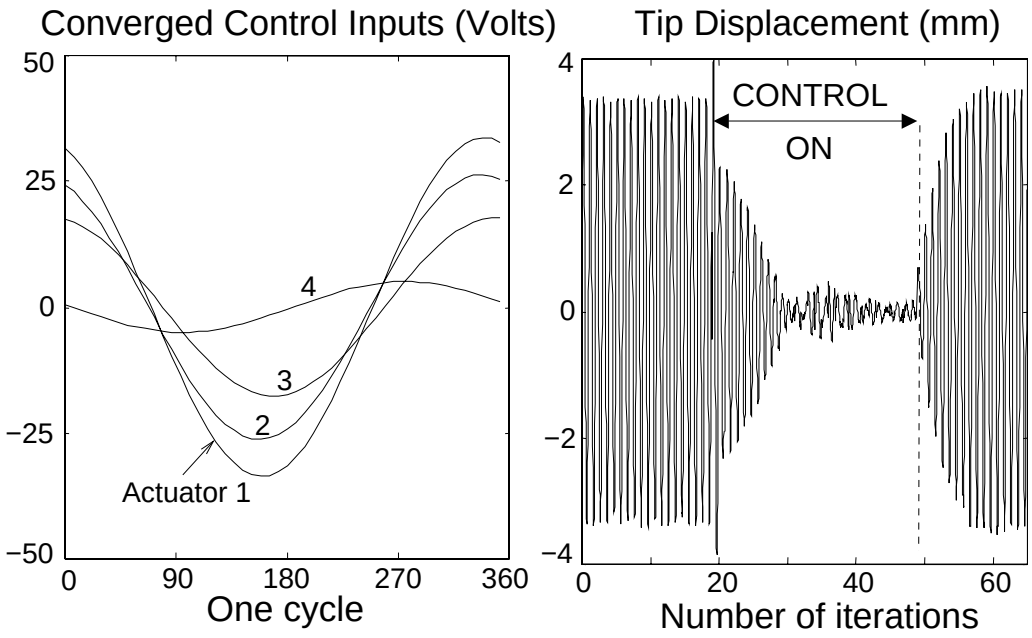

Figure 6.18: Controller test results

mental interface, a simple experiment was set up. A clamped beam was excited in bending by a pair of surface-attached piezoelectric elements located at some distance from the root (figure 6.17). The goal of this test was to reduce the tip displacement using another 4 smaller size piezoelectric benders (two identical piezos on either surface) located near the root. Because the four benders are located at different locations along the beam, their efficiency in affecting the tip vibration is different. It is expected that the controller will adjust the input voltages to each actuator based on their respective efficiency. Test results are shown in figure 6.18. The figure shows that the control algorithm generates four different inputs for piezo benders near the root, and the tip vibration is minimized.

6.6 Summary

In this chapter, the fabrication of a Mach-scaled smart rotor including piezo-bender actuated trailing edge flaps was described. Two trailing edge flap leverage mechanisms were designed. Compared to a hinge based mechanism, a flexure based mechanism showed improved flap deflection with an increase in rpm. The new flexure based mechanism was designed for maximum flap deflection at 1800 rpm in vacuum. A set of four Mach scaled smart blades was fabricated and flap deflections were measured in vacuum. Flap deflections of up to 6.5 degrees half peak-to-peak were achieved at the nominal rotor speed of 1800 rpm. The control code was also adapted for real-time use and tested using a simple experimental set-up.

Chapter 7

Closed Loop Control: Reduction of Rotating Frame Loads

This chapter describes a series of tests conducted on the hover stand and in the Glenn L. Martin wind tunnel at the University of Maryland. The controller closed loop performance was investigated with the control objective limited to rotating frame loads.

7.1 Hover Stand Testing

Hover testing was performed on a rotor test stand equipped with a one-seventh scale Bell-412 Mach-scaled rotor hub. This hub consists of two composite yokes that are stacked perpendicular to each other. Each yoke can accommodate two blades. The yokes are designed to act as virtual hinges for flap and lead-lag motion. Blade feathering is achieved via an elastomeric pitch bearing. Two sets of elastomeric lag dampers are installed on each yoke to ensure aeroelastic stability. In addition to the yoke gages, the rotor rig is equipped with a six-component fixed frame balance. Data are transferred between the rotating and fixed frames though two slip rings, one for actuation and the other for sensing purposes. The

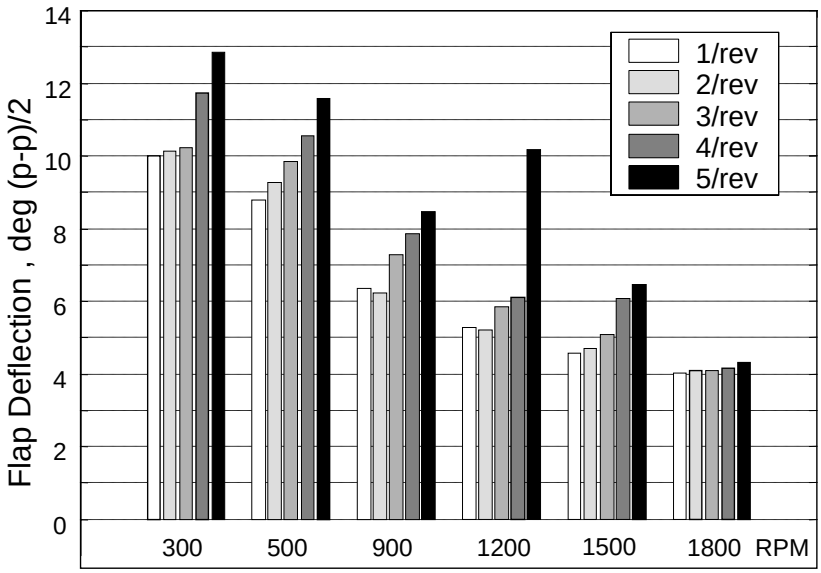

Figure 7.1: Hover Test: Flap deflection variation with rpm, $190V_{RMS}$ excitation

rotor rpm is controlled by a variable speed, water-cooled, hydraulic motor and pump rated for 55 HP (maximum speed 6000 rpm). A belt and pulley arrangement connects the motor to the rotor shaft. The Mach-scaled operating speed for the Bell-412 rotor is 2000 rpm, however for the present testing the operating speed was limited to 1800 rpm in order to stay within the centrifugal load limits for the rotor hub. The nominal tip Mach number at 1800 rpm (5 ft diameter rotor) is 0.45. Figure 7.1 shows the results on a hover stand test where test was carried out at collective angle of 4°, varying the rotor speed from 0 to 1800 rpm, and exciting the actuator at an RMS voltage of 190 V, at frequencies from 1/rev to 5/rev. Results show that flap deflections increase at higher excitation frequencies. The nonrotating first natural frequency for the actuator-flap system is around 35 Hz. This frequency increases somewhat with rotor speed. As the flap excitation frequency nears the resonance frequency, the flap deflection amplitude increases. Flap deflections of more than 8 degrees peak to peak were measured at 1800 rpm.

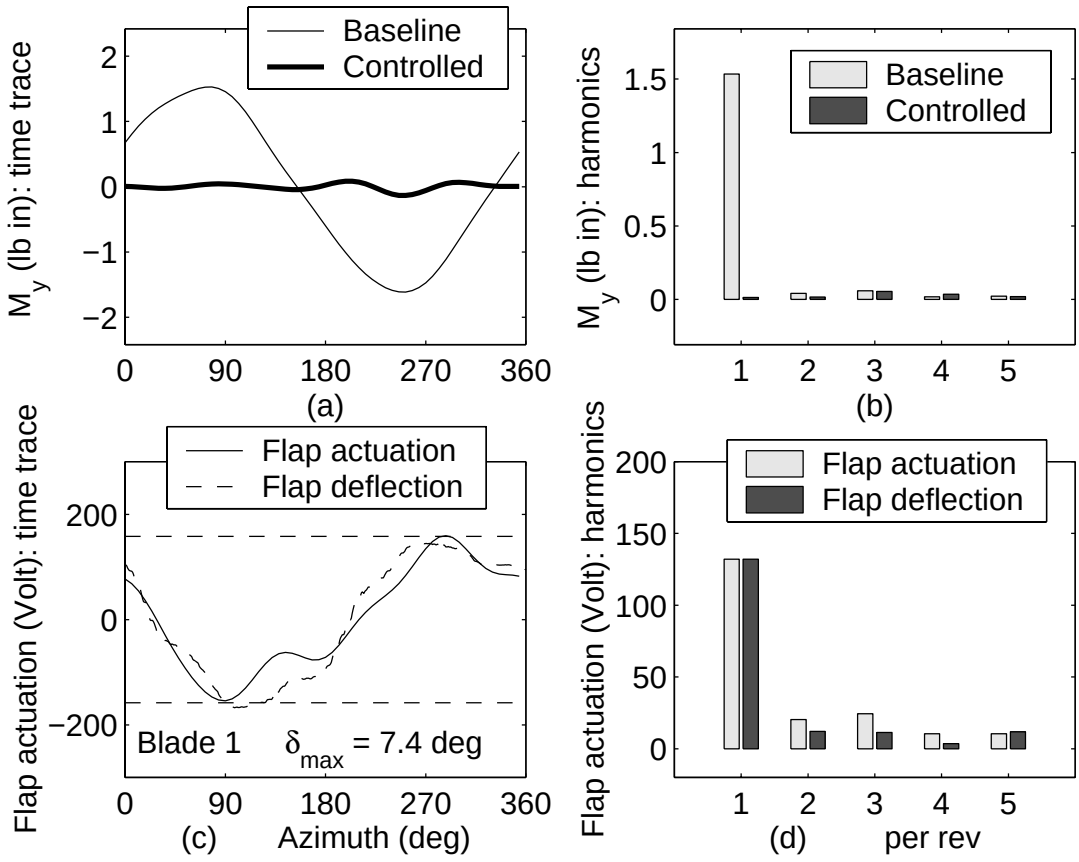

Figure 7.2: Closed loop test, hover, 500 rpm, control objective is M_y at root of blade 1: vibratory load and flap deflection

7.1.1 Closed Loop Tests

Closed loops tests were conducted in hover to demonstrate the controller's ability to minimize the background vibration. For all tests, the control objective to minimize is the vibratory root flap bending moment, M_y.

One iteration of the controller consists of:

1. Output control command to the blades,
2. Wait for three rotor revolutions (to ensure the transient has died out),
3. Acquire vibration data for one rotor revolution,
4. Update system parameters F_0 and T,

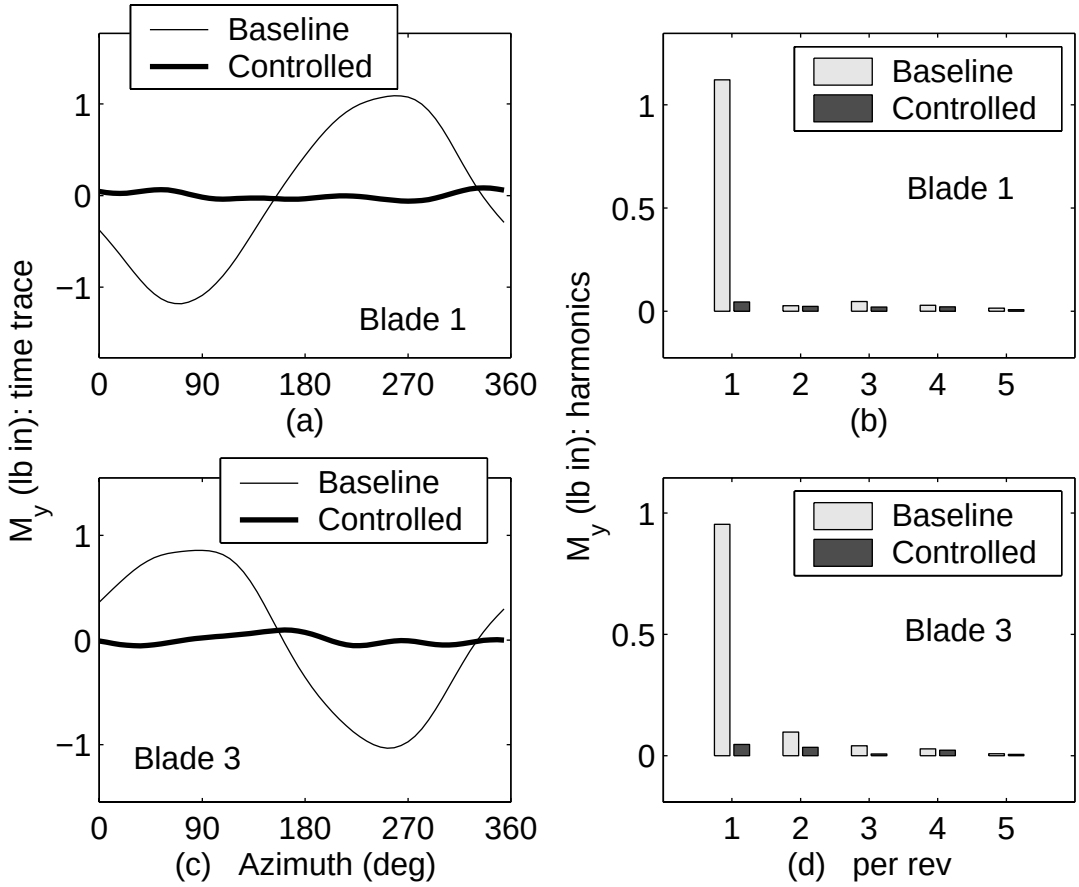

Figure 7.3: Closed loop test, hover, 500 rpm, control objective is M_y at root of blades 1 and 3 : vibratory loads

5. Compute optimal control command.

Zero initial conditions are used for the identification of system parameters (uncontrolled vibration F_0 and transfer matrix T). For the first 100 iterations, the last step (computation of optimal control command) is not performed. Instead a waveform is generated of random phase and frequency content. This ensures more accurate identification of the system parameters. After the 100th iteration, control is turned on: system identification and control are then performed simultaneously.

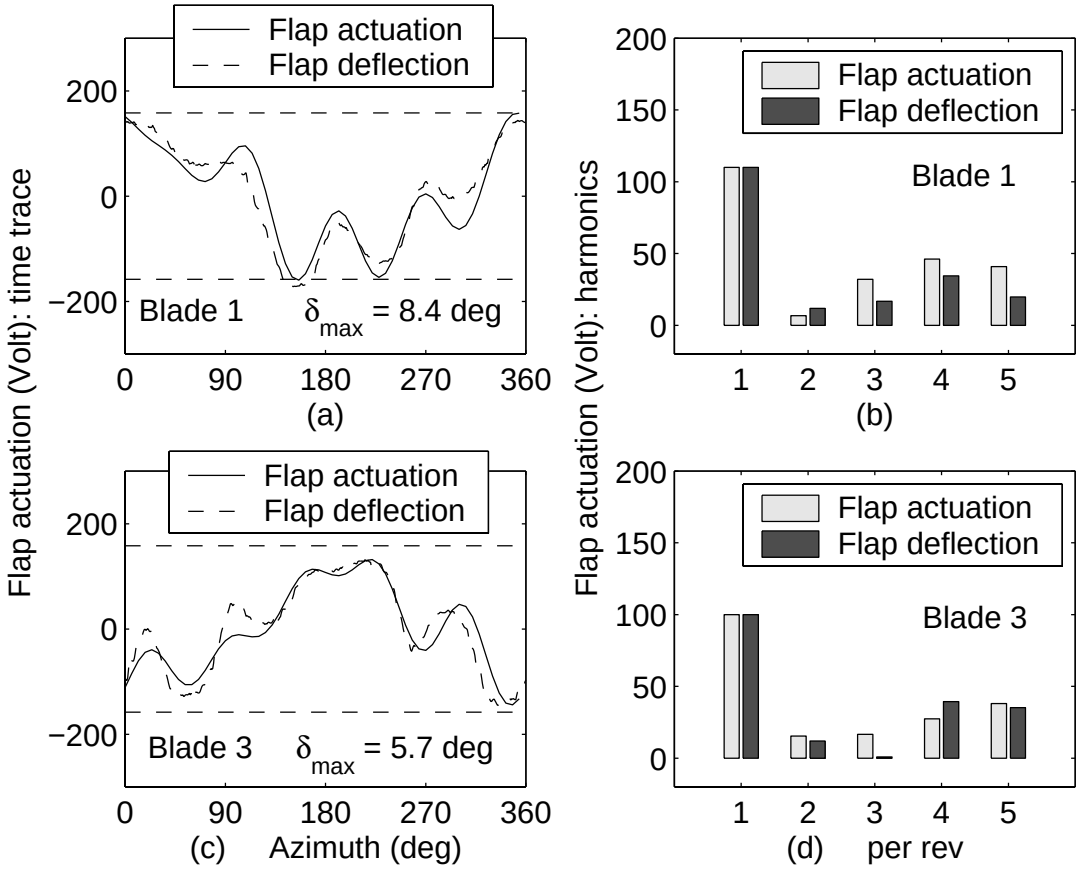

Figure 7.4: Closed loop test, hover, 500 rpm, control objective is M_y at root of blades 1 and 3 : flap deflections

Data sampling and command up-loading are synchronized to the rotor speed via a 60/rev tachometer (data are acquired and waveform is output at a rate of 60 data points per rotor revolution). For all closed loop tests presented here, the collective angle is 2° and the shaft tilt angle is 2°. For the generated flap actuation and acquired vibration data, $Nh = 5$ is used. Also, in order to protect the actuators, an upper limit $\gamma_{max} = 160\, V_{RMS}$ is imposed on the control command.

Figure 7.2 shows the closed loop test results with one active flap (on blade 1). The control objective is M_y at the root of blade 1. Figure 7.2(a) shows the baseline (without flap deflection) and controlled (after controller has converged to optimal flap actuation) vibratory flap bending moment time trace for one rotor revolution (only the first 5 harmonics are included). The vibration in hover is dominated by the 1/rev signal, arising from imperfect trim condition. Figure 7.2(b) shows the harmonic content of these loads. After the controller is set on, the 1/rev component is reduced by over 95%. Figure 7.2(c) shows the time trace of the optimal flap command voltage generated by the controller. Also shown is the actual flap deflection measured by the Hall effect sensor (dashed line). To facilitate comparison, the flap deflection signal is scaled to match the peak-to-peak amplitude of the command voltage. Figure 7.2(d) shows the harmonic content of the flap actuation and resulting flap deflection, again with matched amplitudes. The controller generates a control waveform with a large dominant 1/rev. Note that the control weights for flap actuation W_γ have been adjusted so that the maximum value $\gamma_{max} = 160 V_{RMS}$ is reached, as described in the first section. The maximum half peak-to-peak flap deflection is 7.4°.

Figures 7.3 and 7.4 show closed loop test results for the simultaneous reduction of M_y at the root of blades 1 and 3, with two active flaps. Figure 7.3 shows the vibratory root bending moments before and after control. Time traces as well as harmonic contents are presented. For both blades, vibration is reduced by over 93%. Figure 7.4 shows the corresponding optimal control command

voltage for both blades. Superimposed in dashed line is the matched amplitude resulting flap deflections, as measured by the Hall effect sensors. The signal is again dominantly 1/rev, with small 4 and 5/rev components. Even though the weights for flap actuation are such that the command voltage reaches the maximum value of $160V_{RMS}$ for both actuators, the maximum flap deflection differs (8.4° and 5.7°). Any dissimilarity in blades is automatically compensated through different actuations applied to blades. As a result, vibratory loads on both blades are minimized simultaneously.

Finally, Figures 7.5 and 7.6 show closed loop test results for the simultaneous reduction of M_y at the root of blades 1, 2 and 3, with three active flaps (on blades 1, 2 and 3). Figure 7.5 shows the vibratory root bending moments before and after control. Peak-to-peak vibratory bending moment is reduced by 87% for blade 1, 56% for blade 2, and 75% for blade 3. Overall, the vibration index J is reduced by 77%. Figure 7.6 shows the corresponding optimal control command voltage for each flap. The controller generates command inputs with a dominant 1/rev harmonic for blades 1 and 3, but 5/rev for blade 2. The 5/rev in flap 2 actuation comes from the fact that the weight associated with γ_2 is adjusted so that the maximum voltage is reached. In this case, even a small flap actuation is enough to cancel M_y vibration in blade 2, if only blade 2 is active. Therefore, in order to reach the maximum flap actuation, the weight generated for blade 2 is very small. As a result, higher harmonics which are not very sensitive to flap deflections become large in the command voltage.

Note, simultaneous vibration reduction for all four blades could not be attempted because only three power amplifiers were functional at the time of testing.

7.2 Wind Tunnel Testing

The 4-bladed smart rotor model was then tested in the Glenn L. Martin wind tunnel. It is a closed section, closed circuit wind tunnel with a rectangular test section (dimensions of $11ft \times 7.75ft$). The rotor rig assembly was set up in the test section (Figure 7.7). The rotor rig with the Bell-412 hub and hydraulic motor was mounted on an adjustable post, which could be pivoted to change shaft tilt angle. Before turning on the active controller, the rotor was trimmed for the particular flight condition by adjusting the longitudinal and lateral cyclics to minimize the root cyclic flap bending moment of two consecutive blades.

Figure 7.8 shows closed loop test result at a rotor speed of 1200 rpm, wind speed of 27 miles per hour (advance ratio 0.13), collective angle of 2 degrees, and shaft tilt of 2 degrees. The control objective is the vibratory flap bending moment at the root of blade 3, with a single active blade. Figures 7.8(a) and 7.8(b) show the vibration before and after control. For this forward flight condition, large 1 and 3/rev harmonics are present. After controller is on, the 1/rev harmonic is reduced by 66% and the 3/rev harmonic by 34%. The overall cost function is reduced by 50%. Figures 7.8(c) and 7.8(d) show the command voltage generated and the resulting flap deflection. The major flap deflection harmonics are 1/rev and 3/rev. The maximum actuation voltage of $160V_{RMS}$ (saturation limit) is reached and the controller is not able to reduce vibration further.

Figure 7.9 shows the time traces of several parameters during this test. Figure 7.9(a) shows the variation of the norm of the predicted uncontrolled vibration. System identification begins with zero initial condition and converges after about 40 iterations. Figure 7.9(b) shows the variation of the norm of the predicted transfer matrix. It also starts with zero initial condition, and converges after about 100 iterations. Figure 7.9(c) shows the time history of the prediction error, expressed in percentage of the norm of the uncontrolled vibration.

Prediction error becomes less than 20% after about 40 iterations, even though the transfer matrix is still being adjusted. Figure 7.9(d) shows the time trace of the root flap bending moment. The variations in amplitude for the first 100 iterations are due to the random inputs used for initial system identification. After control is turned on, the vibration level is immediately reduced by about 50%.

Next, another series of wind tunnel tests were performed at 1500 rpm, with wind speed of 32 miles per hour (advance ratio $\mu = 0.12$). For these tests, thicker flexures were used for safety, resulting in smaller flap deflections. As a result, only single harmonics were targeted. Figure 7.10 shows results when the objective is the 3/rev component of the root flap bending moment of blade 2. Once the controller is on, the 3/rev component is reduced by 40%. The main harmonic in the flap deflection is 3/rev, and the maximum flap deflection is only 2.5°. Figure 7.11 shows results when the objective is the 4/rev component of the root flap bending moment of blade 2. The 4/rev component is reduced by 91%. The main harmonic in the flap deflection is 4/rev, and the maximum flap deflection is only 1.6°. Note that in this case, the maximum flap actuation of $160V_{RMS}$ is not reached: a further decrease of the weight associated with flap deflection would not result in any more vibration reduction. Figure 7.12 shows results when the objective is the 5/rev component of the root flap bending moment of blade 2. The 5/rev component is reduced by 91%. The major harmonic component in the flap deflection is 5/rev, and the maximum flap deflection is only 2.8°.

Finally, controller performance during a transient flight condition is investigated. Results are shown in figure 7.13. At iteration zero, the rotor is trimmed at the flight condition of 1000 rpm and 27 mile per hour ($\mu = 0.15$). The control objective is the 1/rev component of the root flap bending moment of blade 1.

For the first 100 iterations, baseline data are collected (flap is inactive) From iteration 100 to 200, random inputs are sent for system identification from

zero initial condition. Figures 7.13(a) and 7.13(b) show the variation of the identified parameters: norm of F_0, the norm of the uncontrolled vibration F_0 (Figure 7.13(a)) and the norm of the transfer matrix T (Figure 7.13(b)). Figure 7.13(c) shows the prediction error decreasing as the parameters are updated to more accurate values. From iteration 200 onward, controller generated command inputs are used instead of the random inputs. Around iteration 225, the rotor speed is suddenly increased to 1100 rpm, without changing the rotor trim. Figure 7.13(a) shows that this sudden change results in increased uncontrolled vibration. Also, the norm of the transfer matrix T decreases (Figure 7.13(b)), indicating that vibration is less sensitive to flap deflections. Figure 7.13(c) shows a brief increase in prediction error between iterations 225 and 240, as the parameters F_0 and T are adjusted to their new values. Figure 7.13(d) shows the time trace of the objective function (1/rev vibration). As soon as the active controller is turned on, the 1/rev is reduced by about 80%. When the rotor speed change occurs, the 1/rev vibration increases, but remains lower than the new baseline vibration level at 1100 rpm. The vibration reduction after rpm change is about 50%, compared to 80% at the lower rotor speed. This is consistent with the changes in F_0 and T described above. After the 300th iteration, the controller is turned off and the new baseline data corresponding to 1100 rpm are collected for the last 100 iterations.

7.3 Summary and concluding remarks

This chapter described wind tunnel testing of a new controller to reduce helicopter vibrations using trailing edge flaps. This new controller takes into account rotor dissimilarities and allows different control inputs to be applied to each trailing edge flap.

A Mach-scaled four-bladed rotor with piezo-bender actuated trailing edge

flaps was used to demonstrate the controller's ability to minimize vibratory loads in the rotating frame. In hover test, at 1800 rpm, flap deflections of 4° half peak-to-peak were measured.

Closed loop tests were conducted in hover and forward flight to minimize the vibratory blade root flap bending moment.

In hover, at 500 rpm, the 1/rev vibration was reduced by more than 90%, for a single active blade as well as for several active blades simultaneously.

In forward flight, the controller performance was limited because of larger vibration levels and smaller available flap deflections. At 1200 rpm, and wind speed of 27 mph ($\mu = 0.13$), vibration in the rotating frame was primarily 1 and 3/rev. The 1/rev component could be reduced by 66% and the 3/rev component by 34% simultaneously. At higher rotor speed (1500 rpm), thicker flexures were used for safety, resulting in smaller flap deflections. As a result, only single harmonics could be targeted. At 1500 rpm, and wind speed of 32 mph ($\mu = 0.15$), the 3/rev harmonic component of vibration was reduced by 40%, and the 4 and 5/rev harmonics were reduced by more than 90% when targeted alone, with flap deflections smaller than 2.8°. The controller performance was also investigated in a transient flight condition (increase of rotor speed), while the adaptive controller was on. Vibration levels were maintained below uncontrolled levels at all times during the flight condition change.

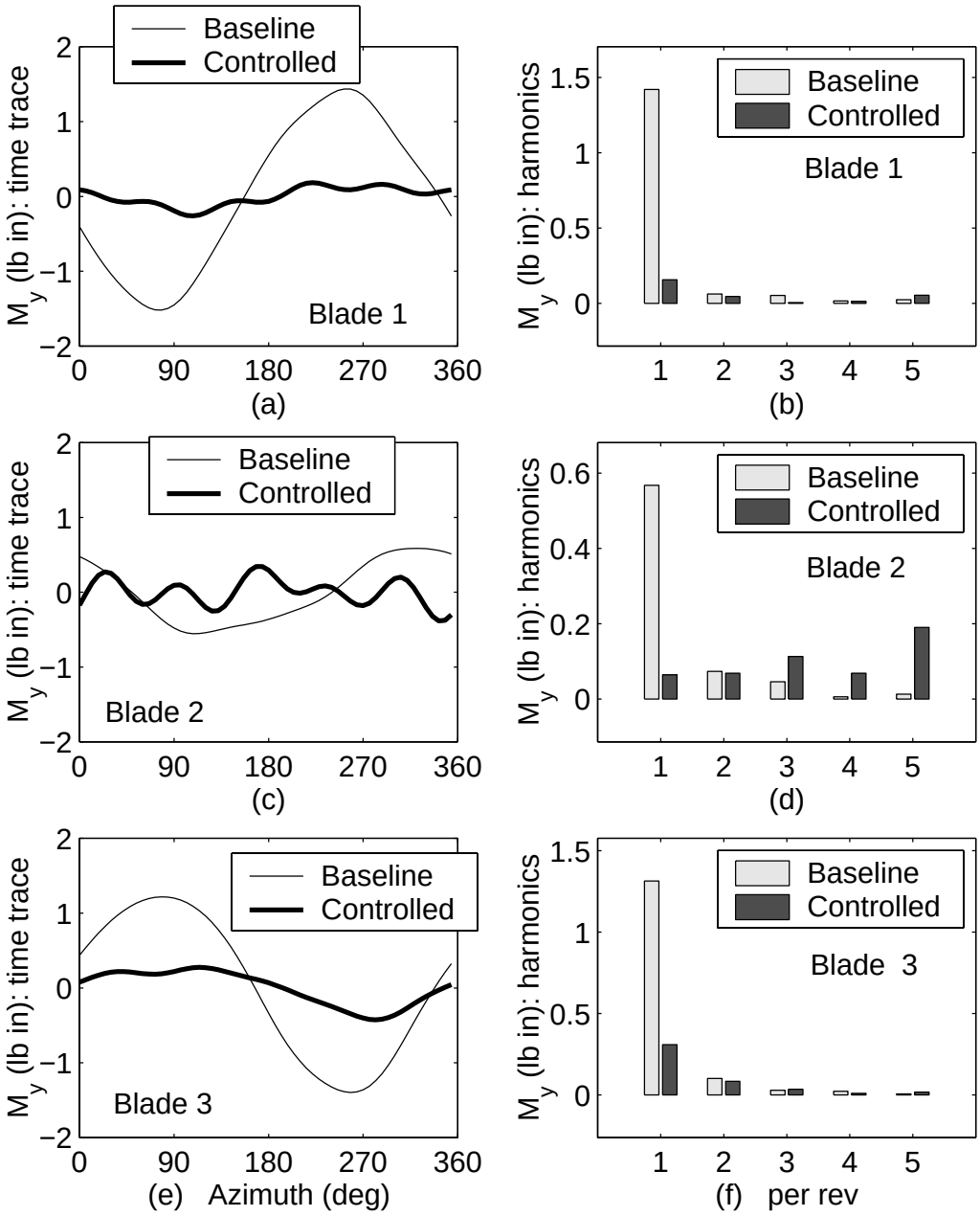

Figure 7.5: Closed loop test, hover, 500 rpm, control objective is M_y at root of blades 1, 2 and 3 : vibratory loads

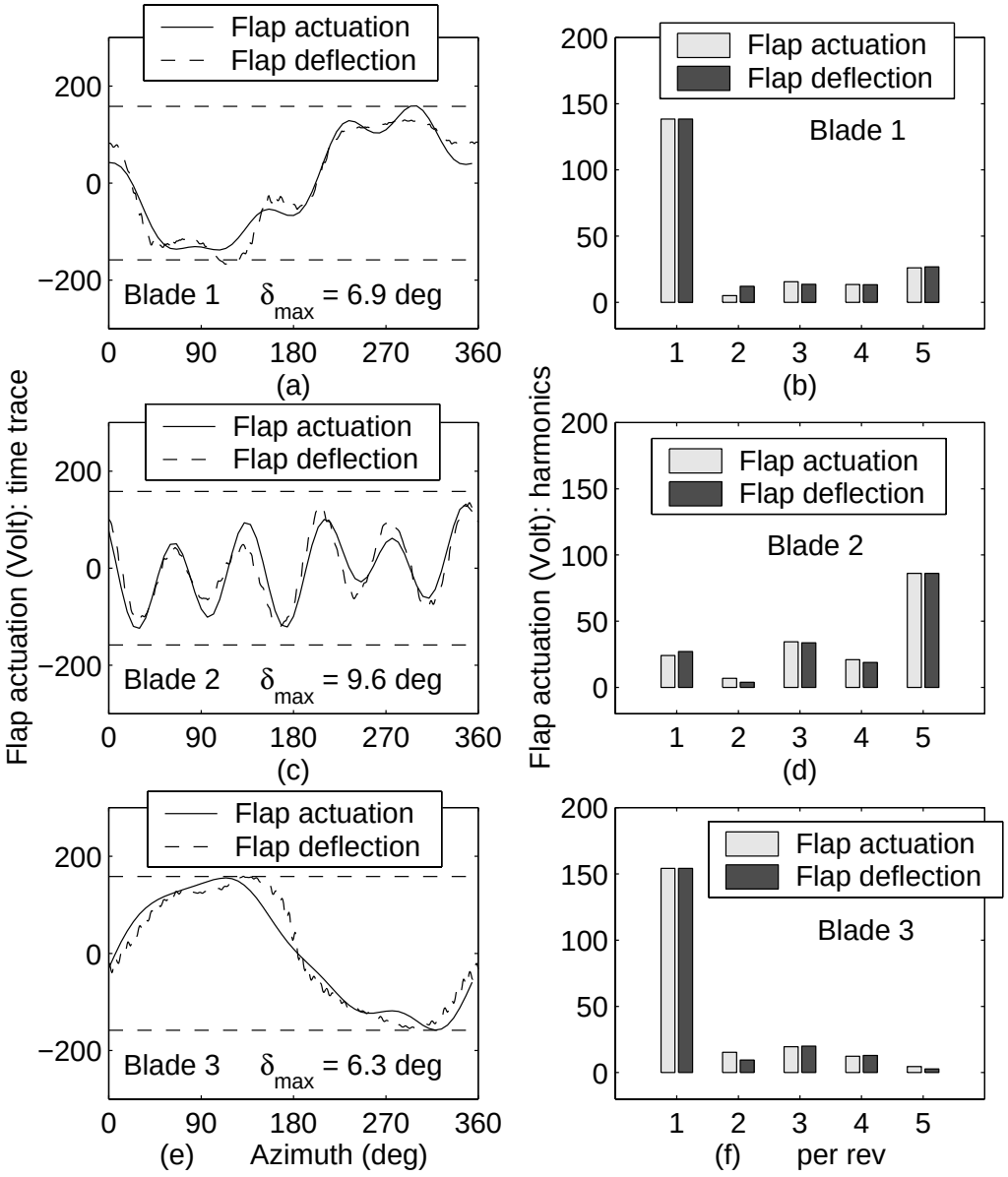

Figure 7.6: Closed loop test, hover, 500 rpm, control objective is M_y at root of blades 1, 2 and 3 : flap deflections

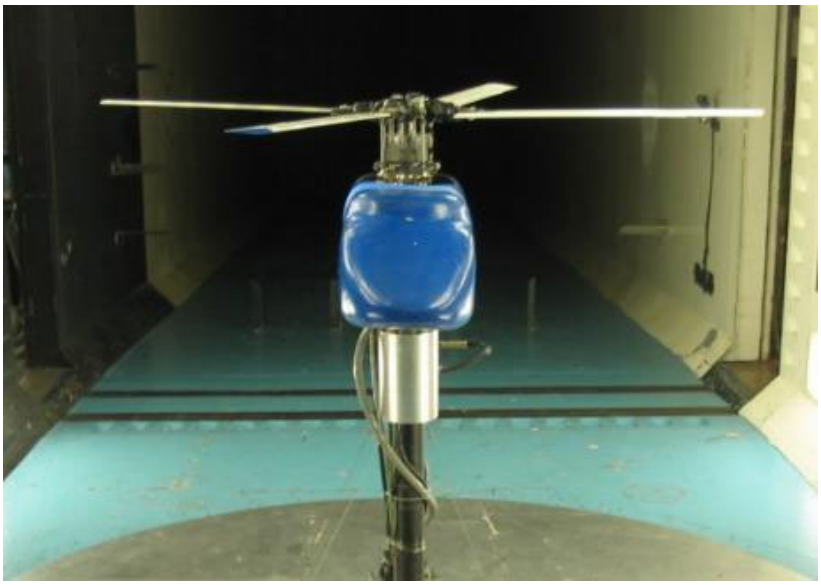

Figure 7.7: Rotor in Wind Tunnel

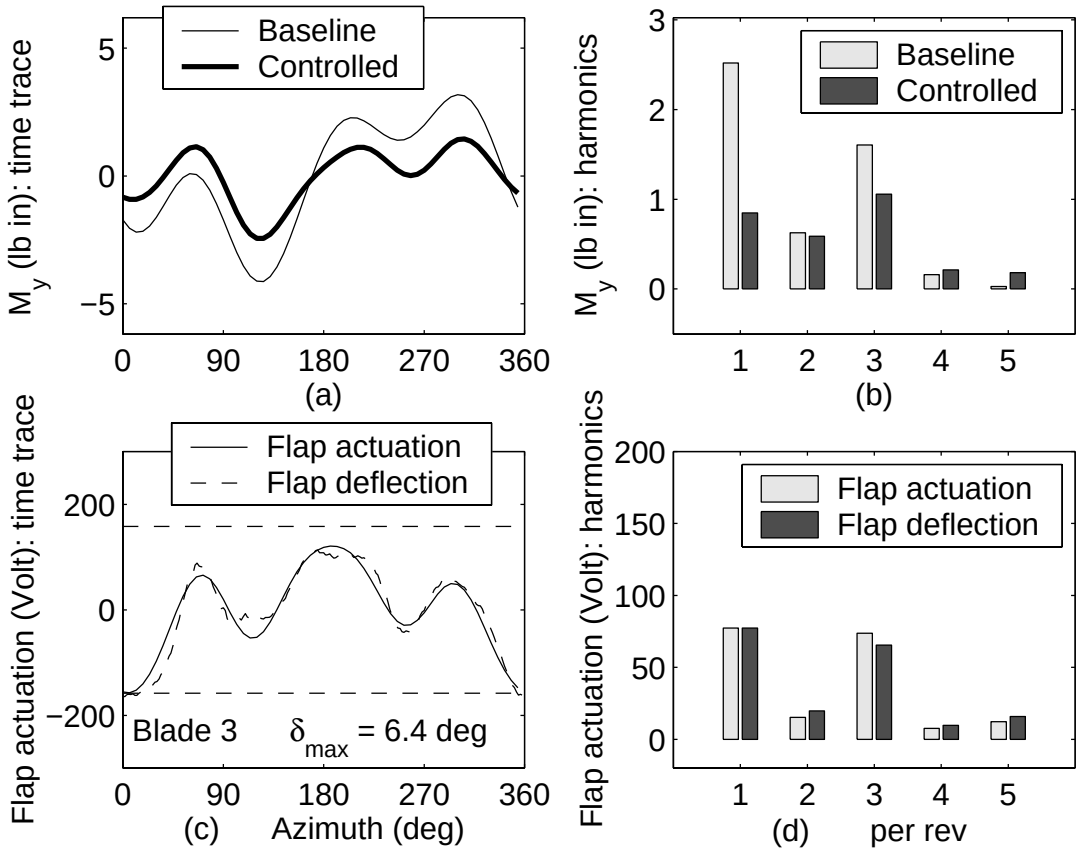

Figure 7.8: Closed loop test, 1200 rpm, 27 mph, control objective is M_y at root of blade 3: vibratory loads and flap deflections

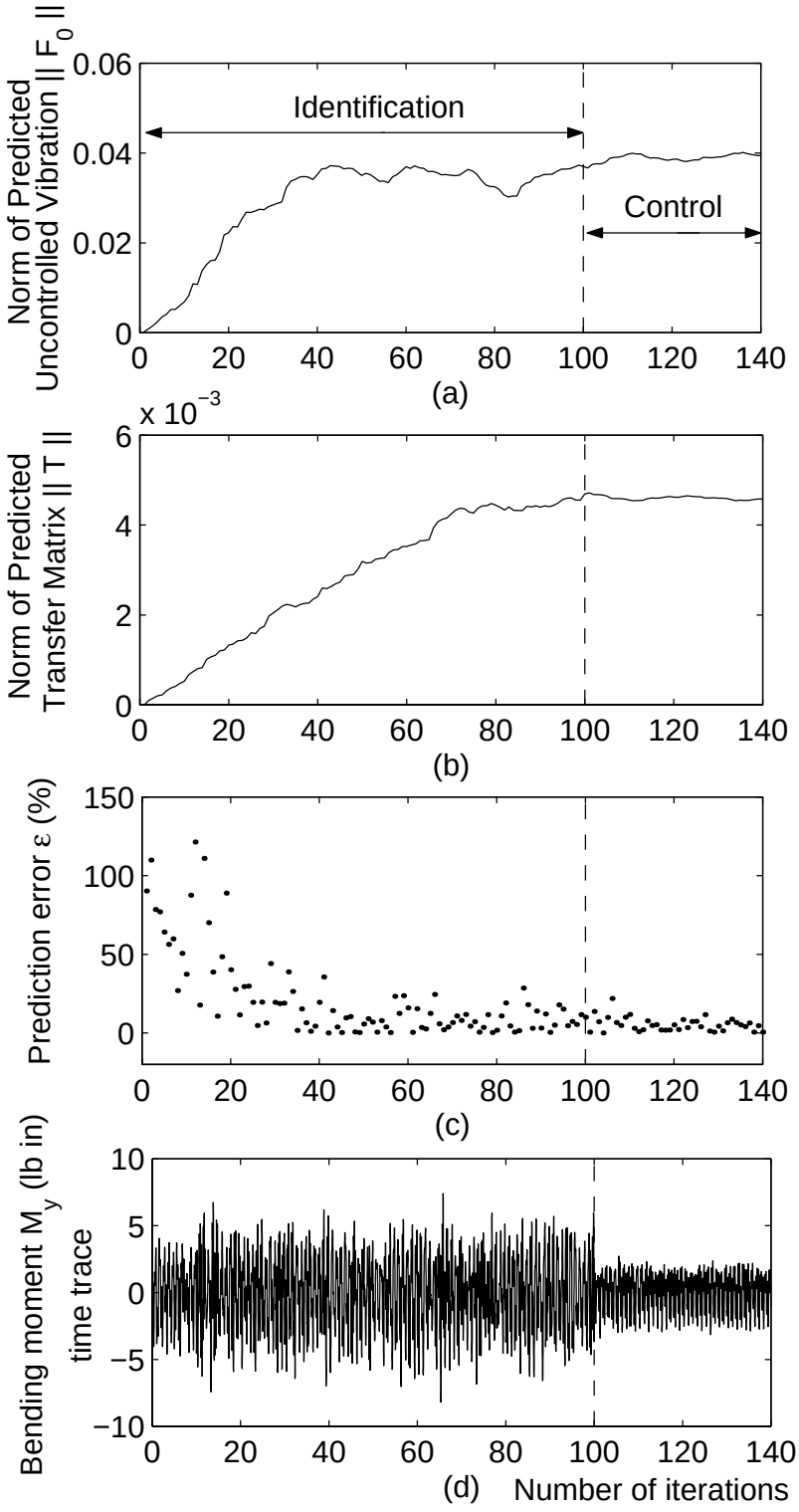

Figure 7.9: Closed loop test, 1200 rpm, 27 mph, control objective is M_y at root of blade 3: time traces

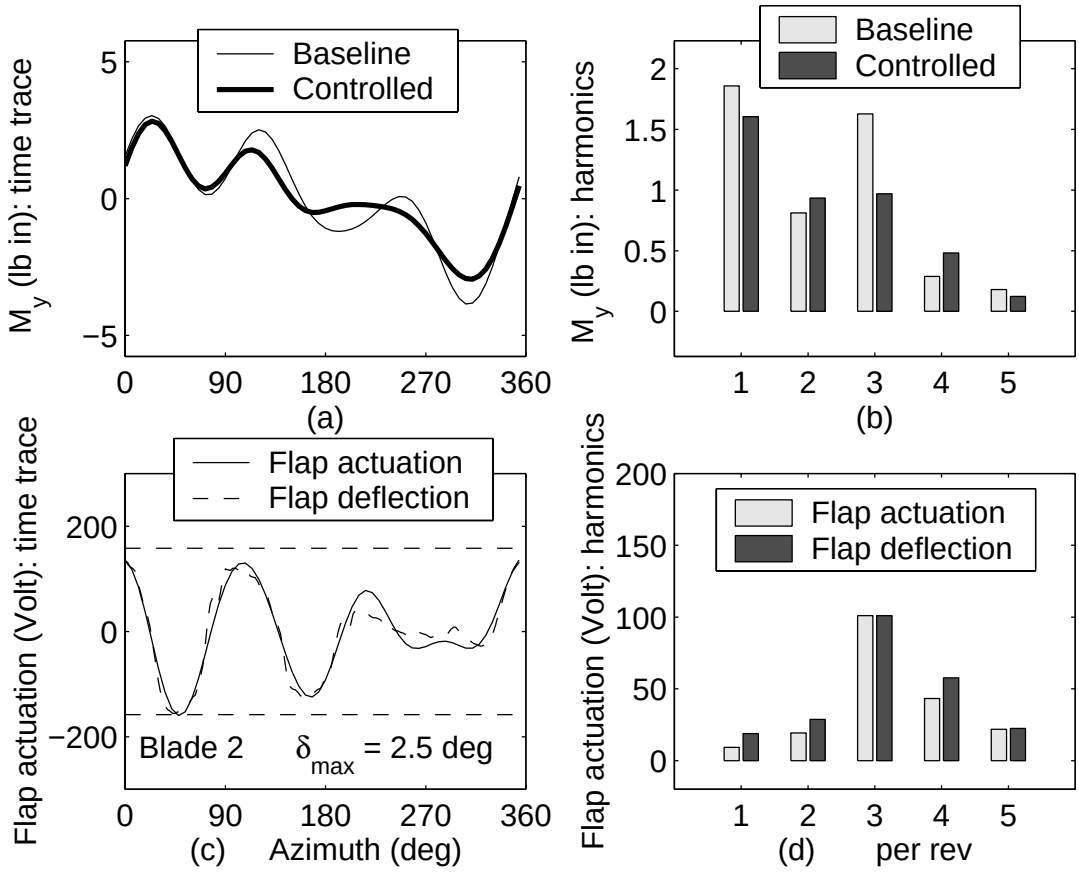

Figure 7.10: Closed loop test, 1500 rpm, 32 mph, control objective is 3/rev M_y at root of blade 2

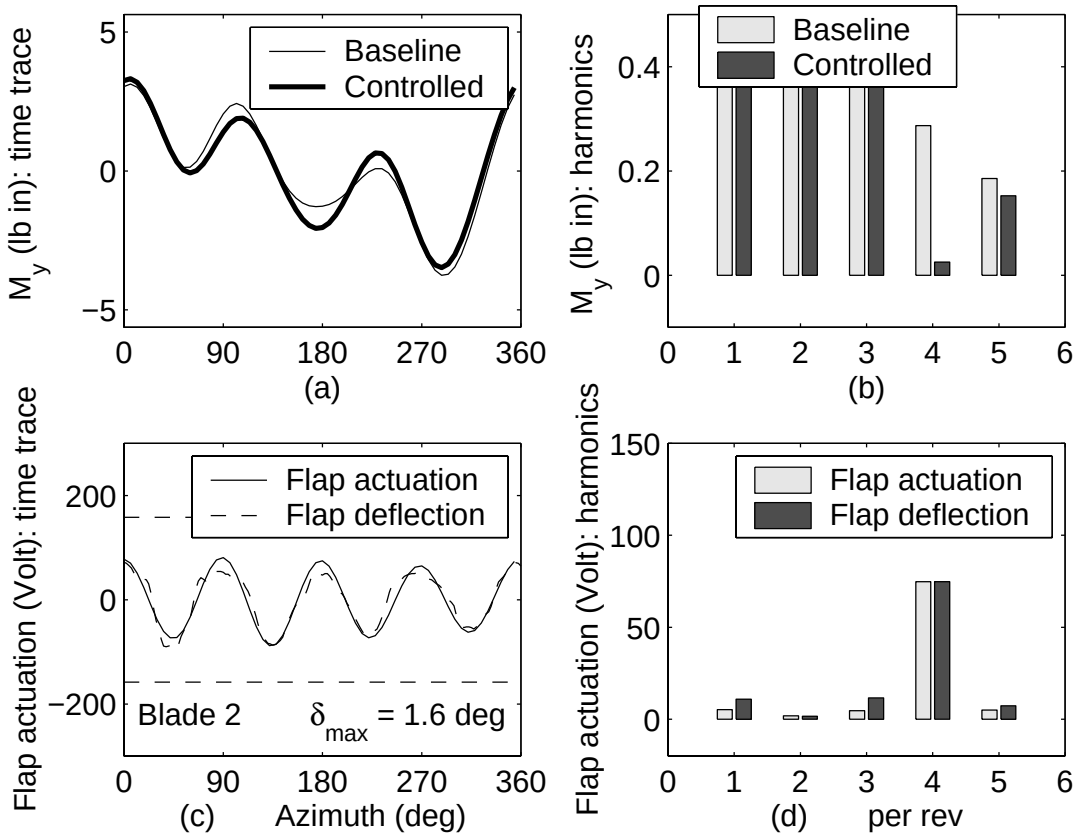

Figure 7.11: Closed loop test, 1500 rpm, 32 mph, control objective is 4/rev M_y at root of blade 2

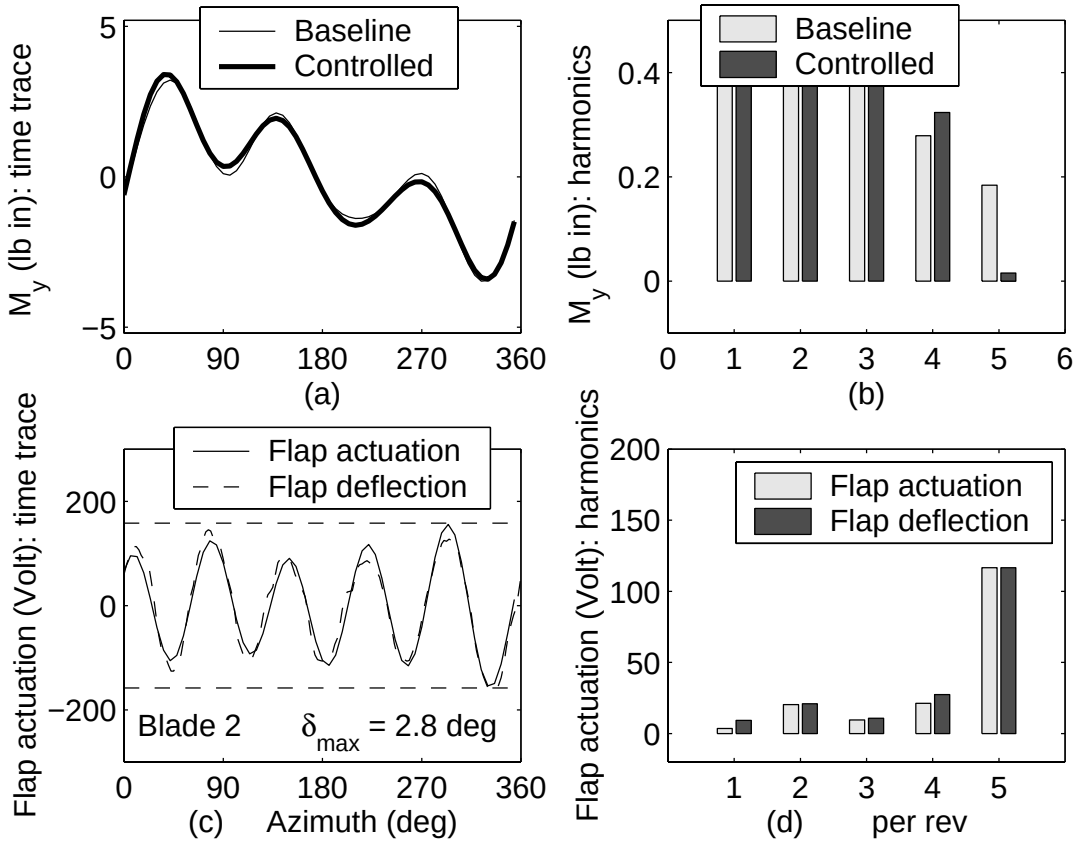

Figure 7.12: Closed loop test, 1500 rpm, 32 mph, control objective is 5/rev M_y at root of blade 2

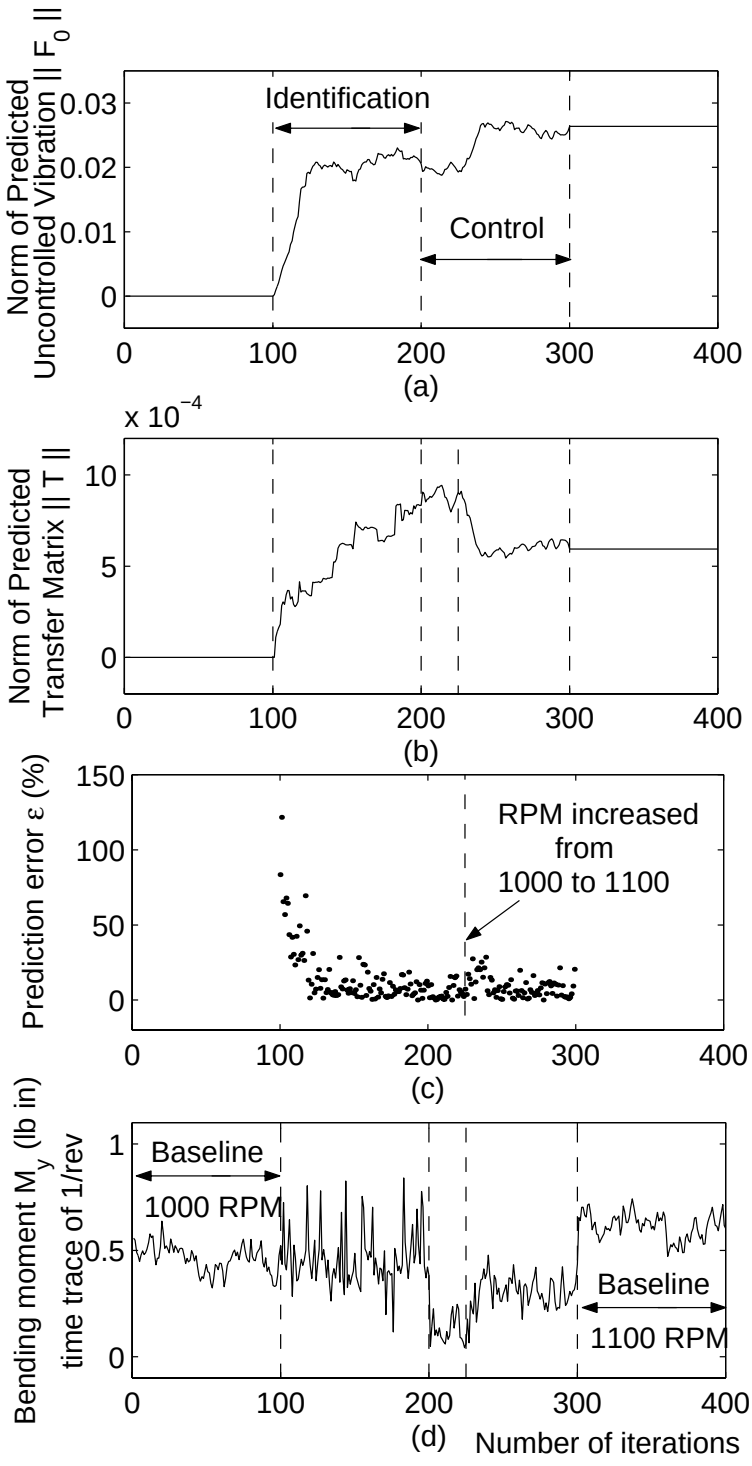

Figure 7.13: Closed loop test, transient, 1000 to 1100 rpm, 27 mph, control objective is 1/rev M_y at root of blade 1

Chapter 8

Closed Loop Control: Reduction of Fixed Frame Loads

In this chapter, the controller's ability to reduce vibratory loads in the fixed frame is experimentally investigated, using the Mach-scaled rotor with all four flaps active simultaneously. First, closed loop tests on the hover stand are presented, followed by closed loop tests in the Glenn L. Martin wind tunnel at the University of Maryland.

8.1 Controller tests on the hover stand

This section describes tests on the hover stand to demonstrate the controller's ability to affect the vertical fixed frame vibration at different frequencies.

In hover, with identical blades, both rotating frame and fixed frame loads are steady with no vibratory components. If the blades are dissimilar and no cyclic input is used, the rotating frame loads are still steady (although steady values will vary from blade to blade), and the vertical load also remain steady. If cyclic inputs are used, the vertical rotating frame loads become oscillatory at 1/rev. This vibration is filtered out in the fixed frame only if the blades are identical.

If the blades are dissimilar, the filtering effect of the rotor is imperfect and some 1/rev vibration is transmitted to the fixed frame via the hub.

Rotor mass imbalance is minimized by adding corrective weights at the root of the blades. However, it is difficult to correct aerodynamic differences between the blades. Therefore, because of a combination of imperfect trim and blade dissimilarities, the vertical hub load is oscillatory. The controller objective can then be set to minimize these vibrations.

In forward flight, because of asymmetric flow-field, unsteady airloads, and blade dynamics, the rotating frame loads consist of multiple harmonics. The control objective would then also include the 4/rev arising from the 3, 4, and 5/rev components of rotating vibration. In hover, the 4/rev component of vibration is negligible. In order to investigate the controller's ability to affect both the 1/rev and 4/rev loads in the fixed frame simultaneously, the control objective for the hover test is set to reduce the 1/rev part but generate a 4/rev load of given amplitude and phase.

The following tests are performed at a rotor RPM of 1500, and collective angle of 2 degrees.

8.1.1 Control using individual blade inputs

In this section, the individual control method is used to control the vertical hub vibration, with separate transfer matrices identified for each blade and independent inputs generated for each flap.

Reduction of the 1/rev component in hover

Figures 8.1 and 8.3 show closed loop results for the reduction of the 1/rev component of vertical vibration. In Figure 8.1, the evolution of four test parameters during the test is shown. The test consists of 4 phases, defined as follows

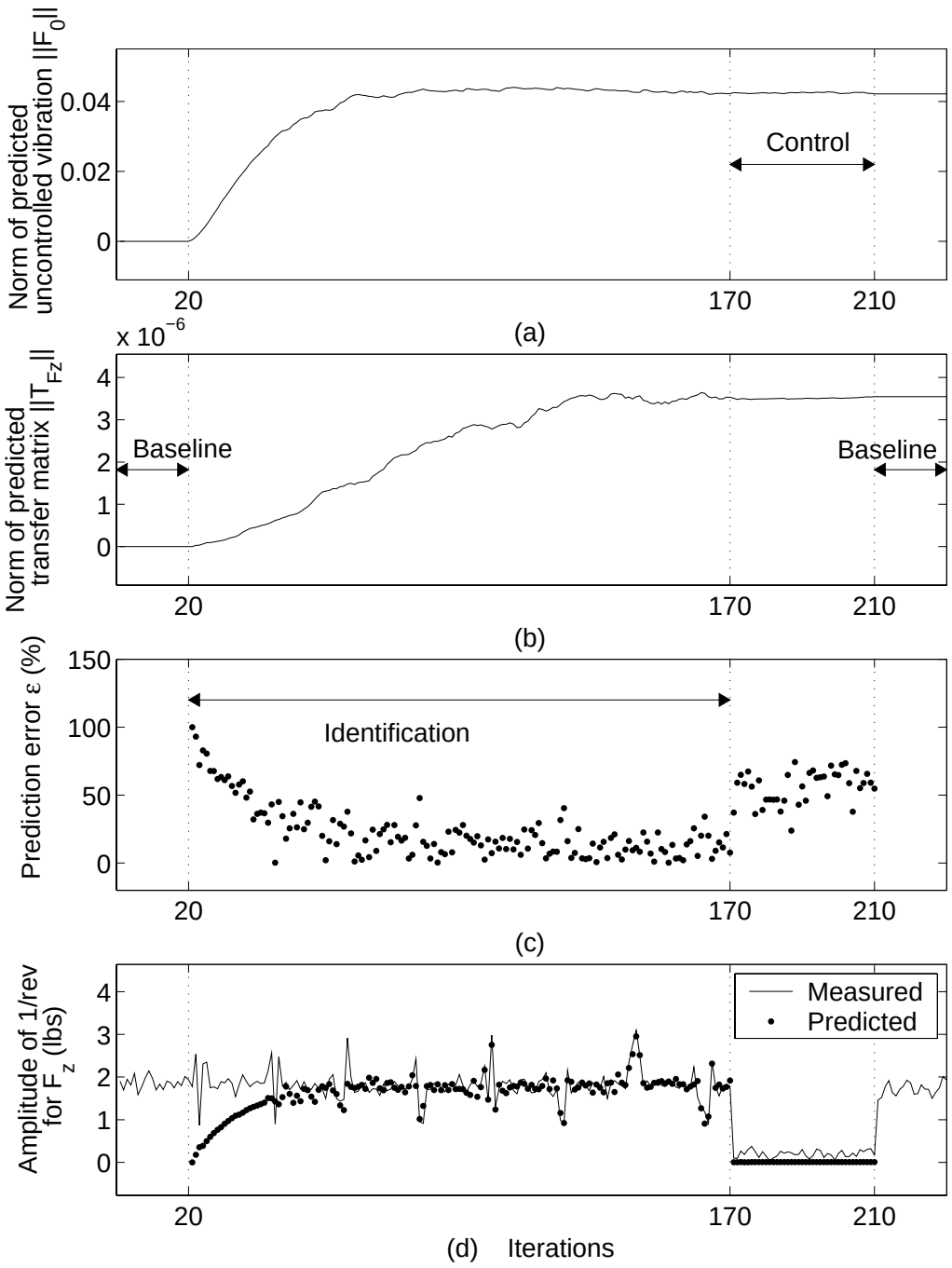

Figure 8.1: Target reduction of 1/rev hub vertical force F_z in hover using individual inputs: time history of various parameters

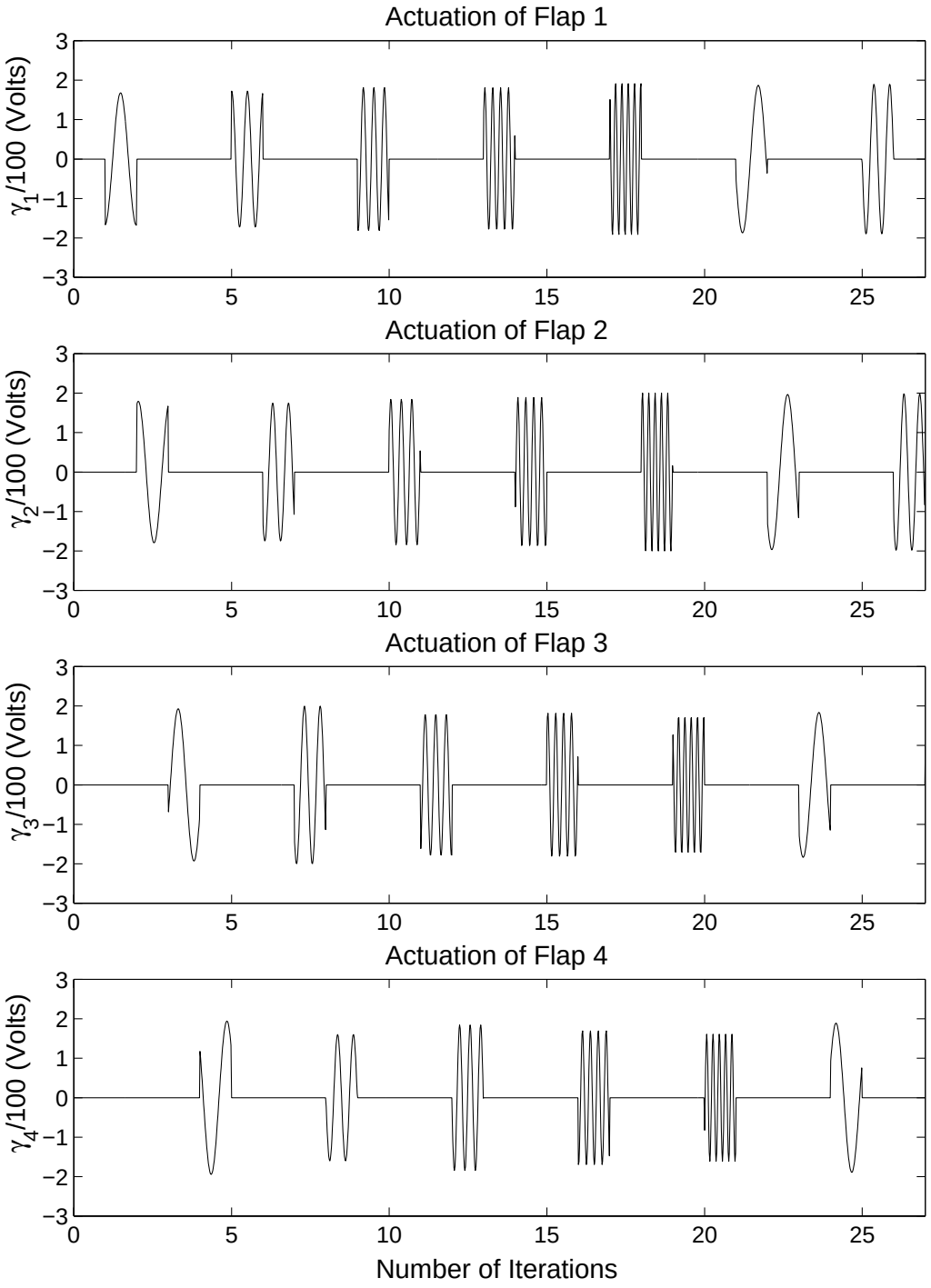

Figure 8.2: Flap inputs used for the identification phase

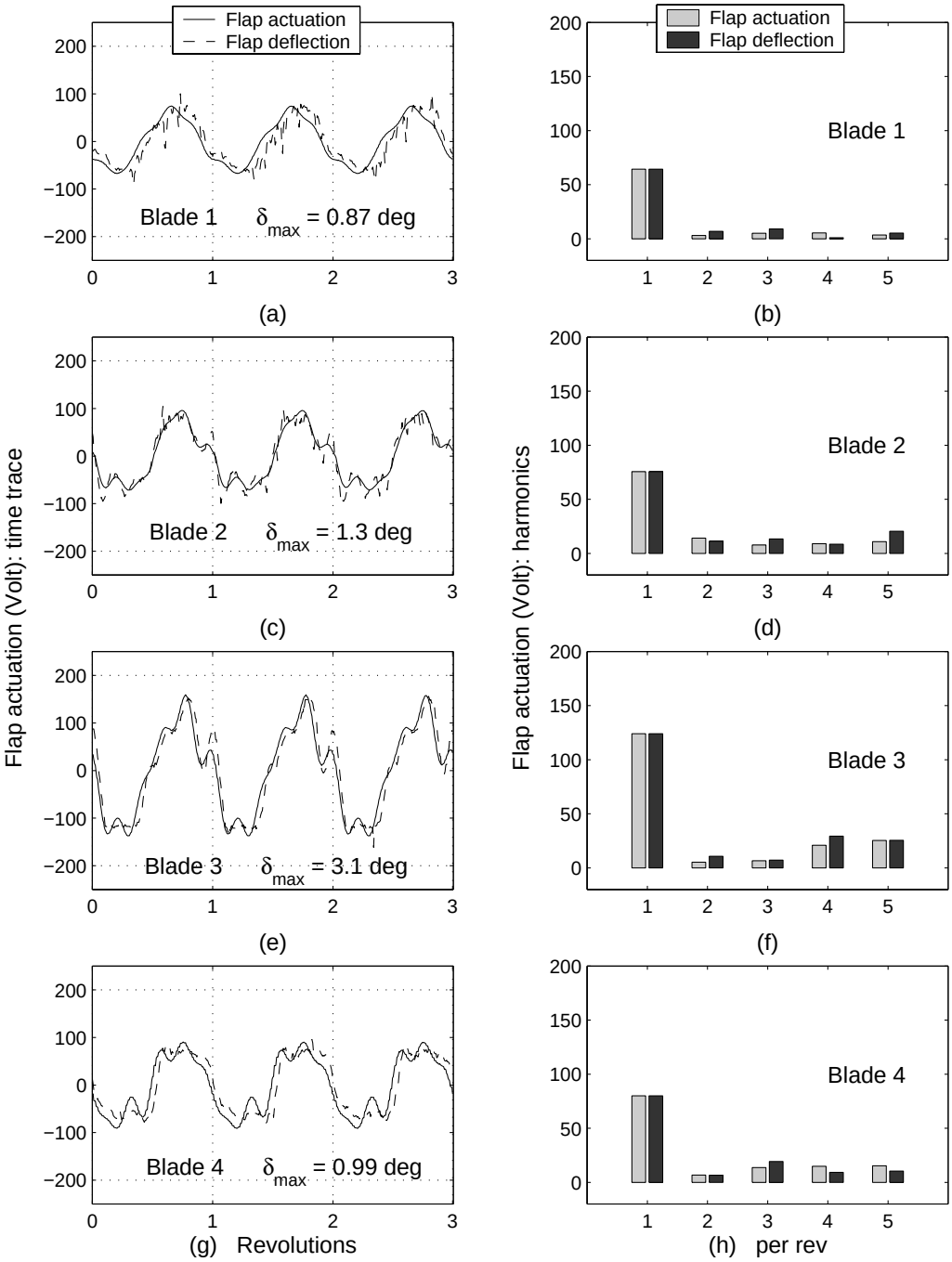

Figure 8.3: Target reduction of 1/rev hub vertical force F_z using individual inputs: optimal flap inputs

and carried out in sequence:

1. Baseline: no command inputs to the flaps
2. Identification: inputs of varying amplitude, frequency and phase are used to identify the transfer matrices
3. Control: optimal inputs are generated, closed loop control and system identification are performed simultaneously
4. Back to baseline: no command inputs to the flaps

The uncontrolled vibration F_0 and the transfer matrix T_{F_z}, between flap inputs and vertical hub vibration, are identified. F_0 converges in about 60 iterations (Figure 8.1(a)), and T_{F_z} in about 140 iterations (Figure 8.1(b)). One iteration corresponds to about 8 rotor revolutions. The prediction error (Figure 8.1(c)) gradually decreases during identification, with a sudden increase after control is started. This is because as soon as optimal control inputs are used, both the measured and predicted vibration levels become very small, as seen in Figure 8.1(d). During identification, the command input is sent to one blade at a time in the manner pictured in Figure 8.2:

1. One blade at a time is actuated, at a frequency from 1/rev to 5/rev.
2. Actuation amplitude is chosen randomly from 160 Volts to 200 Volts.
3. Phase of actuation is random.

In Figure 8.1(d), the spikes observed during identification appear when the applied input is at the frequency of 1/rev, i.e. every 20 iterations. The predicted 1/rev vibration amplitude is also shown in black dots: at the beginning of the identification phase, prediction is zero because no previous information on the rotor is used. Towards the end of the identification phase, measurements and

prediction are in good agreement: in particular, the peaks corresponding to the 1/rev inputs are well predicted. As soon as the control phase starts, the 1/rev is reduced by about 90% and remains at that level until control is off and 1/rev vibration returns to its baseline level (about 2 lbs).

Figure 8.3 shows the converged control inputs. As in the previous section, both the actuation command and the actual deflections measured by the Hall effect sensors are represented, with matched amplitudes to facilitate comparison. The maximum flap deflection reached is also indicated. For the command voltage, an average upper limit of 200 Volts is imposed (100 Volts against the direction of polarization, and 300 Volts in the direction of polarization). This limit, shown in dotted lines in the figure, is not reached for any of the blades. Flap deflections required are small, around 1 degrees for all blades except blade 3 (3.1 degrees). Flap deflections are dominantly 1/rev, and almost exactly in phase with each other. In this way, the 1/rev vertical loads produced at the root of each blade add up and result in a fixed frame 1/rev vertical vibration of same phase and larger amplitude, which cancels the existing vibration.

Reduction of 1/rev component and generation of a prescribed 4/rev component

Figures 8.4 to 8.6 describe a feedback control test with the objective function for the vertical hub load including both the reduction of the 1/rev vibration as well as the generation of a 4/rev vibration, of amplitude 4.7 lbs and phase 90 degrees. The target amplitude was chosen based on open-loop tests which indicated it was possible to generate a 4/rev component of this amplitude. The target phase of 90° is with respect to the time at which continuous data acquisition is started. Starting of continuous data acquisition is triggered by the 1/rev signal from the rotor hub, which occurs when blade 1 is at the rotor azimuth 0°.

However, significant noise in the 1/rev signal causes the continuous data acquisition and waveform generation to start at a random time instead of when the rotor is in a particular configuration. As a result, the actual target phase with respect to rotor azimuth 0° can be different from 90°. This problem is illustrated in Figure 8.7.

Figure 8.4 shows the evolution of parameters during the test. The same phases as in the previous test are followed and indicated on the figure. However in this test, non-zero initial values for the uncontrolled vibration F_0 and the transfer matrix T_{F_z} are used (equal to the converged values after the first test). If the rotor characteristics and flight conditions have not changed, accurate identification and convergence should be obtained as soon as the identification phase is started. However, this is not seen in Figure 8.4, where instead, both F_0 and T_{F_z} are modified significantly from their initial values. This is because of noise in the 1/rev trigger signal: because triggering occurs at a random time, phase information is lost, and it is no longer possible to use previously identified parameters. This problem was later fixed by filtering the 1/rev signal and, as a result, previous data could be effectively used. Note that even though phase is different, amplitude of parameters should still remain same. This is true for the uncontrolled vibration F_0, however, the new transfer matrix T_{F_z} has a significantly smaller norm. This indicates the actuation system has lost efficiency compared to the previous test: a same voltage input results in less effect in the fixed frame.

Figure 8.5 shows the evolution of the 1/rev and 4/rev components of the normal force during the test. Figure 8.5(a) shows the amplitude of the 1/rev component, Figure 8.5(b) shows the amplitude of the 4/rev component, and Figure 8.5(c) shows the phase of the 4/rev component. The 1/rev vibration in vertical hub force is reduced by about 83%, while a 4/rev vibratory component is generated, with amplitude 2 lbs and phase 90 degrees. This amplitude corre-

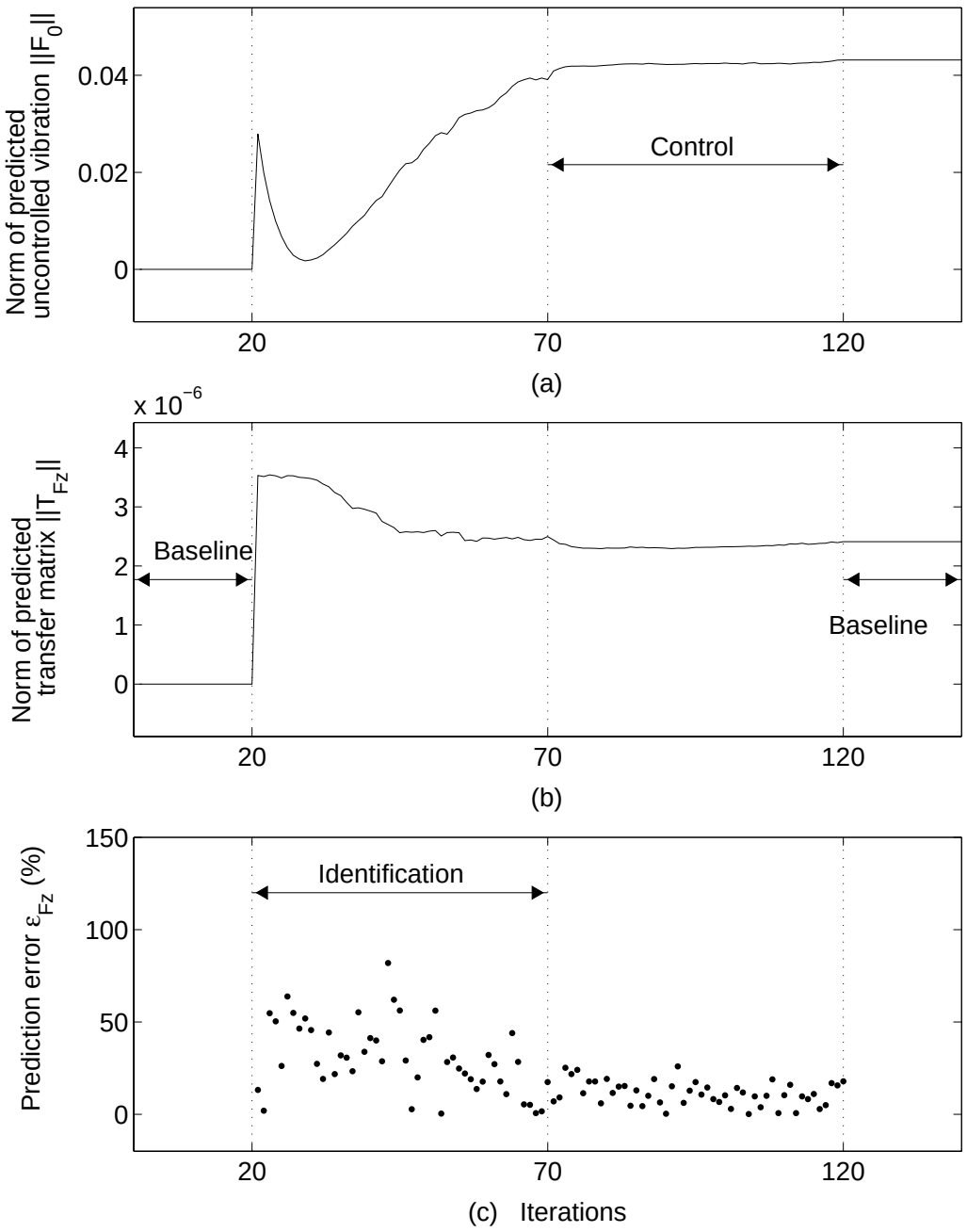

Figure 8.4: Target reduction of 1/rev hub vertical force F_z and generation of a prescribed 4/rev component using individual inputs: time history of various parameters

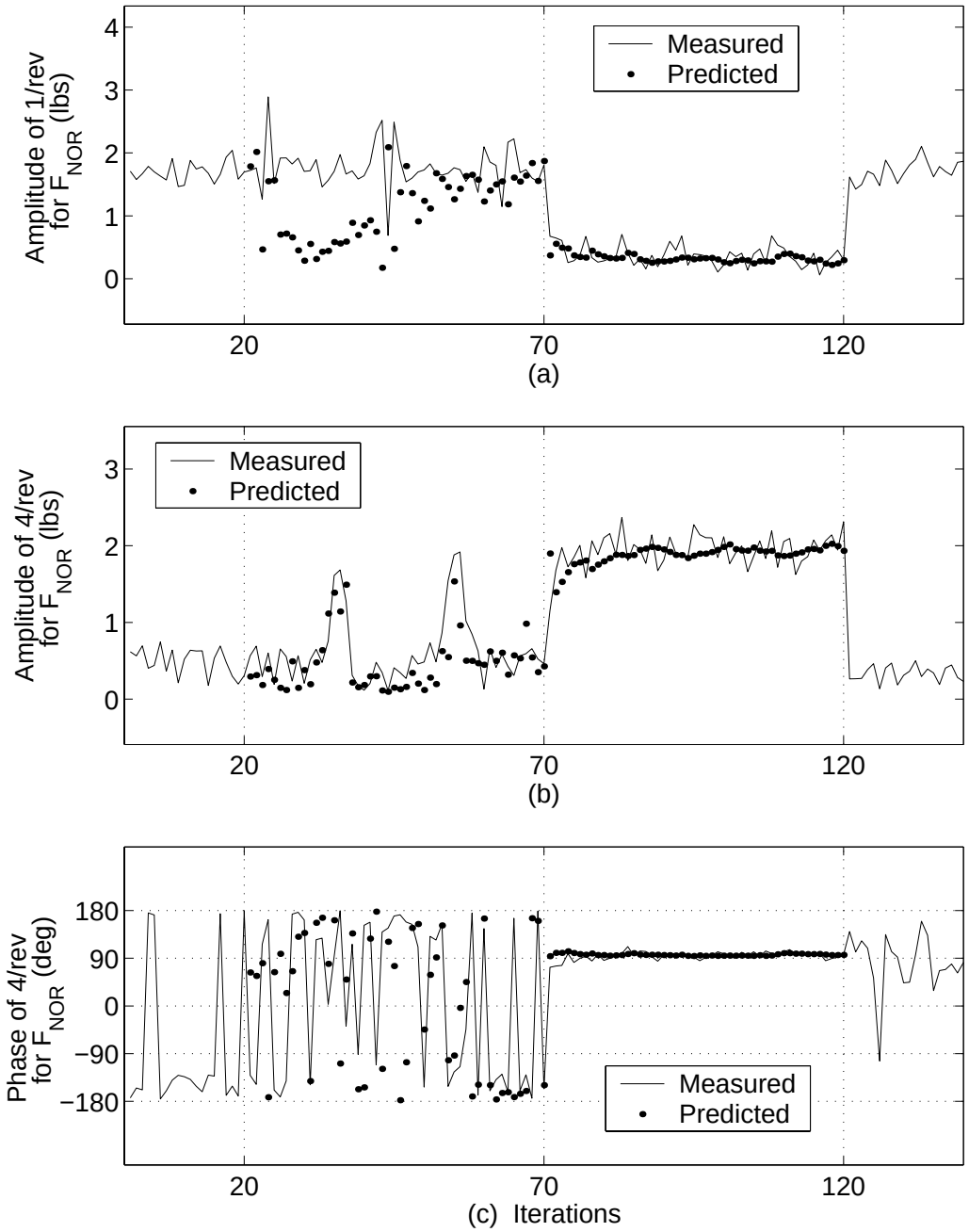

Figure 8.5: Target reduction of 1/rev hub vertical force F_z and generation of a prescribed 4/rev component using individual inputs: variation of target harmonics

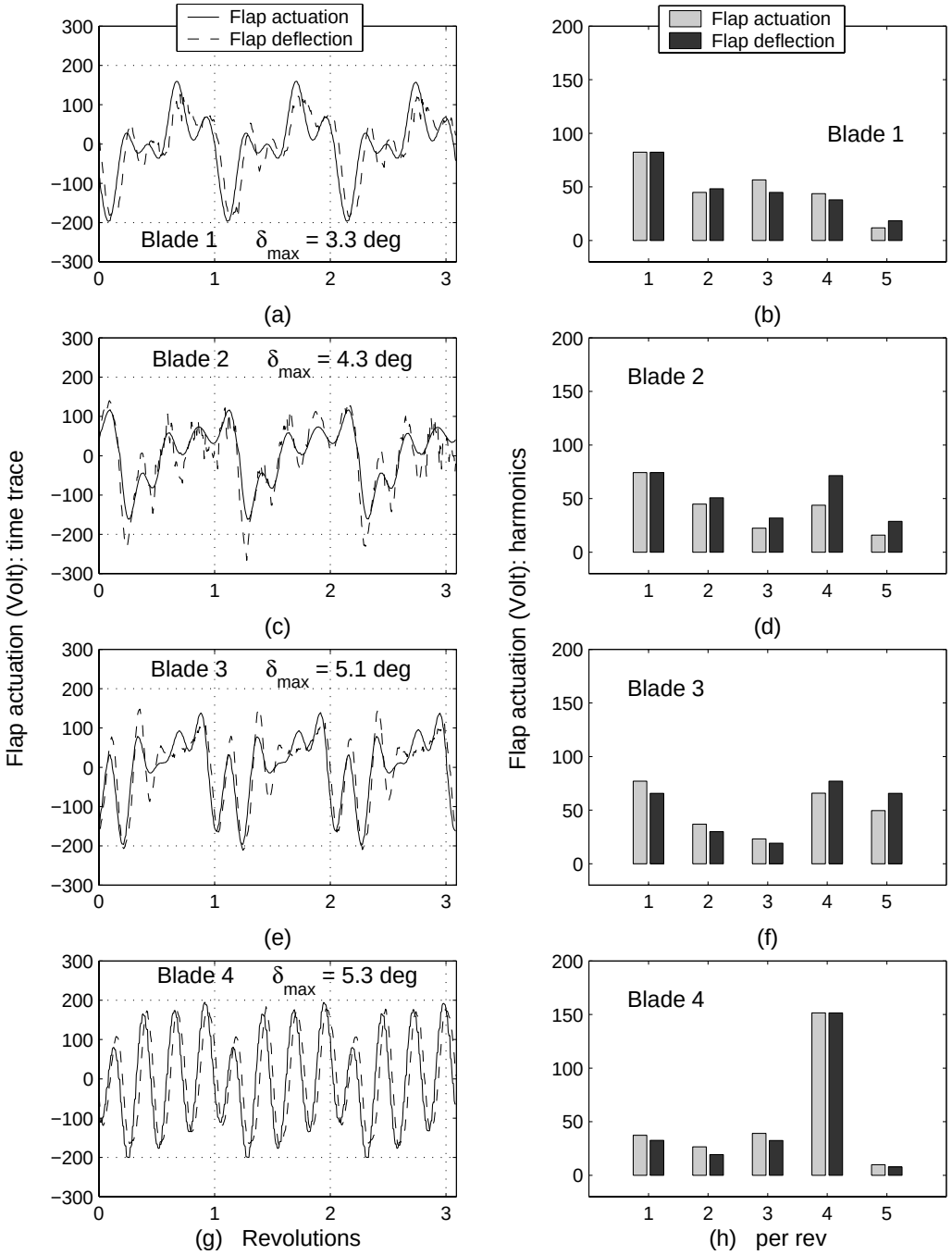

Figure 8.6: Target reduction of 1/rev hub vertical force F_z and generation of a prescribed 4/rev component using individual inputs: optimal flap inputs

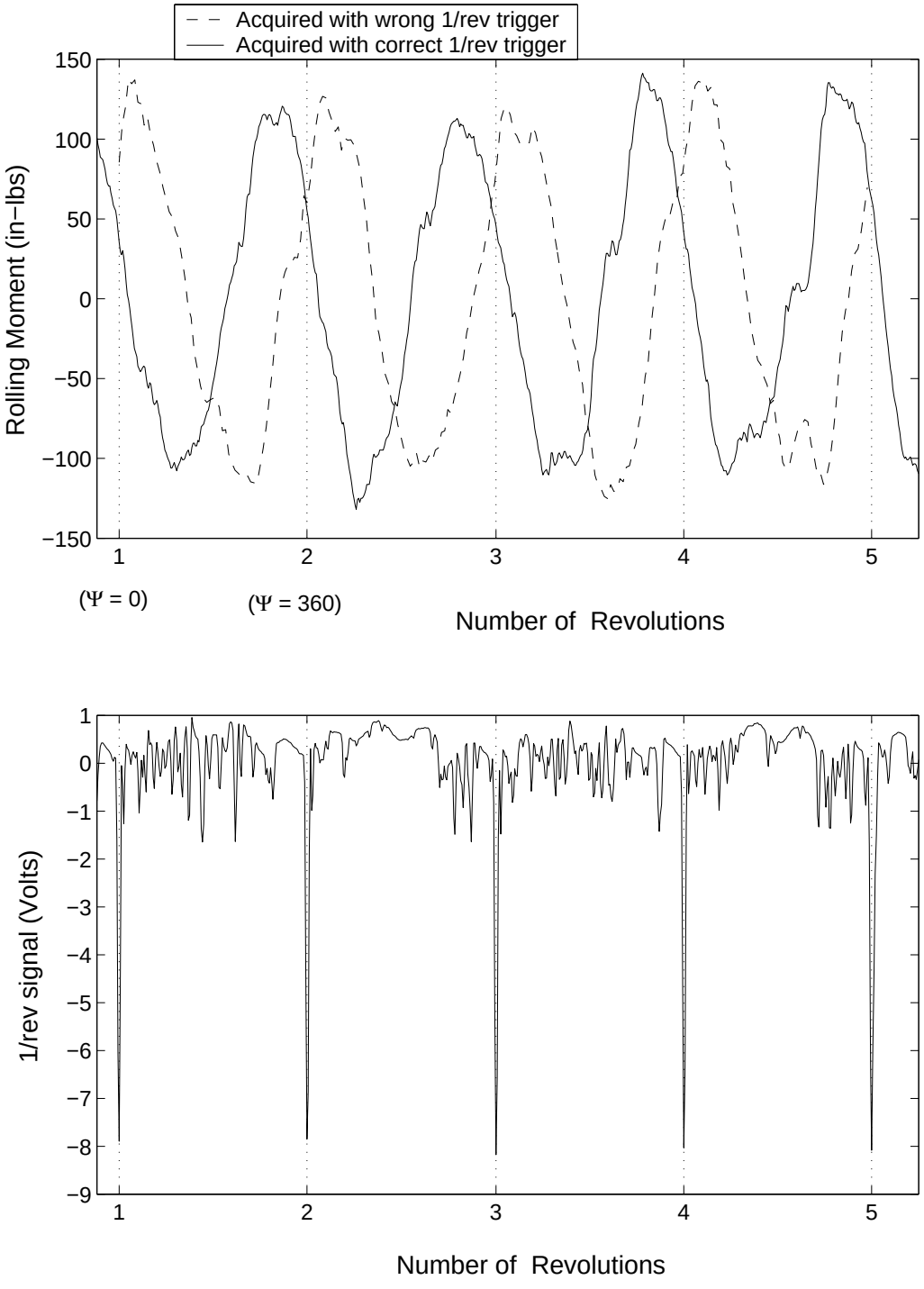

Figure 8.7: Incorrect 1/rev trigger problem

sponds to 40% of the target value. The target amplitude (4.7 lbs) for the 4/rev component is not achieved because the necessary actuation voltage exceeds the maximum allowable value. This is apparent in Figure 8.6, which shows the converged optimal angles. Contrarily to the previous test, the maximum actuation command of 200 V is reached for all blades. Peak deflections between 3.3 degrees and 5.3 degrees are achieved for all flaps. Flap 4 deflection is larger because the control input generated for this particular blade is dominantly 4/rev and near the resonance frequency of the flap and actuator system. For other blades, the control command is mainly at 1/rev, with smaller harmonics such as 4/rev for blade 3 and 3/rev for blade 1.

Generation of a prescribed 4/rev component

The objective of this test is to generate a 4/rev component in the vertical hub load. The target amplitude is 4.7 lbs and the target phase is 90 degrees. Figure 8.8 shows the variation of some identified parameters (uncontrolled vibration, F_0, and transfer matrix T_{F_z}) during the test. Figure 8.9 shows the variation of the 4/rev component, both in amplitude and phase. Before control, the 4/rev component is very small. After control is turned on, a 4/rev component is generated of amplitude 3.2 lbs and phase 90 degrees. Similar to the previous test, initial values were used for identification, equal to the converged values of the previous test, and as a result, the duration of the identification phase was decreased to 50 iterations. However, because of incorrect triggering, this initial condition is incorrect, and identified parameters do not have enough time to converge to accurate values (Figure 8.8(c)). Indeed, the 4/rev peaks observed due to 4/rev flap input during identification are not well predicted. Despite this, the control objective is almost achieved, with correct phase and amplitude equal to 70% the target value. Figure 8.10 shows the flap actuation generated by the

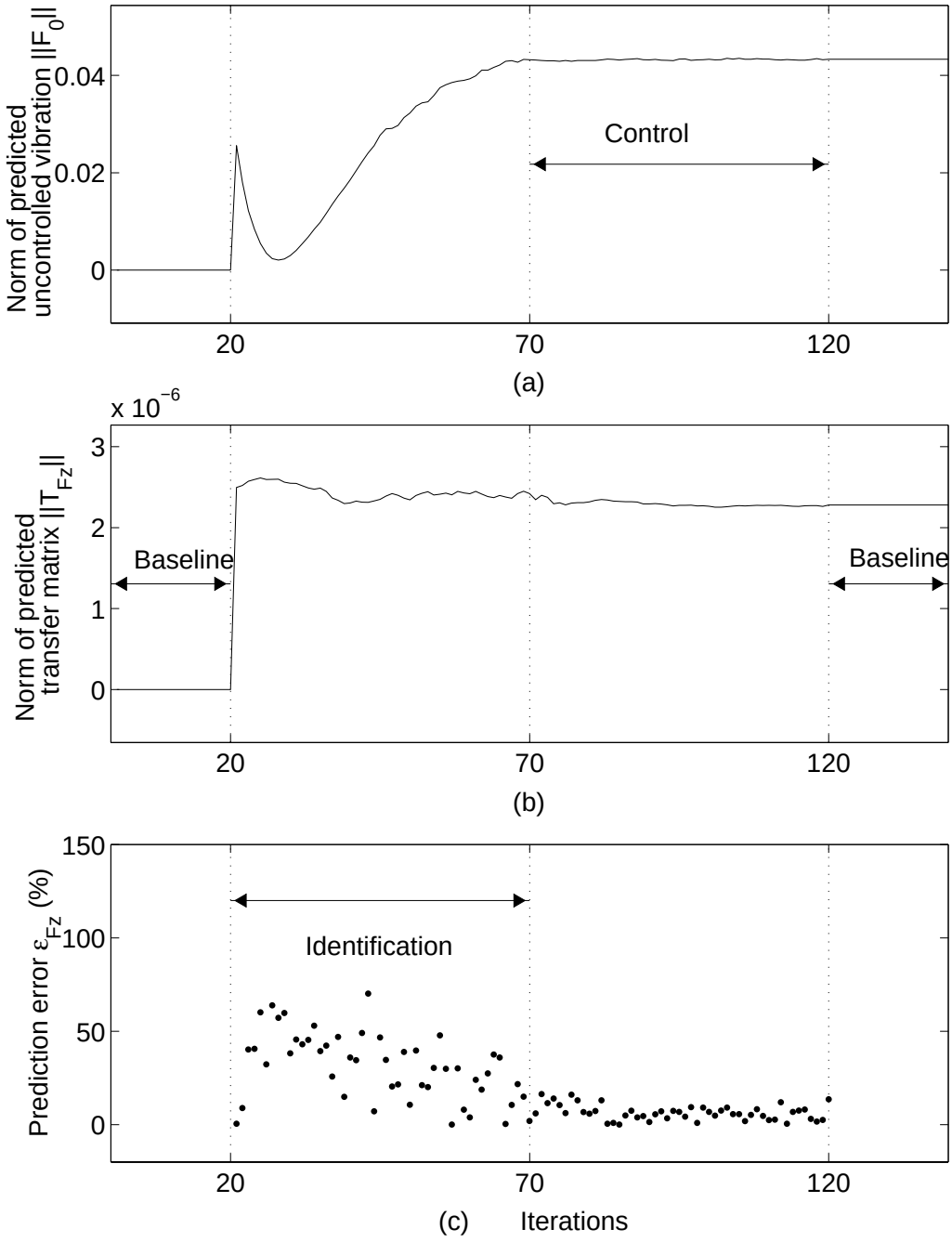

Figure 8.8: Generation of a prescribed 4/rev component in hub vertical force F_z using individual inputs: time history of various parameters

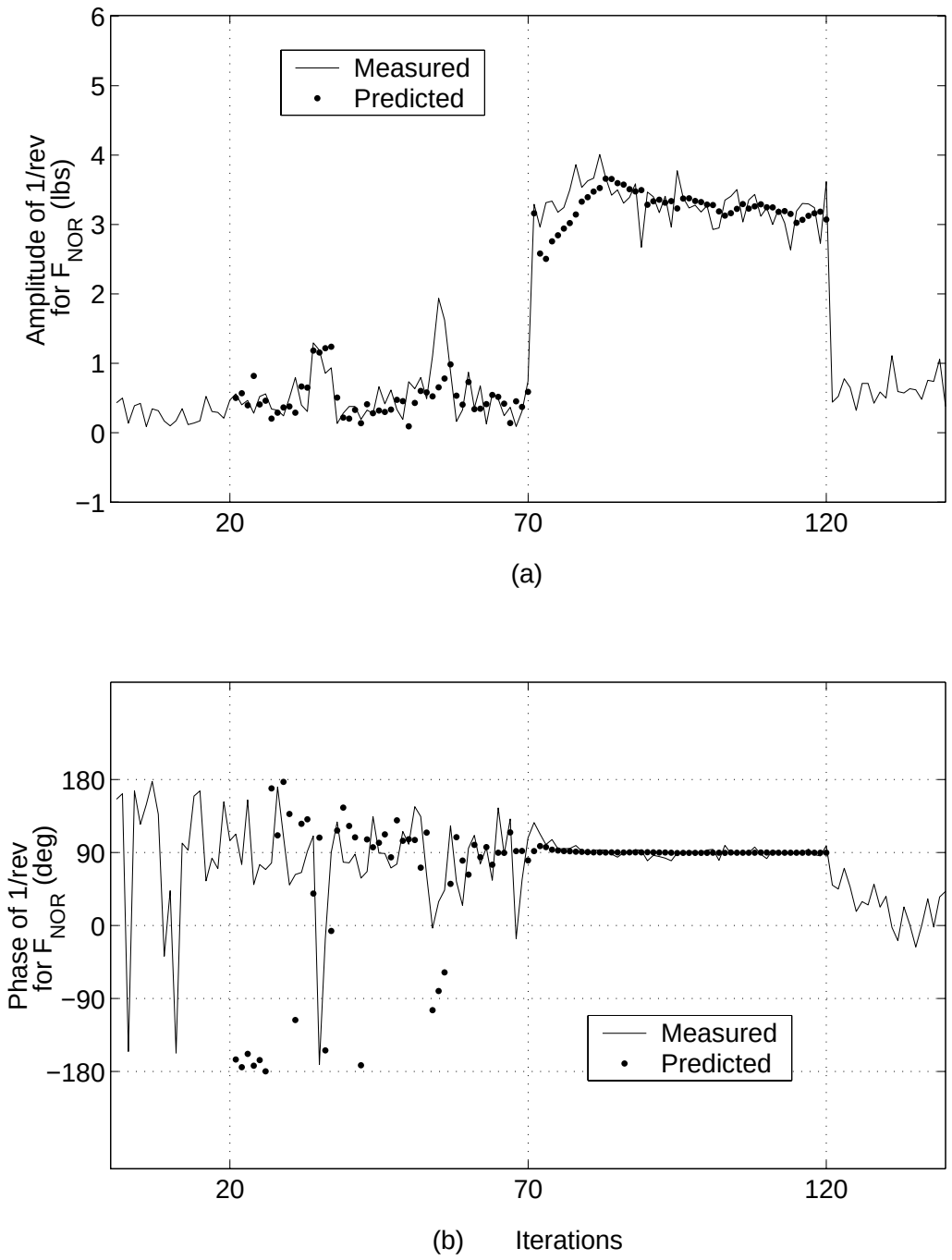

Figure 8.9: Generation of a prescribed 4/rev component in hub vertical force F_z using individual inputs: time history of 4/rev

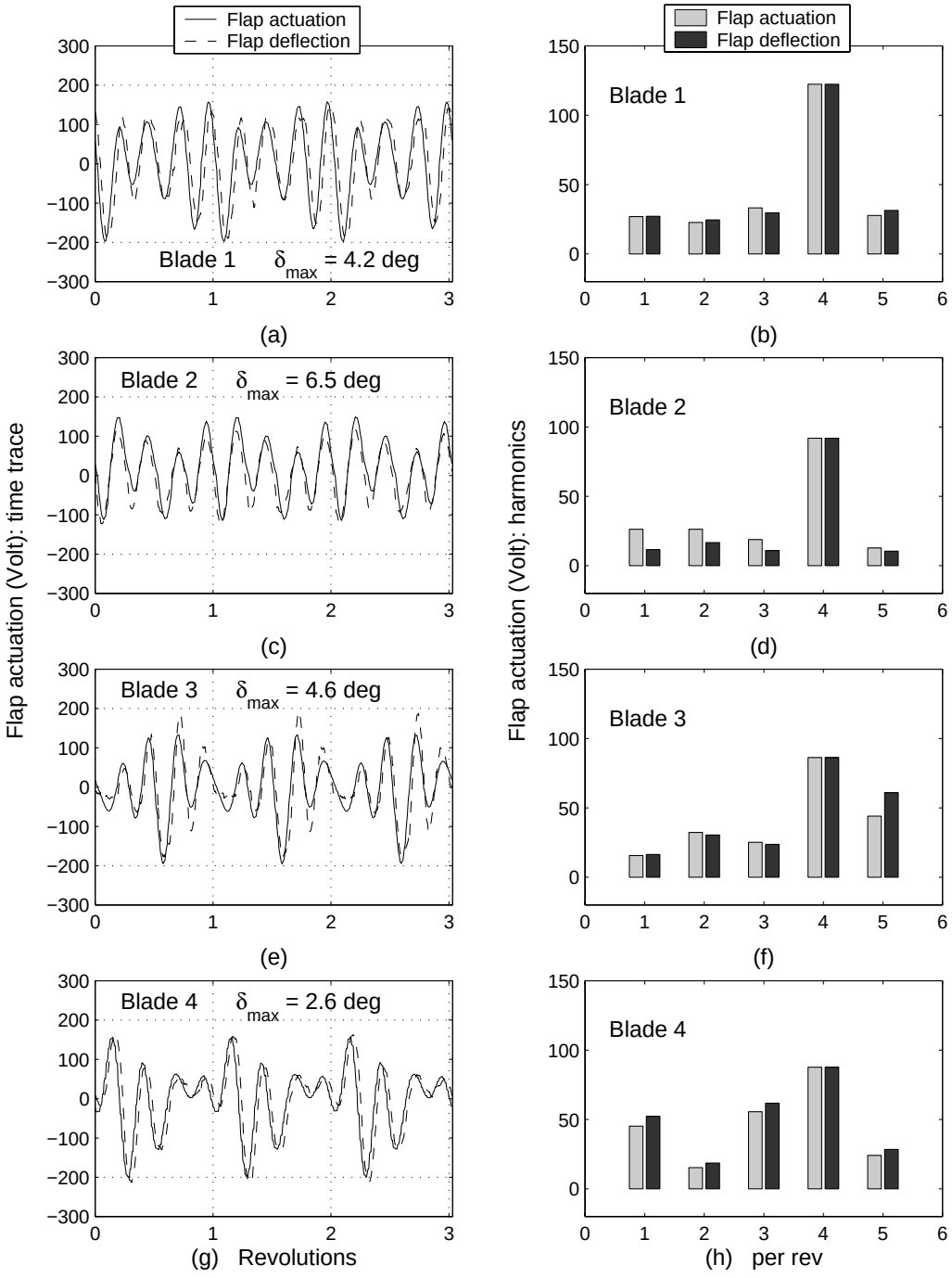

Figure 8.10: Generation of a prescribed 4/rev component in hub vertical force F_z using individual inputs: optimal flap inputs

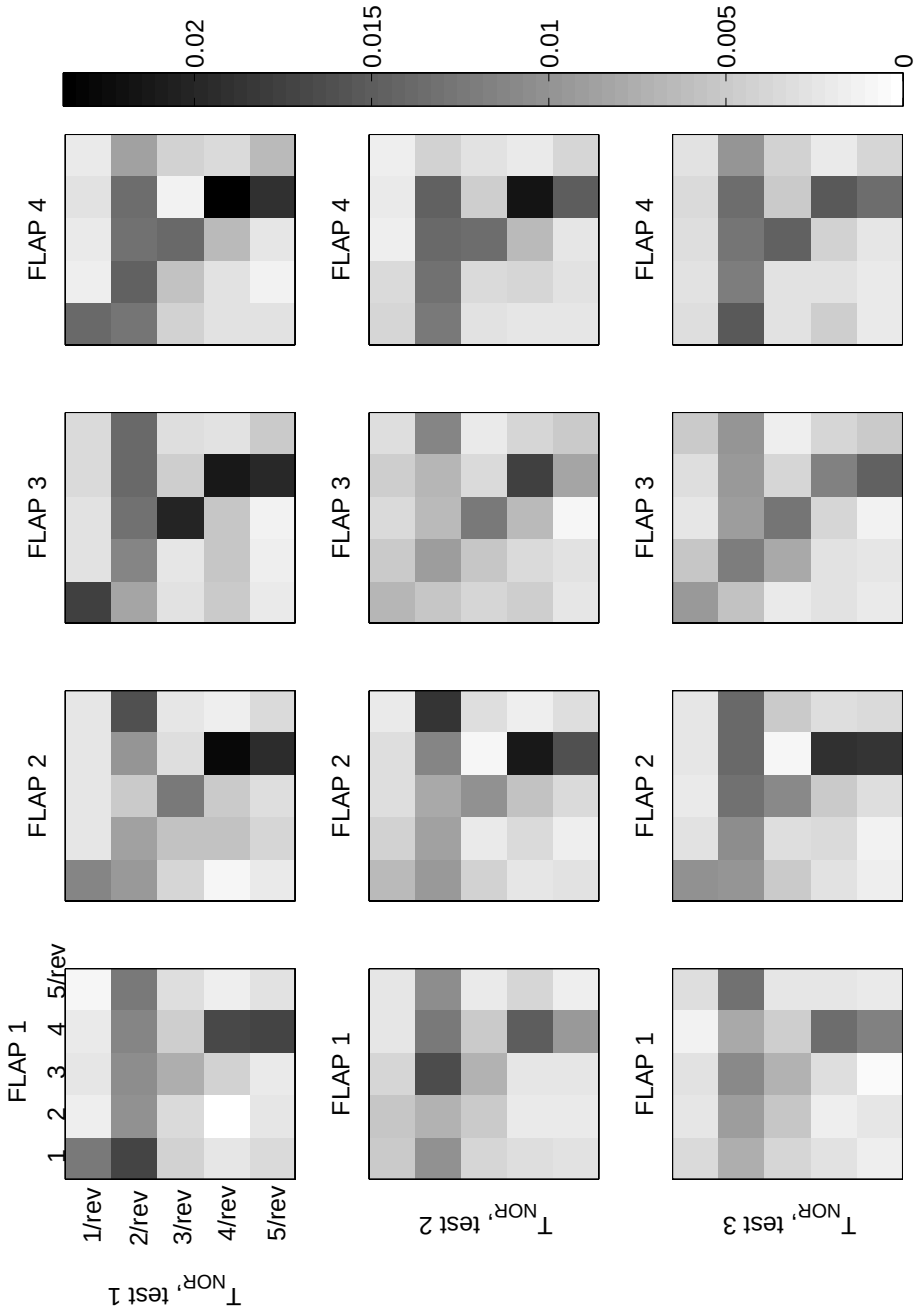

Figure 8.11: Transfer matrices representation for three tests

controller after convergence, together with the resulting flap deflections. The main harmonic, for all flaps, is 4/rev, but other harmonics are significant, for example 5/rev for blade 3, and 3/rev for blade 4.

Actual flap deflections follow closely the actuation command, with a phase lag of about 9 degrees, and peak deflections from 2.6 degrees (for blade 4) to 6.5 degrees (for blade 2).

Figure 8.11 shows a graphical representation of the identified transfer T_{F_z}. This transfer matrix relates the harmonics of flap input to the harmonics of the vertical vibration (5×5 matrix), for each of the 4 blades. In the figure, the 4 matrices are represented for each of the three tests described above. Only the absolute values are shown. The value of matrix elements is indicated by their color: the darker the element, the larger its value. Therefore, a dark square indicates a particular harmonic of flap input that is efficient in affecting a particular harmonic of the vertical hub load. Conversely, white squares signal harmonics of flap input which have little effect on a particular harmonic of the vertical hub load. The same color scale is used for all transfer matrices, allowing comparison between different blades and different tests. For example, in the first test (objective is 1/rev reduction), flap 3 appears to be more efficient than other flaps in affecting the 1/rev in vertical vibration. This explains why the control actuation generated for this blade is larger. Also, other flap harmonics have negligible effect on the 1/rev vibration, which is why the actuation command generated is very dominantly 1/rev. Comparing flap efficiency from test to test, it is apparent that flap 3 becomes less and less efficient in affecting the vertical hub load. Some loss in efficiency is also observed for flaps 1 and 4.

These tests show the ability of the individual blade controller to affect both 4/rev and non-4/rev vibration simultaneously. In the next section, these results are contrasted with performance of a controller which applies the same command input to all flaps, with a 90 degrees phase shift.

8.1.2 Control using phase-shifted blade inputs

The three tests that were described in the previous section are repeated, but flap inputs are no longer independent. Flap inputs are now forced to be identical, except for a 90 degrees phase shift from blade to blade.

Reduction of the 1/rev component and generation of a prescribed 4/rev component

First, the target load is the vertical hub load, and the control objective is reduction of the 1/rev component and generation of a 4.7 lbs amplitude, 90 degree phase 4/rev component.

Identification of parameters is shown in Figure 8.12. Initial conditions equal to zero are used. Convergence is achieved after about 100 iterations, and prediction error becomes less than 20%. Figure 8.13 shows the evolution of the control objectives during the test. Figure 8.13(a) shows the amplitude of the 1/rev component, Figure 8.13(b) shows the amplitude of the 4/rev component, and Figure 8.13(c) shows the phase of the 4/rev component.

This control method is not efficient in affecting the 1/rev component, which is reduced by only 20%. This illustrates the limitation of the classical control method to reduce non-N_b/rev vibration. A 4/rev component is generated, but with amplitude 1.7 lbs, and phase 60 degrees. The small reduction in 1/rev vibration is due to the fact that flaps and actuators are dissimilar, therefore identical actuation can result in slightly dissimilar deflections. Figure 8.14 shows the flap actuation generated by the controller after convergence, together with the resulting flap deflections. Flap actuation is same for all blades, but actual flap deflections differ from blade to blade because of differences in the flap and actuator assembly. The controller generates a flap command with large 1/rev and 4/rev components, and a smaller 2/rev component.

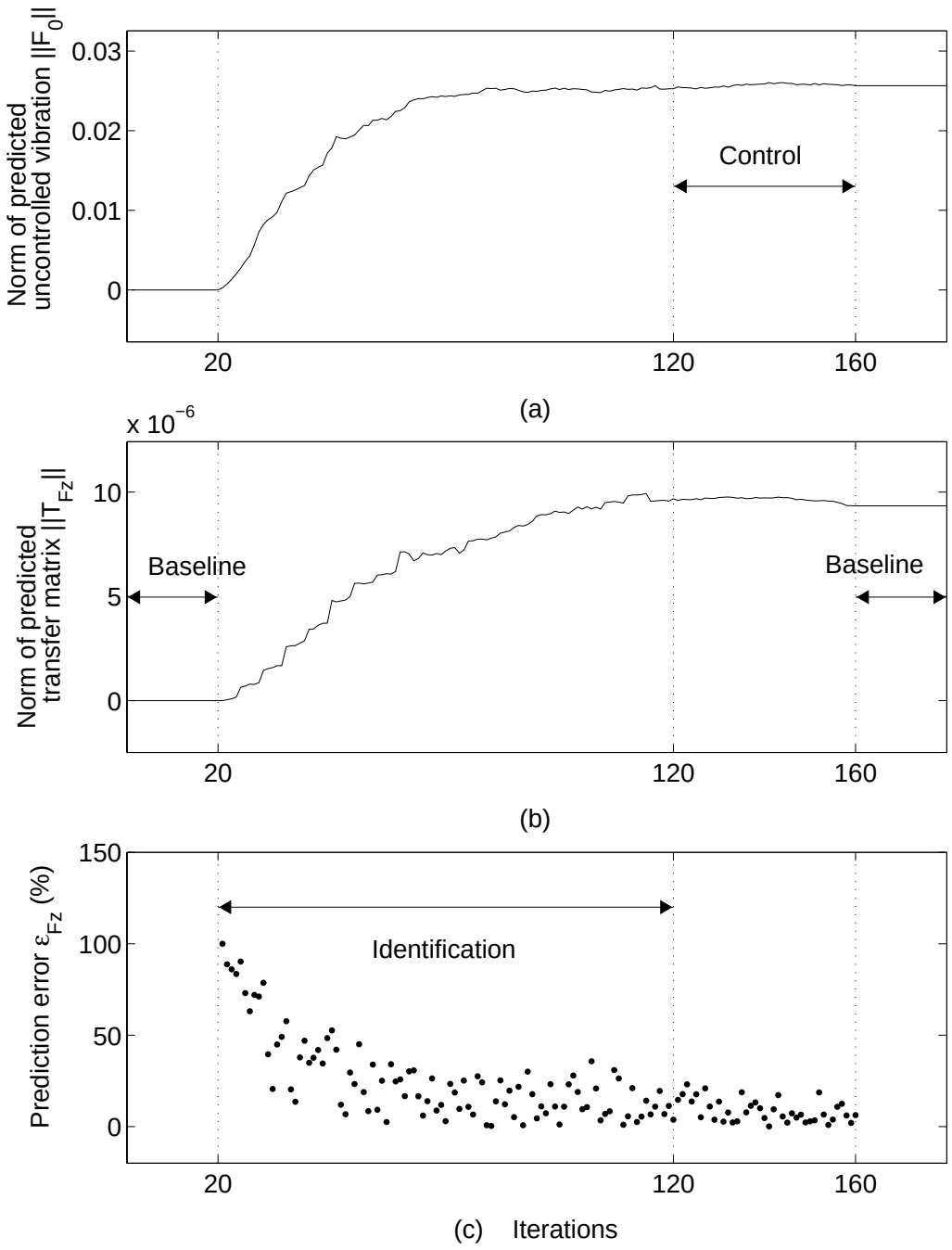

Figure 8.12: Target reduction of 1/rev hub vertical force F_z and generation of a prescribed 4/rev component using phase-shifted inputs: time history of various parameters

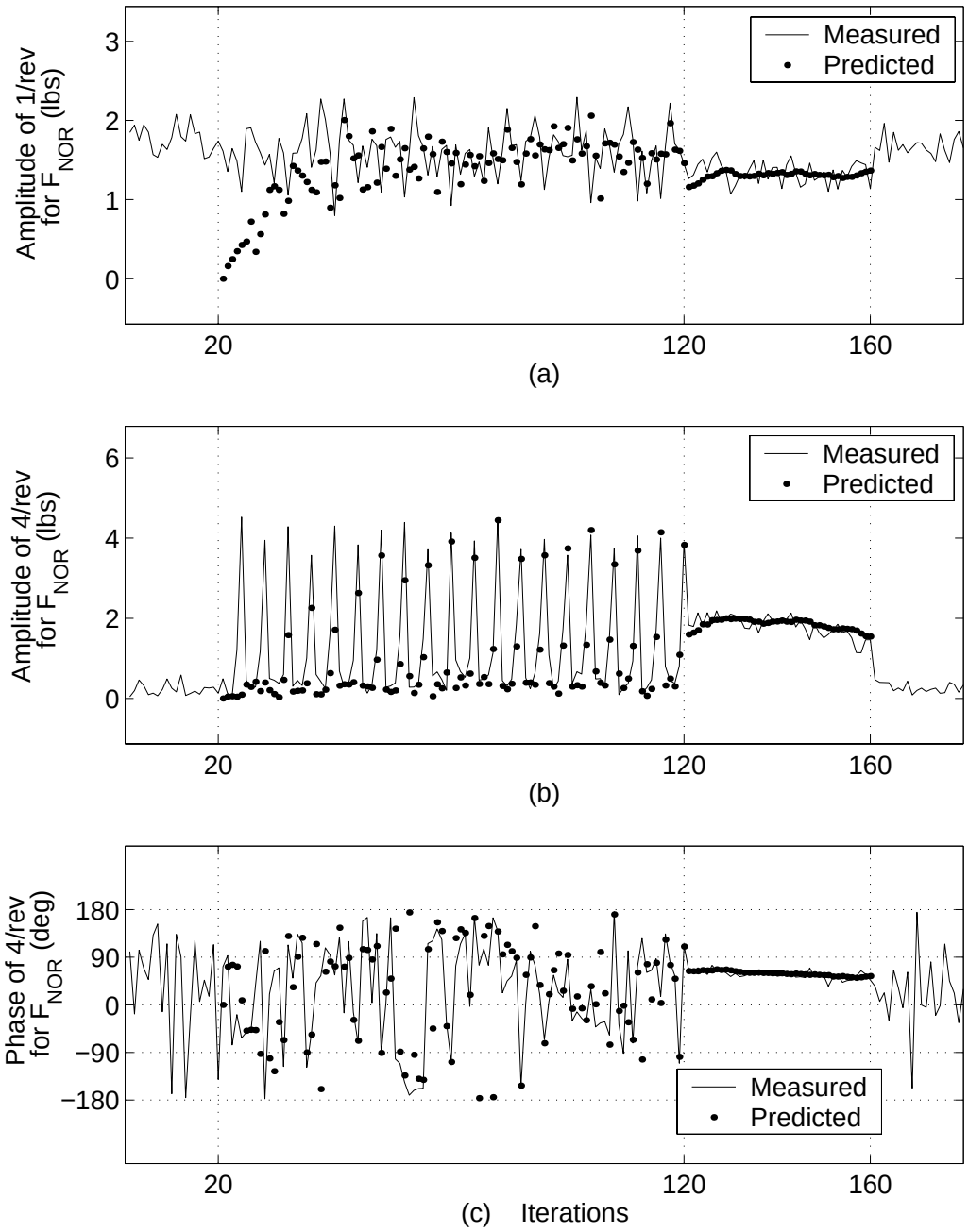

Figure 8.13: Target reduction of 1/rev hub vertical force F_z and generation of a prescribed 4/rev component using phase-shifted inputs: time history of target harmonics

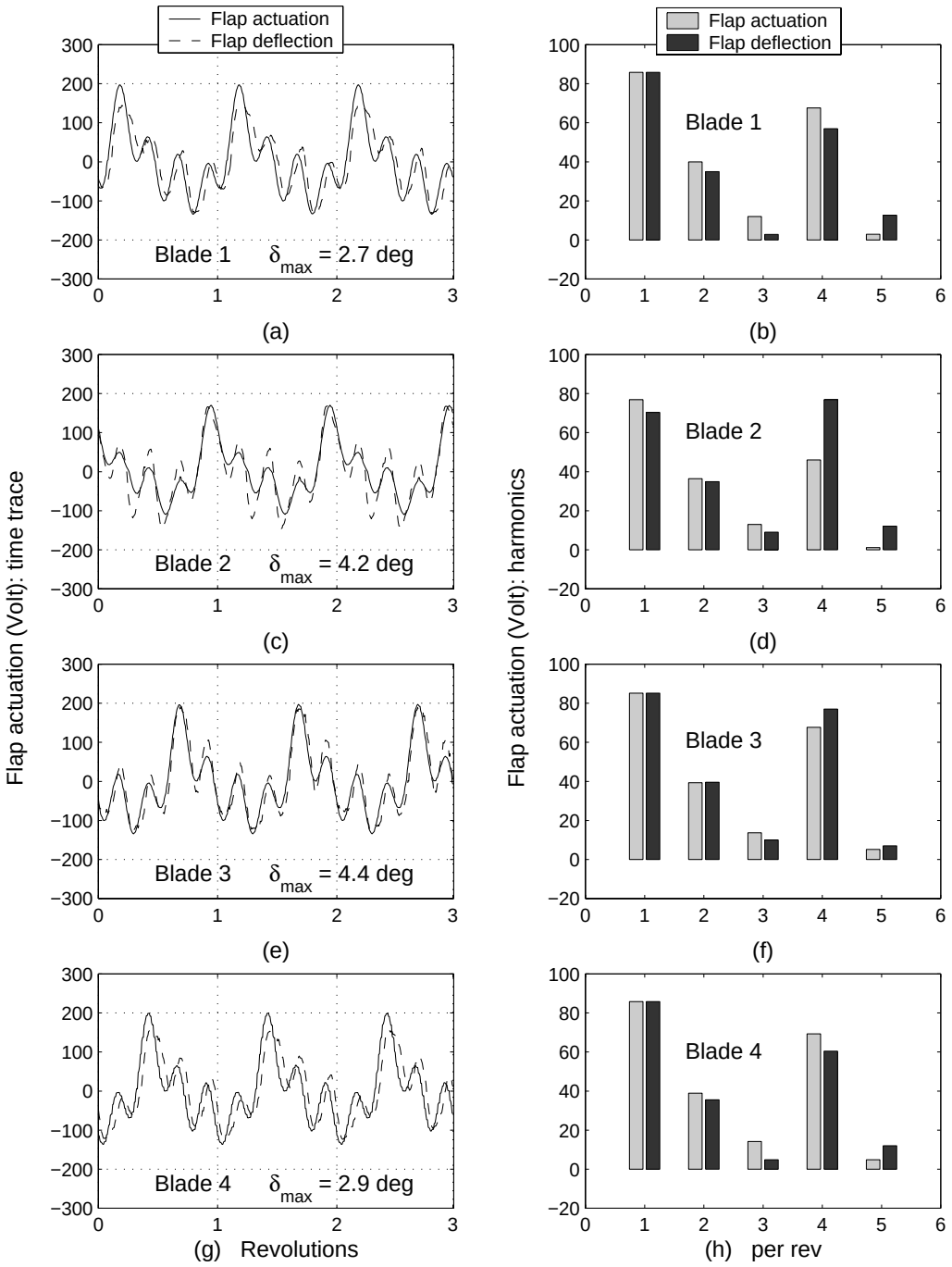

Figure 8.14: Target reduction of 1/rev hub vertical force F_z and generation of a prescribed 4/rev component using phase-shifted inputs: optimal flap inputs

Reduction of the 1/rev component

Next, the target load is set to the vertical hub load, and the control objective is reduction of the 1/rev component alone.

Figure 8.15 shows the flap actuation generated by the controller after convergence, together with the resulting flap deflections. As in the case of individual control, the main harmonic is 1/rev. However, the phase is not identical for all blades but differs by 90 degrees between adjacent blades. Therefore, we expect a smaller effect in the fixed frame than if they were phased together. This is observed in Figure 8.16(d): the 1/rev vibration is only reduced by 35%. Again, this small reduction is due to the dissimilarities between flaps and actuators in different blades. If the blades were identical, no effect at all would be observed.

Generation of a prescribed 4/rev component

Finally, the closed-loop test to generate a 4/rev component in the vertical hub load is repeated, using phase-shifted flap inputs. The target amplitude of this prescribed 4/rev component is 4.7 lbs and the target phase is 90 degrees.

Figure 8.17 shows the optimal flap inputs after controller convergence. The generated flap deflections are dominantly 4/rev for all blades. In this test, no vibration at non-kN_b/rev harmonic is targeted, therefore a control scheme using phase-shifted inputs is expected to perform well.

Indeed, Figure 8.18 shows that the control objective is achieved exactly: a 4/rev component is generated with amplitude 4.7 lbs, and phase 90 degrees. This can be compared with the performance of the control scheme using individual flap inputs (Figures 8.9 and 8.10), which could generate a 4/rev component at the correct phase (90 degrees), but at only 70% the target amplitude (3.2 lbs).

The reason the individual controller is not performing as well as the classical controller in this particular case comes from the way limits are imposed on the

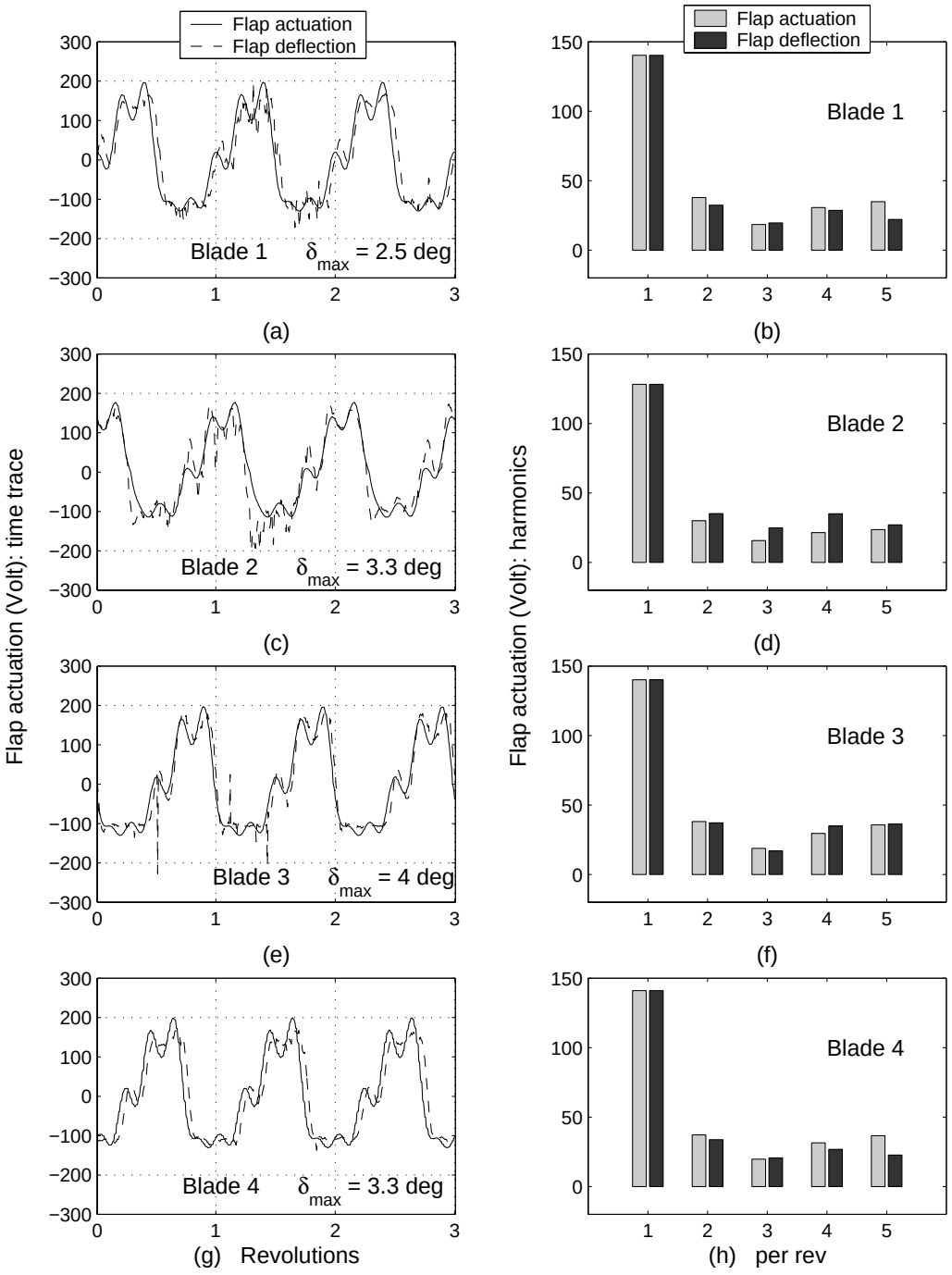

Figure 8.15: Target reduction of 1/rev hub vertical force F_z using phase-shifted inputs: optimal flap inputs

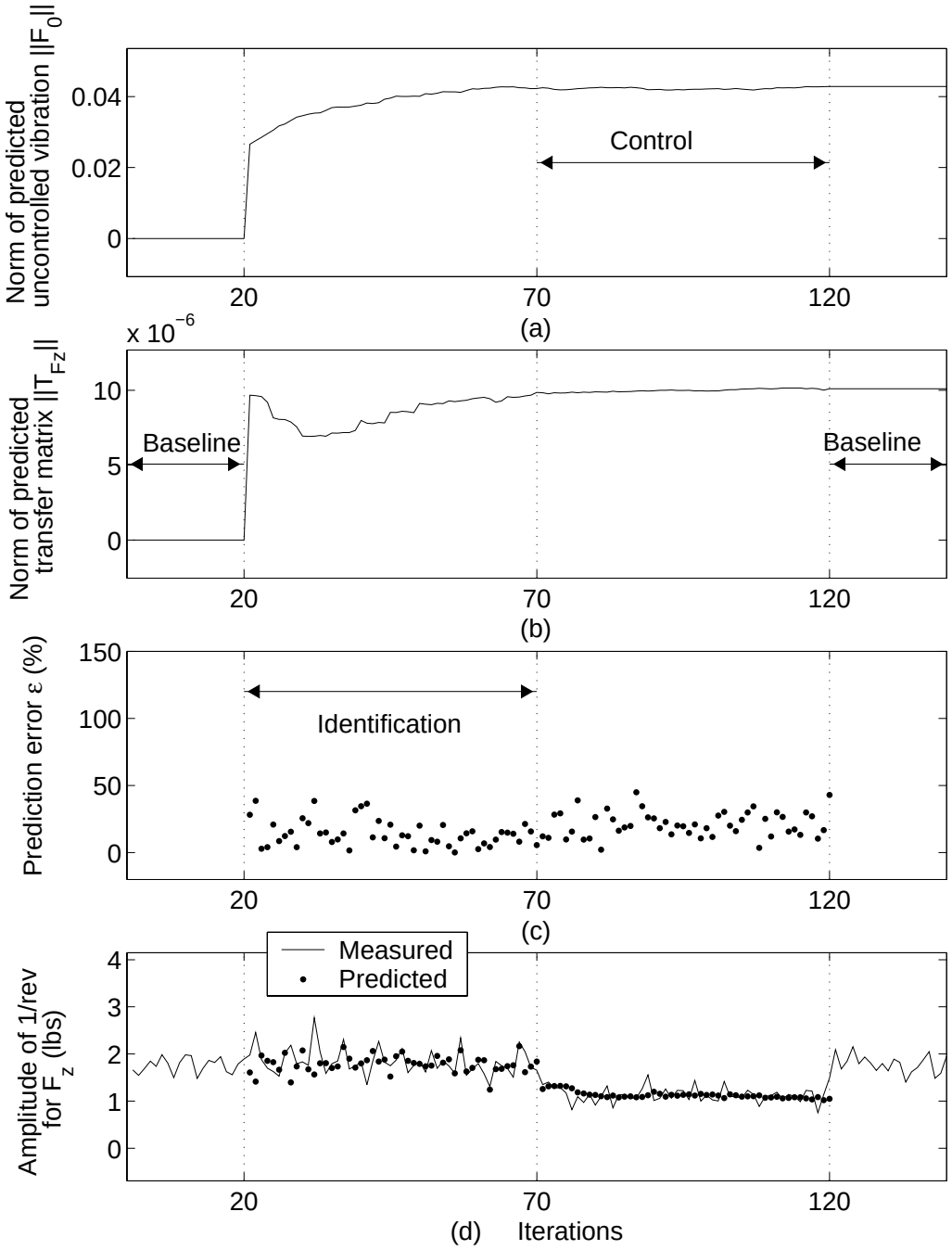

Figure 8.16: Target reduction of 1/rev hub vertical force F_z using phase-shifted inputs: time history of various parameters

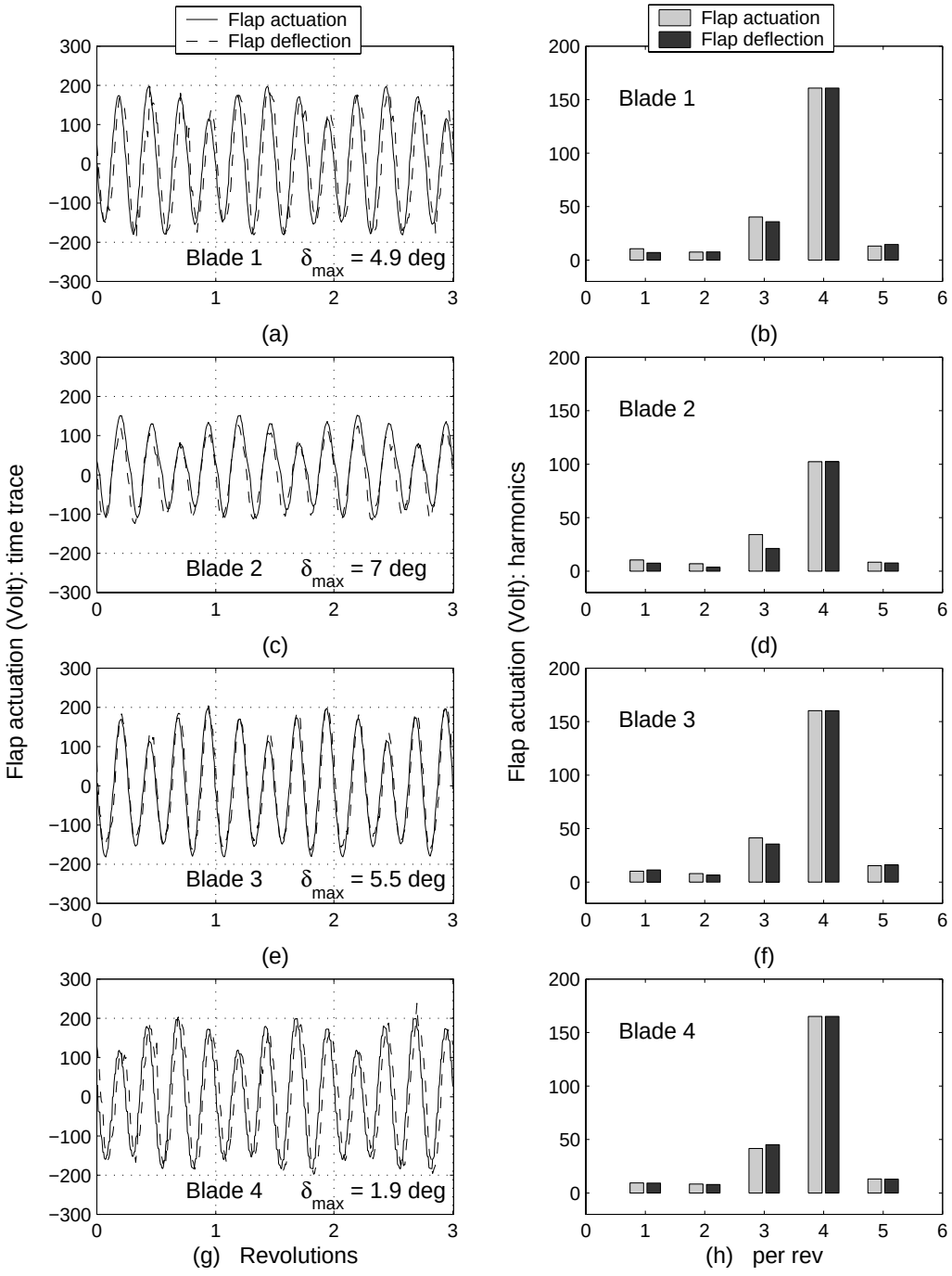

Figure 8.17: Generation of a prescribed 4/rev hub vertical force F_z component using phase-shifted inputs: optimal flap inputs

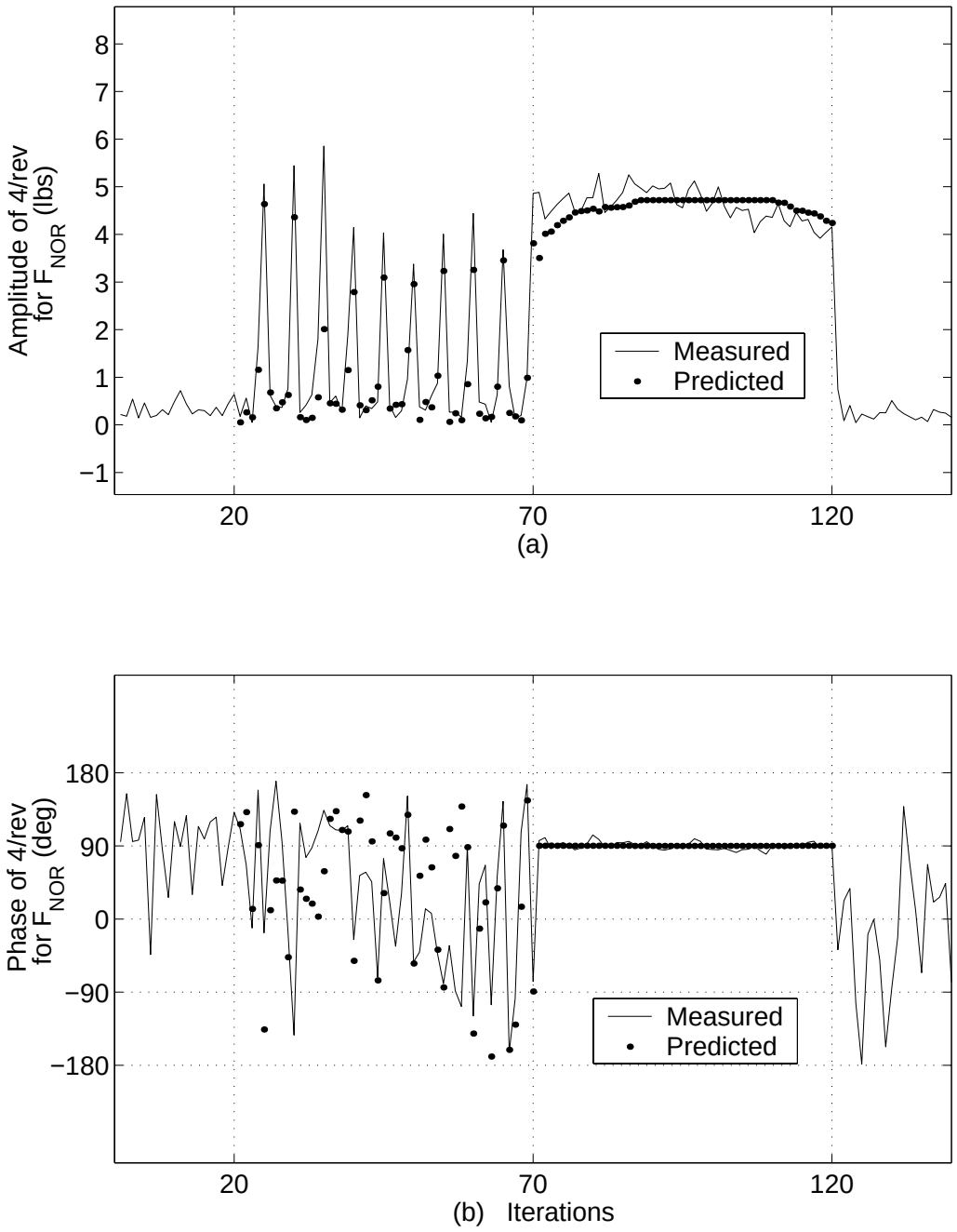

Figure 8.18: Generation of a prescribed 4/rev hub vertical force F_z component using phase-shifted inputs: time history of 4/rev amplitude and phase

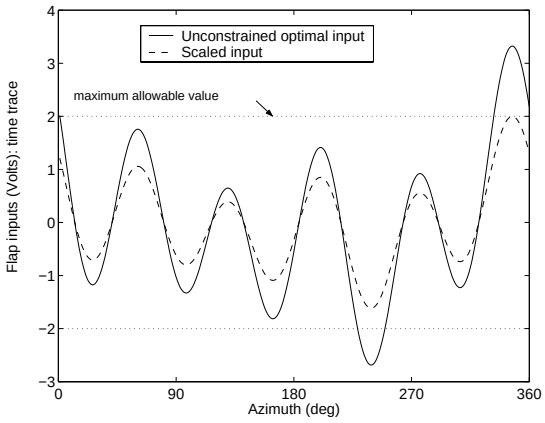

Figure 8.19: Limiting the control inputs by scaling

control inputs. In all the previous tests, flap actuation is limited by applying a scaling factor to the computed optimal actuation if it exceeds the maximum allowable value, as illustrated in Figure 8.19.

This is an unconstrained optimization solution scaled to satisfy practical limitations, and therefore may not coincide with the optimal solution of the constrained minimization problem. The scaling method modifies the unconstrained solution by applying the same scaling factor to all harmonics. In fact, the optimal solution may be to apply different scaling factors to each harmonic, so that the resulting signal in the time domain does not exceed the maximum allowable value. This minimization problem with non-linear constraints can be solved using the Matlab subroutine $FMINCON$. This allows the practical limitation to be part of the optimization process.

Figure 8.20 shows the improvement in performance when the constrained optimization problem is solved. Flap actuations computed using $FMINCON$ are shown in solid line. Flap actuation computed using a weighting function, followed by scaling are shown in dashed line. The control objective is to generate of a 4/rev vibratory load of amplitude 4.7 lbs. Figure 8.20(e) shows the predicted amplitude of the 4/rev, based on the identified transfer matrix. Using

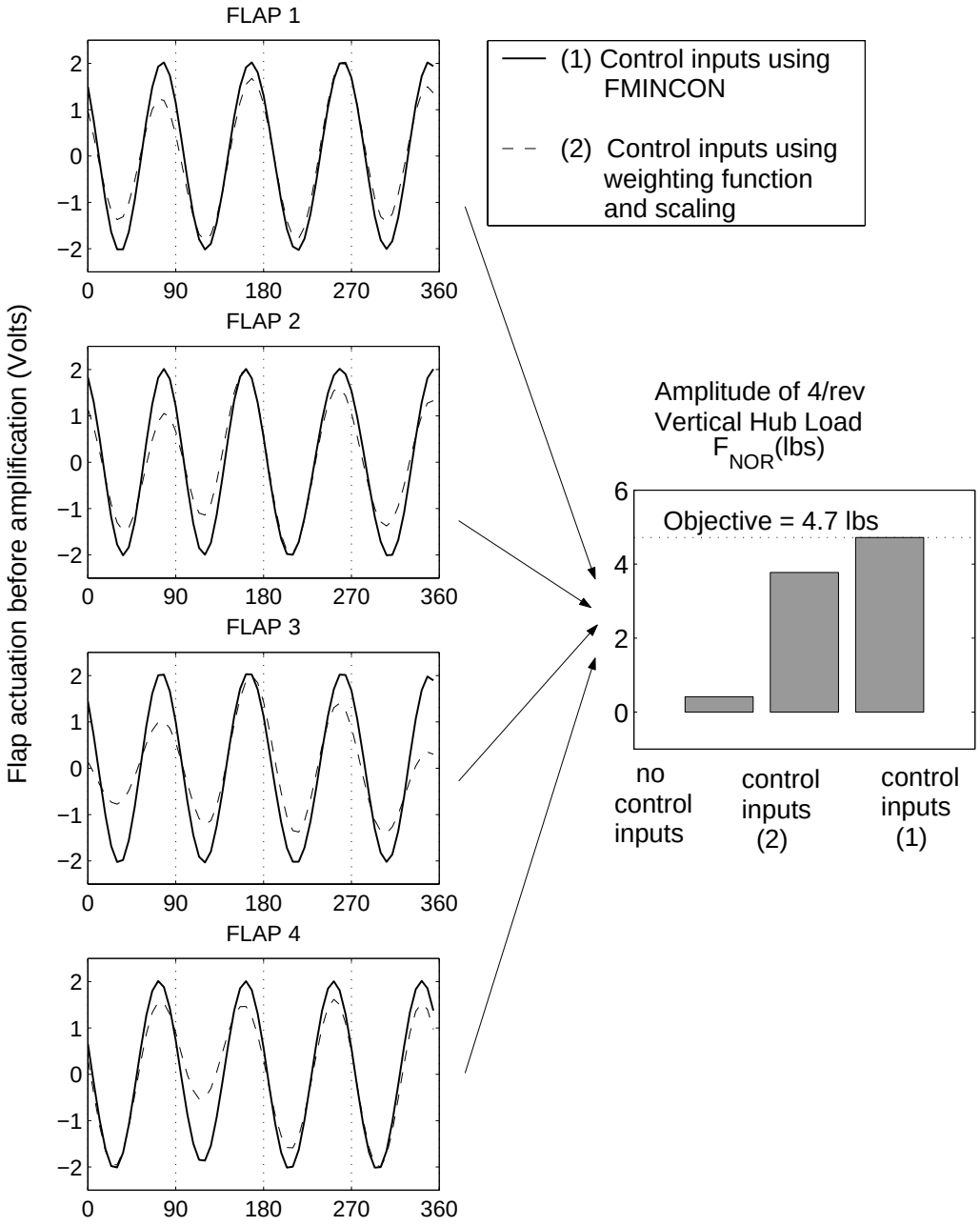

Figure 8.20: Improved performance using a different method to apply limits

constrained optimization, the control objective is achieved. The flap inputs generated are almost exclusively at a frequency of 4/rev and with almost the same phase for all blades. Note that this actuation is very similar to that generated by the classical controller in Figure 8.18. This test demonstrates that solving the constrained optimization problem accurately yields better results. However, this method is prohibitively time consuming and can not be used in real time during the test using the present computer.

8.2 Controller Tests in Wind Tunnel

This section describes closed loop tests performed in the Glenn L. Martin wind tunnel, when the control objective is the reduction of vibratory components of single or several fixed frame loads.

Unless otherwise mentioned, tests are performed at the following flight condition:

1. Rotor speed: 1500 RPM
2. Wind speed: 67 mph (advance ratio $\mu = 0.25$)
3. Collective angle: 2 degrees
4. Shaft tilt angle: 2 degrees

Cyclic angles are adjusted before each closed loop test to minimize the 1/rev blade root bending moments in the rotating frame and subsequently left unchanged during the test. For all tests in this section, the flap actuation is maintained within the $\pm 200 Volts$ limits by using truncated inputs instead of scaled inputs, as illustrated in Figure 8.21.

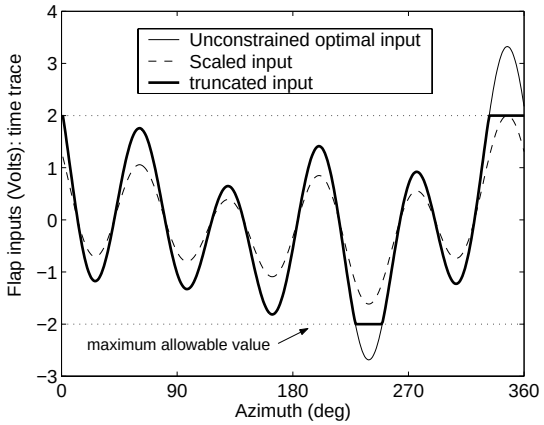

Figure 8.21: Applying limits using scaled inputs or truncated inputs

8.2.1 Test 1: reduction of normal force vibration at 1/rev

Figures 8.22 to 8.24 describe a closed loop test when the control objective is the reduction of the 1/rev component of the vertical hub load. Figure 8.22 shows the magnitude of vibratory hub loads before and after control. At this flight condition, the vertical hub load before control consists of a dominant 1/rev harmonic component (about 10 lbs), and smaller 3/rev (about 5 lbs) and 4/rev (about 1.5 lbs) components. After control, the 1/rev component is reduced by about 50%. However, this reduction in vertical vibration is accompanied by an increase in 1/rev vibration for the pitching moment (by about 40%). Although not included in the cost function, the 3/rev component of the normal force is also reduced by 25%. Other harmonics of the vertical hub force have increased.

Figures 8.23(a) to (c) show the time history of identified parameters, and Figure 8.23(d) shows the time history of the objective function during the test. Control inputs after convergence are shown in Figure 8.24. Flap actuation signals are truncated for all blades. All harmonics (from 1/rev to 5/rev) appear to be important, with a dominant 4/rev component for blades 2 and 3.

For this test, the actuation signal is truncated whenever the controller gener-

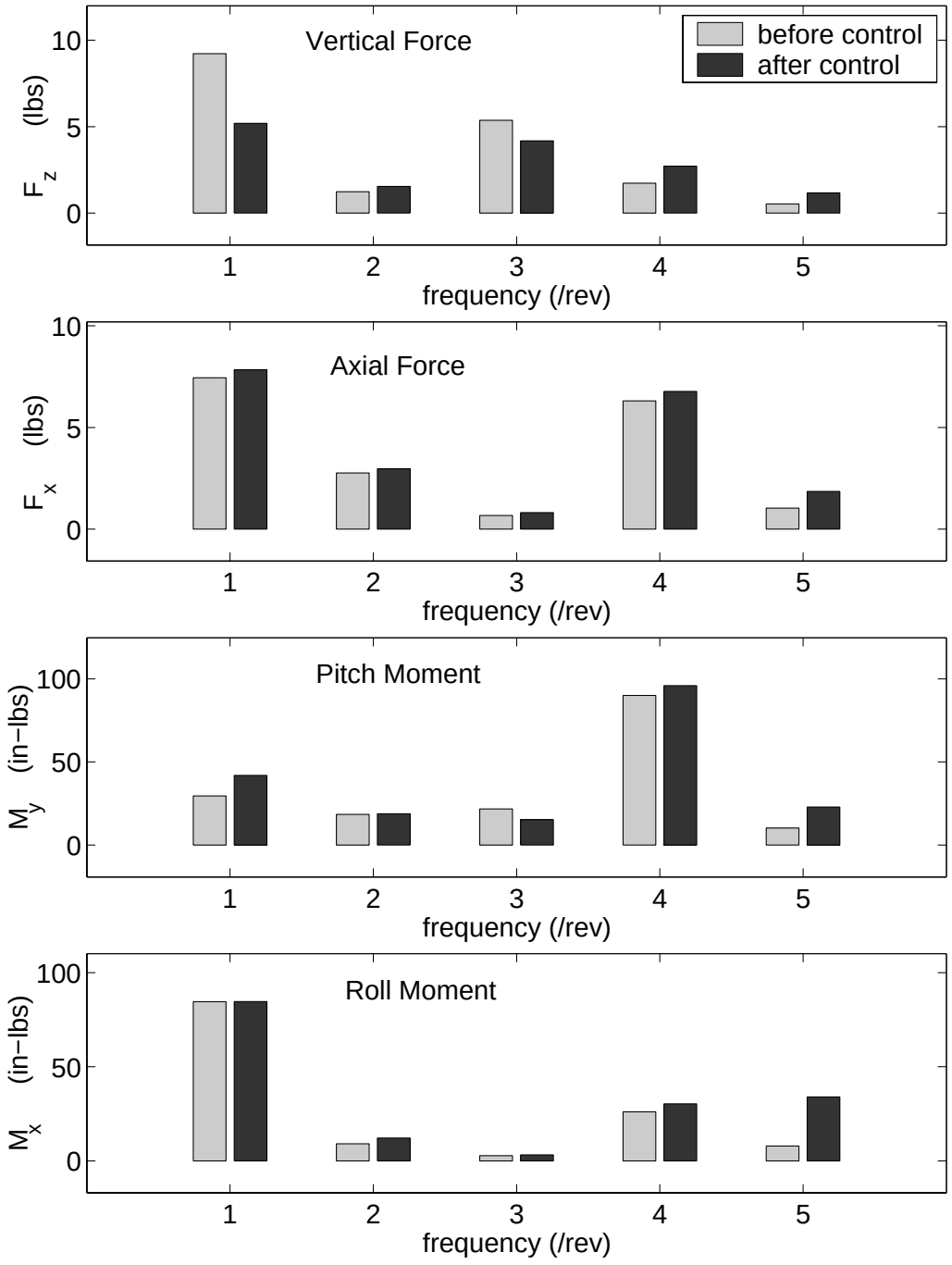

Figure 8.22: Target reduction of 1/rev hub vertical force F_z: effect on hub loads

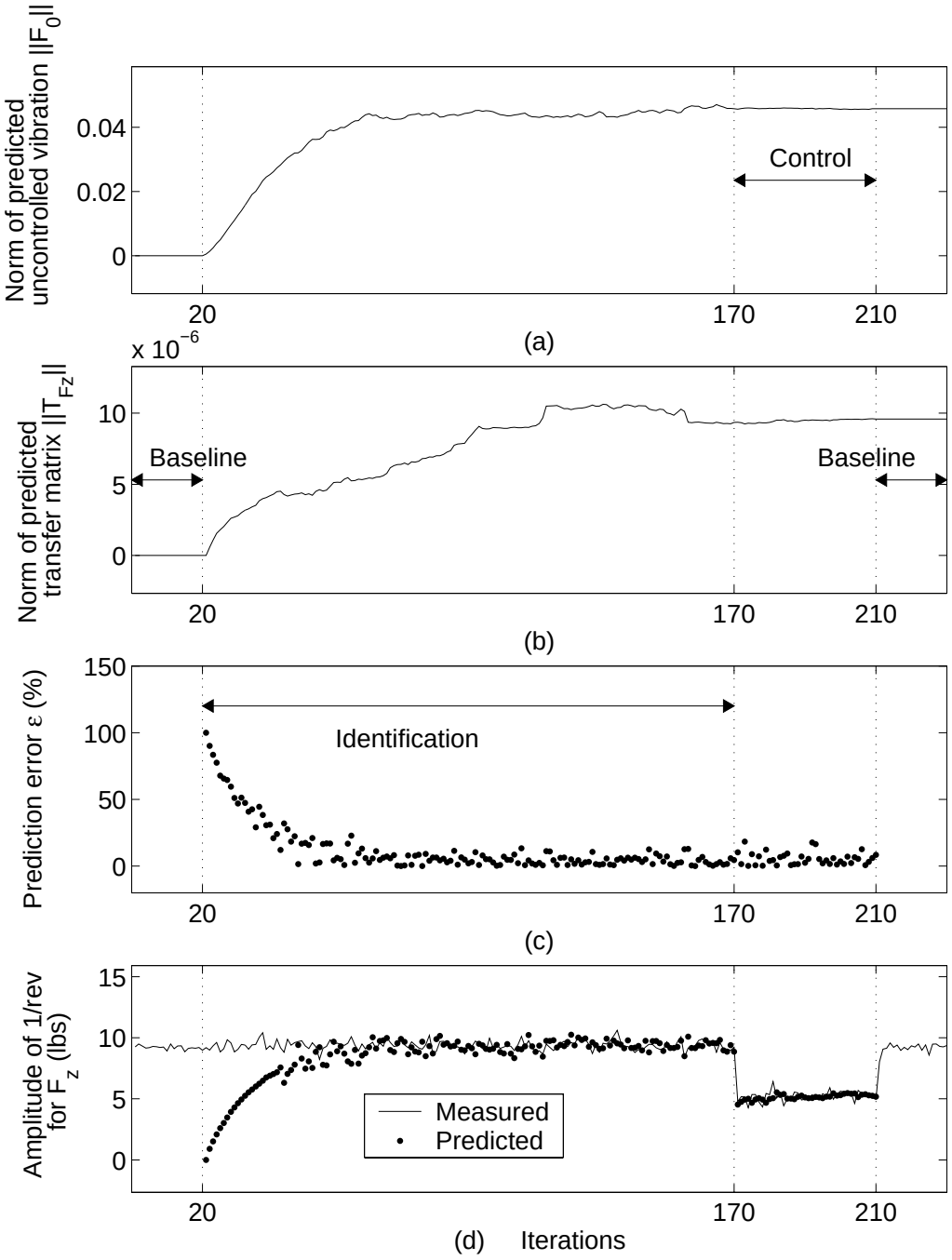

Figure 8.23: Target reduction of 1/rev hub vertical force F_z: time history of various parameters

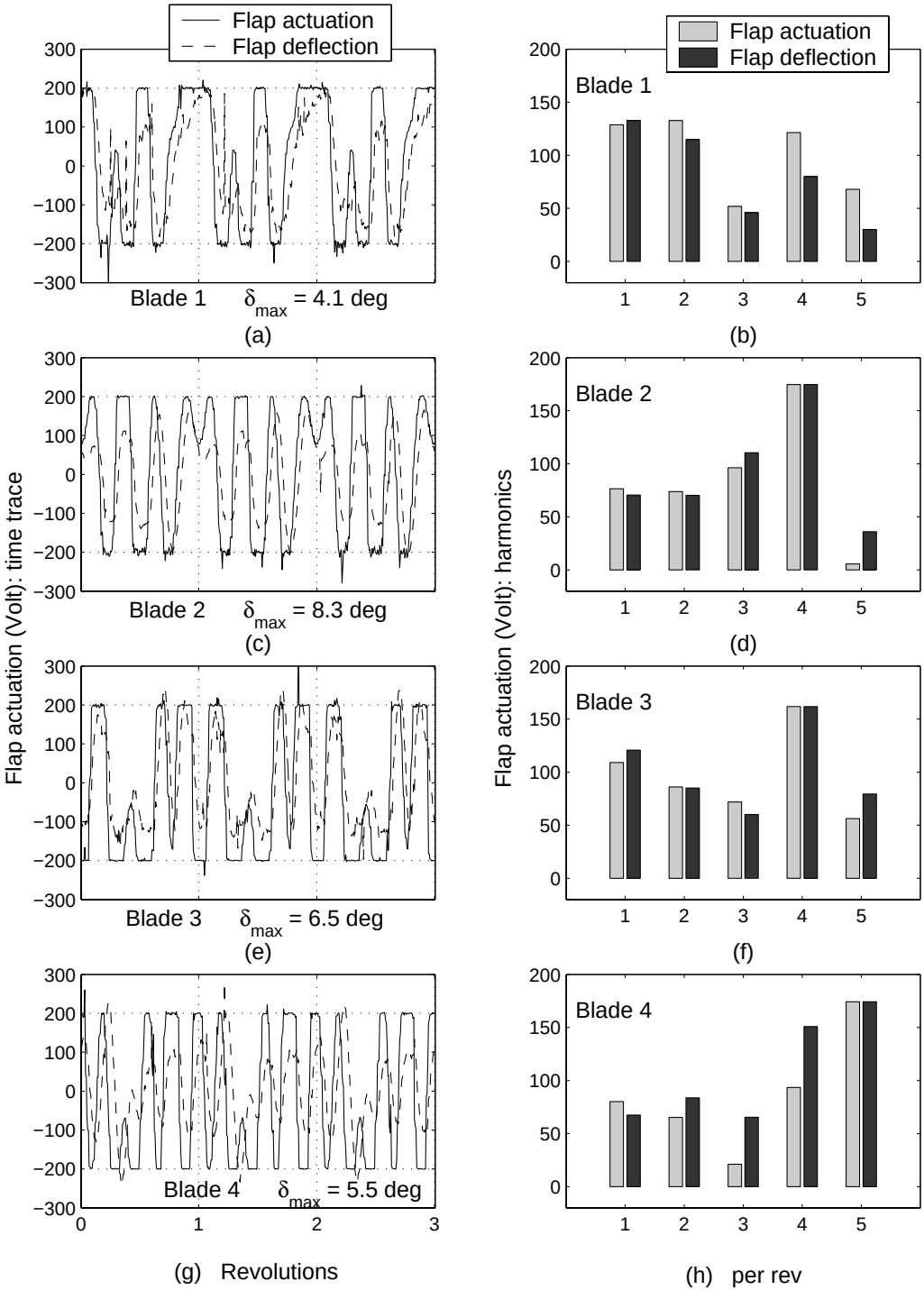

Figure 8.24: Target reduction of 1/rev hub vertical force F_z: optimal flap inputs

ates a signal exceeding the maximum allowable value ($\pm 200 Volts$). Figures 8.25 and 8.26 compare the predicted controller performance using different methods to apply limits: using scaled inputs, using truncated inputs, and solving the constrained minimization problem using the Matlab function $FMINCON$, based on the Sequential Quadratic Programming (SQP) method. Figure 8.25 shows the vibration levels before control, and predicted vibration levels after control. Predictions are obtained using the linear model identified during the test. Using this model, vibration reduction improves when using truncated inputs compared to using scaled inputs, and further improves when solving the problem using the SQP method. Note that predicted vibration using truncated inputs is very close to measured values, but does not match exactly with test data. This is because the actual flap actuation is truncated, and therefore contains harmonics higher than 5/rev, while the model used for prediction assumes this input consists of harmonics from 1 to 5/rev. Figure 8.26 compares flap actuation signals obtained with the three methods. The signals are very similar in phase, but significant differences in amplitude are apparent. Note that the optimal inputs generated using Matlab appear close to a truncated signal (signal becomes flat near ± 2 V limits).

8.2.2 Test 2: reduction of pitching moment vibration at 4/rev

Figures 8.27 to 8.29 describe a closed loop test when the control objective is the reduction of the 4/rev component of the fixed frame pitching moment. The pitching moment vibration at the rotor hub can be a large contributor to vibration at the pilot seat station in the fuselage [142].

Figure 8.27 shows the harmonics of hub loads before and after control. After control, the 4/rev component of the hub pitching moment is reduced by 62%.

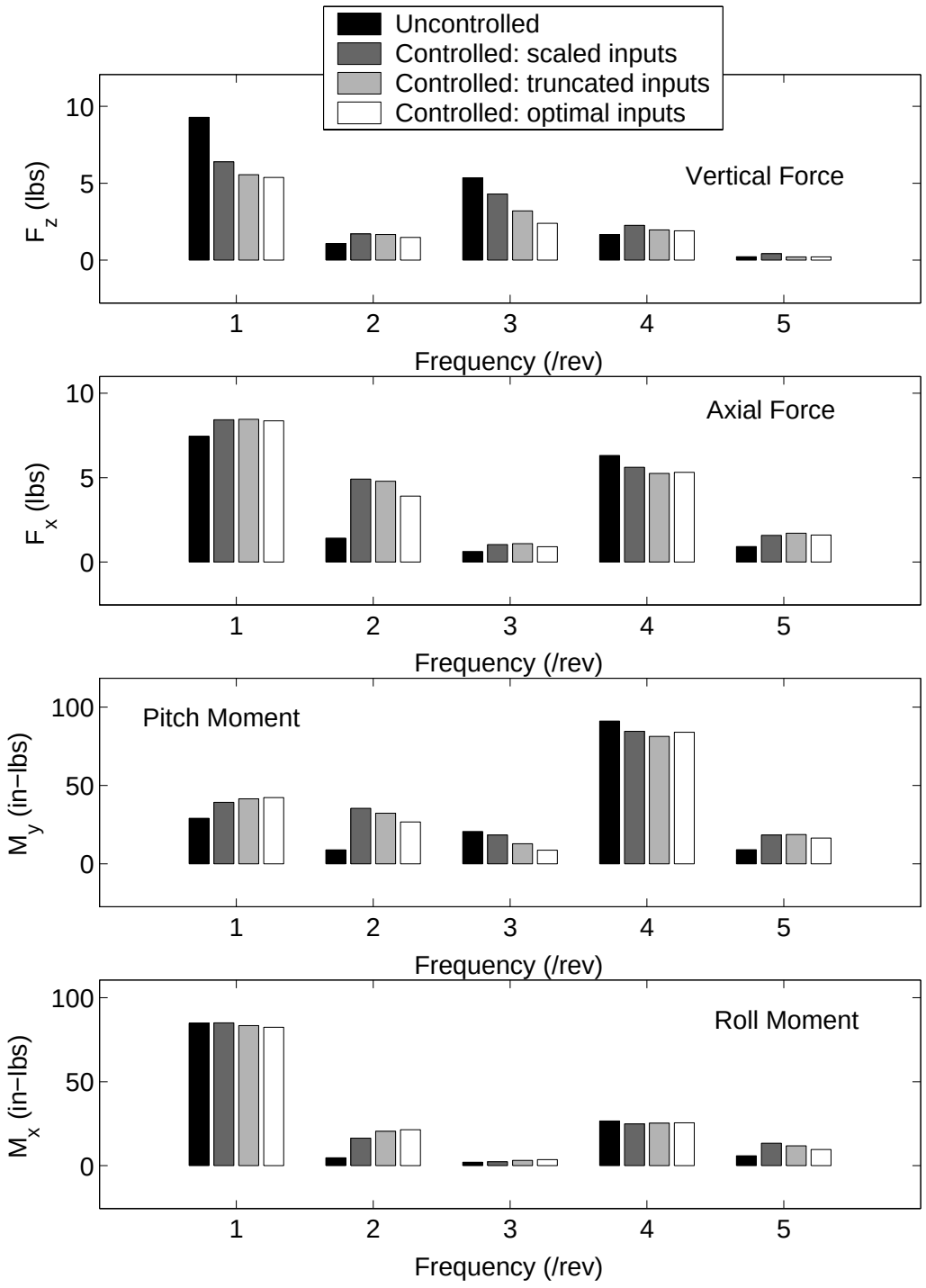

Figure 8.25: Predicted reduction of 1/rev hub vertical force F_z using different limiting methods

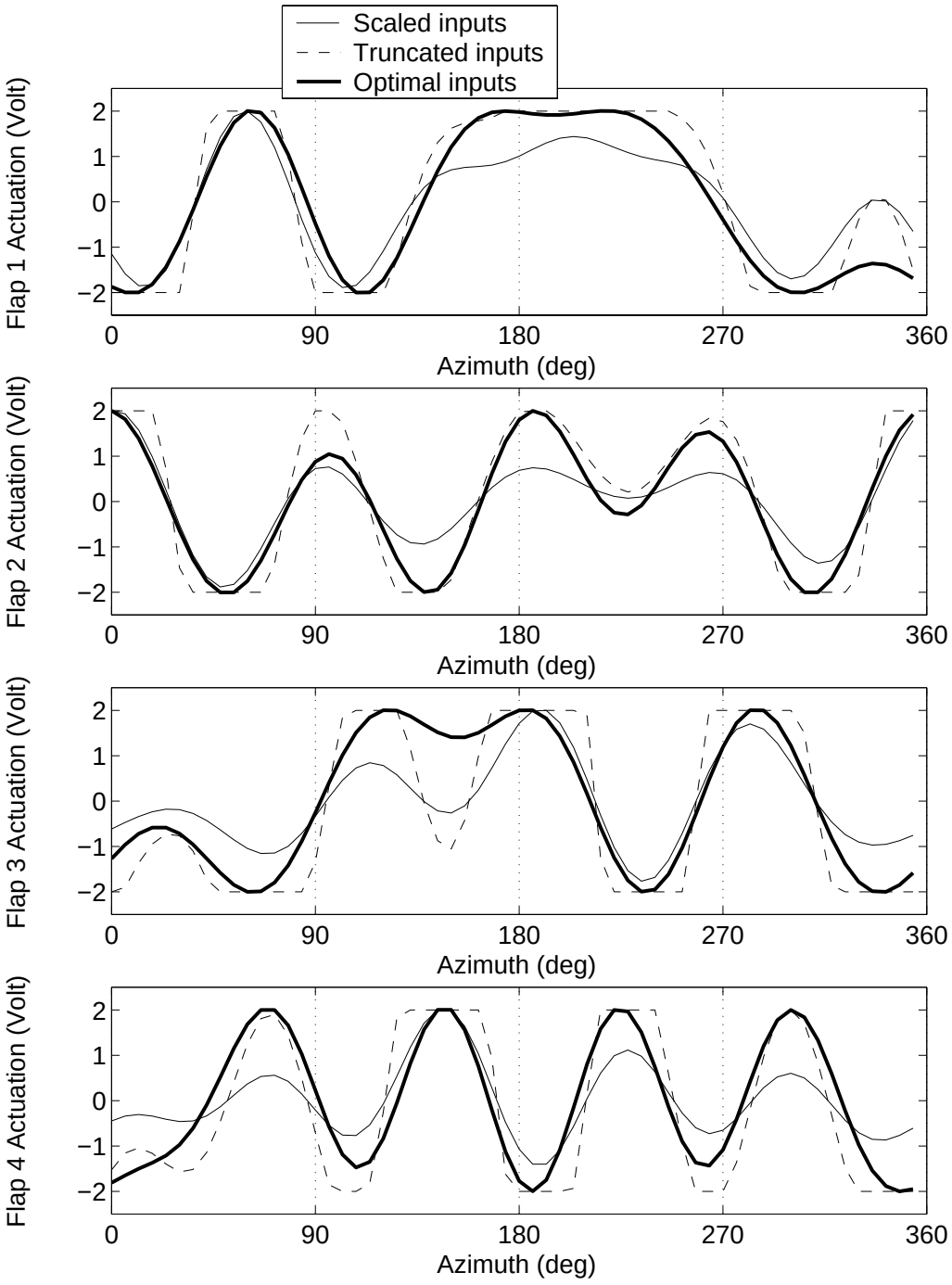

Figure 8.26: Predicted reduction of 1/rev hub vertical force F_z using different limiting methods: optimal flap inputs

Other harmonics of M_y as well as other hub loads are also affected by the control inputs. The 4/rev component of the axial vibration is reduced (by about 40%), however the 4/rev component of the vertical force is increased by a factor of three, from 1.5 lbs to 4.5 lbs. Figure 8.28 shows the evolution of some identification parameters during the test as well as the time history of the pitching moment 4/rev component. Optimal control inputs generated are shown in Figure 8.29. Actuation for flap 2, 3, and 4 have a dominant 4/rev component, with similar phase.

Figures 8.30 and 8.31 compare the predicted controller performance using different methods to apply limits. Figure 8.30 shows the vibration levels before control, and predicted vibration levels after control. Similar to the previous study for vertical vibration, improvements in 4/rev hub pitching moment vibration reduction are predicted using the SQP method. The 4/rev component is reduced by 90% compared to the measured 62%. However, a large increase in the 4/rev normal force is also predicted. Figure 8.31 compares flap actuation signals obtained with the three methods. It is interesting to observe that the optimal inputs generated by the SQP method, which yields the best results, are very close to phase shifted 4/rev signals, except for blade 1.

8.2.3 Test 3: reduction of pitching moment vibration at 1/rev and 4/rev

Figures 8.32 to 8.35 describe a closed loop test when the control objective is the simultaneous reduction of the 4/rev and 1/rev components of the fixed frame pitching moment. Figure 8.32 shows vibration harmonics before and after control for several hub loads. The 1/rev component is reduced by 38% and the 4/rev component by 44%. Some reduction is also observed in the 4/rev component of the axial hub load (29%). However, this is accompanied by an

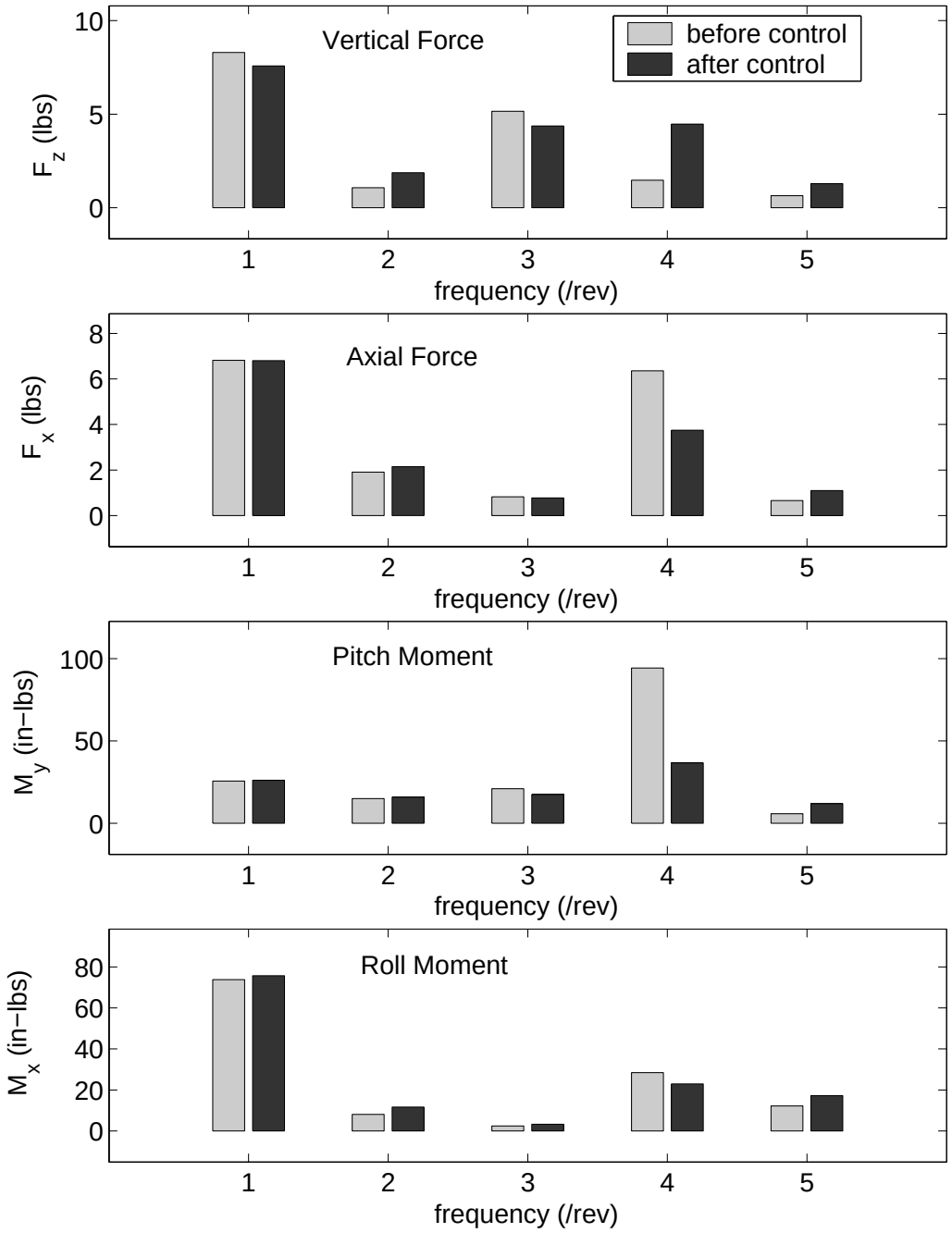

Figure 8.27: Target reduction of 4/rev hub pitching moment M_y: effect on hub loads

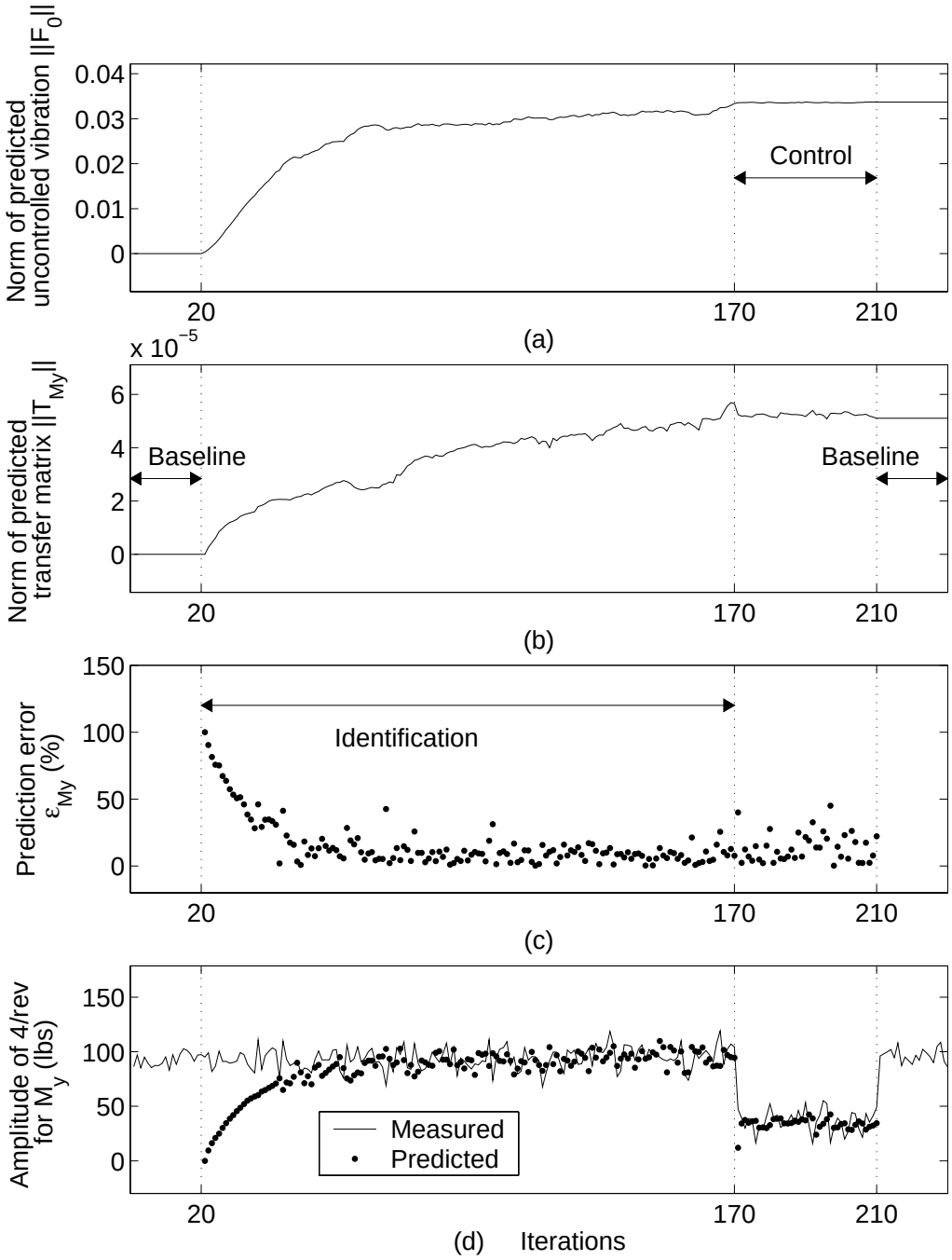

Figure 8.28: Target reduction of 4/rev hub pitching moment M_y: time history of various parameters

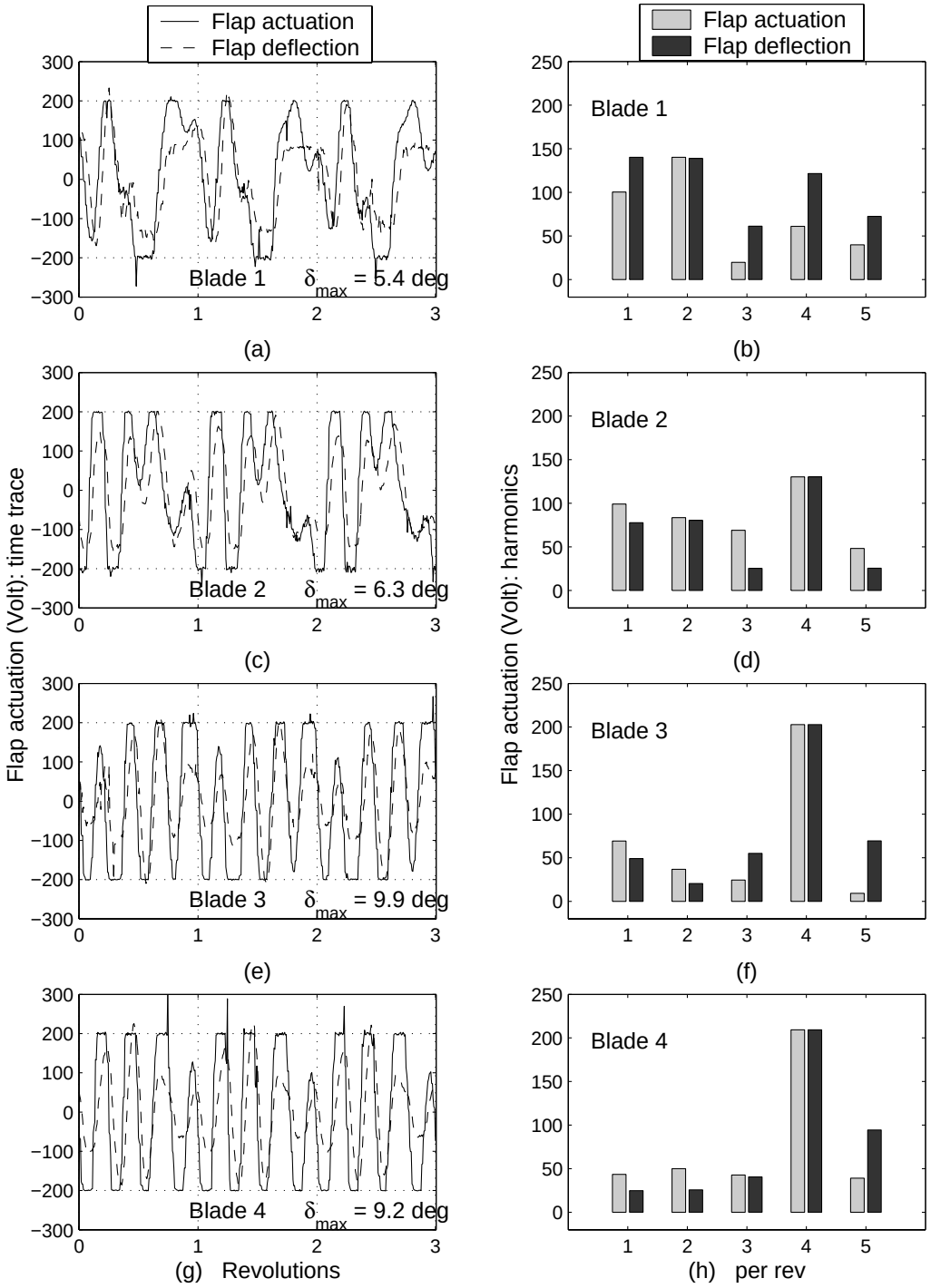

Figure 8.29: Target reduction of 4/rev hub pitching moment M_y: optimal flap inputs

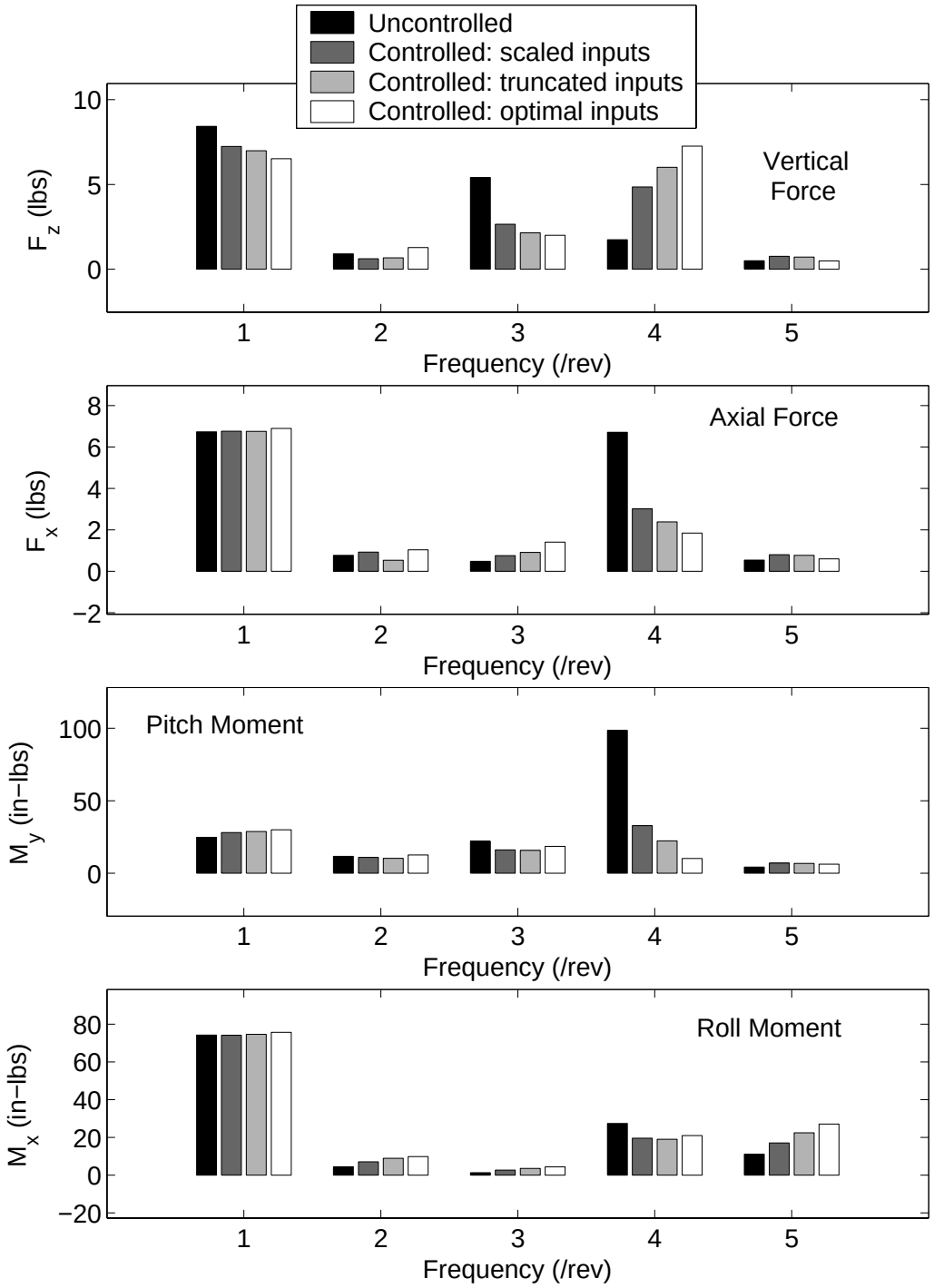

Figure 8.30: Predicted reduction of 4/rev hub pitching moment M_y using different limiting methods

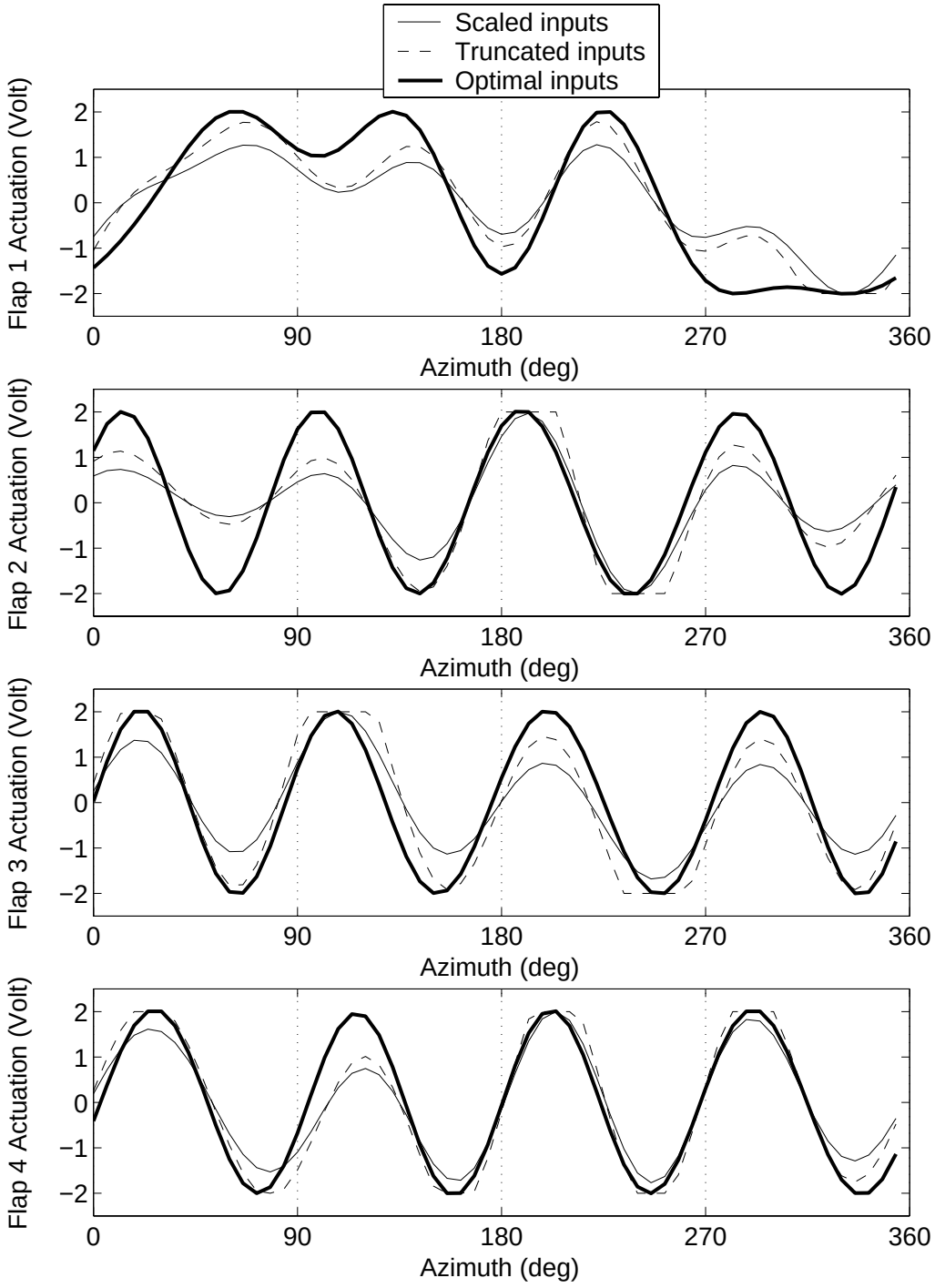

Figure 8.31: Predicted reduction of 4/rev hub pitching moment M_y using different limiting methods: optimal flap inputs

increase in vibratory components of the vertical hub load: the 1/rev increases by 18% and the 4/rev is more than doubled. Figure 8.33 shows the time history of several identified parameters, prediction error, as well as the time history of the 1/rev and 4/rev component for the target hub load. Note that just at the beginning of the control phase, predicted vibration reduction is very good: over 80% for both 1/rev and 4/rev components. However, actual vibration reduction is only about 20% and 40%, respectively. This is because prediction is based on filtered harmonic components (1 to 5/rev) of the truncated signal, and not the truncated signal itself. As illustrated in Figure 8.34, the peak-to-peak amplitude of the filtered signal can be much larger than that of the truncated signal, hence the over-prediction of vibration reduction. The resulting decrease in the transfer matrix norm can be observed in figure 8.33(b) at iteration 170. The norm of identified T_{PIT} increases during control and correspondingly the 4/rev reduction improves: at the end of the control phase (after 50 iterations), the 4/rev is reduced by 55%. The optimal flap inputs generated by the controller are shown in Figure 8.35. Deflections for flaps 2 and 3 are dominated by a large 4/rev component at the same phase. Deflections for flap 1 is largely at the 1/rev frequency, and for flap 4 at the 2/rev frequency.

Figures 8.36 and 8.37 compare the predicted controller performance using different methods to apply limits. Figure 8.36 shows the vibration levels before control, and predicted vibration levels after control. Like for the previous two tests, using the SQP method results in improved vibration reduction: the 4/rev component is reduced by 97% compared to the measured 44%, and the 1/rev component is reduced by 71% compared to the measured 38%. Figure 8.37 compares flap actuation signals obtained with the three methods.

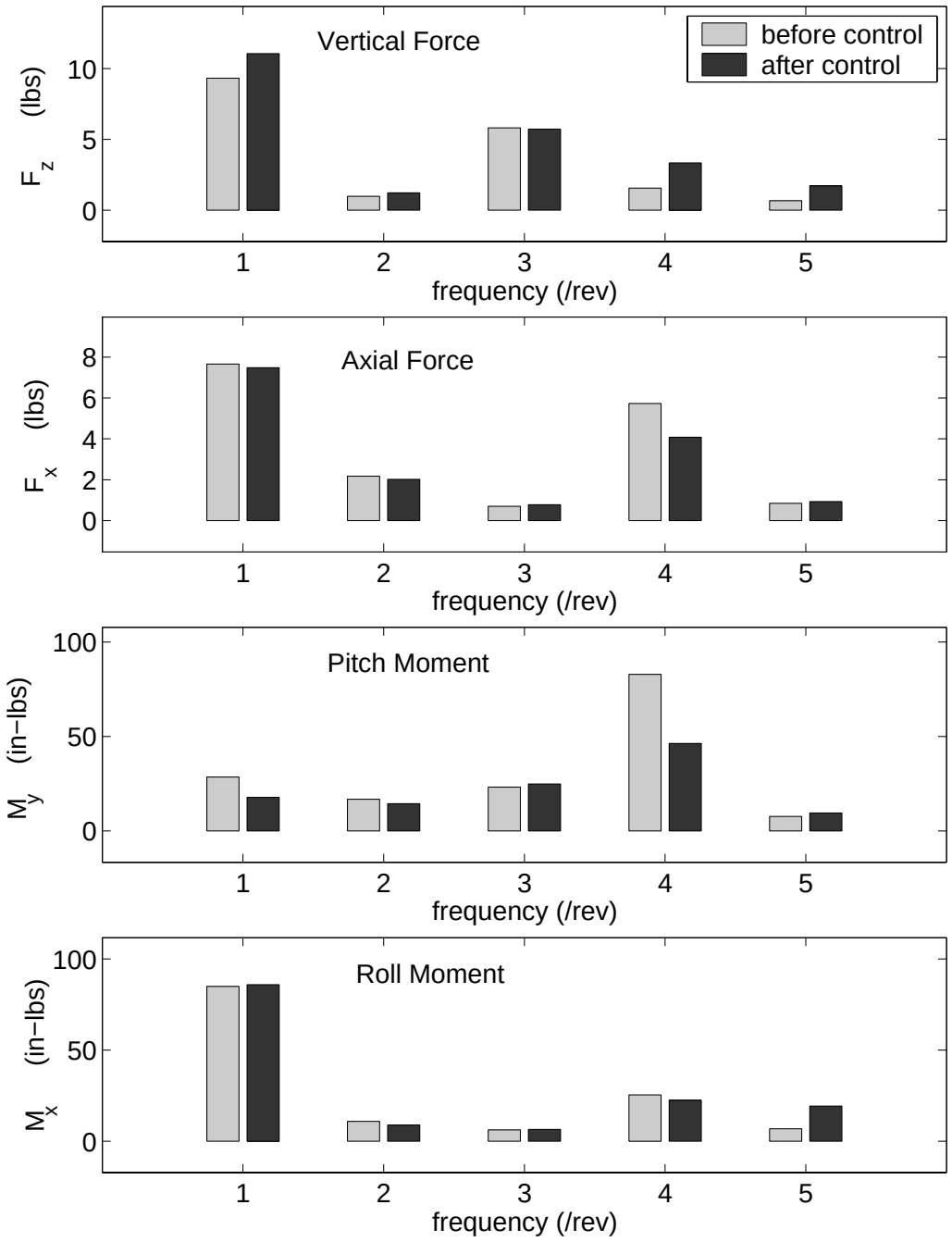

Figure 8.32: Target reduction of 1/rev and 4/rev hub pitching moment M_y: effect on hub loads

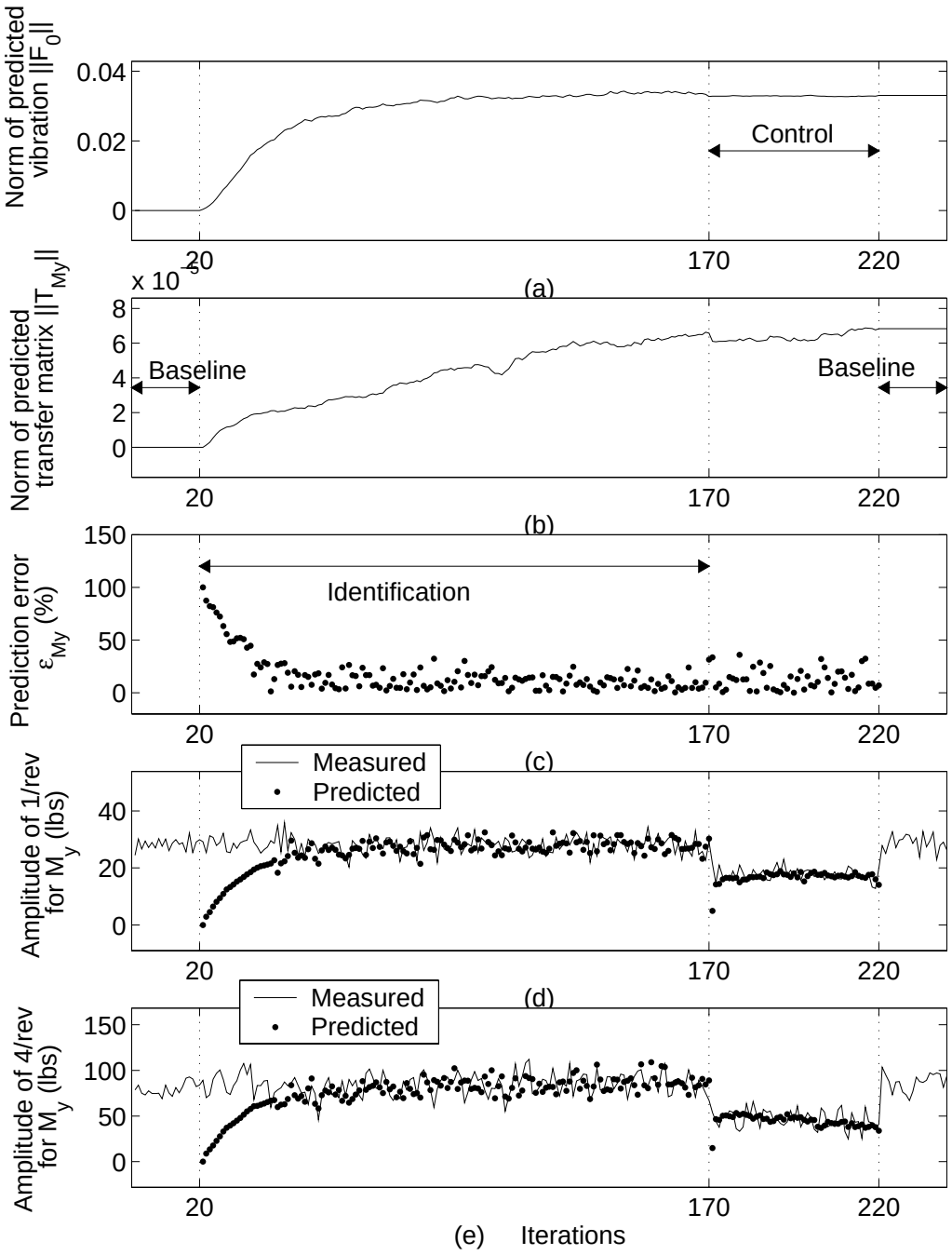

Figure 8.33: Target reduction of 1/rev and 4/rev hub pitching moment M_y: time history of various parameters

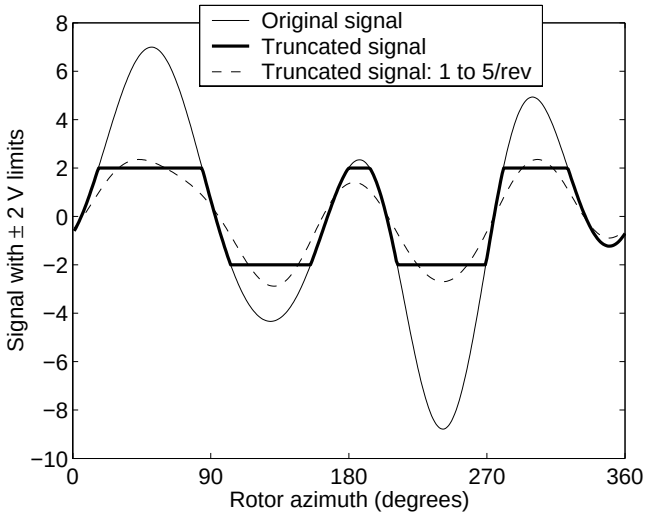

Figure 8.34: Problem with filtering a truncated signal

8.2.4 Test 4: reduction of pitching moment vibration at 4/rev for $\theta_0 = 6^\circ$

Figures 8.38 and 8.39 show results when the control objective is to reduce the 4/rev hub pitching moment. For this test, the collective control angle was increased from 2° to 6°. At this new flight condition, the uncontrolled vibration levels are increased in all loads, as can be seen in Figure 8.38. In particular, the 4/rev component of the hub pitching moment is increased from about $80\,in-lbs$ at 2° collective to more than $450\,in-lbs$ at 6° collective. For the normal force, the 4/rev harmonic component is increased from about 2lbs to about 10 lbs. Both 1/rev and 3/rev components are also slightly increased compared to the lower collective case.

With closed loop control, the hub pitching moment 4/rev component is reduced by about 20% at the beginning of the control phase, and about 25% at the end of the control phase. This is accompanied by changes in other loads, in particular for the normal force: at the start of the control phase, all three

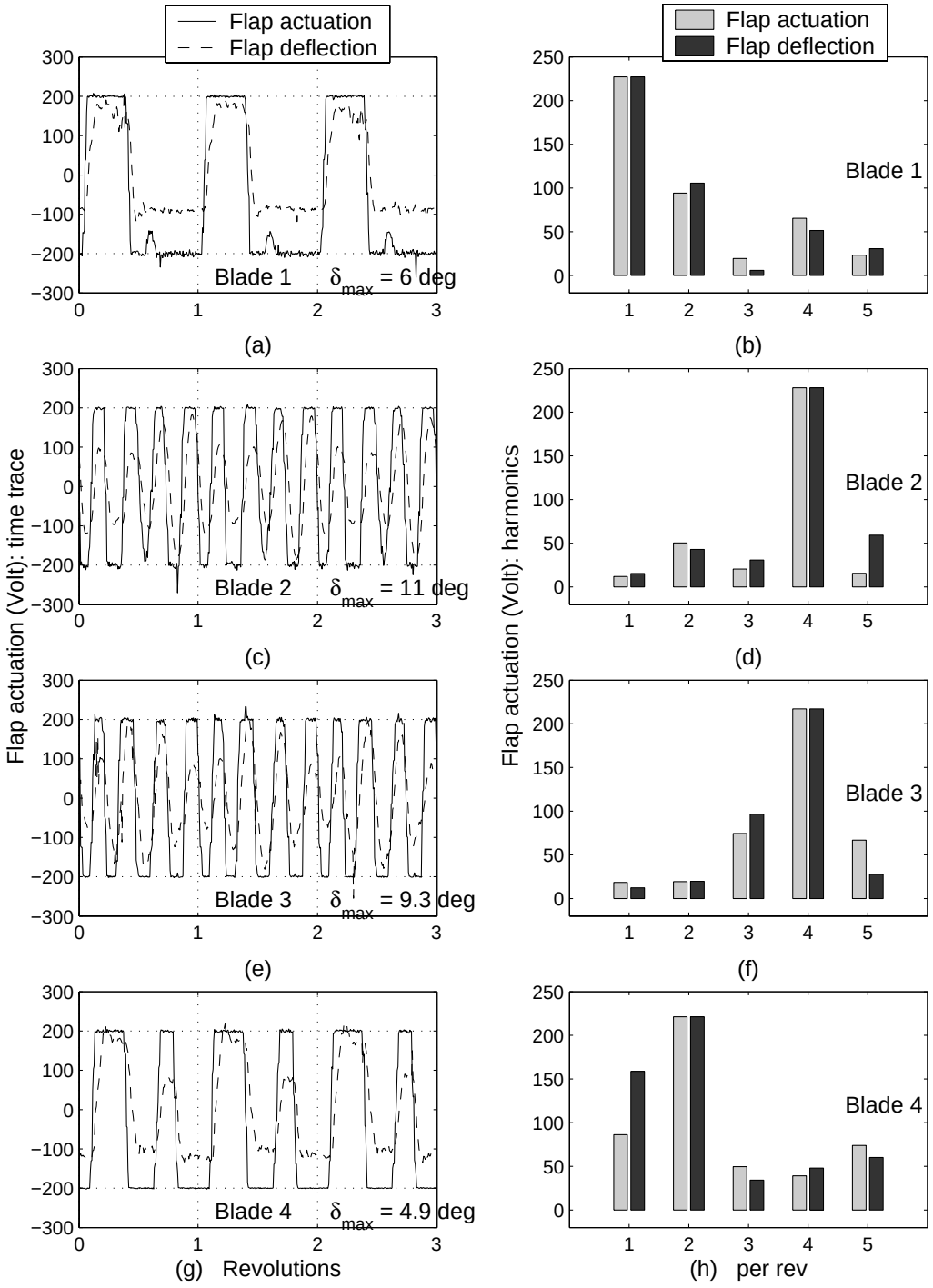

Figure 8.35: Target reduction of 1/rev and 4/rev hub pitching moment M_y: optimal flap inputs

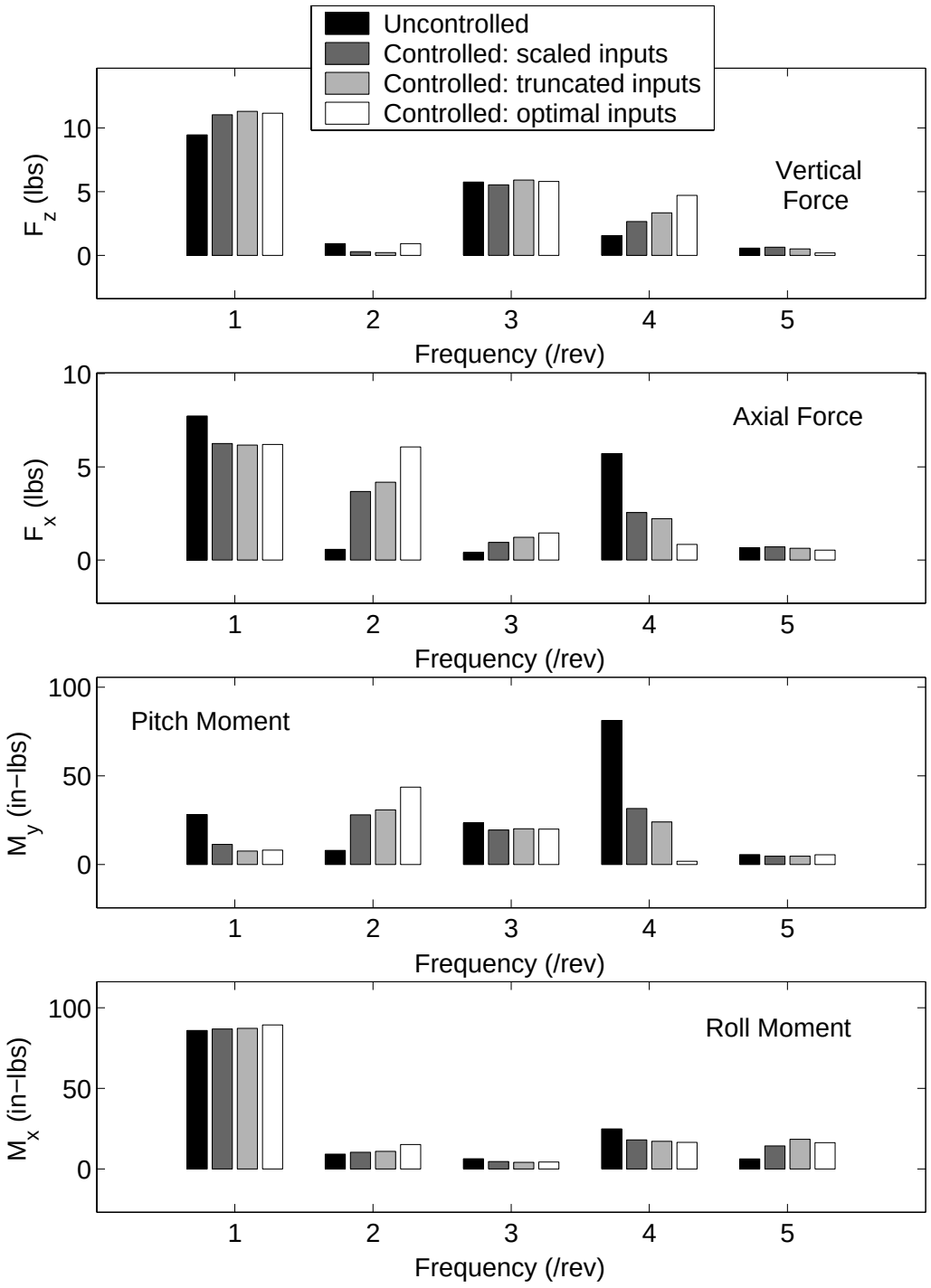

Figure 8.36: Predicted reduction of 1/rev and 4/rev hub pitching moment M_y using different limiting methods

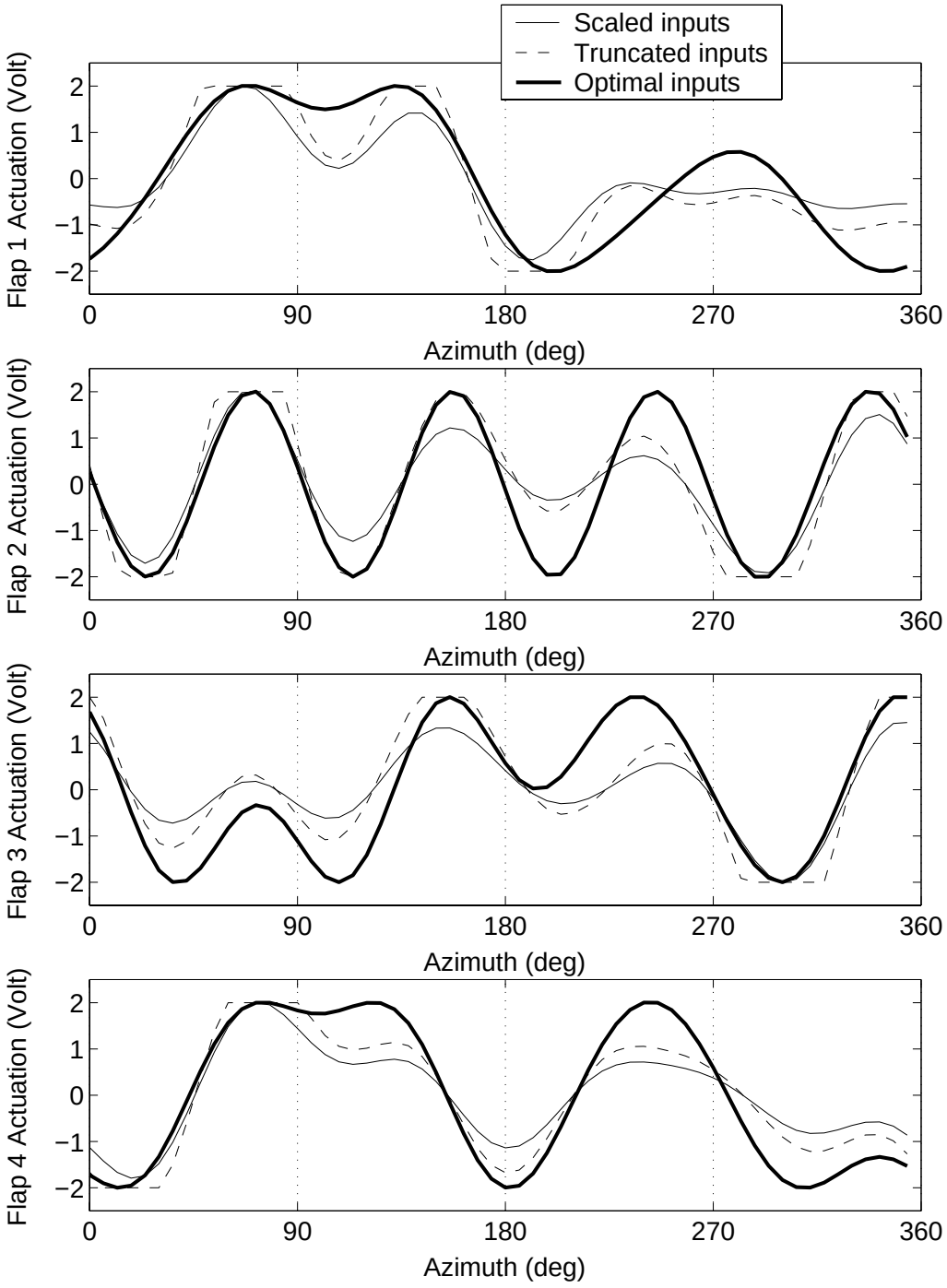

Figure 8.37: Predicted reduction of 1/rev and 4/rev hub pitching moment M_y using different limiting methods: optimal flap inputs

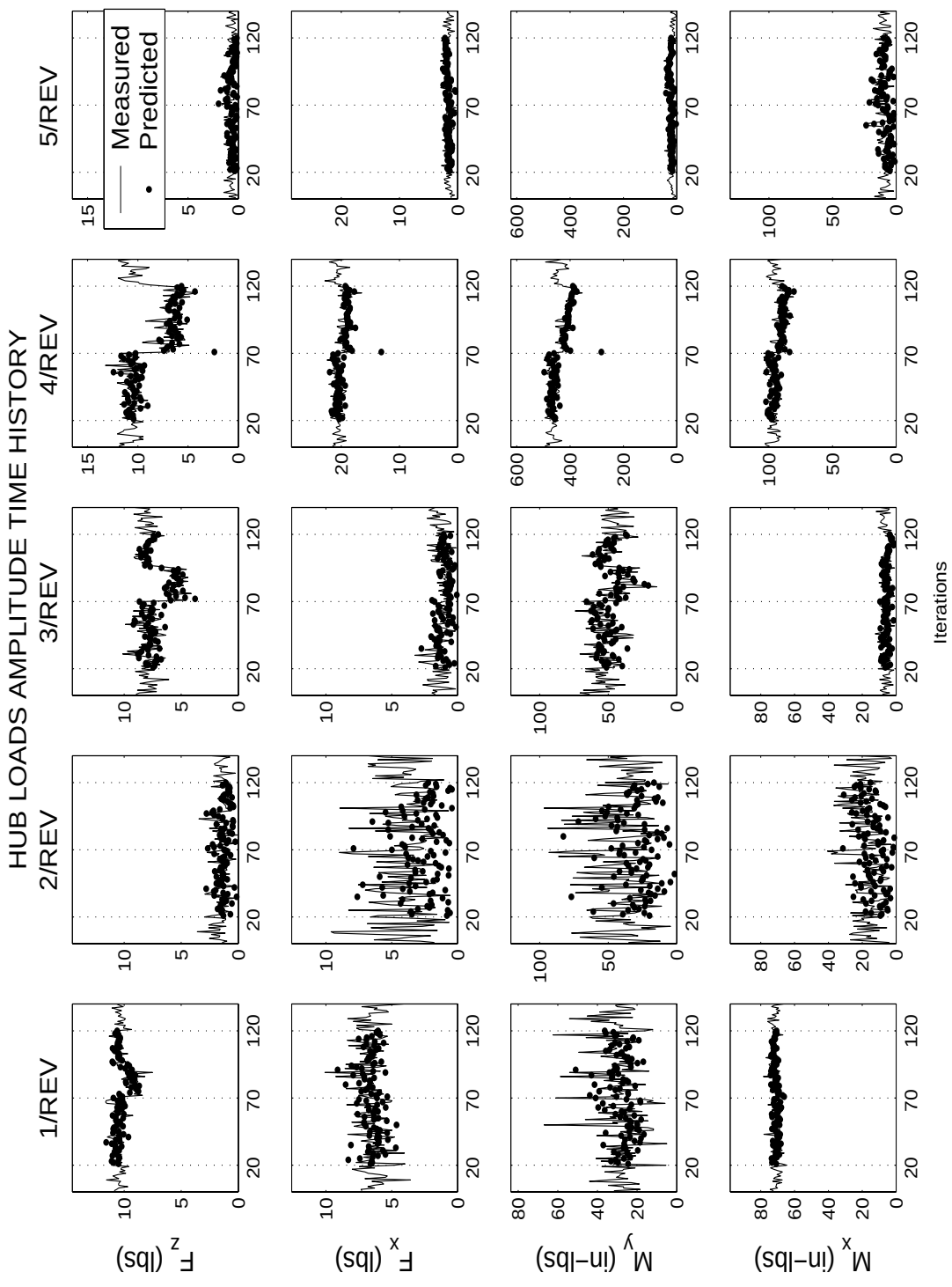

Figure 8.38: Target reduction of 4/rev hub pitching moment M_y with $\theta_0 = 6°$: effect on hub loads

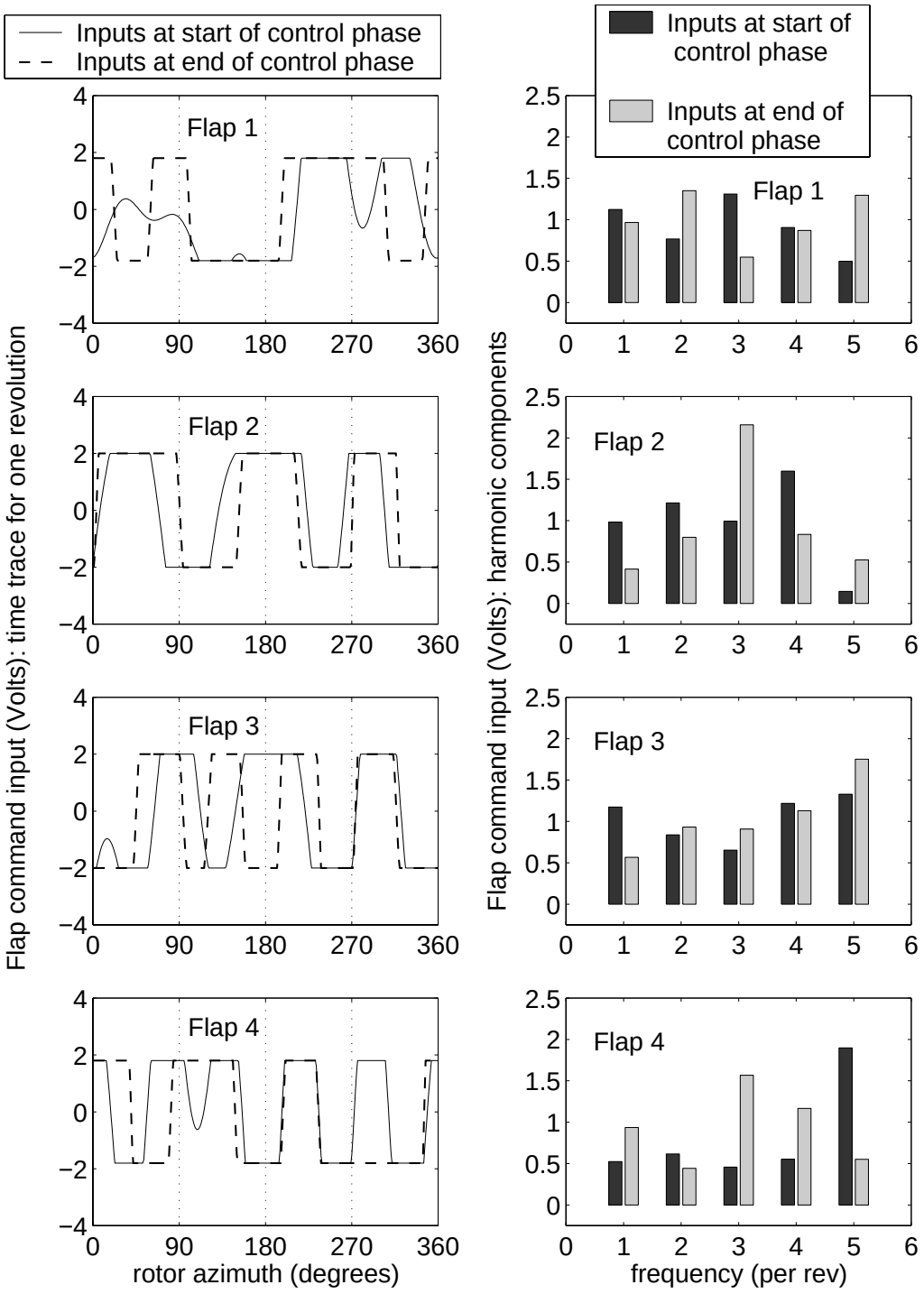

Figure 8.39: Target reduction of 4/rev hub pitching moment M_y with $\theta_0 = 6°$: optimal flap inputs

harmonics are reduced: the 1/rev is reduced by about 10%, the 3/rev by about 30%, and the 4/rev by about 40%. However, the normal force is not included in the objective function. As control inputs are updated and vibration reduction increases for the hub pitching moment, both the 1/rev and 3/rev components for the normal force go back to their baseline value. The 4/rev components of other hub loads are also slightly reduced.

In Figure 8.38, measured values are shown together with values predicted using the identified parameters. The predicted values are shown as black dots. From the time history of the 4/rev pitching moment, it can be seen that at iteration 70, the controller is turned on, and the vibration level suddenly drops. However, the predicted vibration level is much smaller than the measured one. This is because of the truncation method used to limit control inputs to ± 200 Volts. The actual input to the flap is truncated, therefore contains harmonics higher than 5/rev, however identification is performed considering only the first 5 harmonics.

Figure 8.39 compares the control inputs applied to the four flaps at the start and at the end of the control phase. Significant differences exist between the two signals. In particular, the 3/rev component is more than doubled for flaps 2 and 4 during the control phase.

Figures 8.40 and 8.41 compare the predicted controller performance using different methods to apply limits. For this test case, results are comparable using any of the three methods. Slightly improved vibration reduction is predicted using the SQP method (32% reduction in the 4/rev component). Table 8.2.4 summarizes the results from the previous four tests.

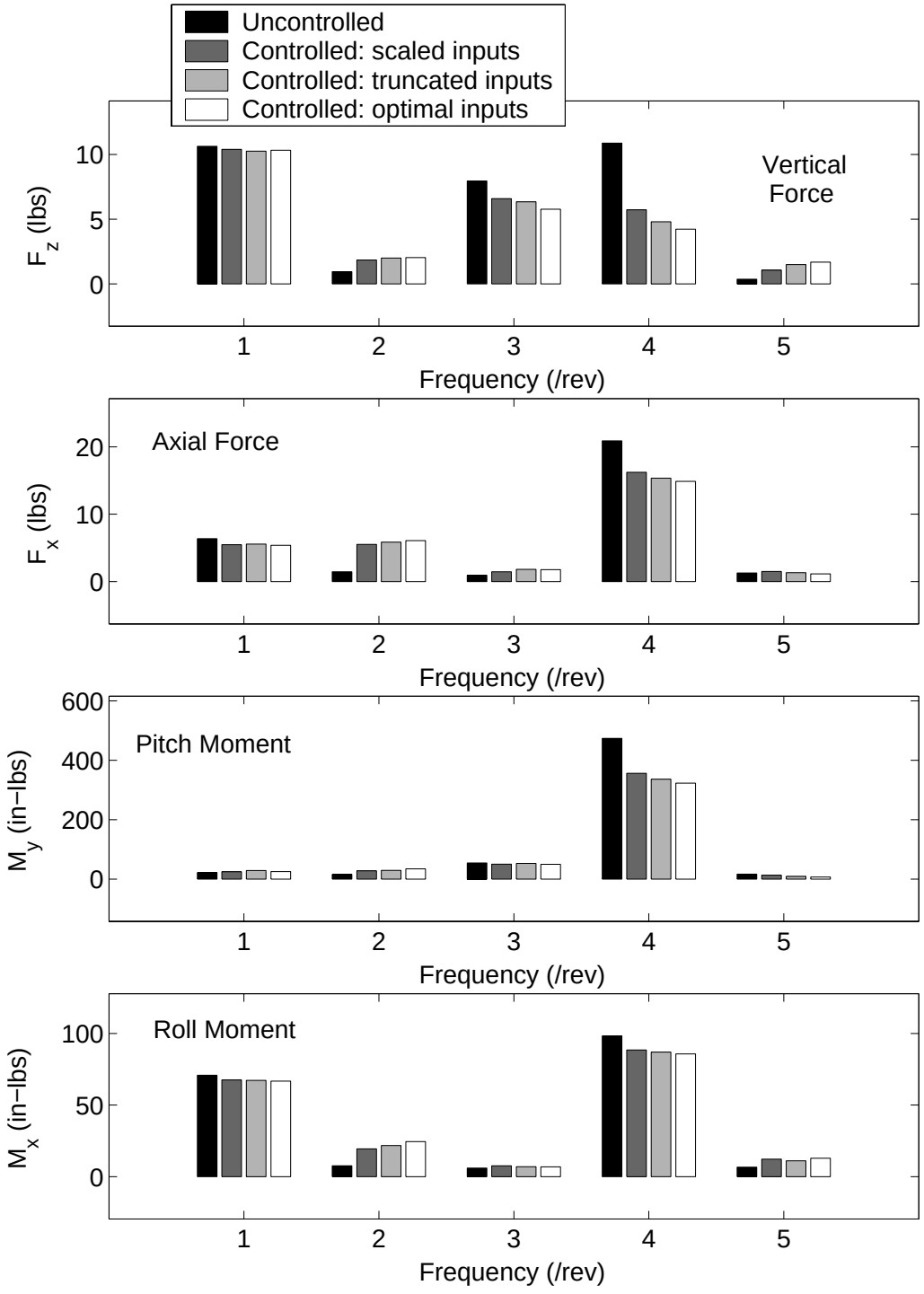

Figure 8.40: Predicted reduction of 4/rev hub pitching moment M_y with $\theta_0 = 6°$ using different limiting methods

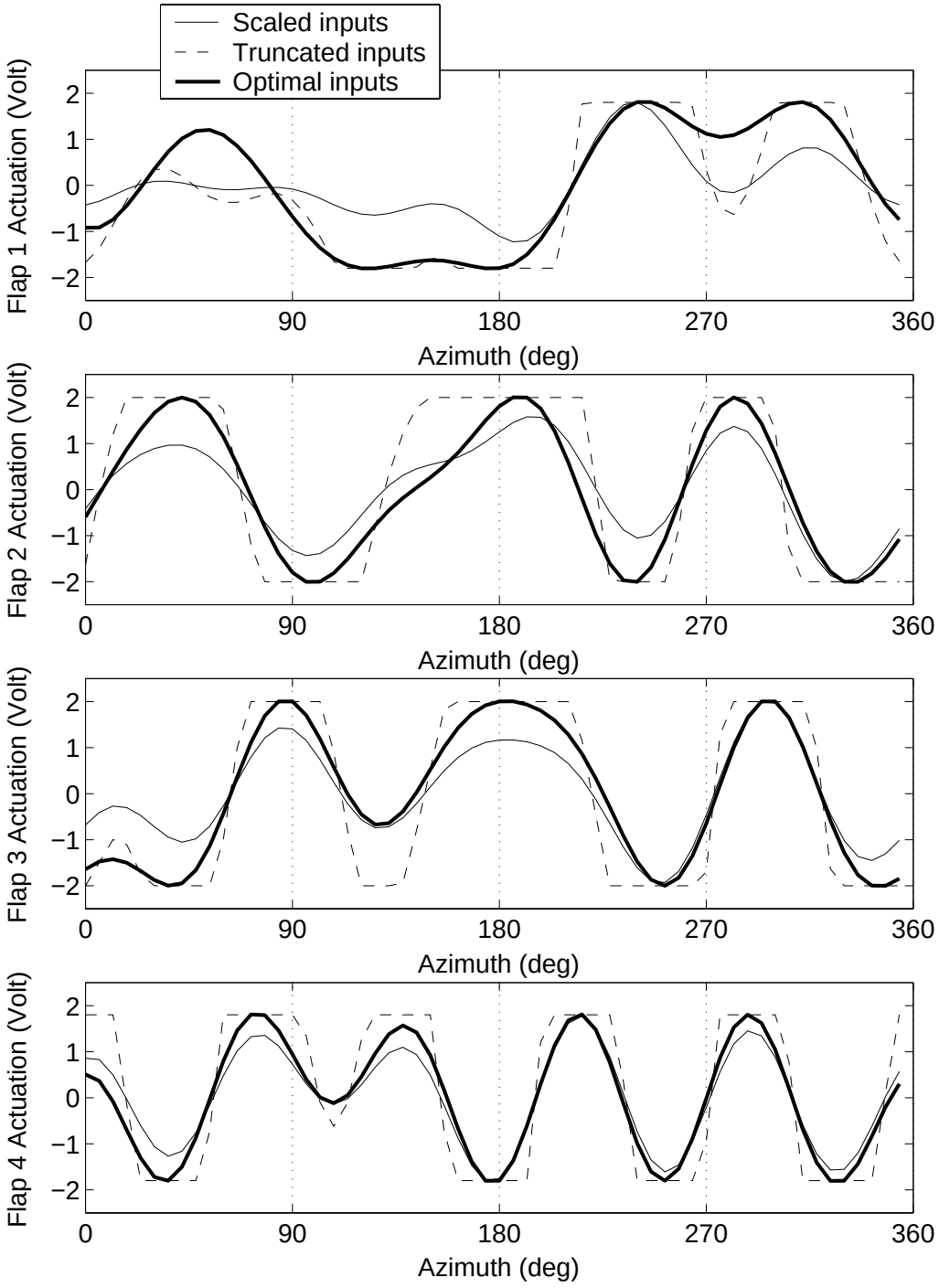

Figure 8.41: Predicted reduction of 4/rev hub pitching moment M_y with $\theta_0 = 6°$ using different limiting methods: optimal flap inputs

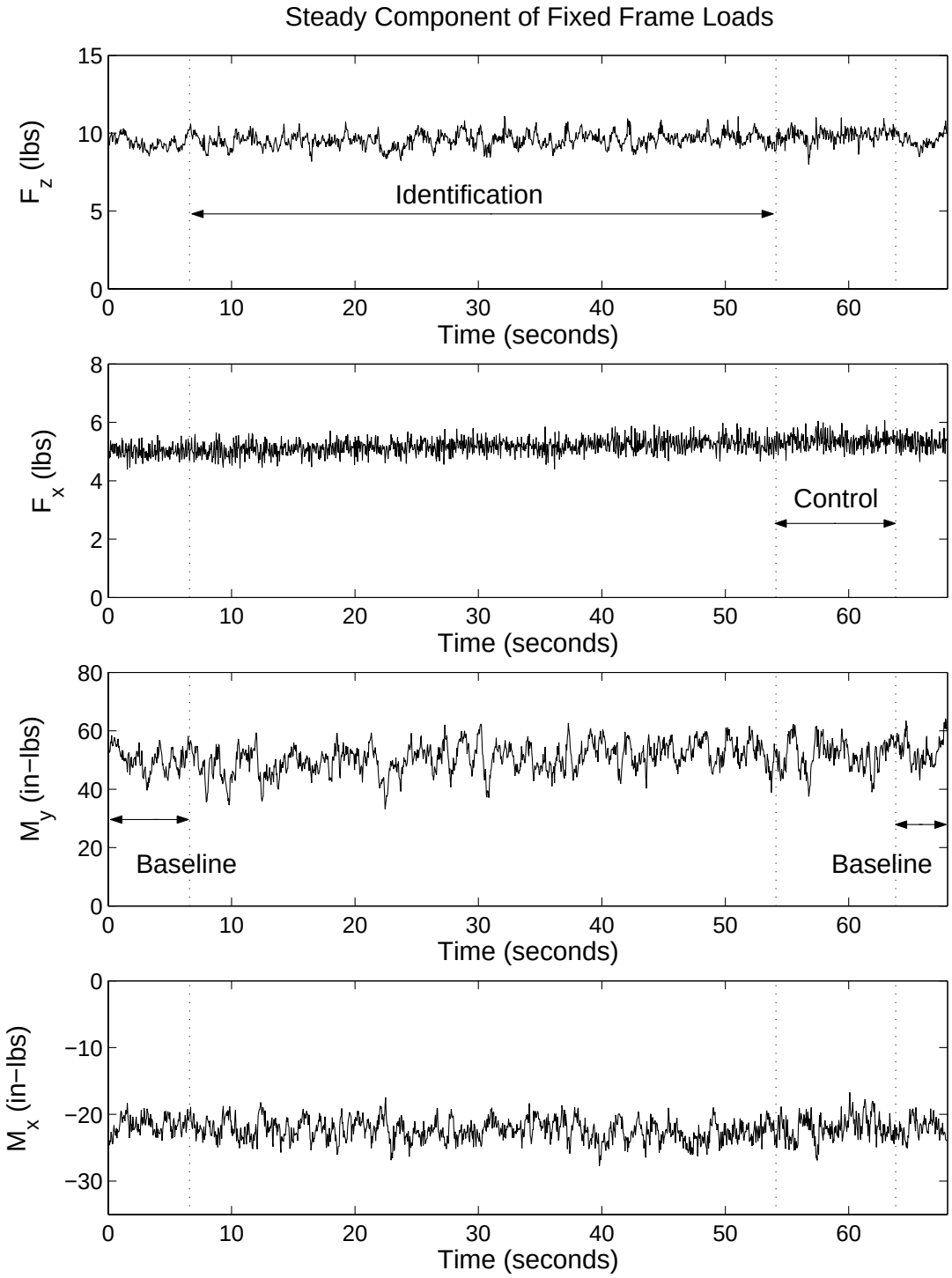

Figure 8.42: Time history of steady hub loads for test 1

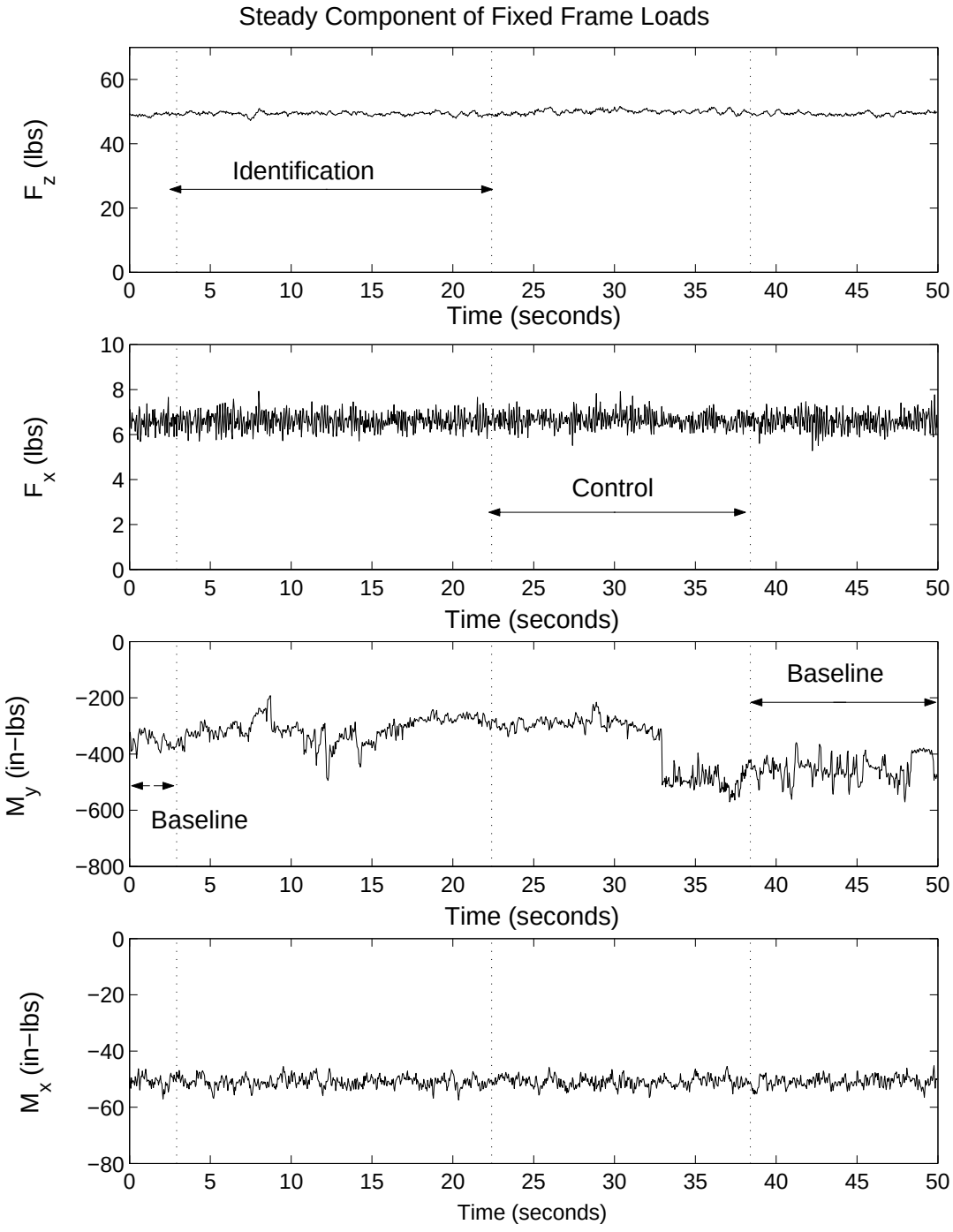

Figure 8.43: Time history of steady hub loads for test 4

Control objective	θ_0	**Measured vibration reduction**	**Predicted vibration reduction**		
			scaled inputs	*truncated inputs*	*optimized inputs*
F_z, 1/rev	2°	50%	31%	40%	42%
M_y, 4/rev	2°	62%	67%	77%	90%
M_y, 1 and 4/rev	2°	43%	61%	71%	90%
M_y, 4/rev	6°	21%	25%	29%	32%

Table 8.1: Test results summary

8.2.5 Effect of flap deflections on steady hub loads

The command input signal to the trailing edge flaps contains harmonics from 5/rev to 1/rev. Low frequency excitation such as 1/rev could affect the steady components of hub loads and perturb the equilibrium of helicopter forces and moments. In the controller simulation using a mathematical model of the helicopter, this potential problem is avoided by including the steady components in the objective function (Chapter 3):

$$\begin{aligned} J_F &= Y^T W_F Y \\ Y &= F - (F_0)_{mean} \end{aligned} \tag{8.1}$$

where F is the vector of the fixed system hub loads and $(F_0)_{mean}$ is the vector of steady components for all hub loads. Therefore, when Y is minimized, the vibratory part of each hub loads is minimized while the trim conditions are still satisfied.

However, in the present experimental investigation, steady components of fixed frame loads are not included, because of concerns over drifting in the steady output of the fixed frame balance. The objective function consists only of the

vibratory part of vibration:

$$\begin{aligned} J_F &= Y^T W_F Y \\ Y &= [F_{1c}\, F_{1s} \cdots F_{5s}\, F_{5s}] \end{aligned} \tag{8.2}$$

The variation of the steady components of four of the fixed frame loads is shown in Figures 8.42 and 8.43 for the entire closed loop test duration. Figure 8.42 corresponds to the first test described in this section (objective is to reduce the 1/rev of the normal force). The total duration of this test is about 70 seconds: the initial identification period lasts about 50 seconds, after which control is turned on for about 10 seconds. Before the identification period and after the control period, no inputs are applied to the flaps ("baseline periods"). Variations can be observed about the steady component of each load, in particular for the hub pitching moment. However, these variations also occur in the baseline phases when the flaps are inactive. Figure 8.43 corresponds to the last test described in this section (objective is to reduce the 4/rev of the hub pitching moment). For this test, the collective blade pitch angle is 6°, compared to 2° for the previous test. The identification period lasts about 20 seconds, after which control is on for about 15 seconds. Large and sudden changes in the steady component of the hub pitching moment can be observed, that occur for all phases of the test, including baseline. These changes do not correlate with any flap deflection but may originate from malfunction of the signal conditioners. Steady components for other fixed frame loads do not show significant variations.

8.2.6 Effect of flap deflections on rotating frame loads

In the present experimental investigation, only fixed frame vibrations were targeted. However, minimization of vibratory fixed frame loads may result in increase in blade loads. Figures 8.44 and 8.45 show the time history of the root

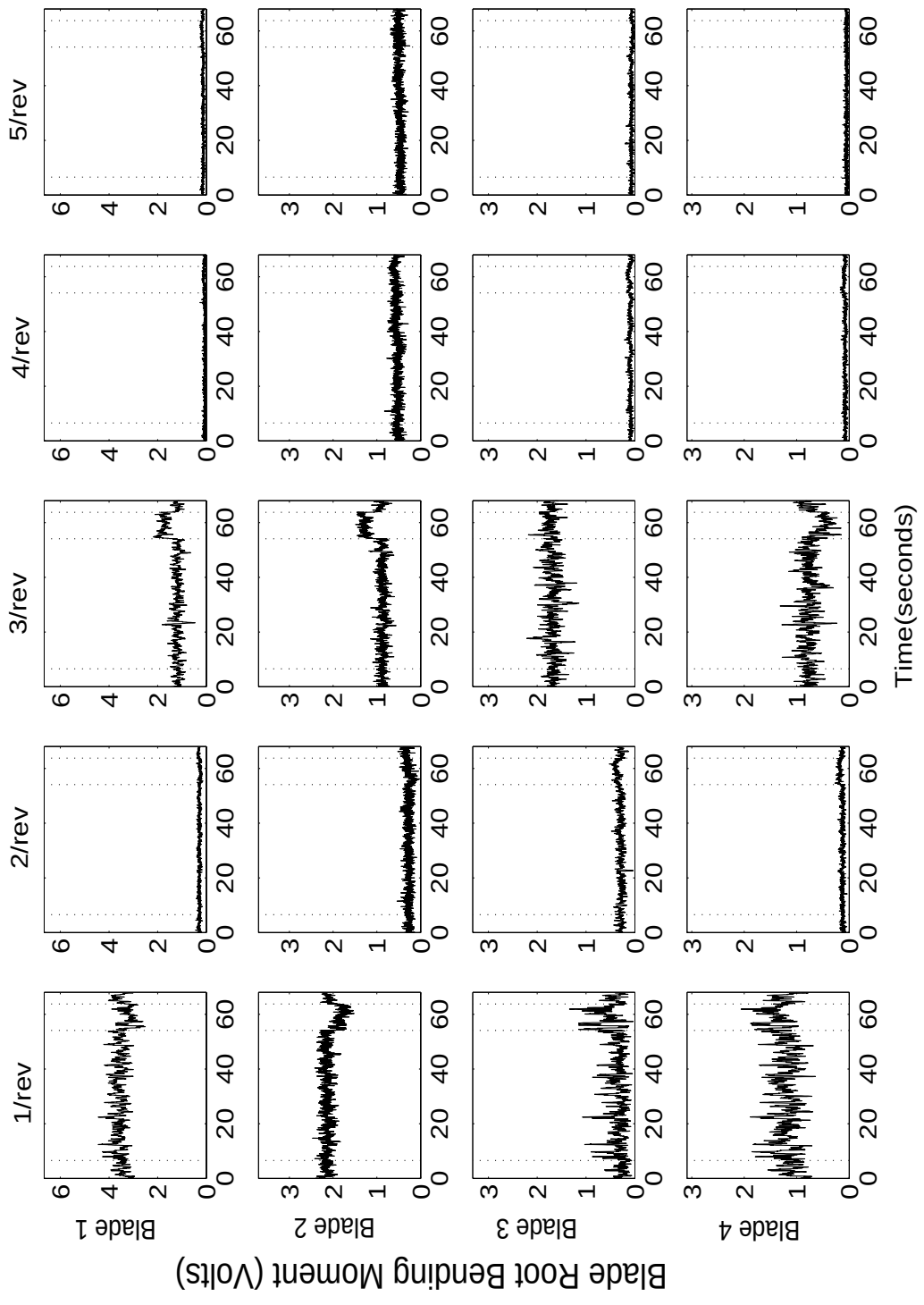

Figure 8.44: Time history of blade root bending moment harmonics during test 1

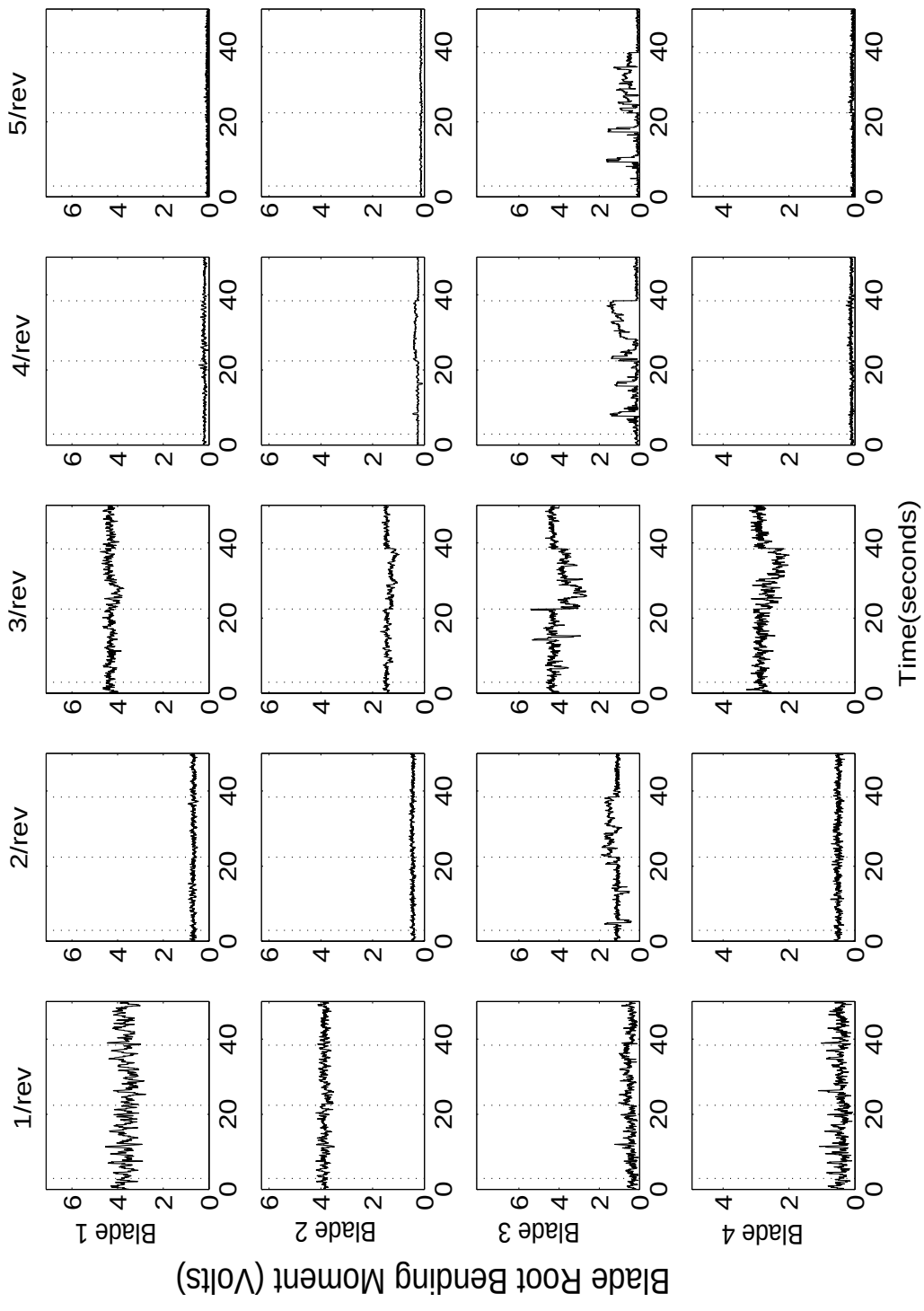

Figure 8.45: Time history of blade root bending moment harmonics during test 4

bending moment for each blade, during two of the closed loop tests. Figure 8.44 corresponds to the first test described in this section (objective is to reduce the 1/rev of the normal force). Blade root bending moments for this flight condition consist mainly of 1/rev and 3/rev components. After closed loop control begins, the 1/rev component of the root bending moment decreases for blade 1 and 2, while for blades 3 and 4, it increases slightly. On the contrary, the 3/rev component increases for blade 1 and 2, while it decreases for blade 4, and no change can be seen for blade 3. Note that the baseline 1/rev blade root bending moments for blade 3 and 4 are much smaller than for blade 1 and 2. This is because the rotor was trimmed by minimizing these signals before the test was started. Figure 8.45 corresponds to the last test described in this section (objective is to reduce the 4/rev harmonic of hub pitching moment, with collective blade pitch angle increased to 6°). The main harmonic components at this flight condition are also 1/rev and 3/rev. Again, 1/rev components are very small for blades 3 and 4, used for trim. After control, the 3/rev components for blade 3 and 4 are slightly reduced, and the 4/rev and 5/rev components for blade 3 are increased. Changes in root bending moment for other blades are very small.

8.3 Chapter Summary

The controller's ability to minimize fixed frame vibratory loads at both 4/rev and 1/rev frequencies is investigated, both on the hover stand and in forward flight. A Mach-scaled rotor with piezo-bender trailing edge flaps is used for this investigation, with all four flaps active simultaneously.

In hover, vibratory hub loads consist mainly of a 1/rev harmonic component. The controller is able to minimize the 1/rev component of the normal force by over 90% using small amplitude flap deflections (about ±2°). In hover, the 4/rev

part of vibration is negligible. In order to investigate the controller's ability to affect both the 1/rev and 4/rev parts of fixed frame vibration simultaneously, the control objective is set to reduce the 1/rev part and simultaneously generate a 4/rev of given amplitude and phase. The controller is able to reduce the 1/rev component by 83%, and generate a 4/rev component with the correct phase. However, the 4/rev amplitude is only about 40% of the target value, because of the actuators' saturation. When the minimization of the 1/rev is removed from the control objective, a 4/rev vibratory component is generated with correct phase and amplitude at 70% of the target value. These results are then contrasted with results obtained using phase-shifted inputs. Phase shifted inputs cannot reduce efficiently the 1/rev component. However, when the control objective is the generation of a 4/rev component, using phase shifted inputs yields better results (both amplitude and phase of the generated signal are equal to the target values). This is explained by the scaling method used to limit the actuation voltage. When the constrained minimization problem is solved off-line, and the output applied to the rotor blades, it is possible to meet the control objective perfectly using individual flap inputs.

After preliminary hover tests, the smart rotor is used to investigate the controller's ability to minimize vibratory hub loads in forward flight. Closed loop tests were conducted in the Glenn L. Martin wind tunnel, at a rotor speed of 1500 RPM, and advance ratio 0.25. The key conclusions are as follows:

1. With collective blade angle of 2°, the hub normal force consists of large 1/rev and 3/rev components and smaller 4/rev component. The 1/rev component is reduced by about 50%. However, this is accompanied by an increase in the 1/rev component of other loads.

2. The hub pitching moment vibration consists mainly of a large 4/rev component, and a small 1/rev component. The 4/rev component can be reduced

by over 60%. This is accompanied by a reduction in the 4/rev hub rolling moment and axial force, however, the 4/rev normal force is increased.

3. With a larger collective angle (6°), the hub pitching moment consists of a large 4/rev component. This component is reduced by 25%. The normal force consists of 1/rev, 3/rev and 4/rev components of comparable magnitude. These components can be reduced simultaneously, by 10%, 30%, and 40%, respectively, without any adverse effects on other loads.

4. Solving the minimization problem with non-linear constraints yields much improved results. However, this procedure is very time consuming and cannot be implemented in real-time during the wind tunnel testing with the computer available.

5. The effect of flap deflections on the steady components of hub loads is very small. There is a small effect on the blade root bending moment. This effect is different for each blade, with vibration increasing at some harmonics and decreasing at other harmonics.

Chapter 9

Closure

9.1 Summary

This dissertation presents an investigation of a control method to reduce vibrations in helicopters using actuators on the rotor blades. The novelty of the method is that each blade is controlled independently, taking into account possible blade dissimilarities. This is different from previous control approaches that assumed blades were identical and generated single control input which is applied with adequate phase shift to each blade.

9.1.1 Control Method

The mathematical problem of the controller is presented in detail in Chapter 3. The controller is developed in discrete time, with the control inputs updated every rotor revolution. The method consists of performing simultaneous system identification (using Kalman filtering technique) and closed loop control (using a deterministic control law) at each time step.

For the system identification, different inputs are applied to each blade, and a Kalman filtering method is used to estimate on-line the relationship between

the individual blade inputs and the resulting loads in the fixed frame. This relationship is assumed to be linear time periodic.

For the control part, optimal inputs are computed based on the minimization of a quadratic cost function, including the vibratory loads to be minimized. The weighted norm of the control inputs is also included in the cost function to maintain the actuation command within practical limits.

Helicopter parameters (actuation command, measured vibration, and the transfer function which relates them) can be expressed either as time samples over one rotor revolution, or as a number of harmonic components. The first approach is chosen for analytical investigations, while the second one is used for the experiments.

9.1.2 Controller simulation using analysis

In order to establish the feasibility of the method, the controller is first investigated using a simplified rotor model with only the blade flap degree of freedom modeled (Chapter 4). Rotor dissimilarities are modeled by changes in mass, stiffness, and aerodynamic properties of the damaged blade. The effects of the measurement noise and varying flight condition are investigated.

A comprehensive rotor analysis, including all blade degrees of freedom and a free wake model for computing the inflow across the rotor disk, is then used to investigate the controller performance in detail (Chapter 5). The rotor model is based on a modern bearingless rotor that includes detailed modeling of trailing edge flap effects. The controller performance is tested at advance ratios from $\mu = 0.10$ to $\mu = 0.40$, both for the baseline rotor with identical blades and the damaged rotor with dissimilar blades. The rotor faults are modeled as changes in inertial and aerodynamic properties for the damaged blades. The performance of the present control method is compared to that of a classical control method

which uses identical inputs for all trailing edge flaps.

9.1.3 Experimental validation of the controller

In order to test the controller experimentally, a Mach-scale rotor model is fabricated (Chapter 6). The rotor model consists of 4 blades with piezo-ceramic actuated trailing edge flaps. Two trailing edge flap leverage mechanisms are designed. Compared to a hinge based mechanism, a flexure based mechanism shows increased flap deflection at the nominal rotor speed. A set of four Mach scaled smart blades incorporating the flexure-hinged trailing-edge flaps are then fabricated. Tests are conducted in the vacuum chamber and at the hover stand to characterize flap deflections under centrifugal and aerodynamic loading. The control algorithm is adapted for real-time use and tested initially using a simple experimental set-up.

The smart rotor model is then fitted on a bearingless model-scale hub and tested both on a hover stand and in a closed section wind tunnel. First, closed loop tests are conducted in hover and forward flight to minimize the vibratory blade root flap bending moment (Chapter 7). For these tests, up to three blades were active simultaneously. The controller performance is also investigated in a transient flight condition during which the rotor speed is increased.

Next, the controller's ability to minimize fixed frame vibratory loads in presence of blade dissimilarities is investigated, both in hover and forward flight conditions (Chapter 8). For these tests, all blades are activated simultaneously.

In hover condition, vibratory hub loads consist mainly of a 1/rev harmonic component while the 4/rev part of vibration is insignificant. In order to investigate the controller's ability to effect both the 1/rev and 4/rev parts of fixed frame vibration simultaneously, the control objective is set to reduce the 1/rev part and simultaneously generate a 4/rev of given amplitude and phase. Closed-loop

tests are conducted using the present control method which uses independent flap inputs, as well as a classical control that uses phase-shifted flap inputs. The performance of both methods is compared. It is observed that performance can be limited by actuator saturation. Different methods to account for actuator saturation are described.

After preliminary hover tests, the smart rotor is used to investigate the controller's ability to minimize vibratory hub loads in forward flight. Closed loop tests are conducted in the Glenn L. Martin wind tunnel, at a rotor speed of 1500 RPM, and an advance ratio of 0.25. The effect of closed loop control on all the vibratory hub loads is discussed, and its effect on the steady values of hub loads and the rotating frame blade loads is examined.

9.2 Conclusions

1. Following are the conclusions obtained from the feasibility study conducted using the rotor comprehensive analysis.

   (a) In the case of the dissimilar rotor, comprehensive analysis predicted that allowing independent control inputs for each blade dramatically would improve the vibration reduction compared to restricting the control inputs to be specific phase shifted versions of each other.

   (b) At $\mu = 0.30$, the vibration index reduction increased from less than 45% to more than 90% using about 2.5° half peak-to-peak flap deflections (compared to the phase shifted approach) for both the structural and aerodynamic faults.

2. From the fabrication efforts, it was observed that for the model-scale rotor, flexures can be used advantageously instead of rod-in-tube type hinges to

provide the flap articulation. Using flexures leads to less friction and free play in the mechanism, as well as a cleaner blade profile. Using a flexure articulation, flap deflection of $\pm 4^{\circ}$ were achieved at 1800 RPM.

3. Following are the conclusions noted from the closed-loop tests conducted to reduce rotating frame loads.

   (a) The controller could successfully reduce rotating frame loads in different blades simultaneously. In hover, at 500 RPM, the 1/rev root bending moment was reduced by 77% with three simultaneously active blades.

   (b) In forward flight, several harmonic components could be reduced simultaneously: At 1200 RPM, and wind speed of 27 MPH ($\mu = 0.13$), vibration in the rotating frame was primarily 1 and 3/rev. The 1/rev component could be reduced by 66% and the 3/rev component by 34% simultaneously.

   (c) The controller performance was also investigated in a transient flight condition (increase of rotor speed), while the adaptive controller feedback system was on. It was demonstrated that vibration levels were maintained below uncontrolled levels at all times during the transient test.

4. Following are the conclusions noted from the closed-loop tests conducted both in hover and forward flight conditions that targeted minimization of fixed frame vibratory loads.

   (a) In hover, at 1500 RPM, the controller was able to minimize the 1/rev component of the normal force by over 90% using small amplitude flap deflections (about $\pm 2^{\circ}$). In order to demonstrate ability of controller

to effect vibration at 4/rev and 1/rev simultaneously, the generation of a 4/rev component of prescribed amplitude and phase was included in the control objective. The controller was then able to reduce the 1/rev component by 83%, and generate a 4/rev component with the correct phase. However, the 4/rev amplitude was only about 40% the target value, as a result of actuator saturation. When the minimization of the 1/rev was removed from the control objective, a 4/rev vibratory component was generated with correct phase and amplitude at 70% of the target value. These results were then contrasted with results obtained using phase-shifted inputs. Phase shifted inputs could not reduce efficiently the 1/rev component. However, when the control objective is the generation of a 4/rev component alone, using phase shifted inputs yields better results (both amplitude and phase of the generated signal were equal to the target values). This is explained by the scaling method used to limit the actuation voltage. When the constrained minimization problem is solved off-line, and the output applied to the rotor blades, it is possible to meet the control objective perfectly using independent flap inputs.

(b) Tests were conducted in the Glenn L. Martin wind tunnel, at a rotor speed of 1500 RPM, and advance ratio 0.25, to reduce vibration in the fixed frame.

1. With collective blade angle of 2°, the hub normal force consists largely of 1/rev and 3/rev components and a smaller 4/rev component. The 1/rev component was reduced by about 50%. However, this was accompanied by an increase in the 1/rev component of other loads.
2. The hub pitching moment vibration consisted mainly of a large

4/rev component, and a small 1/rev component. The 4/rev component could be reduced by over 60%. This was accompanied by a reduction in the 4/rev of the hub rolling moment and axial force, however, the 4/rev of the normal force was increased.

3. At a larger collective angle (6°), the hub pitching moment consisted of a large 4/rev component. This component was reduced by 25%. The normal force consisted of 1/rev, 3/rev and 4/rev components of comparable magnitude. These components could be reduced simultaneously by 10%, 30%, and 40%, respectively, without any adverse effects on other loads.
4. Solving the minimization problem with non-linear constraints yielded much improved results. However, this procedure is very time consuming and could not be implemented in real-time with the available computer.

9.3 Recommendations for Future Work

1. Reduce the computation time by using a faster platform, such as a dSPACE system to run the controller.

2. Refine the method to account for actuator saturation. Ideally, this method should generate optimal blade inputs identical to the solution obtained by solving the optimization problem with non-linear constraints, for example using the Sequential Quadratic Programming method. The method should also be fast enough to be implemented in real-time.

3. Eliminate actuator-flap free play by using flexures to transfer actuator stroke to the flaps, in addition to providing the flap articulation. Also the flexure design can be improved to increase its fatigue life.

4. Optimize actuator design to achieve more force for a given stroke. There is a need to refine analysis of piezo-bender actuators to achieve accurate behavior prediction without using empirical factors.

5. Use the input/output data collected in the present hover and forward flight tests to investigate the performance of different types of controllers (for e.g. using neural network based controllers) both to identify the system and compute control inputs.

6. Validate the data collected in the present hover and forward flights with rotor comprehensive predictions.

7. Devise actuators with greater authority and extend the control objectives to noise reduction, simultaneous reduction of rotating and fixed frame loads and rotor performance enhancement.

REFERENCES

[1] Bousman, W., "Putting the Aero Back Into Aeroelasticity", Eigth ARO Workshop on Aeroelasticity of Rotorcraft Systems, University Park, PA, October 18-20, 1999.

[2] Ellis, C.W., and Jones,R., "Application of an Absorber to Reduce Helicopter Vibration Levels", *Journal of the American Helicopter Society*, 8(3):30-38, July 1963.

[3] Schuett, E.P., "Application of Passive Helicopter Rotor Isolation for Alleviation of Rotor Induced Vibration", *Journal of the American Helicopter Society*, 14(2):34-48, April 1969.

[4] Amer, K.B., and Neff, J.R., "Vertical Plane Pendulum Absorbers for Minimizing Helicopter Vibratory Loads",*Journal of the American Helicopter Society*, 19(4):44-48, October 1974.

[5] Taylor, R.B., "Helicopter Vibration Reduction by Rotor Blade Modal Shaping", American Helicopter Society, Annual Forum, 38th, Anaheim, CA; 4-7 May 1982. pp. 90-101. 1982

[6] Leconte, P., and Geoffroy, P., "Dynamic Optimization of a Rotor Blade", Aeromechanics Specialists Conference on Aerodynamics, Acoustics and Dynamics, San Francisco, CA; 19-21 Jan. 1994. pp. 5.2-1 to 5.2-9.

[7] Lim, J.W., "Aeroelastic Optimization of a Helicopter Rotor", Ph.D. Thesis, University of Maryland, College Park, MD, 1988.

[8] Bao, J., Nagaraj, V.T., Chopra, I., and Bernhard, A.P.F., "Development of a Low Vibration Mach Scale Rotor with Composite Couplings", American

helicopter Society 58th Annual Forum Proceedings - Volume II, Montreal, Canada; 11-13 June 2002. pp. 2081-2094.

[9] Staple, A.E., "An Evaluation of Active Control of Structural Response as a Means of Reducing Helicopter Vibration", 15th European Rotorcraft Forum, pages 51.1-51.18, Amsterdam, The Netherlands, September 1989.

[10] Stape, A.E., and Wells, D.M., "Development and Testing of an Active Control of Structural Response System for the EH101 Helicopter", 16th European Rotorcraft Forum, Glasgow, Scotland, September 1990.

[11] Welsh, W.A., von Hardenberg, P.C., and Staple A.E., "Test and Evaluation of Fuselage Vibration Utilizing Active Control of Structural Response (ACSR) Optimized to ADS-27", American Helicopter Society 46th Forum, pages 21-37, Washington DC, May 1990.

[12] Welsh, W., and Millott, T., "Helicopter Active Noise and Vibration Reduction", 25th European Rotorcraft Forum, Rome, Italy, September 1999, paper G-23.

[13] Shaw, J., and Albion, N., "Active Control of Helicopter Rotor for Vibration Reduction",*Journal of the American Helicopter Society*, Vol.25, (3), pp.32-39, July 1980.

[14] Nguyen, K., and Chopra, I., "Application of Higher Harmonic Control to Rotors Operating at High Speed and Thrust", *Journal of the American Helicopter Society*, Vol 35,(3), 1990, pp. 78-89.

[15] Nguyen, K., and Chopra, I., "Effects of Higher Harmonic Control (HHC) on performance and control loads",*Journal of Aircraft*, Vol.29, (3), May-June 1992.

[16] Payne, P.R., "Higher Harmonic Control",*Aircraft Engineering*, Vol.30, (354), pp.222-226, August 1958.

[17] Nguyen, K., and Chopra, I., "Application of Higher Harmonic Control (HHC) to Hingeless Rotors", Vertica, Vol.14,(4), pp.545-556, October 1990.

[18] Hammond, C. E., "Wind Tunnel Results Showing Rotor Vibratory Loads Reduction Using Higher Harmonic Blade Pitch", *Journal of the American Helicopter Society*, Vol 28,(1), January 1983, pp. 10-15.

[19] Shaw, J., Albion, N., Hanker, E.J., and Teal, R.S., "Higher Harmonic Control: Wind Tunnel Demonstration of Fully Effective Vibratory Hub Forces Suppression", *Journal of the American Helicopter Society*, Vol 34,(1), January 1989, pp. 14-25.

[20] Nguyen, K., Betzina, M., and Kitaplioglu, C., "Full-Scale Demonstration of Higher Harmonic Control for Noise and Vibration Reduction on the XV-15 Rotor", *Journal of the American Helicopter Society*, Vol 46,(3), July 2001, pp. 182-191.

[21] Sissingh, G.J., and Donham, R.E., "Hingeless Rotor Theory and Experiment on Vibration Reduction by Periodic Variation of Conventional Controls", NASA SP-352, 1974, pp.261-277.

[22] Wood, E.R., Powers, R.W., Cline, C.H., and Hammond, C.E., "On Developing and Flight Testing a Higher Harmonic Control System", *Journal of the American Helicopter Society*, Vol 30,(1), January 1985, pp. 3-20.

[23] Miao, W., Kottapali, S.B.R., and Frye, H.M., "Flight Demonstration of Higher Harmonic Control on the S-76", American Helicopter Society Forum, Washington D.C., June 1986.

[24] Achache, M., and Polychroniadis, M., "Higher Harmonic Control: Flight Tests on an Experimental System on an SA-349 Research Gazelle", American Helicopter Society Forum, Washington D.C., June 1986.

[25] Polychroniadis, M., "Generalized Higher Harmonic Control - Ten Years of Aerospatiale Experience", European Rotorcraft Forum, 16th, Glasgow, Scotland; 18-21 Sept. 1990. 10 p. pp. 1990

[26] Guinn, K.F., "A Preliminary Investigation of Individual Blade Control Independent of a Swashplate", American Helicopter Society, National Specialists Meeting on Rotor System Design, Philadelphia, PA 9 p pp. Oct. 1980.

[27] Kretz, M., "Research in Multi-cyclic and Active Control of Rotary Wings", *Vertica*, Vol.1, No.1/2, 1976, pp.95-105.

[28] Guinn, K.F., "Individual Blade Control Independent of a Swashplate", *Journal of the American Helicopter Society*, Vol 27,(3), July 1982, pp. 25-31.

[29] Ham, N.D., "Helicopter Individual Blade Control and its Applications", American Helicopter Society 39th Annual Forum, St. Louis, MO, May 1983, pp. 613-623.

[30] Ham, N.D., "A Simple System for Helicopter Blade Individual Blade Control using Model Decomposition", *Vertica*, Vol.4, (1/2), pp.23-28, 1980.

[31] Ham, N.D., "Helicopter Individual Blade Control Research at M.I.T., 1977-1985", *Vertica*, Vol.11, (1/2), pp.109-122, 1987.

[32] Richter, P., and Blaas, A., "Full Scale Wind Tunnel Investigation of an Individual Blade Control System for the BO-105 Hingeless Rotor", 19th European Rotorcraft Forum, Cernobbio, Italy, September 1993, pp. G5.1-G5.12.

[33] Richter, P., Eisbrecher, H.D., and Kloppel, V., "Design and First Flight Tests of Individual Blade Control Actuators", 16^{th} *European Rotorcraft Forum*, Glasgow, Scotland, September 1990.

[34] Jacklin, S. A., and Nguyen, K., Blaas, A., and Richter, P., "Full-Scale Wind Tunnel test of a Helicopter Individual Blade Control System", American Helicopter Society 50th Annual Forum, Washington, DC, May 1994, pp. 579-596.

[35] Jacklin, S.A., Nguyen, K., Richter, P., and Blaas, A., "Reduction in Helicopter BVI Noise, Vibration, and Power Consumption through Individual Blade Control", American Helicopter Society 51th Annual Forum, Fort Worth, TX, May 1995.

[36] Teves, D., Kloppel, V., and Richter, P., "Development of Active Control Technology in the Rotating System, Flight Testing and Theoretical Investigations", 18^{th} *European Rotorcraft Forum*, September 1992.

[37] Kube, R., Van der Wall, B.G., Schultz, K.J., and Splettstoesser, W.R., "IBC Effects on BVI Noise and Vibrations - A Combined Numerical and Experimental Investigation", AHS International Annual Forum, 55th, Montreal, Canada; 25-27 May 1999. pp. 2282-2291.

[38] Jacklin, S.A., Haber, A., de Simone, G., Norman, T.R., Kitaplioglu, C., Shinoda, P., "Full-Scale Wind Tunnel Test of an Individual Blade Control System for a UH-60 Helicopter", AHS International, 58th Annual Forum Proceedings - Volume I, Montreal, Canada; 11-13 June 2002. pp. 1103-1114.

[39] Haber, A., Jacklin, S., deSimone, G., "Development, Manufacturing, and Component Testing of a Control System or a UH-60 Helicopter Rotor", American Helicopter Society Aerodynamics, Acoustics, and Test and Evaluation

Technical Specialists Meeting , San Francisco, CA, January 23-25, 2002.

[40] Arnold, U.T.P., and Strecker, G., "Certification, Ground and Flight-Testing of an Experimental IBC System for the CH-53G Helicopter", AHS International, 58th Annual Forum Proceedings - Volume I, Montreal, Canada; 11-13 June 2002. pp. 297-308.

[41] Kessler, C., Fuerst, D., and Arnold, U.T.P., "Open Loop Flight Test Results and Closed Loop Status of the IBC system on the CH-53G Helicopter", American Helicopter Society International 59^{th} Forum, Phoenix, AZ, May 6-8, 2003.

[42] Wei, F.S., and Gallagher, F., "Servo-Flap Rotor Performance Flight Testing and Data Identification", AHS International Annual Forum, 57th, Washington, DC, May 9-11, 2001.

[43] Rocconella, B., and Wei, F., "Wind Tunnel Model Testing of the Improved K-MAX Servo-Flap Blade Section", American Helicopter Society International 57^{th} Forum, Washington D.C., May 9-11 2001, pp.1805-1911.

[44] Lemnios, A.Z., and Dunn, F.K., "Theoretical Study of Multicyclic Control of a Controllable Twist Rotor", Technical reports NASA-CR-141959, NASA, April 1976.

[45] McCloud, J.L., and Weisbrich, A.L., "Wind Tunnel Test Results of a Full Scale Multicyclic Controllable Twist Rotor", American Helicopter Society 34^{th} Forum, Washington, DC, May 1978.

[46] Dawson, S., Hassan, A., and Straub, F.K., "Wind Tunnel Test of an Active Flap Rotor: BVI Noise and Vibration Reduction", American Helicopter Society 51^{th} Forum, Fort Worth, TZ, May 1995, pp. 631-648.

[47] Dawson, S., and Straub, F.K., "Design, Validation, and Testing of a Model Rotor with Tip Mounted Active Flaps", American Helicopter Society 50^{th} Forum, Washington, DC, May 1994.

[48] Straub, F.K., "Active Flap Control for Vibration Reduction and Performance Improvement", American Helicopter Society 51^{th} Forum, Fort Worth, TZ, May 1995.

[49] Bernhard, A.P.F., O'Neill, J., Kohlhepp, F., Welsh, W., and Lorber, P., "Active Rotor Control (ARC) of a Mach-Scale Trailing Edge Flap Rotor", American Helicopter Society 57^{th} Forum, Washington, DC, May 2001.

[50] Millott, T.A., and Friedmann, P.P., "Vibration Reduction in Helicopter Rotors Using an Active Control Surface Located on the Blade", 33rd AIAA/ASME/ASCE/AHS/ASC Structures, Structural Dynamics and Materials Conference, Dallas, TX, April 13-15, 1992, pp. 1975.

[51] Millott, T.A., and Friedmann, P.P., "Vibration Reduction in Rotorcraft using Active Control: a Comparison of Various Approaches", *Journal of Guidance, Control, and Dynamics*, Vol.18, (4), 664-673, August 1995.

[52] Millott, T.A., and Friedmann, P.P., "Vibration Reduction in Rotorcraft using the Actively Controlled Trailing Edge Flap and Issues Related to Practical Implementation", American Helicopter Society 54th Annual Forum, Washington, DC, May 1998

[53] Milgram, J., and Chopra, I., "Parametric Design Study for Actively Controlled Trailing Edge Flaps", *Journal of the American helicopter Society*, Vol 43,(2), 1998, pp. 110-115.

[54] Milgram, J., "A Comprehensive Aeroelastic Analysis of Helicopter Main Rotors With Trailing Edge Flaps For Vibration Reduction," Ph.D Thesis,

University of Maryland, 1997.

[55] Chopra, I., "Status of Application of Smart Structures Technology to Rotorcraft Systems", *Journal of the American Helicopter Society*, Vol 45,(4), October 2000, pp. 228-252.

[56] Straub, F.K., "A Feasibility Study of Using Smart Materials for Rotor Control", *Smart Materials and Structures*, Vol 5,(1), February 1996, pp. 1-10.

[57] Friedmann, P.P., and Millott, T.A., "Vibration Reduction in Rotorcraft using Active Control - A Comparison of Various Approaches", *Journal of Guidance, Control, and Dynamics*, Vol. 18, no. 4, pp. 664-673. July-Aug. 1995.

[58] Chopra, I., "Review of State of Art of Smart Structures and Integrated Systems",*AIAA journal*, Vol.40, (11), November 2002.

[59] Samak, D.K., and Chopra, I., "Design of High Force, High Displacement Actuators for Helicopter Rotors", Smart structures and intelligent systems; Proceedings of the Conference, Orlando, FL, pp. 86-98, 14-16 Feb. 1994.

[60] Walz, C., Chopra, I, "Design and Testing of a Helicopter Rotor Model with Smart Trailing Edge Flaps", AIAA/ASME Adaptive Structures Forum, Hilton Head, SC, pp. 309-319, 21-22 Apr. 1994.

[61] Ben-Zeev, O., and Chopra, I., "Advances in the Development of an Intelligent Helicopter Rotor Employing Smart Trailing Edge Flaps", *Smart Materials and Structures*, Vol.5,(1), pp.11-25, Feb.1996.

[62] Koratkar, N.A., and Chopra, I., "Wind Tunnel Testing of a Smart Rotor Model with Trailing-Edge Flaps", *Journal of the American helicopter Society*, Vol 47,(4), 2002, pp. 263-272.

[63] Hall, S.R., and Spangler, R., "Piezoelectric Actuators for Helicopter Rotor Control", AIAA/ASME/ASCE/AHS/ASC Structures, Structural Dynamics and Materials Conference, 31st, Long Beach, CA, pp. 1589-1599, 2-4 Apr. 1990.

[64] Fulton, M.V., and Ormiston, R.A., "Hover Testing of a Small-Scale Rotor with On-Blade Elevons", *Journal of the American Helicopter Society*, Vol. 46, no. 2, pp. 96-106. Apr. 2001.

[65] Moskalik, A.J., and Brei, D., "Quasi-Static Behavior of Individual C-block Piezoelectric Actuators", *Journal of Intelligent Material Systems and Structures*, Vol. 8, no. 7, pp. 571-587. July 1997.

[66] Clement, J.W., Brei, D., and Barrett, R., "Wind Tunnel Testing of a High Authority Airspeed Insensitive Rotor Blade Flap", AIAA/ASME/ASCE/AHS/ASC Structures, Structural Dynamics, and Materials Conference and Exhibit, 40th, St. Louis, MO, pp. 2414-2424, 12-15 Apr. 1999.

[67] Prechtl, E.F., and Hall, R.S., "Design of a High Efficiency, Large Stroke, Electromechanical Actuator", *Smart Materials and Structures*, Vol 8,(1), February 1999, pp. 13-30.

[68] Prechtl, E F; Hall, S R, "An X-frame Actuator Servo-Flap Actuation System for Rotor Control", Smart structures and integrated systems; Proceedings of the Meeting, San Diego, CA; pp. 309-320, 2-5 Mar. 1998.

[69] Hall, S R; Tzianetopoulou, T, "Design and Testing of a Double X-Frame Piezoelectric Actuator", Smart structures and materials 2000 - Smart structures and integrated systems; Proceedings of the Conference, Newport Beach, CA; 6-9 Mar. 2000. pp. 26-37.

[70] Chen, P.C., "Development of a Smart Rotor with Induced-Strain Actuation of Blade Twist", PhD thesis, University of Maryland, Aerospace Department, College Park, MD, 1996.

[71] Chen, P.C., and Chopra, I., "Hover Test of a Smart Rotor with Induced Strain Actuation of Blade Twist",*AIAA journal*, Vol.35(1),p.6-16, January 1997.

[72] Chen, P.C., and Chopra, I., "Development of a Smart Rotor with Induced Strain Actuation of Blade Twist",*Journal of Intelligent Material Systems and Structures*, Vol.8,(4),p.414-425.

[73] Hagood, N.W., and Bent, A.A., "Development of Piezoelectric Fiber Composites for Structural Actuation", AIAA/ASME/ASCE/AHS/ASC Structures, Structural Dynamics, and Materials Conference, 34th and AIAA/ASME Adaptive Structures Forum, La Jolla, CA, pp. 3625-3638, 19-22 April 1993.

[74] Bent, A.A., and Hagood, N.W., "Piezoelectric Fiber Composites with Interdigitated Electrodes", *Journal of Intelligent Material Systems and Structures*, vol. 8, no. 11, pp. 903-919. Nov. 1997

[75] Rodgers, J.P., and Hagood, N.W., "Preliminary Mach-scale Hover Testing of an Integral Twist-Actuated Rotor Blade", Smart structures and integrated systems, Proceedings of the Meeting, San Diego, CA; pp. 291-308, 2-5 Mar. 1998.

[76] Wickramasinghe, V.K., Hagood, N.W., "Durability Characterization of Active Fiber Composite Actuators for Helicopter Rotor Blade Applications", *Journal of Aircraft*, vol. 41, no. 4, July 2004, p. 931-937

[77] Rodgers, J.P., "Development of an Integral Twist-actuated Rotor Blade for Individual Control", PhD thesis, Massachusetts Institute of Technology,

Department of Aeronautics and Astronautics, Cambridge, MA, October 1998.

[78] Cesnik, C.E.S., Shin, S., Wilkie, W.K., Wilbur, M.L., and Mirick, P.H., "Modeling, Design, and Testing of the NASA/ARMY/MIT Active Twist Rotor Prototype Blade" American Helicopter Society International Annual Forum, 55th, Montreal, Canada; pp. 533-544, 25-27 May 1999.

[79] Derham, R., Weems, D., Mathew, M.B., and Bussom, R., "The Design Evolution of an Active Materials Rotor", American Helicopter Society International Annual Forum, 57th, Washington, DC; May 9-11 2001.

[80] Bernhard, A.P.F., Chopra, I., "Development of a Smart Moving Blade Tip Activated by a Piezo-Induced Bending-Torsion Coupled Beam" Smart structures and materials 1996: Smart structures and integrated systems; Proceedings of the Meeting, San Diego, CA, pp. 63-79, 26-29 Feb. 1996.

[81] Bernhard, A.P.F., Chopra, I., "Hover Testing of Active Rotor Blade-Tips using a Piezo-Induced Bending-Torsion Coupled Beam", *Journal of Intelligent Material Systems and Structures*, Vol. 9, no. 12, pp. 963-974, Dec. 1998.

[82] Bernhard, A.P.F., "Smart Helicopter Rotor with Active Blade Tips", Ph.D. thesis, University of Maryland, Department of Aerospace Engineering, College Park, MD, 2000.

[83] Schimke, D., Jaenker, P., Wendt, V., and Junker, B., "Wind Tunnel Evaluation of a Full Scale Piezoelectric Flap Control Unit", European Rotorcraft Forum, 24^{th}, Marseilles, France; pp. TE02.1-TE02.12, 15-17 Sept. 1998.

[84] Janker, P., Kloppel, V., Hermle, F., Lorkowski, T., Storm, S., Christmann, M., and Wettemann, M., "Development and Evaluation of a hybrid piezoelectric actuator for advanced flap control technology", European Rotorcraft Forum, 25th, Rome, Italy, Paper G-21, Sept. 1999.

[85] Duvernier, M., Reithler, L., Guerrero, J.Y., and Rossi, R., "Active Control System for a Rotor Blade Trailing-Edge Flap" Smart structures and materials 2000 - Smart structures and integrated systems; Proceedings of the Conference, Newport Beach, CA, pp. 52-61. 6-9 Mar. 2000.

[86] Toulmay, F., Kloppel, V., Lorin, F., Enenki, B., and Gaffiero, J., "Active Blade Flaps - the Needs and Current Capabilities", American Helicopter Society 57th Annual Forum, Washington DC, May 9-11, 2001.

[87] Fink, D.A., Hawkey, T.J., Gaudreau, M.P.J., Wellman, B, and Ormiston, R.A., "An Electromagnetic Actuator for Individual Blade Control" American Helicopter Society International 56th Annual Forum, Virginia Beach, VA, pp. 786-797, 2-4 May 2000.

[88] Straub, F.K., Ealey, M.A., and Schetky, L.M.D., "Application of Smart Materials to Helicopter Rotor Active Control", Smart structures and materials 1997: Industrial and commercial applications of smart structures technologies; Proceedings of the Meeting, San Diego, CA, pp.99-113, 4-6 Mar. 1997.

[89] Straub, F.K., and Charles, B.D., "Comprehensive Modeling of Rotors with Trailing Edge Flaps", AHS International Annual Forum, 55th, Montreal, Canada, pp. 523-532, 25-27 May 1999.

[90] Straub, F.K., Ngo, H.T., Anand, V., and Domzalski, D.B., "Development of a Piezoelectric Actuator for Trailing Edge Flap Control of Full Scale Rotor Blades", *Smart Materials and Structures*, Vol. 10, no. 1, pp. 25-34. Feb. 2001.

[91] Lee, T., and Chopra, I., "Design of Piezostack-Driven Trailing-Edge Flap Actuator for Helicopter Rotors", *Smart Materials and Structures*, Vol. 10, no. 1, pp. 15-24. Feb. 2001.

[92] McKillip, R. M. Jr, "Periodic Control of The Individual Blade Control Helicopter Rotor," *vertica*, Vol. 9, (2), Feb 1985, pp. 23-28.

[93] Epps, J J; Chopra, I, "In-Flight Tracking of Helicopter Rotor Blades using Shape Memory Alloy Actuators", AIAA/ASME/ASCE/AHS/ASC Structures, Structural Dynamics, and Materials Conference and Exhibit, 40th, St. Louis, MO; 12-15 Apr. 1999. pp. 2734-2743.

[94] Singh, K., Sirohi, J., and Chopra, I., "An Improved Shape Memory Alloy Actuator for Rotor Blade Tracking", *Journal of Intelligent Material Systems and Structures*, Vol. 14, No. 12, 767-786, 2003.

[95] Giurgiutiu, V; Rogers, C A; Zuidervaart, J, "Incrementally Adjustable Rotor-Blade Tracking Tab using SMA Composites", AIAA/ASME/ASCE/AHS/ASC Structures, Structural Dynamics, and Materials Conference and Exhibit, 38th, and AIAA/ASME/AHS Adaptive Structures Forum, Kissimmee, FL; 7-10 Apr. 1997. pp. 1456-1466.

[96] Kennedy, D.K., Straub, F.K., Schetky, L.M., Chaudhry, Z. and Roznoy, R., "Development of a SMA Actuator for In-Flight Rotor Blade Tracking", Smart structures and materials 2000 - Smart structures and integrated systems; Proceedings of the Conference, Newport Beach, CA; 6-9 Mar. 2000. pp. 62-75.

[97] Hall, S.R.; Spangler, Jr.; Ronald L., "Piezoelectric Helicopter Blade Flap Actuator", Massachusetts Institute of Technology (Cambridge, MA), U.S. patent 5,224,826 , July 1989.

[98] McKillip, R., " "Digital" SMA-based Tracking Tabs for One-Per-Rev Vibration Reduction", American helicopter Society 59th Annual Forum Proceedings Phoenix, AZ, pp.1692-1719, May 2003.

[99] Kretz, M., Auburn, J. N. and Larche, M., "Wind Tunnel Tests for Dorand DH 2011 Jet Flap Rotor," Vol. 1, NASA CR-114693, 1973a.

[100] McCloud, J. L., III, and Kretz, M., "Multicyclic Jet-Flap Control for Alleviation of Helicopter Blade Stresses and Fuselage Vibration," Rotorcraft Dynamics, NASA SP-352, pp. 233-238.

[101] McCloud, J. L., III, "The Promise of Multicyclic Control of Helicopter Vibration Reduction," *vertica*, Vol. 4, no. 1, 1980a.

[102] Shaw, J., "Higher Harmonic Pitch Control : A System for Helicopter Vibration Reduction," Ph.D. Thesis, Massachusetts Institute of Technology, May 1980.

[103] Johnson, W., "Self-Tuning Regulators for Multicyclic Control of Helicopter Vibration", NASA TP 1996, March 1982.

[104] Chopra, I., and McCloud, J.L., "Numerical Simulation Study of Open-Loop, Closed-Loop and Adaptive Multicyclic Control Systems", *Journal of the American helicopter Society*, Vol 28,(1), 1983, pp. 63-77.

[105] Gupta, N.K., and Du Val, R.W., "A New Approach for Active Control of Rotorcraft Vibration",*Journal of Guidance and Control*, April 1982.

[106] Du Val, R. W., Gregory, C. Z. Jr., and Gupta, N. K., "Design and Evaluation of a State-Feedback Vibration Controller," *Journal of the American Helicopter Society*, Vol 29, (3), Jul. 1984, pp. 30-37.

[107] Hall, S. R. and Wereley, N. M., "Linear Control Issues in the Higher Harmonic Control of Helicopter Vibrations", AHS, Annual Forum, 45th, Boston, MA, pp. 955-971, 22-24 May 1989.

[108] Hall, S. R. and Wereley, N. M., "Performance of Higher Harmonic Control Algorithms for Helicopter Vibration Reductions," *Journal of Guidance, Control and Dynamics*, Vol. 16, (4), April 1992, pp. 793-797.

[109] Kottapilli, S., "Identification and Control of Rotorcraft Hub Loads using Neural Networks," Presented at the American Helicopter Society 53rd Annual Forum, Virginia Beach, Virginia, April 29 - May 1, 1997.

[110] Spencer, M., G., "Development of a Real Time Adaptive Neural Network Controller For Active Rotorcraft Vibration Reduction" Ph.D Thesis, University of Maryland, 2000.

[111] Bernhard, A.P.F., and Chopra, I., "Hover Test of Mach-Scale Active Twist Rotor using Piezo-Bending-Torsion Actuators", *Journal of Aircraft*, Vol 39,(4), 2002, pp. 678-688.

[112] Spencer, M.G., Sanner, R.M., and Chopra, I., "Adaptive Neurocontrol of Simulated Rotor Vibrations Using Trailing Edge Flaps", *Journal of Intelligent Material Systems and Structures*, Vol 10,(11), 2000, pp. 855-871.

[113] Spencer, M.G., Sanner, R.M., and Chopra, I., "Closed-Loop Neurocontroller Tests on Piezoactuated Smart Rotor Blades in Hover", *AIAA journal*, Vol 40,(8), 2002, pp. 1596-1602.

[114] Spencer, M.G., Sanner, R.M., and Chopra, I., "Adaptive Neurocontroller for Vibration Suppression and Shape Control of a Flexible Beam", *Journal of Intelligent Material Systems and Structures*, Vol 9,(3), 1998, pp. 160-170.

[115] Roget, B., and Chopra, I., "Individual Blade Control Methodology for a Rotor with Dissimilar Blades", *Journal of the American Helicopter Society*, Vol 48,(3), Jul 2003, pp. 176-185.

[116] Bir., G., Chopra, I., et al., "University of Maryland Advanced Rotorcraft Code (UMARC) Theory Manual", Technical report UM-AERO 94-18, Alfred Gessow Rotorcraft Center, University of Maryland, College Park, MD, July 1994.

[117] Hodges D. H. and Dowell, E. H., "Nonlinear Equations of Motion for the Elastic Bending and Torsion of Twisted Nonuniform Rotor Blades," NASA TND-7818, 1974.

[118] Bagai, A. and Leishman, J.G., "The Maryland Free-Wake Analysis - Theory, Implementation and User's Manual," University of Maryland, Department of Aerospace Engineering, Technical Report Prepared for NASA Langley Research Center, Aeroacoustics Branch, Fluid Mechanics and Acoustics Division, Contract No. 015-2685, December 1995.

[119] Leishman, J.G., "Validation of Approximate Indicial Aerodynamics Functions for Two-Dimensional Subsonic Flow," *AIAA Journal*, Vol. 25, No. 10, Oct. 1993, pp. 914-922.

[120] Leishman, J. G., "Unsteady Aerodynamics of Airfoils Encountering Traveling Gusts and Vortices," *Journal of Aircraft*, Vol. 34, No. 6, 1997, pp. 719-729

[121] Theodorsen, T., "General Theory of Aerodynamic Instability and the Mechanism of Flutter," NACA Report 496, 1935.

[122] Wagner, H., "Uber die Entstehung des dynamischen Auftriesbes von Tragflugeln," *Zeitschrift fur angewandte Mathematik un Mechanick*, Vol. 5, No . 1, 1925, pp. 17-35.

[123] Hariharan, N., and Leishman, J. G., "Unsteady Aerodynamics of a Flapped Airfoil in Subsonic Flow by Indicial Concepts", *Journal of Aircraft*, Vol 33, (5), Sep-Oct 1996, pp. 855-868.

[124] Gelb, A., Kasper, J.F., Nash, R.A., Price, C.F., and Sutherland, A.A., *Applied Optimal Estimation*, the M.I.T. press, 1974, pp. 110.

[125] Roget, B., and Chopra, I., "Robust Individual Blade Control Algorithm for a Dissimilar Rotor", *Journal of Guidance, Control, and Dynamics*, Vol 25,(5), Sep-Oct 2002, pp. 915-923.

[126] Gandhi, F., and Chopra, I., "Aeroelastic Analysis Methodology for Bearingless Main Rotor Helicopters", *Journal of the American Helicopter Society*, Vol 43,(1), Jan 1998, pp. 66-75.

[127] Bagai, A., and Leishman, J.G., "Rotor Free-Wake Modeling using a Pseudo-Implicit Technique - Including Comparisons with Experimental Data", *Journal of the American Helicopter Society*, Vol 40,(3), 1995, pp. 29-41.

[128] Khanh, N., Lauzon, D., and Anand, V., "Computation of Loads on the McDonnell Douglas Advanced Bearingless Rotor", American Helicopter Society 50th Annual Forum, Washington, DC, May 1994, pp. 337-346.

[129] Ganguli, R., Chopra, I., and Haas, D.J., "Helicopter Rotor System Health Monitoring Using Numerical Simulation and Neural Networks", Proceedings of the American Helicopter Society 53^{rd} Annual Forum, Virginia Beach, April 29-May 1, 1997.

[130] Abbot, I.H., Von Doenhoff, A.E.,*Theory of Wing Section*, Dover publications, Inc., N.Y., 1959.

[131] Fletcher, R. and M.J.D. Powell, "A Rapidly Convergent Descent Method for Minimization", *Computer Journal*, Vol. 6, pp. 163-168, 1963.

[132] Goldfarb, D., "A Family of Variable Metric Updates Derived by Variational Means", *Mathematics of Computing*, Vol. 24, pp. 23-26, 1970.

[133] Koratkar, N., "Smart Helicopter Rotor with Piezoelectric Bender Actuated Trailing-Edge Flaps", Ph.D. Thesis, Aerospace Department, University of Maryland, College Park, MD, 2000.

[134] Morgan Matroc, Inc., electroceramics division, "Guide to piezoelectric ceramics", Manufacturers Data Sheet, Morgan Matroc Inc., Bedford, OH, May 1993.

[135] Rohm Performance Plastics, Rohacell 71 IG rigid foam, Product data sheet.

[136] Cytek Engineered Materials, Inc., Material Selector Guide, Havre de Grace, MD, 1995.

[137] Newport Adhesive and Composites, Inc., E-glass NB-11-1-12- product data sheet, Irvine, CA, June 1993.

[138] Vishay Micro Measurements, M-Bond 610 Adhesive, Instruction Manual B-130.

[139] Hall, S.R., and Prechtl, E.F., "Development of a Piezoelectric Servoflap for Helicopter Rotor Control",*Journal of Smart Materials and Structures*, Vol.5, pp.26-34, 1996.

[140] Xu, W., and King, T., "Flexure Hinges for Piezoactuator Displacement Amplifiers: Flexibility, Accuracy, and Stress Considerations",*Precision Engineering*, Vol 19, (1), pp. 4-10, July 1996.

[141] Quackenbush, T.R., "Testing and Evaluation of a Stall-Flutter-Suppression System for Helicopter Rotors Using Individual-Blade-Control", NASA-CR-166233, 1981.

[142] Yeo, H., and Chopra, I."Coupled Rotor/Fuselage Vibration Analysis Using Detailed 3-D Airframe Models", *Mathematical and Computer Modelling*, Vol.33, p.1035-1054, 2001.